CHARLES UNIVERSITY PRAGUE

faculty of mathematics and physics

GAS STRIPPING IN GALAXY CLUSTERS
A NEW SPH SIMULATION APPROACH

by

Pavel Jáchym

A thesis submitted in partial fulfillment
of the requirements for the degree of

Philosophiae Doctor

under a Cotutelle arrangement with
Charles University in Prague
and
Pierre & Marie Curie University in Paris

Supervisors:
Prof. Jan Palouš and **Prof. Françoise Combes**

Prague, September 2006

To my parents

Abstract

In this work, we present the results of numerical simulations of the ram pressure stripping occurring in galaxy clusters, using tree/SPH N-body code GADGET (Springel et al. 2001) that we had adapted for two unlike gas phases: the hot and diffuse intracluster medium (ICM), and the colder and denser interstellar medium (ISM). A galaxy moving in a cluster crosses the ICM and experiences a wind. Local density of the ICM and orbital velocity of the galaxy determine effects of the ram pressure on the galactic ISM. We perform an analysis of the influence of the galactic, cluster and orbital parameters on the stripping efficiency, including different galaxy types, sizes, masses and disk inclinations with respect to the ICM wind direction, diverse distributions of the cluster ICM, and various orbital shapes. The goal is in particular to take into account the finite time for the stripping interaction, as the galaxy passes quickly through the central region of the cluster. We compare the results with analytical approximations, with simple estimates of Gunn & Gott (1972) formula and with other recent simulations. Early and late type galaxies in large or small galaxy clusters show different rates of the stripping, with varying amount of the reaccreting ISM after the stripping event. Final mass of the ISM in the disk depends on the duration of the interaction. We discuss the origin of the ICM and its large metallicity.

Results of the part of the thesis dealing with the face-on stripping and with analytic approximations of the ISM-ICM interaction have been submitted to Astronomy & Astrophysics journal in September 2006.

Résumé

Dans ce travail, nous présentons les résultats de simulations numériques de balayage du gaz des galaxies par pression dynamique dans les amas, qui utilisent le code N-corps Tree/SPH GADGET développé par Springel et al. (2001), et que nous avons adapté pour traiter deux phases gazeuses différentes: le milieu chaud et diffus intra-amas (ICM), et le milieu interstellaire plus froid et plus dense (ISM). Une galaxie se déplaant dans l'amas ressent l'équivalent d'un vent provenant de l'ICM. La densité locale du gaz intra-amas et la vitesse orbitale de la galaxie déterminent les effets de la pression dynamique sur l'ISM de la galaxie. Nous avons effectué une analyse de l'influence des paramètres de l'amas de galaxies, des paramètres de la galaxie et de son orbite dans l'amas sur l'efficacité du balayage, incluant différents types de galaxies, différentes tailles, masses et inclinaisons du disque par rapport à la direction du vent, diverses distributions radiales de l'ICM dans l'amas, et diverses formes orbitales. Le but est en particulier de tenir compte de l'intermittence de l'interaction de balayage, car la galaxie passe rapidement par la région centrale de l'amas. Nous comparons les résultats aux approximations analytiques, aux évaluations simples par la formule de Gunn & Gott (1972) et aux autres simulations récentes. Les résultats dépendent du type morphologique de la galaxie (précoce ou tardif), de la taille et de la richesse de l'amas de galaxies, avec une perte de gaz plus ou moins grande, et méme une ré-accrétion ultérieure de gaz. La masse finale de l'ISM dans le disque dépend essentiellement de la durée de l'interaction. Nous discutons l'origine de l'ICM et de sa grande de métallicité.

Des résultats de la partie de la thèse traitant du balayage d'une galaxie vent de face et des approximations analytiques de l'interaction ISM-ICM ont été soumis au Journal Astronomy & Astrophysics en septembre 2006.

Preface

This thesis was written under a cotutelle arrangement between Charles University in Prague, Faculty of Mathematics and Physics and Pierre & Marie Curie University in Paris. I would like to thank my French supervisor, Mme Françoise Combes from the Paris Observatory and my Czech supervisor, Mr. Jan Palouš from the Astronomical Institute of the Academy of Sciences of the Czech Republic, for all their helpful advice, useful ideas and pertinent comments on this work and my research. I also wish to thank to Joachim Köppen for his fruitful inputs and discussions. Many thanks go to everyone whom I worked with at the Astronomical Institute of the Academy of Sciences for their valuable contributions to this project. I gratefully acknowledge support by the Institutional Research Plan AV0Z10030501 of the Academy of Sciences of the Czech Republic, by the project LC06014 Center for Theoretical Astrophysics and by the grant of EARA Marie Curie Training Site "EARASTARGAL". Some of the simulations have been carried out on the IBM Power 4 processors of the CNRS computing center at IDRIS (Palaiseau, France). I also thank to Volker Springel for his release of the code GADGET for cosmological N-body/SPH simulations on massively parallel computers with distributed memory.

I would like to thank my family, and Magdalena for their understanding, support and patience.

Préface

Cette thèse a été écrite dans le cadre d'un contrat de cotutelle entre l'Université Charles de Prague, et la faculté des Mathématiques et de Physique de Pierre et Marie Curie à Paris. Je voudrais remercier mon directeur de thèse français, Mme Françoise Combes de l'Observatoire de Paris et mon directeur de thèse tchèque, Mr Jan Palouš de l'Institut Astronomique de l'Académie des Sciences de la République Tchèque, de tous leurs conseils avisés, des idées utiles et des commentaires très précieux sur ce travail et ma recherche. Je souhaite également remercier Joachim Köppen pour ses contributions et discussions fructueuses. Beaucoup de remerciements vont à tous ceux avec qui j'ai travaillé à l'Institut Astronomique de l'Académie des Sciences pour leurs contributions à ce projet. Je remercie l'appui financier du plan institutionnel de recherches AV0Z10030501 de l'Académie des Sciences de la République Tchèque, du projet LC06014 du Centre d'Astrophysique Théorique et la subvention du réseau de formation "EARASTARGAL" du projet "Marie Curie" EARA. Certaines des simulations ont été effectuées sur le super-ordinateur IBM Power 4 du centre de calcul du CNRS à l'IDRIS (Palaiseau, France). Je remercie également Volker Springel pour sa mise à disposition du code GADGET de simulations cosmologiques N-corps/SPH pour des ordinateurs massivement parallèles à mémoire distribuée.

Je voudrais remercier ma famille, et Magdalena pour leur compréhension, appui et patience.

Contents

Introduction

Galaxies in clusters and rich environments are observed to be stripped of their interstellar medium, which quenches their subsequent star formation. The stripping can be due either to tidal interactions, spiral galaxy mergers into ellipticals, or ram pressure stripping from the intracluster gas. Both tidal and ram-pressure stripping are always tightly linked. Gunn & Gott (1972) assume that after the formation of a galaxy cluster, the remaining gaseous debris are thermalized via shock heating to virial temperatures corresponding to random motions in the cluster, e.g. to a few times 10^7K. This hot plasma at densities of about 5 10^{-4} cm^{-3} influences the ISM in disks of spiral galaxies, and can remove part of their gas through the ram pressure induced by the galaxy motions through the ICM.

The ram pressure stripping is difficult to model, since several complex gaseous phenomena are involved. The first aspect is the simple pressure force, and this can be modeled with a simple algorithm, with ballistic and sticky particles, to represent the gas (e.g. Vollmer et al. 2001). But the full hydrodynamical processes include thermal evaporation, turbulent and viscous stripping, and also outflows due to star formation.

The first note on the three-dimensional N-body/SPH simulations with the gravity tree to mimic the dynamical effect of the ram pressure on galaxies in clusters is by Kundić et al. (1993). The same approach has been adopted by Abadi et al. (1999) who represent the ICM as a flow of particles along a cylindric box of radius 30 kpc and thickness 10 kpc with periodic boundary conditions. For a spiral galaxy in face-on, edge-on or an inclined orientation relative to the ICM flow, they examine with the simulations the radius up to which the ISM is removed and compare the results with the prediction of Gunn & Gott (1972) criterion which assumes that the ISM is removed from the disk if the ICM ram pressure exceeds the restoring force.

The ISM is far from continuous: it consists of several components: hot, warm and cold medium. Hot ionized and warm neutral HI medium are much more continuous compared to cloudy, cold and molecular component. The SPH description relates more to the continuous ISM components, molecular clouds are not represented well in the SPH simulations. Vollmer et al. (2001a) adopted another approach: they use N-body simulations with sticky particles representing the inelastic collisions between molecular clouds. The ram pressure is included with an additional force acting on clouds in the wind direction. They introduced a time dependent ram pressure, which corresponds to the variations of the ICM density and of relative ICM-ISM velocity along the galaxy orbit in the cluster. They allow a moving ICM, which may increase its velocity relative the ISM to values higher than 4000 km s^{-1}.

With an isothermal SPH gas model, Abadi et al. (1999) show that gas stripping can be quite efficient in the core of rich clusters, on a time-scale of 10^7 yrs. The most efficient is face-on orientation. With an Eulerian code, Quilis et al. (2000) probed the efficiency of viscous coupling, enhanced by the presence of HI deficiencies in the center of galaxies. The ram pressure stripping does not depend strongly on the vertical structure and thickness of the gas disk (Roediger & Hensler 2005). In more details, the effect of inclination of the moving galaxy is important as long as the ram pressure is comparable to the gas pressure in the galaxy plane. In general the effect is similar for all inclinations except for edge-on (Roediger & Brüggen 2006). The orientation of the gas tail behind the galaxy is not a good tracer of the galaxy motion on its orbit. Acreman et al. (2003) simulate the infall of an elliptical galaxy, and its gas stripping by the ICM: the formation of an X-ray wake at the first passage should be observable.

The principal competing mechanism to perturb galaxies in clusters and strip their gas is tidal

interactions. High speed galaxy encounters in clusters, galaxy harassment events are efficient mechanisms to disturb galaxy disks, and provide stars to the intracluster space (Moore et al. 1995). Also low speed galaxy encounters in groups before the formation of the cluster are able to drag out tidal stellar tails and lead to galaxy mergers and formation of ellipticals, that are then known to be more numerous in clusters. The evolution of encounter debris in galaxy haloes has been followed by Mihos (2004).

Intracluster light is a consequence of tidal stripping of galaxies. It has been determined that intra-cluster stars are older than galaxy stellar populations, and more centrally concentrated in the cluster. The fraction of stars in the ICM is increasing with the richness of the cluster, it is usually a few percent of all stars, up to 20% (Arnaboldi et al. 2003, Murante et al. 2004). If the ICM metallicity can be explained partly by gas stripping from galaxies (Domainko et al. 2005), it can also come from intra-cluster supernovae exploding in the ICM. The irregular structures in galaxy clusters found in X-ray are tracing cold fronts and shocks due to galaxy interactions, or the infall of a group.

The fate of the stripped ISM in clusters is not clear: it can end very hot and become part of the ICM, or it can stay quite cold condensing into clouds with a molecular core and an HI outer boundary. Oosterloo & van Gorkom (2005) observe a large HI cloud near the center of the Virgo cluster, and suggest that this cloud has been ram-pressure stripped from the galaxy NGC 4388. The dense clumps in the HI plume might be molecular, and star formation could occur precisely at these high density places.

In this work, we focus on computations of the ram pressure stripping, to evaluate more precisely its efficiency and to determine the fate of the stripped gas. The goal is in particular to take into account the finite time for this stripping interaction, as the galaxy passes quickly through the central region of the cluster. Most computations until now were carried out in the hypothesis of a stationary wind of hot gas. But the ram-pressure acts only in a short lapse of time, as simulated by Vollmer et al. (2001). After this short period, certain fraction of the gas falls back onto the galaxy. These latter simulations did not take into account the pressure forces, and the hydrodynamical physics of the ISM-ICM interactions. Roediger, Brüggen & Hoeft (2006) have followed the wake of gas produced by a quasi-stationary wind; in the present work, the impulsive character of ram pressure stripping is on the contrary emphasized.

Assuming a static ICM described with a β-profile, we explore in detail the ISM-ICM during the galaxy crossing the central part of the cluster. The mass-loss rates are examined as a function of the galaxy type, size and mass. We are able to follow the gas stripped from the galaxy, forming a giant tail of material. We tackle the issue of the origin of the ICM, the actual role of gas stripping in building it, as a function of the cluster mass and richness. The importance of gas stripping could account for the metal enrichment of the ICM as a function of cluster type (e.g. Domainko et al. 2005, Schindler et al. 2005).

After general introduction in Chapter 1, we describe the environmental mechanism working in galaxy clusters and groups in Chapter 2. The model of stripped galaxies and of the cluster, together with the description of the initial condition are introduced in Chapter 3. A detailed description of the used numerical code and of our simulation method including the simulation tests is in Chapter 4. After that, in Chapter 5 we discuss the results of the numerical simulations in the case of face-on galaxy orientation, concluded with a comparison to other existing simulations. It is followed by an analytic description of the ISM-ICM interaction in Chapter 6 with the equation of motion of an individual ISM gas element and the impulse approximation given and applied to the stripping. Chapters 7 and 8 show simulation results of galaxies with inclined disks, and of galaxies crossing the cluster on non-radial orbits, respectively. Finally, Chapter 9 contains the conclusion and our future plans.

Chapter 1

Galaxy clusters

Most of galaxies are not isolated islands in space but form groups of gravitationally bound individuals in a very wide range from several galaxies to large clusters of several thousands members (Stevens et al. 1999). The most visible part of galaxy clusters, the stellar components of all the galaxies constitutes only a small fraction of the total mass of the cluster. The X-rays coming from hot gas cluster component, the intracluster material, corresponds to a much larger part of the total mass, roughly by a factor of two higher than that of the galaxies. The ICM has temperature between 10^7 K and 10^8 K, and it hence emits in the form of bremsstrahlung and atomic line emission. The remaining part is in the dark matter component that constitutes up to 90% of the total gravitating mass. In the first section of this chapter we give an overview of Hubble galaxy types, then we concentrate on different components of galaxy clusters and on the system of classification of galaxy clusters. The differences found when comparing the cluster galaxies with field galaxies are mentioned further. Finally, we focus on the Virgo cluster as it is the nearest cluster that thus can be studied in most detail.

1.1 Galaxy types

Fig. 1.1 shows a standard classification of galaxies according to their morphology into the following types: elliptical galaxies E differing in the degree of ellipticity, lenticular galaxies S0, normal spiral galaxies (Sa – Sc), barred spiral galaxies (Sba – Sbc), and irregular galaxies Irr. From historical reasons the spiral galaxies with heavy central bulge were called early–types, while the spiral galaxies with only light bulge late–types. The fraction of barred galaxies constitutes about 2/3 of the all spirals. The natural evolution proceeds from right to left side of the tuning–fork diagram, from late to early–type galaxies, with transitions between the two branches corresponding to the bar destruction due to the accumulation of mass towards the center, or corresponding to the bar formation due to a strong accretion of the gas from the intergalactic medium. Such crossing between the two branches can repeat in series, and even a backward evolution (rejuvenation) can occur (Bournaud & Combes 2002).

Elliptical galaxies consist mainly of old (population II) stars, contain only very little or no interstellar matter, and motion of their stars are dominated by random motions. Their red color indicates no current star formation. Ellipticals occur in a wide range of sizes with masses from 10^7 to $\sim 10^{13}$ $M_\odot$. Shapes of the elliptical galaxies vary from boxy to disky, with anisotropic random motions, or with nearly isotropic random velocities but flattened due to rotation, respectively. Elliptical galaxies may be produced by galaxy mergers and they occur in the cores of galaxy clusters. Elliptical galaxies are surrounded by hot gaseous halos. The gas is heated by the gravitational force of their enormous masses.

Spiral galaxies are composed of a central bulge surrounded by a thin disk rotating at a typical

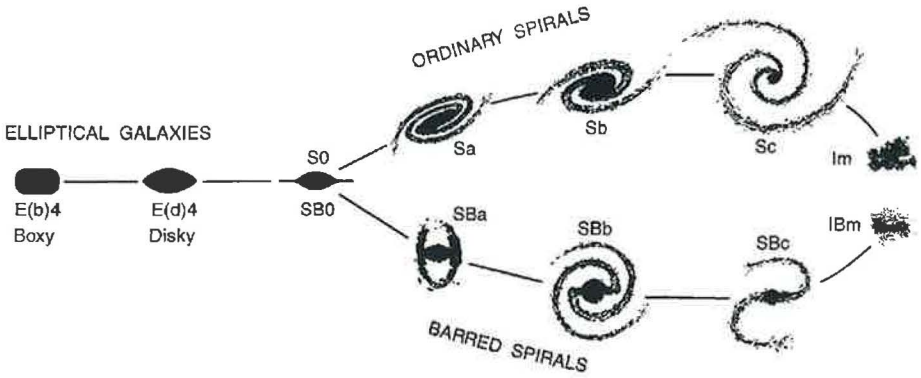

Figure 1.1: Hubble tuning fork of the galaxy types. From Kormendy & Bender (1996)

revolution time scale of about 5 10^7 to 3 10^8 yr. The disk consists of interstellar matter, young (population I) stars and open star clusters. The central bulges resemble the elliptical galaxies with population II stars and a supermassive black hole in the center. the bright spiral arms are the locations of the active star formation. The radial profiles profiles are approximated by exponential laws. The rotation curves are flat which requires an extended spherical component – the dark matter halo.

Lenticular (S0) galaxies are characterized by disks with spent or lost interstellar matter with no observable features, i.e. they resemble spiral galaxies but with no spiral arms. They form an intermediate class between the elliptical and spiral galaxies. Their old and red population II stars are smoothly and evenly distributed in the disk. Lenticular galaxies are most often found in dense clusters of galaxies. Therefore, environmental effects in galaxy clusters are assumed to be responsible for the absence of gas in these galaxies.

1.1.1 Interstellar matter

In most galaxies, diffuse interstellar material constitutes about 10% of the stellar mass. It has a number of distinct phases occurring in different atomic or molecular states, with different temperatures, spatial distribution, and dynamics (Barnes 1998). Five gas phases are usually listed: the molecular medium, the cold neutral medium, the warm neutral medium, the warm ionized medium, and the hot ionized medium (Dahlem 1997). Since the individual phases emit over a very wide range of the electromagnetic spectrum, the ISM must be investigated in multifrequency observations. The cold molecular medium is the most studied in CO lines observations, the cold neutral phase that is associated with molecular gas existing in compact clouds is traced through HI absorption, information about the warm neutral medium comes from HI line emission, the warm ionized medium that dominates HII regions is detected in Hα line emission, and the hot ionized medium ($T \sim 10^6$ K) is detected in a Bremsstrahlung continuum and in complex line radiation of electronic transitions in highly excited atoms (0.1 – 2 keV).

The various phases of the ISM are in rough pressure equilibrium, with exception of the molecular clouds. Hence, their density is inversely proportional to the temperature. The particle densities are then of ~ 100 cm^{-3} in the cold atomic clouds, ~ 1 cm^{-3} in the diffuse atomic and ionized gas, and $\sim 10^{-3}$ cm^{-3} in the very hot plasma. The molecular clouds have densities ranging from 100 to 10^8 cm^{-3}. The HI gas is the most extended component of the ISM in galactic disks.

1.1.2 Gaseous halos of warm gas

Besides the dark matter halos, several phases of the ISM have been detected outside the thin disks of spiral galaxies, in gaseous halos: the HI, the warm, and the hot ionized material. It is

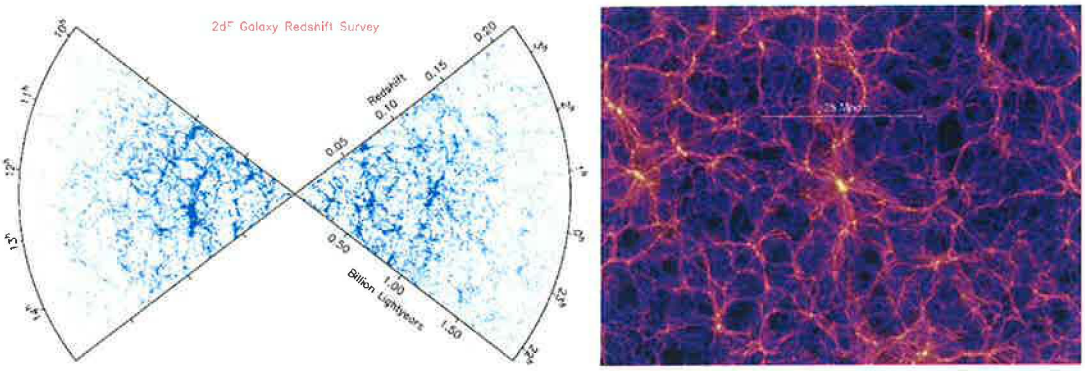

Figure 1.2: Left: Map of the galaxy distribution from observations of the 2dF Galaxy Redshift Survey (Colless et al. 2003). Right: Numerical simulation showing the hierarchical formation of galaxies at $z = 0$ ($t = 13.6$ Gyr) out of the small fluctuations in matter density presented in the primordial universe providing the cold dark matter (Springel et al. 2005).

assumed that the Milky Way has an extended gaseous halo reaching to at least 10 kpc galactocentric distance. Larson et al. (1980) suggested that supply from the gaseous halos might be important for continuing star formation in the disk. To maintain such halos, it must be fed with matter and energy through different processes. The most important ones are the outflows from SN regions and the strong winds of massive stars. Energy sources of the halo are then photoionization, shocks, and cosmic rays. By means of environmental mechanisms described in Chapter 2, the gaseous halos may be stripped and consequently the star formation in the disk quenched. This may lead to morphological transformation of spirals to S0s (Bekki et al. 2002).

1.2 Galaxy clusters and groups

On large scales, distribution of galaxies in space is not homogeneous. It was long though that only a minor fraction of galaxies were assembled in observed clumps of galaxies till Abell and Zwicky started to identify many rich and poorer clusters in all-sky surveys observations. Galaxies are concentrated in regions forming a network structure with clusters of galaxies settling in the nodes of the net and with large voids among the filaments. Observations of the 2dF Galaxy Redshift Survey (Colless et al. 2003) give clear insight into the clustering of the galaxy distributions on scales of hundreds of Mpc. Fig. 1.2 shows the map of the galaxy distribution produced from the completed 2dF survey.

Galaxy clusters can provide an important insight into the formation of cosmic structures and may prompt values of many cosmological parameters. Nowadays, the hierarchical scenario of formation of galaxy clusters is widely accepted. Number of X-ray observations show clusters with complex structure which reveal ongoing merging of subcluster components. It means that some of the clusters have not yet reached dynamical equilibrium and are recently under the process of formation. Numerical simulations confirm the hierarchical scenario and show in detail the formation of galaxy clusters in the intersections of filaments of the net structure. Fig. 1.2 displays a slice through the simulated volume of the "Millenium run" (Springel et al. 2005).

Number of galaxies in large clusters can reach several thousands. Their smaller relatives, galaxy groups, contain from tens to hundreds of galaxies. Sizes of clusters and groups variate on a wide scale yielding into many types with different properties. Diameters of clusters can reach several Mpc. In the centers of galaxy clusters the giant elliptical galaxies are located. Fig. 1.3 shows X-ray observations of the ROSAT satellite of two morphologically different galaxy clusters: the Coma cluster representing a relaxed cluster with almost regular shape, and the Virgo cluster with strongly irregular structure with several subclusters merging and other structures falling into the cluster.

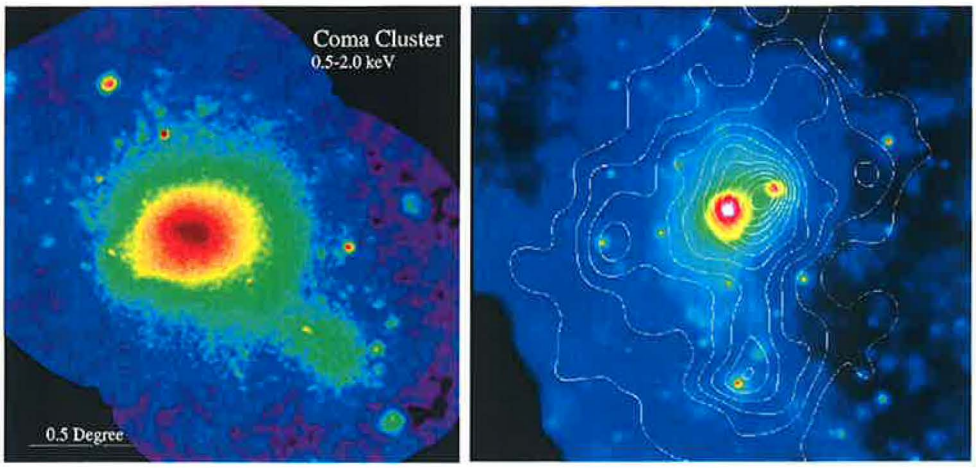

Figure 1.3: ROSAT views of the Coma cluster (Abell 1656) and the Virgo cluster as an example of a relaxed versus non-relaxed clusters.

1.2.1 Classification of galaxy clusters

In an effort to create a classification of (rich) galaxy clusters, one has to make a definition of a representative member cluster. Such a definition is not straightforward since galaxy clusters exist on a very wide range of angular and intensity scales. It has to then specify the surface number density enhancement above the background galaxy density, and the linear or angular scale of the enhancement. It is equivalent to specifying the number of galaxies and the scale size. Of course, only cluster within a given magnitude and redshift range should be included since the number of observed galaxies increases as their brightness diminishes, and galaxies are fainter with increasing distance (Sarazin 1988).

Abell catalog

In the mid 1950's, George Abell studied the National Geographic Society – Palomar Sky Survey plates (Abell 1958), and identified 2712 richest clusters in the northern areas of sky. In early 1980's, Abell completed the catalogue with 4073 clusters from observations of the southern hemisphere via UK Schmidt telescope in Australia (Abell et al. 1989).

His system of classification is based on the following criteria:

- **The richness class**
  The clusters were divided into six richness groups according to the number of galaxies with magnitudes between m_3 and $m_3 + 2$, where m_3 denotes the magnitude of the third brightest galaxy in the cluster, and $m_3 + 2$ is the brightness of a galaxy two magnitudes fainter than the third brightest one. To be included into the catalog, a cluster had to contain at least 50 galaxies. The numbers of galaxies in the individual groups are as follows: Group 0: 30 – 49, Group 1: 50 – 79, Group 2: 80 – 129, Group 3: 130 – 199, Group 4: 200 – 299, Group 5: more than 300.

- **The compactness class**
  The galaxies of the cluster have to be contained within a counting radius $R_A = 1.72/z$ arcmin, where z is the estimated cluster's redshift, or $R_A = 1.5H^{-1}$ Mpc, where the Hubble constant was thought to be 180 km s^{-1} Mpc^{-1} in times of Abell.

- **The distance class**
  The estimated redshift of the cluster have to be in the range $0.02 \leq z \leq 0.2$, which corresponded to the range of distances of about 33 and 330 Mpc. Seven distance groups were created according to the magnitude of the tenth brightest galaxy, that was assumed to be more-or-less a standard candle.

Zwicky catalog

Zwicky et al. in a series of publications within years 1961 – 1968 created a catalogue of clusters based on the richness criterium that at least 50 galaxies in the magnitude range from m_1 to $m_1 + 3$ is contained within the boundary of the cluster that is defined by the contour where the surface density falls to twice the local background density. The magnitude m_1 corresponds to the brightest galaxy. No distance criterion was included.

Zwicky et al. introduced three groups of clusters according to their morphology: compact, medium compact, and open clusters. Compact clusters show a central concentration of galaxies, while the open clusters lack any pronounced concentration.

Bautz-Morgan classification

Bautz & Morgan (1970) completed the Abell system with a morphological classification based on a relative contrast of the brightest galaxy, i.e., on the degree to which the clusters are dominated by the brightest galaxy. It recognizes three main types. Type I has a single supergiant cD galaxy, while Type III (e.g. Virgo Cluster) has no dominating members significantly brighter than the general bright population. Type II (e.g. Coma Cluster) is intermediate between Type I and III with the brightest galaxies intermediate between cD and normal giant ellipticals.

Rood-Sastry's classification

Rood & Sastry (1971) classification scheme organizes the overall morphological properties of a cluster. It is based on the projected distribution of the brightest 10 member galaxies and arranges clusters into a tuning-fork diagram with regular, roughly spherical cD clusters at the base of the tuning fork, followed by binary clusters (type B) dominated by two bright central galaxies. Then the tuning fork divides into roughly spherical C systems with the bright galaxies located near the cluster core, and irregular I clusters on one side, and linear clusters L, in which all the bright galaxies lie along a line, and flattened F clusters on the other side.

Struble & Rood (1982) rearranged the tuning-fork diagram into a split linear diagram that reflects the evolutionary sequence of clusters from irregular types I to types cD.

1.2.2 X-ray nature of galaxy clusters

The intergalactic space in galaxy clusters and groups is filled with hot intracluster (intragroup) medium. Many reviews of both the ICM and IGM exist, e.g. Bahcall (1996), Rosati (2002), Fabian & Allen (2003), Mushotzky (2003), Schindler (2004); Mulchaey (2000). Most of the baryons and metals of the clusters reside in the ICM. Due to extremely deep potential wells of clusters, the matter which falls into the clusters gains significant gravitational potential energy and heats up to temperatures of $10^7 - 10^8$ K. Typical values of the density are about 10^{-4} to 10^{-2} cm^{-3} and the gas is almost fully ionized. The ICM gas with such properties emits due to the thermal bremsstrahlung from hydrogen and helium, only a small part comes from line emission, particularly from iron. It indicates that most of the gas has a mean metallicity of about $0.2 - 0.4\ Z_\odot$ which means that it cannot be purely primordial but it must have come from galaxies early on and must have been by certain processes transported to the ICM. These processes are described in Chapter 2. Since clusters probably retain all the enriched material produced in their galaxies, they provide a record of the nucleosynthesis in the Universe.

Observations of X-ray satellites (Chandra and XMM-Newton) show the ICM present in almost all observed cluster, but only in about 50% of the nearby groups. The total mass of the intracluster medium is about 10 – 20% of the total cluster mass (2 – 10% for the IGM in groups), compared to stellar mass which is about 5% (3 – 20% in groups). During the hierarchical formation of structures under the action of gravity, the intracluster gas follows the dark matter potential and is heated by adiabatic compression and shocks induced by supersonic mergers of subcluster components. Assuming that the pressure of the gas sufficiently opposes to the gravity, the gas can be considered

to be in hydrostatic equilibrium. Then the total mass distribution of clusters can be determined:

$$M_{tot}(R) = -\frac{kTR}{G\mu m_p}\left(\frac{d\ln\rho}{d\ln R} + \frac{d\ln T}{d\ln R}\right), \tag{1.1}$$

where ρ and T are the density and the temperature of the ICM, R, k, μ, m_p are the radius, the Boltzmann constant, the molecular weight, and the mass of proton.

Providing that the fraction of the total gas mass is constant with radius, analytic and numerical predictions expect a declining temperature profile with radius. However, observation show isothermal profiles out to $R \sim 0.5R_{virial}$. The relation between the cluster luminosity and the temperature should from simple theoretical scaling relations follow $L \propto \rho T^2$. However, observations show that the luminosity scales as T^3.

Rosat and XMM observations show that the X-ray surface brightness profiles of most clusters can be well fit by β-model, with an excess above it in cooling flow centers. The β-profile (Cavaliere & Fusco-Femiano 1978) is

$$S = S_0\left(1 + \frac{R^2}{R_c^2}\right)^{-3\beta/2+1/2}, \tag{1.2}$$

where S_0 is the central surface brightness, R is the projected radius, R_c is the core radius and β is the slope parameter. The density of the ICM decreases with radius, and in the central parts its slope is observed to be steeper than that of galaxies. Schindler et al. (1999) state that to make the optical observations of the projected galaxy density in the plane of the sky comparable to the X-ray surface brightness observations, one has to derive spatial densities of the galactic and gaseous components by deprojecting the observed quantities. When the projected galaxy density is modeled by another β-profile

$$n = n_0\left(1 + \frac{R^2}{R_c^2}\right)^{-3\beta/2+1/2}, \tag{1.3}$$

with the central galaxy density n_0, the resulting deprojected density for both the galaxy and gas distribution is then

$$\rho = \rho_0\left(1 + \frac{R^2}{R_c^2}\right)^{-3\beta/2}, \tag{1.4}$$

with the central spatial density ρ_0. Although the Navarro, Frank, & White (1997) or King (1962) profiles would correspond better to the observed galaxy distribution, these profiles cannot be easily deprojected.

The velocity dispersions of galaxies in clusters are of order of 1000 km s^{-1}. These motions of the member galaxies form a vast source of the heat of the cluster since $kT \sim m\sigma^2$, which implies virial temperatures of $\sim 2.4 \cdot 10^7$ K. Since both the galaxies and ICM respond to the same gravitational potential well of the cluster, a relation between their density distributions and typical velocities exists. The ratio of the specific kinetic energy of the galaxies to the specific thermal energy of the gas

$$\beta = \frac{(1/2)\mu m_p \sigma_{gal}^2}{(3/2)kT} = \frac{\mu m_p \sigma_{gal}^2}{3kT} = \frac{\sigma_{gal}^2}{\sigma_{ICM}^2}, \tag{1.5}$$

expresses the relation between the the line-of-sight velocity dispersion of the galaxies σ_{gal} and the typical ICM velocity σ_{ICM}. This can also be interpreted as the ratio of the respective scale heights at the center (Cavaliere & Fusco-Femiano 1978). A typical value of the β parameter is about 2/3.

1.2.3 Observational characteristics of galaxy clusters

Galaxy clusters are dense concentrations of matter, where evolution proceeds at a higher rate than in the field, because of galaxy interactions and influence of environment. With present-day observational techniques, it is possible to study in detail the nearby clusters (and groups) and using the large survey programs like 2dF (Colless et al. 2003) or SDSS (Sloan Digital Survey, e.g.

Goto 2006) enable us to obtain statistically reliable results. Several correlations have been found to occur in dense environments of the galaxy clusters: the morphology–density relation (Dressler 1980); the star formation–density relation (Lewis et al. 2002) ; the Butcher–Oemler effect (Butcher & Oemler (1978, 1984)).

Butcher-Oemler effect

It has been known for a long time that the population of galaxy clusters changed with redshift. The Butcher–Oemler effect represents the excess of optically blue galaxies in clusters at increasing redshifts: at $z > 0.1 - 0.2$ as compared to nearby clusters. The blue galaxies are mostly bright spirals and irregulars with very strong star formation activity. Rakos & Schombert (1995) found that the fraction of blue galaxies increases from about 20% at z=0.4 to about 80% at z=0.9. This suggested the evolution in clusters to be even stronger than previously thought. Although all later observations confirm the Butcher-Oemler effect, some of them may suffer of strong selection biases. The effect is confirmed in recent studied, however, there exists a large scatter in this correlation. Margoniner et al. (2001) have found a richness dependence in their observations: richer clusters have smaller blue fractions. They suggest that this richness dependence may cause a large scatter in the blue fraction vs. redshift diagram.

Morphology–density relation

Dressler (1980) studied 55 nearby clusters and found that the fraction of elliptical galaxies are higher in dense cluster cores. Thus, the morphological segregation in nearby clusters means that the fraction of elliptical and lenticular (early–type) galaxies is higher in regions of high galaxy density than in less dense environments, which are populated mostly by spiral galaxies. Postman & Geller (1984) extended the morphology study to galaxy groups and showed that this relation extends over six orders of magnitude in galaxy space density – at densities of about 5 Mpc^{-3} the population of galaxies contain 65% of spirals, 23% of S0's and 12% of ellipticals, while at densities at 5 – 600 Mpc^{-3} a dramatic decrease of the fraction of spirals occurs, and at densities over 3000 Mpc^{-3} the fraction of ellipticals steeply rises. The morphology-density relation thus corresponds to the hierarchical scenario suggesting that elliptical galaxies formed before the cluster virialisation (Combes 2004).

Star formation–density relation

Lewis et al. (2002) studied over 11 000 galaxies in the 2dF survey. They find that the star formation rate in galaxies of nearby clusters depend on the distance from the cluster center: it increases gradually from low values in the cluster centers to the field value at ~ 3 virial radii. In environments with the galaxy density > 1 Mpc^{-2}, a strong correlation between the star formation rate and the local projected density appeared.

HI–deficiency

We describe the effect of HI–deficient galaxies observed in more than 2/3 of galaxy clusters in Chapter 2.

1.2.4 The Virgo cluster

In this subsection we follow the paper of Schindler et al. (1999) that gives an excellent overview of the distribution of galaxies and the ICM in the Virgo cluster based on the Virgo Cluster Catalog (Binggeli et al. 1985) and the ROSAT All-Sky Survey (Voges et al. 1996). For our simulations discussed in the following chapters, we have chosen the DM and the ICM distribution corresponding to the Virgo northern subclump about the giant elliptical galaxy M87.

Virgo Cluster is the best laboratory for studying the processes occurring in galaxy clusters since it is our nearest cluster with the distance of about 52 million lyr ($\sim$ 16 Mpc). It comprises

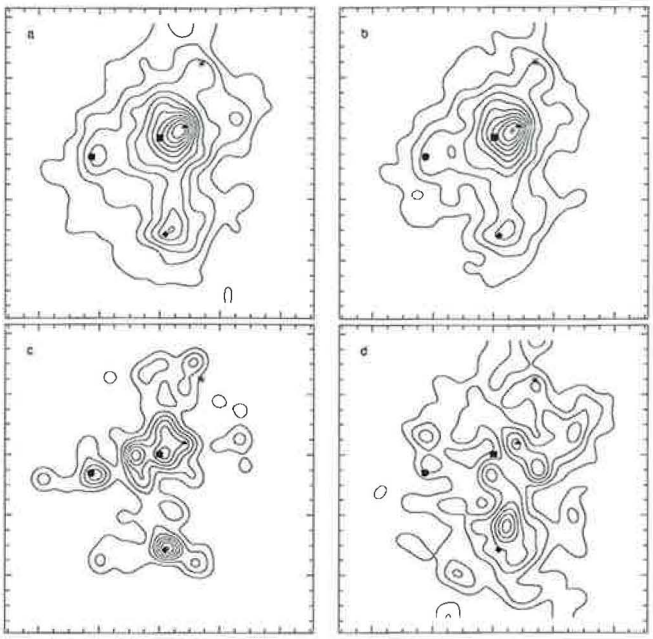

Figure 1.4: The Virgo cluster: distribution of different galaxy populations: a) all galaxy types, b) dwarf elliptical dE and dwarf S0 galaxies, c) elliptical E and S0 galaxies, d) spiral Sp and irregular Irr galaxies. From Schindler et al. (1999).

almost 2000 member galaxies. Due to its proximity, its angular extent in the sky is enormous (about 100 deg^2) which causes that some of its galaxies show blue shifts indicating that they are moving towards us faster than the cluster is mowing away. The Virgo cluster constitutes a center of our Local Supercluster and with its complex structure it is a typical example of an irregular rich cluster (see Fig. 1.3). Its complex structure shows three main subclusters centered on the supergiant elliptical galaxies M87, M49 and M86. The northern clump about the M87 galaxy is called "cluster A", the southern clump about the M49 "cluster B". Position of the M87 coincides with the maximum X-ray emission in the whole cluster, but the not with the maximum of the galaxy density. That is shifted towards the smaller subcluster about the M86. The probable evolutionary scenario is that the this double system in fact undergo ongoing merging event with the M86 subcluster falling into the M87 subcluster.

Mamon et al. (2004) look at how far from the center in M87 occur the surrounding substructures. In the case of the cluster A, the substructure around M86 is at a distance of 0.44 R_{100} well within the virial radius $R_{100} = 1.65 h_{2/3}^{-1}$ Mpc of M87, where $h_{2/3} = H_0/(66.7 \text{ km s}^{-1} \text{ Mpc}^{-1})$. Similarly, the substructure of the cluster B lies within the virial radius of M87, at a distance of 0.88 R_{100}. However, e.g. galaxy M89 lies just at the virial radius, and M59 outside of it.

According to the morphology–density relation, different galaxy types show in the Virgo cluster very different distributions (see Fig. 1.4). It is clearly visible that the early–type galaxies are more concentrated to the subcluster centers where the X-ray emission peaks, while the late–type galaxies occur in the outskirts and show no correlation with the X-ray emission. The dwarf galaxies almost coincide with the overall galaxy distribution since they constitute about 3/4 of the total cluster population. The southern subcluster is dominated by the spiral population.

By modeling the distribution of galaxies with the β-profiles (see the previous subsection), Schindler et al. (1999) derived that a) more massive subclusters have less compact structure, which means that their radial profile is less steep, b) different galaxy types are distributed with different slopes, c) by comparison with the X-ray distribution, the X-ray profiles of the subclusters are steeper than tho optical profiles. Table 1.1 summarizes the core radii of β-profiles and the

		M87	M49	M86
R_c	E+S0	420	420	260
	dE+dS0	570	570	340
	Sp+Irr	1220	1220	680
σ	E+S0	670	320	120
	dE+dS0	720	370	120
	Sp+Irr	850	580	120

Table 1.1: Properties of the different galaxy types in the three main subclusters of the Virgo cluster: the core radii R_c of corresponding β-profiles (in kpc) and the velocity dispersions (in km s^{-1}). From Schindler et al. (1999).

velocity dispersions of different galaxy types in different subclusters.

In Chapter 3, we will introduce our model of the galaxy cluster through which orbit the model galaxies under the influence of the ram pressure of the ICM. As we constrain our simulations to the central parts of the cluster, we are interested in realistic profiles of the ICM distribution. Table 1.2 gives the summary of properties of the three main subclumps of the Virgo cluster according to Schindler et al. (1999): the total masses M_{tot} and fractions of the galaxy masses M_{gal} and the ICM masses M_{ICM}.

Subcluster	M_{tot} (10^{13} M$_\odot$)	M_{ICM}/M_{tot}	M_{gal}/M_{tot}
M87	14 ($R < 1000$ kpc)	14 %	4 %
M49	8.7 ($R < 750$ kpc)	0.5 %	4 %
M86	1 – 3 ($R < 240$ kpc)	–	2 – 6 %

Table 1.2: Properties of the three main subclusters of the Virgo cluster. M_{tot} denotes the total gravitational mass of a subcluster including dark matter, galaxies, and ICM components. M_{gal} is the total galaxy mass, and M_{ICM} the total ICM mass.

As a consequence of its clumpiness, the ICM distribution of the Virgo cluster as a whole cannot be represented in a simple detailed model using only one β-profile. Nevertheless, the dominant member of the Virgo cluster is the M87 subclump (see Table 1.2). Thus, for purposes of our numerical simulations it is sufficient to constrain the model only to this principal subcluster and not to take into account the other cluster components. Table 1.3 resumes the values of the parameters of the β-profile corresponding to the ICM distribution in the M87 subclump according to several papers.

paper	r_c (kpc)	n_0 (10^{-3} cm^{-3})	β
Matsumoto et al. (2000)	14	19	0.4
Schindler et al. (1999)	16.2	–	0.47
Vollmer et al. (2001a)	13.4	40	0.5

Table 1.3: Parameters of the β-profile of the ICM distribution in the M87 subclump after several papers. Matsumoto et al.(2000) give parameters for the Virgo cluster as a whole obtained from ASCA observations.

Chapter 2

Environmental effects in galaxy clusters

Galaxies in groups and clusters are influenced by many types of interactions, both with their surrounding environment, and with other member galaxies. Such interactions are believed to drive galaxy evolution in clusters and thus invoke a variety in galaxy properties. From times of Hubble, it has been known that galaxy types are related to the local density, with ellipticals and S0's occurring in the densest regions, while spirals mostly in low density regions of the field (the morphology–density relation). Another correlations show up when going from low to higher redshifts: nearby clusters at $z = 0$ are fully formed and evolved, clusters observed at $z = 0.2 - 0.5$ show the same fraction of the elliptical galaxies but an increasing number of spirals (Butcher–Oemler effect) and decreasing fraction of S0's. At redshifts of $z = 0.5 - 1$, one observe the young clusters being under the process of construction by merging of smaller clusters and groups and tidal interactions and merging of galaxies form the S0 galaxies. At even higher redshifts, from about $z = 3$, one would see formation of ellipticals long before the formation of clusters (Boselli & Gavazzi 2006).

In this chapter we first give a brief summary of the environmental effects that occur in galaxy clusters and affect the evolution of their member galaxies, either their stellar or/and gaseous content. In the next section, we give a short overview of the observations depicting the effects caused by the environmental interactions – the ram pressure stripping by the intracluster medium or tidal interactions with close companions. The Virgo cluster is thanks to its proximity an excellent laboratory to study in detail the effects of the intracluster environment on the cluster galaxies. Thus, most of the mentioned observations concerns it. In the third section, we come to numerical simulations of the ram pressure stripping phenomenon and provide a summary of recent papers.

2.1 Mechanisms

In galaxy clusters and groups, several competitive mechanisms affect the member galaxies and can remove matter from them. Such processes cause the subsequent starvation and star formation quenching and evoke observable properties of both cluster member galaxies and the cluster environment itself described in the previous chapter.

Ram pressure stripping

Galaxies falling into a cluster interact with the ICM and experience a ram pressure that scales as $\rho_{ICM} v_{gal}^2$, where ρ_{ICM} is the cluster gas density and v_{gal} is the relative velocity of the galaxy with respect to the ICM. If the ICM density is high enough, it can remove most of the galaxy's gas on a time scale of about 100 Myr. The ram pressure stripping thus causes truncation of gas disks in cluster galaxies. This process is the main topic of present work and it will be described in detail

in the following chapters.

As a consequence of the ram pressure, an enhanced but short-term star formation can occur either by the compression of the ISM at the windward side of the disk (Fujita et al. 1999), or by an indirect compression by the reaccreting gas previously only shifted out of the disk but staying bound to the galaxy (Vollmer et al. 2001b).

Tidal interactions

Gravitational interactions including tidal interactions among galaxies (Toomre & Toomre 1972, Mihos 2004), tidal interactions between galaxies and the cluster potential (Byrd & Valtonen 1990), or multiple high-speed galaxy-galaxy encounters (Moore et al. 1996, 1998) occur in galaxy clusters and can affect the gas content of the member galaxies. Tidal interactions affect all galaxy components whose gravitational bound to the galaxy is however different. This leads to selective morphological transformations. Galaxy haloes are strongly susceptible to the tidal forces and may result in substantial removal of matter. Tidal forces act as M/r^3. Due to high relative velocities, tidal interactions among cluster galaxies have significantly shorter duration than in the case of field galaxies. An encounter with the same impact parameter is much more likely to cause disruption in a poor group than in a cluster. Of course, the high density regions of cluster make on the contrary the probability of an interaction higher.

- **Merging**
  If the galaxy-galaxy encounter is slow, the mutual tidal fields disturb strongly all galactic components. The gas may be strongly compressed, and induced shock waves are likely to trigger star formation. Stellar disks heat up, bar instabilities can occur, and gas inflows can cause active galactic nuclei. Long tails and bridges (Toomre & Toomre 1972) of the pulled material form, and only slowly returns to galaxies.

  If the impact parameter of the encounter is small, a galaxy is caught by a massive dark halo, and its orbit is affected by dynamical friction, and galaxies merge. Naab & Burkert (2003) show that the galaxy merging might be important in the formation of large elliptical galaxies. Major mergers with mass ratios from 1:1 to 3:1 result in remnants that have properties similar to elliptical galaxies, while minor mergers below 10:1 result in disturbed spiral galaxies. Bournaud et al. (2004) have shown that the intermediate mergers in a range of mass ratios 4:1 – 10:1 can result in systems with a morphology of the spiral galaxy with an exponential profile, but with kinematics resembling that of elliptical systems. The transition between disk-like and elliptical remnants occurs between a narrow mass range of 4.5:1 – 3:1.

  Mergers occur in the unrelaxed parts of clusters where local velocity dispersion may be lower than that within the virialized inner parts. Thus, giant ellipticals are formed before the virialization of clusters (Merritt 1983).

- **Galaxy harassment**
  The tidal interactions in clusters were originally thought unimportant because of high relative velocities of galaxies and thus short time scales ($\sim 10^8$ yr) of the interactions. However, due to high number density of galaxies in galaxy cluster, a large number of interactions occur, and their effect accumulates. Moore et al. (1996, 1998) called the effect of the multiple high speed galaxy-galaxy close ($\sim$ 50 kpc) encounters with the background effect of the potential of the cluster as a whole, galaxy harassment. Its effect depends on the frequency of collisions, on their strength, on the cluster's tidal field, and on the potential distribution of individual galaxies. Moore et al. (1996, 1998) show that galaxies on radial orbits experience stronger harassment than galaxies on circular orbits. Due to multiple encounters, the stellar disks of galaxies heat up, their velocity dispersions increase, and the angular momentum decreases. Consequently, the gas flows towards the galaxy center.

  As a consequence of the harassment effect, low surface brightness galaxies are strongly perturbed because of their low mass concentration. They loose up to 90 % of their stars, increase their central velocity dispersion and consequently their central surface brightness. Their remnants resemble dwarf ellipticals or dwarf spheroidals. The high surface brightness galaxies

have on the contrary steeply rising rotation curves in the central parts and by the harassment they lose only a small part of their stars, but the disk scale heights increase by a factor of 2 – 4, and the spiral features fade.

Cosmological simulations of Gnedin (2003) show that the maximum of the tidal forces do not always occur close to the cluster center but the interactions are intensified by density irregularities – massive galaxies, or unvirialized infalling groups of galaxies. Presence of such substructures favor the interaction by 10 – 50 %. The typical frequency is estimated to 10 interactions at 10 kpc impact parameter per galaxy.

- **Galaxies versus cluster potential**
  In addition to tidal influences by other galaxies, the cluster galaxies experience tidal forces as they move through the cluster potential. As the total cluster mass can exceed 10^{14} $M_{\odot}$, the tides exerted by the whole cluster potential can perturb cluster galaxies and induce a number of effects like gas inflow, bar formation, nuclear and disk star formation (Merritt 1983, Byrd & Valtonen 1990). If the disk is oriented perpendicularly to the orbital plane or is inclined, a bulge is developed, and if it is parallel with respect to the orbital plane, a spiral pattern forms. In any case, the disk thickness slightly increases (Valluri 1993). Valluri (1993) further indicate that the gravitational potential of the galaxy does not change significantly when passing near the cluster center.

  When calculating the tidal radius r_{tidal}, outside which the tidal perturbation is effective in removing gas, it is found to be either much larger than the optical radius (e.g. Coma cluster) or comparable to the optical radius (e.g. Virgo cluster). Thus, tidal interactions with cluster potential can hardly directly remove the ISM of cluster galaxies.

Viscous stripping

The effect of the ram pressure stripping is accompanied by occurence of the viscous stripping. Nulsen (1982) suggested that outer layers of a spherical galaxy traveling through the hot ICM experience a viscosity momentum transfer that is sufficient enough to drag out some gas at rates depending on the character of the flow (laminar/turbulent). In the turbulent case, the drag force acting on the ISM is proportional $\rho_{ICM} v_{gal}^2$, just as the ram pressure is. Nulsen (1982) conclude that the observable features of the viscous stripping are expected to be similar to those of ram pressure. In the Virgo cluster, galaxies with radius larger than 15 kpc are subject to turbulent stripping. The time scale for complete stripping are in the Virgo cluster about 10^8 yr.

Cooling flow

Within about 50 kpc of the cluster center the radiative cooling time scale of the gas is shorter than the age of the cluster. The temperature of the ICM there smoothly drops by a factor of 2 – 3 from that of the outer gas. Since X-ray observations show that radiative cooling is much reduced and thus some form of distributed heating has to take place there (Fabian & Allen 2003): either heating by a central active nucleus (AGN), or heating by conduction from the hot outer gas.

Thermal evaporation

Cowie & Songaila (1977) studied the effects of heat conduction and consequent evaporation of the ISM in contact with the hot ICM. This effect can efficiently remove gas from cluster galaxies. At the interface between the hot ICM and cold ISM the temperature of the ISM steeply rises and the gas evaporates and is not retained by the gravitational field. Cowie & Songaila (1977) estimated that by operation of the ICM, a typical spiral galaxy should evaporate in 100 Myr. Thermal evaporation depends on the ICM temperature and on the magnetic field, and to a lesser extent on the density. In absence of the magnetic field, a typical spiral with 15 kpc radius and 5 10^9 $M_{\odot}$ of the HI mass can be completely stripped in about 4 10^7 yr in Coma, and 10^9 yr in Virgo.

However, Fujita (2004a) analytically estimates the time-scales of the evaporation in clusters, subclusters, and groups and finds a substantially longer times of about 1 – 3 Gyr, 2 – 7 Gyr, and 10 Gyr, respectively.

Starvation

Starvation (or strangulation) effect was proposed by Larson et al. (1980) to explain the transformation of spirals to S0s. It is a consequence of the stripping of gas from the galaxy's surroundings (like gaseous halo-reservoirs) that otherwise would be accreted by the galaxy (Balogh et al. 2000). Bekki et al. (2002) suggest that the gas reservoirs, that are likely candidates for the source of gas replenishment for star formation in spirals, are hot and diffuse and may thus be efficiently stripped. They show that even if the galaxy is on an non-radial orbit with a pericenter distance of ~ 3 core radii, about 80 % of the halo gas (if its density is $\simeq 3\ 10^{-5}$ cm^{-3}) is stripped within few Gyr. This leads to a dramatic decline in the gaseous infall rate, an increase of the Toomre's Q parameter of the disk, whose spiral arms become less pronounced as the SFR gradually decreases, and finally a possible transformation of these passive or anemic spirals into S0s. The process of halo reservoir stripping is likely to be a large-scale common effect of the ram pressure stripping and the global tidal field of the cluster.

Preprocessing

Nowadays, the hierarchical scenario for the formation of large-scale structures, galaxy clusters and groups is adopted. Then galaxy groups represent natural places where galaxies are preprocessed by tidal interactions, ram pressure, starvation and evaporation, before they become part of a cluster. Preprocessing then might lead to formation of lenticular galaxies through unequal-mass or minor mergers and consequently heat up the disk, producing high bulge-to-disk lenticulars observed in clusters (Kodama & Smail 2001).

Outflows

Galaxies infalling into the clusters may be due to various discussed mechanisms deprived of their haloes which then facilitates to escape the stellar winds.

Chemical enrichment

In clusters, most of the metals is contained in the ICM which comprises almost all baryons of the cluster. From the analysis of X-ray spectra of the ICM it follows that the metal abundances in the ICM differ from one type of cluster to another and that the distribution of metals within clusters can be non-uniform (see Toniazo & Schindler 2001). This suggests that either part of the hot gas comes directly from galaxies by stripping processes (enrichment in Fe) or that the ICM is enriched by winds (mainly in Si).

IC light

The existence of the intracluster diffuse light has been proved in many observations (see Rudick et al. 2006). It corresponds to stars occurring in between the galaxies, due to tidal interactions that pulled them out of their parent galaxies. The intra-cluster stars are older than galaxy stellar populations, and more centrally concentrated in the cluster. The fraction of stars in the ICM increases with the richness of the cluster and it is usually a few percent of all stars, up to about 20% (Arnaboldi et al. 2003, Murante et al. 2004). Its existence may partly contribute to the ICM metallicity by intra-cluster supernovae exploding in the ICM.

2.2 Gas in the cluster galaxies

Single-dish observations have shown number of HI deficient galaxies in galaxy clusters. The galaxies at radii closer to the cluster center show stronger HI deficiency, and since the deficient galaxies usually have normal stellar disks, the ram pressure is provided to be the responsible process. Galaxy properties seem to play a role in the HI stripping since the HI from early–types is found to be more easily removed than from the late–types.

In the following text we first mention important observations of the HI-deficient galaxies in the Virgo cluster and other nearby clusters, and then we give several examples of the molecular gas content observations.

2.2.1 HI deficiency

Giovanelli & Haynes

Observing with the Arecibo telescope, Giovanelli & Haynes (1982) produced maps of the neutral hydrogen for 24 spirals in the Virgo cluster and compared them to similar samples of isolated galaxies. They found out that galaxies in the core of the Virgo cluster had a smaller HI diameter than their optical counterparts. Defining the HI-deficiency parameter as

$$\mathrm{def} = \log \frac{M_{HI,observed}}{M_{HI,expected}}, \tag{2.1}$$

where the expected HI mass corresponds to an isolated galaxy of the same morphological type and optical diameter, they found that the Virgo core galaxies are on average deficient by a factor of 2.6 with respect to the isolated galaxies. They conclude that the removal of the ISM is caused by the ram pressure of the ICM in the central Virgo regions.

Giovanelli & Haynes (1985) gathered 21 cm data for nine clusters and a total sample of over 300 galaxies. A substantial HI deficiency is found for galaxies in six of the clusters, and its strong correlation with radial distance from the cluster center is shown. A comparison of the environments in different clusters shows that the fraction of deficient galaxies is correlated with the X-ray luminosity, and the fraction of spirals is systematically lower in strong X-ray clusters, while that of S0's is correspondingly higher there.

Cayatte et al. (1990, 1994)

Their VLA atlas of the 25 brightest spiral galaxies located in the center of the Virgo cluster confirms that the galaxies located within 3° of M87 have significantly smaller HI disks than the optical disks. Further away, there is a number of galaxies have very asymmetric HI distributions and a sharp edge on the side pointing towards the M87 galaxy. They find three face-on anemic galaxies showing a ring structure, several gas-rich dwarf galaxies located in the vicinity of HI deficient galaxies, and one close to the cluster center. They note that the western part of the Virgo cluster contains larger galaxies than the eastern part, and that asymmetric galaxies show an enhanced star formation at the compressed side of their gaseous disk.

Their further analysis show that the effects of the cluster environment vary with galaxy types. They suggest that galaxies with the smallest HI disks but normal central surface densities are currently undergoing ram-pressure sweeping, while galaxies with only slightly smaller HI diameters than usual but globally depressed HI surface density across the disk experience effects of turbulent viscous stripping or thermal conduction.

Warmels (1990a, 1990b)

Measurements in the Virgo cluster revealed for all galaxies located near the cluster center small HI distributions compared to optical dimensions. Such small sizes and asymmetric shapes of HI disks were not observed in galaxies outside the region of about 5° from M87. The isophotal HI sizes for a given optical diameter of galaxies in the cluster core are about a factor 2 smaller than the HI sizes in the outer regions. They note that HI is mainly removed from outer parts of galaxies. And since all HI deficient galaxies also had velocities different from the cluster average, they proposed the ram pressure stripping to be responsible for the observed HI properties. The size ratio of the HI to optical disks correlated with the velocities of the galaxies with respect to the cluster average.

Valluri & Jog (1991)

Studying HI data from three rich Abell clusters and the Virgo Cluster, they show that the HI deficiency correlates with the optical sizes of the galaxies: those with medium to large sizes tend

to be more deficient than the small ones. This trend is opposite to what is expected from various currently accepted gas removal mechanisms, like ram pressure stripping. They conclude that the disagreement may result from mass segregation in clusters – if large galaxies are more concentrated to the cluster core, they would be more severely affected by the ICM and the gas removal processes which may give the trends observed in the size dependence of HI deficiency.

Solanes et al. (2001)

In the field of 18 nearby clusters they follow the HI content for 1900 spirals. Two thirds of the studied clusters show HI deficient galaxies. The HI gas poor galaxies can extend out to 2 Abell radii from the cluster center, i.e. far behind the reach of the dense ICM environment. In the outskirts, the fraction of these deficient galaxies are comparable with the field values, but towards the central cluster regions the deficiency strongly increases. They remark that the amount of gas depletion is related to the galaxy morphology, but is not a function of the disk optical size. For early-types and probably dwarf spirals, both the fraction of gas-deficient galaxies and degree of deficiency are higher that for late-types, which can be caused by higher central HI depression in the early-type galaxies. They propose a scenario in which gas losses are due to the interaction of the disks with the inner hot ICM around M87 and this is supported by evidence HI deficient spirals have more eccentric orbits than the gas-rich objects.

Fig. 2.1 shows the fraction of the HI galaxies with def > 0.3 as a function of the projected radius from the cluster center, as observed by Solanes et al. (2001). Deficiency higher than 0.3 corresponds to a state when a galaxy is deficient in neutral hydrogen by a factor two or more compared to isolated galaxies.

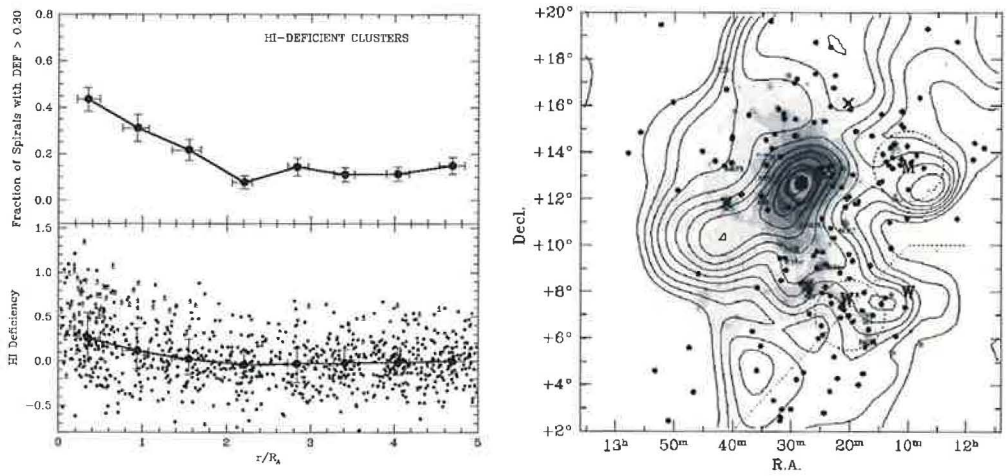

Figure 2.1: Left: Fraction of HI–deficient galaxies in bins of projected radius from the cluster center for the superposition of the HI–deficient clusters (top); HI–deficiency as a function of projected radius from the cluster center. Dots correspond to individual galaxies (bottom). From Solanes et al. (2001) Right: Map of the HI deficiency pattern in the Virgo cluster area showing besides the expected fact that the maximum depletion occurs at the cluster center, also peripheral groups of galaxies with lack of the HI gas. From Solanes et al. (2002)

However, Solanes et al. (2001) state that no correlation of the HI deficiency with global cluster properties, like X-ray luminosity, temperature, or radial velocity dispersion was found.

HI deficiency on cluster outskirts

Solanes et al. (2002) found out surprising occurrance of groups of HI deficient galaxies at the outskirts of the Virgo cluster (see Fig. 2.1), in regions where the density of the X-ray–luminous gas is very low. This impeaches the feasibility of the ram pressure stripping as the responsible process

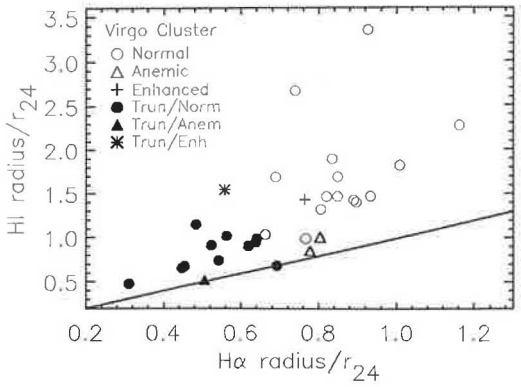

Figure 2.2: Comparison of Hα radii to HI radii. The symbols indicate the Hα morphology classes. Note that galaxies with truncated Hα disks have truncated HI disks. From Koopmann & Kenney (2004).

of the deficiency. Mamon et al. (2004) calculater the maximum radial distance from the cluster center to which galaxies may get out of a virialized system. They find that such distance is for infalling galaxies in a range of $(1-2.5)\ R_{100}$ (i.e. 1.7 – 4.1 Mpc). However, the HI deficient galaxies are observed at distances much larger (25 – 30 Mpc). Mamon et al. (2004) speculate about three possible explanations: incorrect estimation of either distances of galaxies or the HI deficiencies, or tidal disturbance by nearby companions. The most plausible explanation is that these peripheral HI deficient galaxies are in groups that newly enter the Virgo cluster.

2.2.2 Molecular gas

Observations of the molecular content of the cluster galaxies tend to show that it is not affected by the environment. However, this findings are at variance with observations of galaxies whose star formation is truncated at lower radii, since the star formation is connected to the molecular gas.

Kenney & Young (1986)

Following CO emission along the major axis of 23 Virgo cluster spiral galaxies they found that these galaxies had roughly normal CO luminosities and extents, relative to optical properties. Further, they note that while the molecular gas is intact, the atomic gas is removed, indicating that processes like ram pressure stripping, thermal evaporation, or turbulent viscous stripping selectively affect low-density material. This is supported by observations that CO to HI diameters ratio decreases when going away from M87.

Koopmann & Kenney (2004)

They study Hα star formation morphologies of Virgo Cluster and isolated spiral galaxies and associate them with various types of environmental interactions. They find about half of Virgo spirals to have truncated Hα disks, a small fraction of Virgo spirals to be anemic, or to have enhanced star formation. About 37% are classified as normal. Most of the Hα–truncated galaxies have undisturbed stellar disks and normal or only slightly enhanced inner disk star formation rates (SFR). They suggest that ICM-ISM stripping is the main mechanism causing the reduced SFR in Virgo spiral galaxies. Several peculiarities, like enhanced central SFR, disturbed stellar disks, or barlike distributions of luminous HII complexes within the central 1 kpc but no star formation beyond, are observed. These effects suggest the importance of recent tidal interactions or minor mergers. They show that the normal galaxies are absent from the cluster core, while truncated galaxies are strongly concentrated in the core, but with several exceptions found in the cluster outskirts. Two observations of highly inclined Hα–truncated spirals likely correspond to an ongoing ram pressure stripping. Several galaxies show asymmetric Hα enhancements at the outer

edge of their truncated Hα disks. All results indicate that most Virgo spirals experience ICM-ISM stripping, many of them in combinations with tidal effects. There is a correlation between the HI and Hα radial distribution of large Virgo spirals (see Fig. 2.2): the galaxies with strongly truncated HI also have the most truncated Hα.

2.2.3 The dust

Their exist several observations with non-planar distribution of the dust. We mention one of it, NGC 4406, with a complex observed structure including a displaced dust component.

White et al. (1991)

Analyzing multiwavelength observations of the elliptical galaxy M86 (NGC 4406), White et al. (1991) reveal unusual characteristics reflecting its strong supersonic interaction with the ICM in the Virgo Cluster core, and its subsequent heating. The stripped gas is observable as a X-ray plume in the northwest side of the galaxy. At the same position, a displaced infrared emission is observed and interpreted as a collisionally heated dust exposed to hot gas where ram pressure and turbulence have disrupted the stripped ISM of the galaxy. Consequently, the outer optical isophotes displaced in the direction of the stripped gas are suggested to correspond to reflection of star-light on the dust grains. They conclude that the ram pressure has separated in M86 elliptical galaxy the various components of the multiphase ISM, enabling thus their separated analysis which is difficult in normal elliptical galaxies.

2.3 Examples of the ongoing ram pressure stripping

Nowadays, a number of observations of galaxies probably currently undergoing the process of the ram pressure stripping have appeared. Here we focus on several individual galaxies and provide a detailed information of their state from various observations. At the end of this section, we mention the stripping sequence proposed by Vollmer et al. (2004a) for the discussed observational cases.

NGC 4522

The NGC 4522 is highly inclined, medium sized HI–deficient Virgo Cluster galaxy with a small bulge-to-disk ratio, one of the best spiral candidates for intracluster medium-interstellar medium stripping in action (Kenney & Koopmann, 1999; Kenney et al., 2004a). It is located within a southern subclump of the Virgo cluster centered on the galaxy M49. The HI is spatially coincident with the stellar disk in the central 3 kpc, but beyond it is sharply truncated, and is observable only at extraplanar positions up to 3 kpc on the northwest side of the disk (see Fig. 2.3. Almost half of the total HI is extraplanar. The distribution of the Hα emission is peculiar and similar to HI, truncated in the disk at 3 kpc. Ten percent of it arises from extraplanar H II regions which appear to coincide with the HI distribution. The distribution of the Hα is reminiscent of a bow shock morphology. This implies that ISM of NGC 4522 is being stripped by the ram pressure of the ICM. And along with the HI, the star-forming molecular ISM has been effectively stripped from the outer disk of the galaxy. With the line-of-sight velocity of about 1300 km s^{-1} with respect to the mean Virgo Cluster velocity, the galaxy is expected to experience a strong interaction with the ICM. But it is about 1 Mpc from the M87 galaxy, where the ram pressure, assuming a static smooth ICM and standard values for ICM density and galaxy velocity, appears to be too low to cause the observed stripping. Therefore, large bulk motions or local density enhancements of the ICM may be needed to explain the inconsistency. The absence of HII in the disk at larger disk radii and the existence of H II regions in the filaments of the stripped gas suggest that even molecular gas has been removed from the disk of the galaxy! Recent simulations suggest that the extraplanar gas occurs at relatively early stages of the stripping and not during later gas reaccretion as proposed by Vollmer et al. (2000).

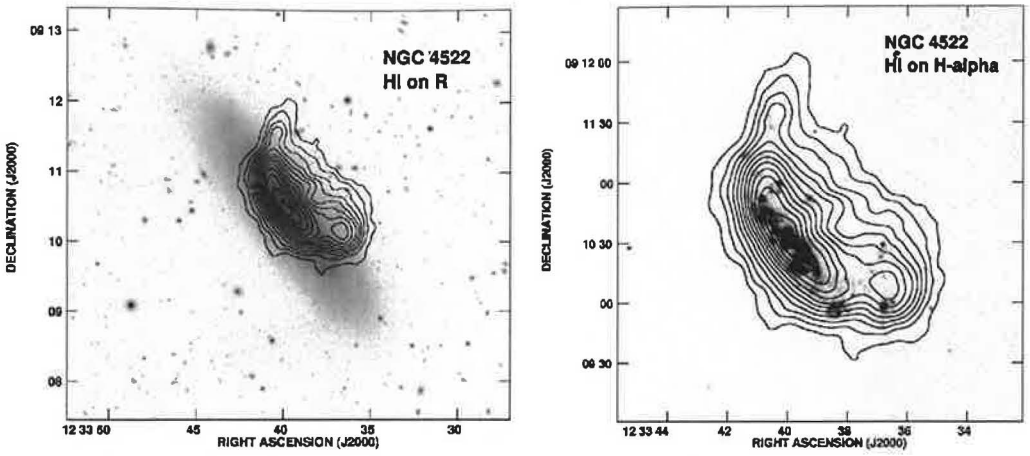

Figure 2.3: NGC 4522. Left: HI contour map overlaid on R-band gray-scale image from the WIYN telescope. Note the undisturbed outer stellar disk. Right: HI contour map on Hα gray-scale image. Note HII regions associated with each of the three major extraplanar HI peaks. From Kenney & Koopmann (2004)

Vollmer et al. (2004b) observed the NGC 4522 in radio continuum. It shows symmetric emission distribution with an extended component to the west, coinciding with the extraplanar atomic gas and Hα emission. Following the polarized radio continuum emission gives additional information of the dynamics of the gas. It traces the ordered large scale magnetic field in the ISM which is very sensitive to compression and shear motion. The founding is consistent with a scenario of a large-scale shock at the side opposite to the extraplanar gas, due to due to ram pressure located at the east of the galaxy. They conclude that the galaxy is likely to experience an active ram pressure.

Vollmer et al. (2006) further propose a dynamical model of the evolution of the ISM and solve the induction equation on the obtained velocity fields to calculate the large-scale magnetic fields. The model successfully reproduces the large-scale gas distribution and the velocity field but does not reproduce the observed large HI linewidths in the extraplanar component. Obtained distribution of polarized radio continuum emission successfully reproduces the observed maximum. The model predicts that the ram pressure maximum occurred only recently, about 50 Myr ago. They propose two possible explanation to the inconsistency in the local ram pressure and the observed stripping amount: a) the galaxy is just passing through the cluster, or b) the ICM is moving due to the infall of the M 49 group of galaxies.

NGC 4569 (M90)

The spiral galaxy NGC 4569 is a very large, peculiar galaxy of the Virgo cluster. Its rotation velocity is about 250 km s^{-1}, it occurs close to the cluster center, and it has lost more than 90% of its HI gas due to a heavily truncated gas disk. Vollmer et al. (2004a) obtained deep HI line observations using the VLA and the Effelsberg telescope and found a low surface density arm in the downstream side of the galaxy. Its velocity field differs from that of the disk rotation. A dynamical model tends to a post-stripping scenario with the peak stripping that occurred about 300 Myr ago, rather than to an ongoing stripping process, but cannot exclude that it had already been truncated the stripping occurred.

Kenney et al. (2004b) refer to an anomalous arm of the HII regions (see Fig. 2.4) and a diffuse nebulosity near the minor axis. The Hα disk is truncated at about 30% of the optical radius. They propose the ICM ram pressure origin of both effects – in combination with the galaxy rotation in the case of the arm, and disrupting a starburst outflow bubble in the case of the nebulosity.

Boselli et al. (2006b) show a combination of multifrequency observations of the NGC 4569 (see Fig. 2.5) and state that the ram pressure stripping scenario can explain and reconstruct the

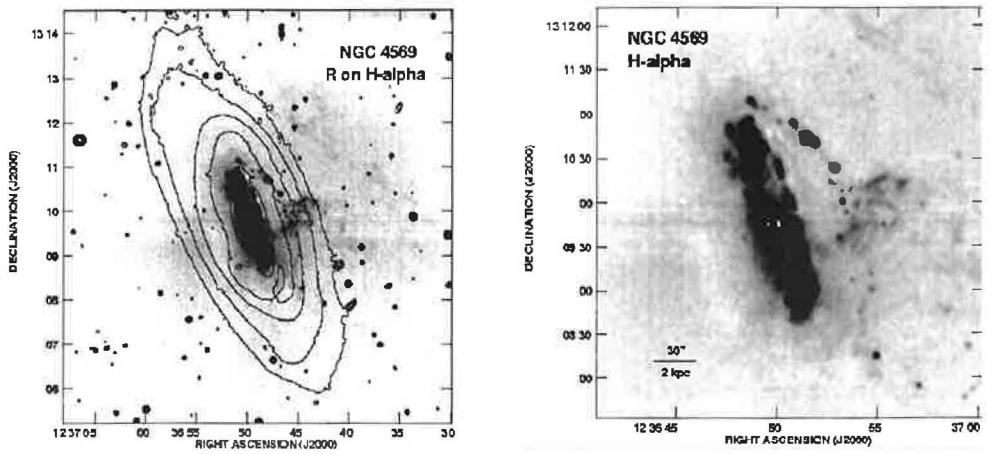

Figure 2.4: Left: Hα image of the NGC 4569 overlaid by R-band contours. Right: Note the anomalous HII arm and the diffuse nebulosity. From Kenney et al. (2004b)

observed total-gas radial density profile and the light surface-brightness profiles. They confirm the conclusion of Vollmer et al. (2004a).

Chyży et al. (2006) using radio polarimetry discovered very large symmetric lobes of polarized radio emission around the NGC 4569 extending up to 24 kpc from the disk. Such extended lobes are very rare in field spirals, as well as in cluster spirals. The lobes had presumably formed due to galactic superwind-like flows induced by a starburst lasting several 10 Myr that occurred $\sim$ 30 Myr ago and produced about 10^5 supernovae. This is consistent with a stellar population that is dominated by A supergiants in the central galaxy region. The radio lobes resist to the galaxy's rapid motion through the ICM since they are symmetric.

NGC 4254 (M99) & NGC 4654 & NGC 4438

The bright spiral NGC 4254 is located at the Virgo cluster periphery, at a distance of about 1 Mpc from the cluster center. It is a one-armed galaxy with a low surface density gas occurring around galaxy and in an extended tail. Vollmer et al. (2005a), using a dynamical model, are able to reproduce the observed one-armed spiral structure by a rapid tidal encounter with a massive galaxy, possibly NGC 4262. The gas pulled out of the galaxy by the tidal interaction is subsequently stripped by the ram pressure as the galaxy enters the Virgo cluster in almost face-on configuration.

A very asymmetric HI Virgo cluster spiral galaxy NGC 4654 represents another candidate for ongoing ram pressure stripping. It shows a compressed edge on the windward side, and a long tail on the other side of the galaxy. Since NGC 4654 has also an asymmetric stellar disk, it may underwent a gravitational interaction with the nearby spiral NGC 4639. Vollmer (2003a) shows that this strong edge-on interaction has probably occurred about 500 Myr ago, and as the galaxy enters the Virgo cluster with a velocity of about 1000 km s^{-1}, it experiences a weak ram pressure that consequently produces the observed low surface density gas tail.

The Virgo spiral NGC 4438 has a highly perturbed stellar disk with strong evidence of a tidal interaction and with stellar debris displaced to the west of the disk. Combes et al. (1988) present a ^{12}CO(J = 1-0) map showing an extraplanar molecular emission at the NW side of the galaxy in the direction coinciding with the neutral-gas, radio-continuum, and X-ray emissions. Since the molecular material is too dense to be easily swept, and the stellar tails only can be of tidal origin, they propose a scenario of the tidal interaction with the nearby NGC 4435 galaxy. Vollmer et al. (2005b) show that some observed features can be reproduced with a ram pressure wind. Most probably, the NGC 4438 is on its first passage through the cluster center, being stripped of its HI over the past 100 Myr. The ram pressure has a strong effect that is combined with the interaction with NGC 4435 that pulls the gas further from NGC 4438 where the ram pressure is efficient enough to strips it away.

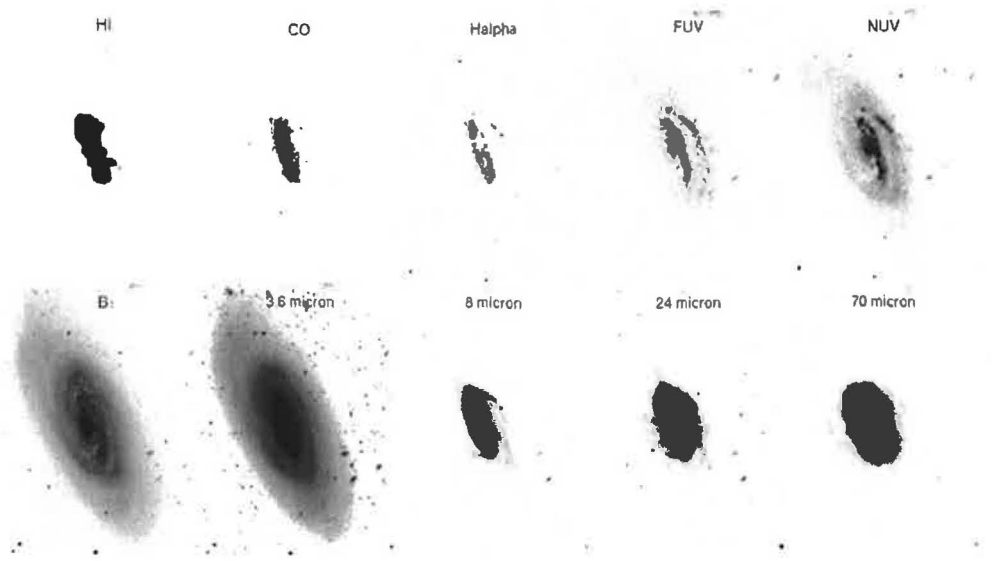

Figure 2.5: The multifrequency images of NGC 4569 at their intrinsic resolution: from top left to bottom right – HI, CO, H_α, FUV, NUV, B, 3.6 μm, 8 μm, 24 μm, and 70 μm all on the same scale. From Boselli et al. (2006b)

Chemin et al. (2005) found a very faint filamentary structures in Hα observation of NGC 4438 By producing a complete velocity field of the galaxy, they show that the off-plane filaments are still bound to the disk.

NGC 4548

Vollmer et al. (1999) study the anemic galaxy NGC 4548 located about 2.4° from the Virgo cluster center. They focus on the kinematics in detail, comparing HI map to an Hα map and an optical B observation. CO observations are added to give more information about kinematics at low galactic radii. The HI distribution shows a ring structure that is at its northern edge distorted. Again, the scenario of the ram pressure stripping is in accordance with all observations. The ram pressure may be decreasing after the galaxy's passage through the cluster center or increasing again as the galaxy sets out for its second approach to the center.

NGC 4388

Veilleux et al. (1999) found evidence of supersonic (Mach number $M = 3$) ram pressure stripping in Hα observations. Gerhard et al. (2002) discovered an isolated HII region at a projected distance of several kpc from the Virgo cluster galaxy NGC 4388. They evaluated its age to about 3 Myr indicating that it has formed outside the galaxy. They conclude that the star formation can take place far outside the main regions of the star formation in the galaxies. Vollmer et al. (2003b) detected a large HI cloud most probably connected to an extended Hα plume. Their numerical simulations match the observed HI spectra. The Hα plume and the HII regions can be explained as a stripped gas cloud that collapsed and decoupled from the ram pressure wind due to its increased surface density. The star-forming cloud is now falling back onto the galaxy.

NGC 4402

NGC 4402 is an HI–deficient Sc Virgo cluster galaxy located near the M87 galaxy (about 1.4°) and also the M86 giant elliptical galaxy. Crowl et al. (2005) present high-resolution optical, H I, and radio continuum observations indicating that the ram pressure stripping and dense cloud ablation

Figure 2.6: NGC 4402. From Crowl et al. (2005)

occur in the galaxy. The near side of the galaxy contains the leading edge of the ICM-ISM interaction. The galaxy is moderately HI deficient (def = 0.61), while the stellar disk appears undisturbed. Both the HI and radio continuum are truncated at about 0.6–0.7 r_{25}. In the undisturbed part of the disk, heavy dust lanes are clearly visible (see Fig. 2.6). The truncation radii differ on opposite sides of the disk. Both the HI and radio continuum emission is displaced to the northwest of the disk, which is consistent with the ICM wind direction. At the windward side of the disk the radio continuum contours are compressed, while at the downstream side they are stretched and reach about 500 pc above the disk. The Hα emission is strong along the windward edge of the disk, possibly indicating star formation triggered by the ICM pressure. It appears that the southeast star clusters show less dust reddening and extinction since the ICM wind has pushed away much of the dust at the leading edge of the galaxy. One can observe the dust plumes extending from the star-forming regions. Only about 0.3% of the total Hα luminosity is from extraplanar HII regions. While the HI traces the warm, neutral medium, the radio continuum traces relativistic electrons spiraling in magnetic field. Crowl et al. (2005) interpret the dust filaments as large, dense clouds that were initially left behind as the low-density ISM was stripped but were later ablated by the ICM wind.

NGC 4485 and NGC 4490

Closely interacting spiral galaxies NGC 4485 and NGC 4490 (located in the NGC 4631 Group) separated by a projected distance of 7.7 kpc are surrounded by a very extended HI envelope. Elmegreen et al. (1998) observe the star-forming regions in their tidal features, including a faint tail of the tidally sheared material from NGC 4490. They estimate the encounter occurred about 4 10^8 yr ago. Clemens et al. (2000) investigate the evolution of the ISM in the system. They suggest that the atomic, molecular and dust components of NGC 4485 were stripped via ram pressure during the passage through the extended HI distribution of NGC 4490; a bow shock in the HI is identified ahead of the stripped gas.

NGC 4064 and NGC 4424

The Virgo Cluster galaxies NGC 4064 and NGC 4424 show peculiarities almost in all components: their Hα emission originates in the central kiloparsec from bar-like strings of star-forming complexes. Outside this radius, almost no Hα emission occurs. Complexes of young stars are found at places aside the recent star formation regions. Both the galaxies are strongly HI deficient, truncated at about 5 kpc radius, and NGC 4424 has a strongly disturbed stellar disk with shell-like features indicating that it has undergone a merger event. NGC 4064 is located at the outskirts of the cluster. In both galaxies the dust is distributed far beyond the Hα or CO gas. CO observation then reveal symmetrically located molecular gas lobes. Gas kinematics indicates that the material is radially infalling towards the central regions.

Cortés et al. (2006) suggest that the peculiarities of NGC 4064 and NGC 4424 can be results of the independent effects of the ram pressure stripping removing the outer gas, and gravitational

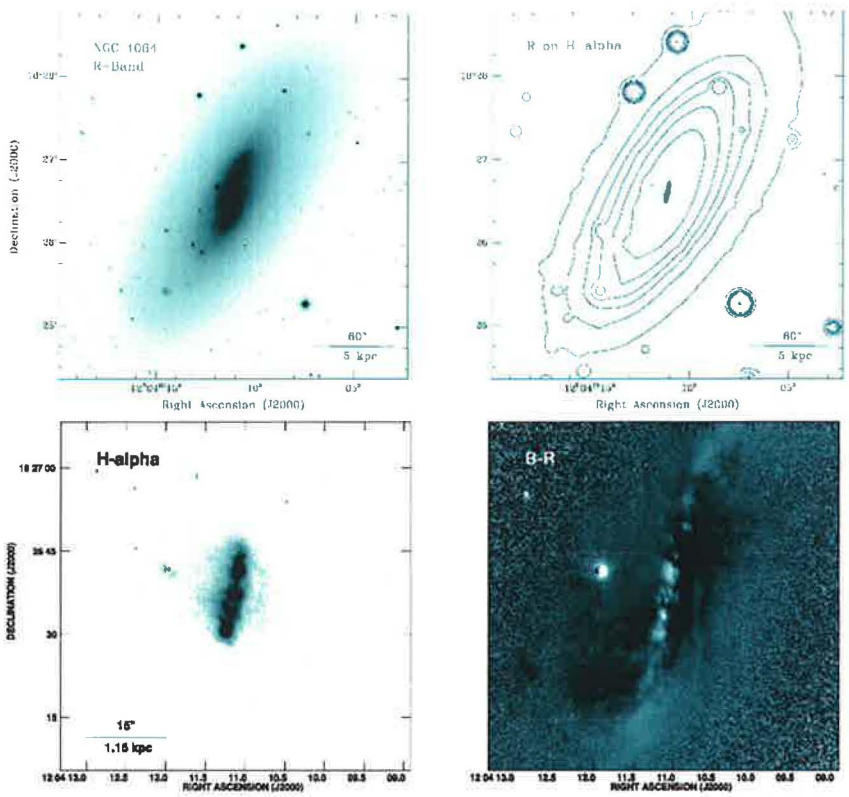

Figure 2.7: NGC 4064: a) R-band image, b) Hα-continuum with R-band contours, c) Hα-continuum with four complexes along the barlike structure and a filament at the eastern side, d) B-R image with visible dust lanes. From Cortés et al. (2006)

interactions (mergers), which heat stellar disks and drive gas to the central kiloparsec. It is likely, that NGC 4424 is an intermediate-mass merger with an ongoing ram pressure stripping of the gas driven out by the merger. NGC 4064 probably recently undergoes a minor merger with a large inclination angle or a close tidal interaction with a nearby spiral galaxy. Its outer disk gas was either stripped about 2 Gyr ago during a core crossing, or more recently by a locally enhanced ram pressure. However, the gravitational interactions, together with the ram pressure stripping transform the morphology of these galaxies. Within the next 3 Gyr they will probably become small-bulge S0s.

A stripping sequence

As summarized above, many individual cases have been studied in detail, showing the galaxies occurring in different evolutionary stages due to their interaction with the surrounding environment. Vollmer et al. (2004a) propose a time sequence of the galaxy vs. environment interaction built up from individual observed cases: The ISM with high surface density is shifted out of the disk when the galaxy crosses the central cluster regions where the ram pressure is strongest. From HI and CO observations, this is seen e.g. in galaxies NGC 4438, and NGC 4522. When the shifted ISM reaches larger distances from the disk, it expands and evaporates and after about 100 Myr only low surface density HI features are observed (e.g. NGC 4388). After another 100–200 Myr, the shifted but bound ISM reaccretes to the disk, forming low surface density arms like in NGC 4569 or NGC 4548. When the operation of the ram pressure is combined with a tidal interaction with a nearby galaxy, and eventually with evaporation, galaxies evolve like e.g. NGC 4654 or NGC 4254.

2.4 Further observations

In this section we give examples of several observations of further interesting features connected to the ram pressure stripping effect.

A bow shock

Markevitch et al. (2002) reveal in the Chandra observation of the merging, hot galaxy cluster 1E 0657-56 a bow shock propagating in front of a cooler gas cloud exiting the cluster core (see Fig. 2.8. The gas cloud is a remnant of a dense central region of the merging subcluster whose gas is swept back by the ram pressure of the ambient cluster gas. The subcluster crossed the main cluster core about 0.1 – 0.2 Gyr ago, at velocity of about 3000 – 4000 km s−1.

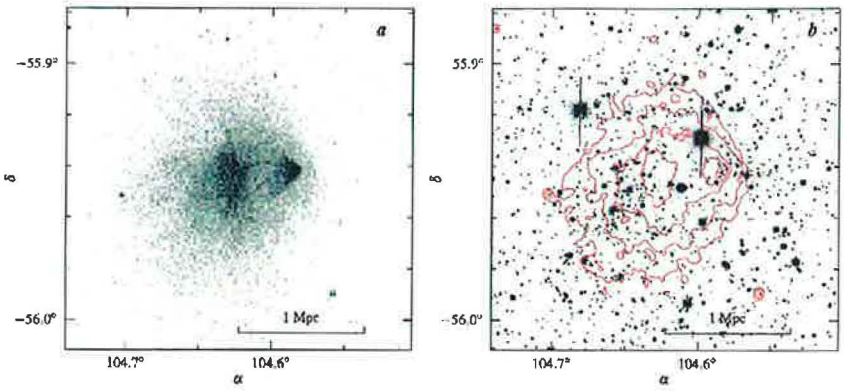

Figure 2.8: Chandra observation of a bow shock formed in front of a subcluster traversing the central region of cluster 1E 0657-56. From Markevitch et al. (2002)

An X-ray trail

Wang et al. (2004) present the Chandra observation of a large-scale hierarchical complex associated with the A2125 complex (z=0.247) consisting of various clusters/groups of galaxies and a low surface brightness X-ray emission. They note a distinct X-ray trail appearing on one side of the fast-moving galaxy C153, clearly due to ram pressure stripping (see Fig. 2.9).

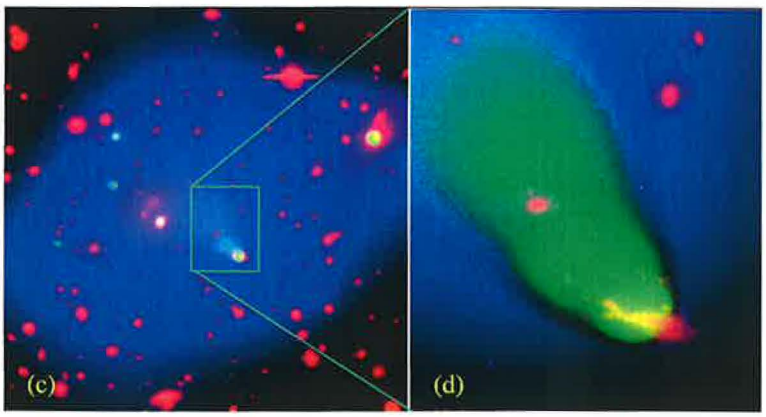

Figure 2.9: The core of the A2125 cluster (left) with a close-up of C153 and its diffuse X-ray trail. From Wang et al. (2004)

An X-ray edge

In a Chandra observation of the UGC 6697 starburst galaxy, a clear evidence for the interaction with the surrounding hot ICM is found by Sun & Vikhlinin (2005). As the galaxy crosses the ICM, a very sharp X-ray edge at the southeast side, and about 60 kpc long tail at the northwest side of the galaxy form (see Fig. 2.10). The X-ray edge coincides with the position of the Hα truncation and with a radio sharp edge. Due to ram pressure compression, the X-ray diffuse emission is enhanced at the windward side of the galaxy. They conclude that the ram pressure is an apparent trigger of the starburst in UGC 6697.

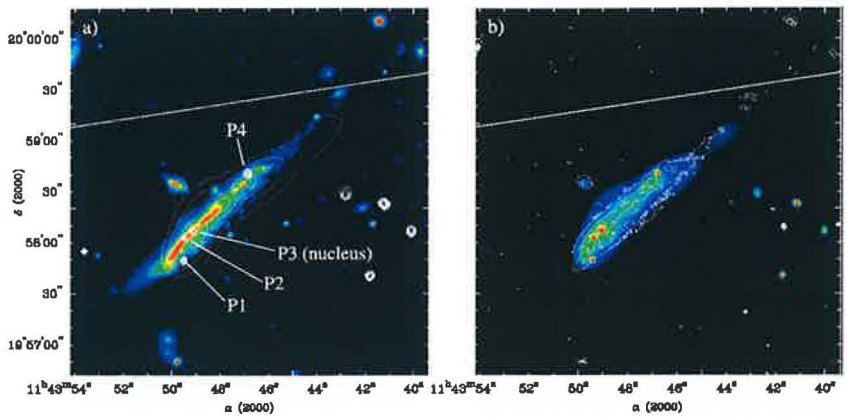

Figure 2.10: Chandra contours superposed on the B-band image of UGC 6697 (left). The Hα contours of UGC 6697 superposed on the Chandra color image in the same field (right). From Sun & Vikhlinin (2005)

NGC 4476 & NGC 4552 (M89) – Virgo elliptical galaxies

Lucero et al. (2005) study HI emission from the low-luminosity Virgo Cluster elliptical galaxy NGC 4476, which contains an undisturbed molecular gas disk, while almost no HI gas, even in the inner disk. The H_2/HI mass ratio is greater than 7, compared to ratios for typical elliptical galaxies less than 2. Therefore, NGC 4476 has either undergone ram pressure stripping on a highly radial orbit through the Virgo Cluster core, or its physical conditions in the molecular ISM are very different (about a factor of 10 higher average density, coupled with lower UV fields) from those of typical Virgo spiral galaxies.

Machacek et al. (2006) focus on another Virgo Cluster elliptical galaxy NGC 4552 (M89) undergoing ram pressure stripping due to its supersonic crossing of the Virgo ICM. Chandra observations reveal characteristic signs of the ram pressure operation: a sharp leading edge in the surface brightness 3.1 kpc of the galaxy center, a tail extending ~10 kpc behind the galaxy, and two 3 – 4 kpc horns of emission that extend to either side of the edge. The galaxy gas inside the edge is cooler and denser than the surrounding Virgo ICM.

An X-ray wake

Sakelliou et al. (2005) discover an X-ray wake trailing behind the radio galaxy 4C 34.16 moving through the ICM (see Fig. 2.11). The wake is cooler and denser than the surrounding ICM. The X-ray trails can be produced by two effects taking place simultaneously: the ram pressure stripping of the galactic material, and the Bondi-Hoyle accretion of the ICM. Since large-scale BH wakes can be found only in low-temperature clusters behind slowly moving and massive galaxies, the most probable scenario for the observed wake is the ram pressure stripping.

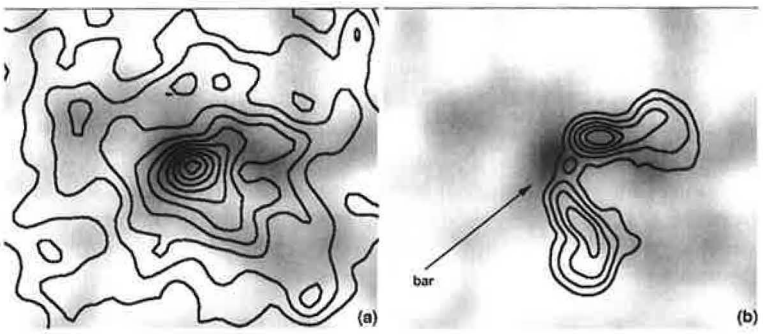

Figure 2.11: (5.0-8.0) keV image of the galaxy 4C 34.16. overlaid by the (0.3-5.0) keV contours (left), and the radio map (right). From Sakelliou et al. (2005)

Stellar vs. Hα scale lengths

For a large sample of field and Virgo Cluster galaxies, Koopmann et al. (2006) have compared exponential scale lengths of the stellar and massive star-forming populations, using R-band and Hα surface photometry. They revealed that in the field, Hα scale lengths are on average about 1.14-times longer than those measured in the R-band. On the contrary, the Hα scale lengths of the Virgo Cluster galaxies are on average about 20% smaller than their stellar lengths. While in the field, the scale lengths ratios are not dependent on other galaxy properties, in the Virgo Cluster, the ratios are strongly dependent on the environment of the galaxy: galaxies with smaller star-forming disks have steeper falloff of star formation activity with radius. It means that likely environmental processes responsible for the shortening of Hα disks in the Virgo Cluster galaxies have to conform to the constraints of the environmental dependence of the Hα scale lengths.

2.5 Ram pressure stripping: recent simulations

Numerical simulations of the ram pressure stripping phenomenon first occurred in late 1970s as a reaction to the X-ray observations. Since that time many simulation results have occurred, using different numerical methods (finite difference vs. SPH vs. sticky particles). In this section we give an overview of existing simulations based on a well-arranged introduction of Schulz & Struck (2001).

Lea & De Young (1976)

Lea & De Young (1976) propose the first hydrodynamical calculations of the ISM-ICM interaction at velocities of $M \sim 1$. In their model, a spherical galaxy is used due to its deep symmetric potential and an assumption that if gas is stripped from this galaxy, it can be stripped from a less symmetric galaxy with the same mass, as well. The galaxy has a total mass of 10^{11} $M_\odot$ and, density distribution of an isothermal sphere, radius 15 kpc, and the central density of about 400 $M_\odot/pc^3$. The cluster model is the Coma-like cluster with the King profile. From observations they deduce the velocity dispersions of about 500 – 1500 km s^{-1}, giving a Mach number $M \sim 1 - 2$. For such velocities, and temperature of the ICM $\sim 5\ 10^7$ K they do not expect the accumulation of the ICM.

The galaxy is embedded into a 2D axisymmetric volume with maintained the appropriate values of density, temperature and inflow velocity on the upstream side of the volume. Initially, from computing-time reasons, they put the galaxy virtually at some distance from the cluster center and not to the outskirts. In their first simulation, the galaxy was placed with a constant velocity in a homogeneous medium with $T_{ICM} = 10^7$ K and density $5\ 10^{-4}$ cm^{-3} corresponding to 0.7 Mpc distance from the cluster center. In the second case, the galaxy was at 4.5 Mpc distance, with density of $1.4\ 10^{-4}$ cm^{-3} and temperature $T_{ICM} = 3.2\ 10^7$ K, and velocity of 1000 km s^{-1}. The changes in the ambient density and temperature along the radial orbit towards the center were included, leading to a decrease of the Mach number.

They describe a formation of the steeping compression ahead of the galaxy moving through the ICM, and a rarefied regions behind the galaxy. The stripping then proceeds by two processes: an ablation by the flow around the galaxy, and an expansion of the ISM into the rarefied shadow. The results show that in both the cases of initial conditions, the interaction with the ICM is able to remove about 80 – 90 % of the ISM within $\sim 10^9$ yr. Further, they describe a tail forming behind the stripped galaxy, with an average density of a few times 10^{-3} cm^{-3} and temperature $\sim 10^6$ K.

Lea & De Young (1976) conclude from their numerical simulations that the ISM-ICM interaction influences both the evolution of the galaxy and the cluster. They show that the mass of the galaxy can be reduced to a few times 10^9 $M_\odot$ within 10^9 yr, i.e. within one crossing time, and note that the central density of the galaxy has been reduced by a factor of 5 and the entire density profile has broadened. They estimate the total amount of gas shed to the intracluster medium to few times 10^{12} $M_\odot$ which is small compared to the observed amount of the X-ray emitting gas in the cluster.

Farouki & Shapiro (1980)

Farouki & Shapiro (1980, 1981, 1982) study three processes resulting from the proximity of galaxies in galaxy clusters: the ram pressure stripping, the tidal interactions, and the galaxy mergers. To follow the morphological changes of initially flat disk galaxies under operation of the ram pressure and rapid tidal forces, Farouki & Shapiro (1980) perform 3D direct N-body simulations with a galaxy model consisting of 1000 stellar particles and 100 diffuse gas cloud particles rotating as an equilibrium disk in a fixed spherical halo. The gaseous particles possess larger mass and larger softening parameter compared to the stellar ones. The disk radius is 15 kpc, and the total mass of the galaxy is $2\ 10^{11}$ $M_\odot$. The disk-to-halo mass ratio is 1. In simulations, no gas dynamics is treated.

They assume that a gas cloud in a flat galaxy of radius r and thickness h, is due to a ram pressure of the ICM through which the galaxy traverses ejected to a height h above the disk plane

on a time scale

$$\Delta t \approx \frac{h}{v_g}\sqrt{\frac{\rho_{ISM}}{\rho_{ICM}}}, \tag{2.2}$$

where ρ_{ISM} and ρ_{ICM} denote the density of the interstellar medium and the intracluster gas, and v_g the velocity at which the galaxy traverses the ICM. They further note that a) a replenishment of the gas may play an important role when the mixing of the ICM stream momentum with the static ISM yields an output velocity that is lower than the escape velocity, and b) if the gas mass fraction is not small, tidal forces on the galaxy arising from the escaping gas may be significant and induce a velocity dispersion perpendicular to the disk plane.

The effect of the ram pressure is included only analytically in a form of the time-dependent "ejection force":

$$\boldsymbol{F}(t) = -\hat{v}_g\,\rho_{ICM}[v_g - v_{ISM}(t)]^2 \Delta A\, cos\,\theta, \tag{2.3}$$

where $\hat{v}_g$ is a unit vector in the galactic orbital direction, and $v_{ISM}(t)$ is the velocity of the followed gas cloud with the cross-section ΔA. θ is the inclination angle of the disk, and ρ_{ICM} the ICM mass density. The force operates during a time of 4 galaxy rotations, however, the most of the stripping was completed within one or two rotations. They note that only the gas clouds from outer disk regions are ejected in the wind direction. For the ICM density of 1 10^{-3} cm^{-3}, depending on the galaxy velocity varying in a range from 1200 to 2700 km s^{-1}, from more than 90 % to 75 % of the gas is found to be stripped from the disk (see Fig. 2.12). One simulation run with an inclined disk is performed.

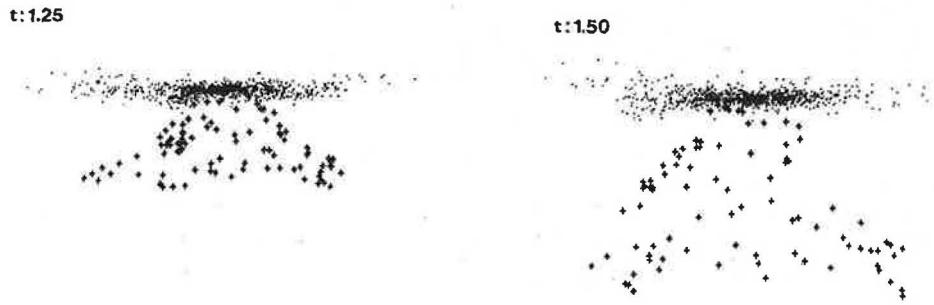

Figure 2.12: The progress of ram pressure stripping with dots representing stars and crosses gas clouds. From Farouki & Shapiro (1980)

They conclude that the stripping of the gas component disrupts and thickens the outer galaxy disk, but does not alone explain the effect of the transformation of spiral galaxies into SO systems in dense galaxy clusters.

Kritsuk (1984)

Integrating the equation of motion of interstellar clouds in a disk galaxy, including the effect of gravity of the disk and of the ram pressure of the ICM, Kritsuk (1984) derived stripping radii of galaxies with arbitrary inclination of the disk with respect to the ICM wind orientation. He found that HI clouds are swept out easily, while dense molecular clouds mostly resist to the effect of the ram pressure stripping and stay in galaxies. Further he notes that the efficiency of the sweeping decreases with increasing degree of mass concentration towards the galaxy center. The stripping probability in inclined cases is found to depend on the mass concentration towards the disk plane but is generally nonzero.

Takeda et al. (1984)

They consider a spherical galaxy with the total mass of 10^{12} $M_\odot$ in 2D simulations using a fluid-in-cell algorithm with 32 × 42 grid. The gravitating component of the cluster was modeled with a β-profile with core radius of 250 kpc and central density 6.3 10^{-2} cm^{-3}. It was filled with hydrostatic isothermal ICM at 6.6 10^7 K, and central density of 10^{-4} cm^{-3} falling to 10^{-5} cm^{-3} at 1 Mpc distance from the cluster center. By varying the upstream velocity and density at the grid boundary, the radial motion through the cluster was modeled.

The model galaxy was initially set out a) from 1 Mpc distance with 100 km s^{-1} velocity and b) from 250 kpc distance with the same velocity, in the former case leading to 2240 km s^{-1} velocity in the cluster center, and in the latter case to 1130 km s^{-1}.

The half periods of the orbits are 2.2 10^9 yr, and 8.2 10^8 yr, respectively. Since they assume that the galaxy accumulated the gas shed by stars, periodic phases of stripping and accumulation of gas are visible in their simulations as the galaxy orbits in the cluster. At cluster outskirts the stripping is low and the galaxy supplies the gas via stellar mass loss. Results for both the cases are found to be very similar – the galaxy accumulates during a half orbital period about 30% of the gas lost by its stars. They identify three phases of the stripping process: a) sudden removing of gas whose gravitational binding is lower than the ram pressure, i.e. corresponding to Gunn & Gott (1972) criterion, b) continuous phase when the gas shed by galactic stars is constantly swept from the galaxy, and c) cyclical stripping of the gas at cluster cores and its subsequent replenishment in the outer parts of the orbit. Fig. 2.13 shows an example of their simulation results.

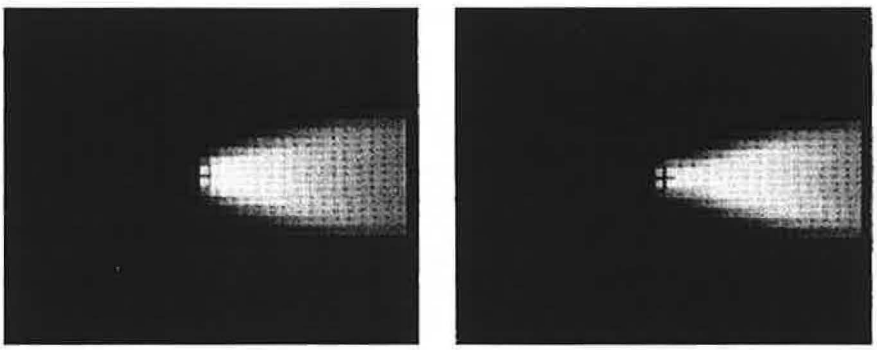

Figure 2.13: The density distribution of the galaxy experiencing the ram pressure stripping in simulations of Takeda et al. (1984).

Gaetz et al. (1987)

Gaetz et al. (1987) present results of numerical simulations of gasdynamical stripping of spherical galaxies using a 2D second order Eulerian hydrodynamics code. They include the treatment of a number of physical processes into the simulations: replenishment of the ISM, removal of cold dense gas by the star formation process, radiative cooling by thermal bremsstrahlung and collisionally excited line emission. These processes are characterized by proper time-scales and their ratios. They perform a set of simulations covering a large range in two parameters: the ratio of mass flux in the external medium to the gas replenishment rate within the galaxy, and the square of the ration of the external flow velocity to the velocity dispersion within the galaxy. They provide approximate numerical fitting formulas for the steady state fraction of the replenished gas retained by the galaxy, and the degree of stripping by excess of the ambient intergalactic medium.

Portnoy et al. (1993)

Assuming a spherical galaxy moving in the cluster gas, Portnoy et al. (1993) start their calculations with the initial conditions of uniform gas density and temperature, and evolve a time-dependent model until the steady state is reached. Then they study the physical conditions in the cluster gas

from the point of view of two fluid model. They derive the hydrodynamic equations, solve them numerically and examine them for the case of the ram pressure stripping of elliptical galaxies.

They find that formation of a bow shock in a galaxy is due to the replenished gas from stellar mass loss, and that the velocity dispersion of the galaxy stars strongly influences the injection temperature of the replenished gas. They provide fitting formulae for the effects of various parameters.

Kundić et al. (1993)

First note on the 3D N-body/SPH simulations with the gravity tree of the dynamical effect of the ram pressure on galaxies in rich clusters is by Kundić et al. (1993). The galactic HI is modeled as a smoothly distributed single phase medium. In agreement with expectations, they find that significant gas ablation can occur in the outer parts of the galaxy, while the dense central regions of the disk suffer almost no effect. In their face-on simulation run with a uniform density of the ICM of 10^{-3} cm^{-3} and the galaxy velocity of 1500 km s^{-1}, a typical spiral loses all of its atomic gas.

They further think over the dynamical effects of the ram pressure to a cluster spiral as a whole. They show that in rich clusters where the ICM constitutes a significant fraction of the total mass, the momentum loss timescale due to gas drag is comparable to the momentum loss timescale caused by dynamical friction. However, neither process reveals as effective enough to produce a velocity bias through a significant settling of spiral galaxies relative to the dark matter. Comparison of a simple analytical estimate for the gas drag timescale with the results of their numerical simulations shows a good agreement.

Murakami & Ikeuchi (1994)

Murakami & Ikeuchi (1994) study the effects of the supersonic ram pressure of the intergalactic matter or of a blast wave caused by the activity of quasars to so-called minihalos. The minihalo is a model proposed in the CDM cosmogony to explain the Lyα absorption line systems of quasars. They occur due to change of the diffuse UV flux irradiating the intergalactic gas and their intervence produce the Lyα forest.

Using a 2D hydrodynamical calculations, Murakami & Ikeuchi (1994) study the evolution of minihalos due to their interaction with supersonic gas flows. The behavior of the minihalo experiencing the ram pressure is classified into three cases: a) when the central pressure in the cloud is lower than the ram pressure, the cloud is destructed instantaneously, b) when the ram pressure exceeds the central cloud pressure but the flow velocity inside the bow shock is higher than the escape velocity of the gas, the cloud is gradually stripped, and c) when the central pressure is much higher than the ram pressure and the flow velocity inside the bow shock is smaller than the escape velocity, the cloud is unaffected. They determine the conditions for cloud destruction and obtain the time scale for gas ablation.

After studying an isolated cloud, they explore the case when minihalos make a cluster evolving into a group of minihalos or protogalaxies which is again exposed to the ram pressure of surrounding ICM. They reach an agreement with observation when suggesting that the gas of a given minihalo would be completely stripped in the viral stage and thus the net clustering of Ly alpha clouds will be suppressed.

Sofue (1994)

Sofue (1994) does not focus on the galaxy interaction with the surrounding intracluster medium, but study the behavior of the interstellar gas clouds in a galaxy during its gasdynamical interaction with the halo and disk of a spiral companion galaxy. The stripping of the ISM from the companion galaxy and its accretion onto a disk galaxy is numerically calculated integrating the equation of motion of the center of a test-companion galaxy around the major galaxy, including the dynamical friction. The ram pressure effect is introduced in the equation of motion of the test cloud

$$\frac{d^2\boldsymbol{r}}{dt^2} = \sum_{i=1}^{2} \frac{\partial \Phi_i}{\partial \boldsymbol{r}} - \frac{3\rho(\boldsymbol{r})}{4R\rho_c}\Delta\boldsymbol{v}\Delta\boldsymbol{v}, \tag{2.4}$$

where $\boldsymbol{v}$ and $\boldsymbol{r}$ are the cloud's velocity and position with respect to the galaxy center, and ρ_c is the cloud density. Gravitational potentials of the major and the companion galaxy are marked with Φ_i. The rightmost term is the ram force on the test cloud with radius R, where $\Delta\boldsymbol{v}$ is the relative velocity, and $\rho(\boldsymbol{r})$ the density of the diffuse gas of the galaxy.

Their simulations show that due to the ram pressure, the gas clouds are stripped from the companion galaxy and accreted toward the disk of the spiral galaxy. Then, the behavior of the accreted gas depends on the orbital geometry of the interaction: a) when the companion's orbit is retrograde with respect to the rotation of the spiral galaxy, the infalling clouds hit the nuclear region and due to angular momentum transfer the inner gaseous disk is disrupted and a void of the ISM makes in the bulge, b) if the companion's orbit is then prograde or polar, infalling clouds are accreted by the outer disk, forming a rotating gas ring.

Thus, they have found that the ram-pressure process is significant during the merger of galaxies, in which interstellar gas is stripped and accreted prior to the stellar body merger.

Tosa (1994)

Representing the clouds of the ISM by particles and following their orbits by solving numerically the equations of motion, Tosa (1994) studies the effect of the ram pressure to the galactic disk. The ram pressure on the cloud exerts a force

$$\boldsymbol{F} = C\rho_{ICM}|\boldsymbol{v}_{ICM} - \boldsymbol{v}|(\boldsymbol{v}_{ICM} - \boldsymbol{v}), \tag{2.5}$$

with $\boldsymbol{v}_{ICM}$, and $\boldsymbol{v}$ corresponding to the velocity of the ICM, and to the velocity of the cloud in the galaxy, respectively. The constant $C \approx (d\rho_c)^{-1}$, where ρ_c and d are the cloud gas density and its diameter.

Then, the disk gas clouds moving along circular orbits in an axisymmetric galactic potential with asymptotically flat rotation curve are followed under the effect of the ram pressure operating edge-on and gradually rising to a constant value. A development of an induced prominent spiral structure is observed in the disk. It is a wave phenomenon, and contrary to the normal spiral waves, it is single-armed and slowly rotating in a retrograde direction. The spiral is apparently leading with respect to the galactic rotation and slowly winds up in a retrograde direction. Tosa (1994) stresses that a ram pressure leading arm should be distinguishable from gravitationally created leading arms in observation.

Balsara et al. (1994)

Balsara et al. (1994) using 2D PPM (Piecewise Parabolic Method) hydrodynamical simulations with high resolution study the flow and the process of gas ablation in a spherical galaxy on a very small scales compared to previous simulations. They include the processes of star formation and mass replenishment. The total gravitational mass of the galaxy model is 1.2 10^{10} $M_\odot$. They observe a weak bow shock forming in front of the galaxy followed by development of a second bow shock in $\sim 3\ 10^8$ yr in front of the galaxy core (see Fig. 2.14). The second bow shock is supported by an accretion inflow into the core which develops on the downstream side. The successive phases of the ram pressure process are separated by a few times 10^7 yr.

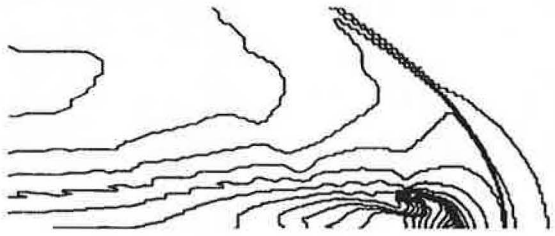

Figure 2.14: Density contours in the standard run of Balsara et al. (1994). Formation of bow shock in front of the galaxy and in front of the galactic core is visible.

Murakami & Babul (1999)

In their work, Murakami & Babul (1999) study the interaction between supernova-powered gas outflows from dwarf galaxies and the intergalactic medium, using 2D hydrodynamical simulations. They find that a high-pressure IGM in clusters of galaxies can prevent the gas outflowing from supernovae explosions from escaping from the galaxy. Once halted, the IGM pressure pushes the shell back into the galaxy, which can lead to its non-uniform collapse and enhancement of small perturbations in the shell.

But galaxies in such high-pressure environments are subject to ram pressure, which acts to strip the gas from the galaxy. Their simulations show that when the ram pressure exceeds the ambient thermal pressure, it can distort the shell which consequently fragments into high-density clouds which are then carried downstream by the ram pressure. These high-density clouds are then potential sites of star formation, following a diffuse tail-like structure.

Stevens et al. (1999)

To simulate the gas dynamics in and around a galaxy moving through the ICM, Stevens et al. (1999) use 2D hydrodynamical PPM code resolving shocks in complex flows, at resolution of 240 $\times$ 180. The method is similar to that used by Balsara et al. (1994). They include replenishment of the galaxy ISM by stellar populations. The model galaxy with the total mass of 1.2 10^{12} $M_{\odot}$ experiences the ram pressure in three models of galaxy cluster: cool, intermediate, and hot cluster differing in temperature (1, 4, and 8 keV), and the gas density profile and surface brightness distribution, both modeled with a β-profile with $\beta = 2/3$.

Using the described model, Stevens et al. (1999) attempt to quantify the observational characteristics of structures resulting from the ISM-ICM interaction. They suggest a criterion for galaxies to show observable features of the interaction: a) galaxies with younger stellar population are more likely to shows the features due to their substantial mass loss, b) galaxies in cooler environments possess observable stripped tails, c) galaxies at the periphery of rich clusters should show tails.

In the three different cluster environments, spherical galaxies move with velocities ranging from Mach 1.2 to 2.1. The results fall into two groups: a mass retention mode when high velocity galaxies in hot clusters are stripped of the entire gas content on a time scale of 10^8 yr, and a mass retention mode when slower galaxies in cool clusters retain 30 – 80 % of the gas.

The dynamical features that can be identified in their simulations are: a leading bow shock (in the case of supersonic galaxy motion), a weak gravitationally focused (by Bondi-Hoyle accretion) wake or tail behind the galaxy, and a dense ram-pressure stripped tail behind the galaxies with higher mass replenishment rates and a denser ISM. Further, they find that the ram pressure stripping occurs in an episodic manner. They conclude, that according to their calculations, the ram-pressure stripped tail should be usually the most visible X-ray feature of the ISM-ICM interaction, and potentially the bow shock preceding the galaxy.

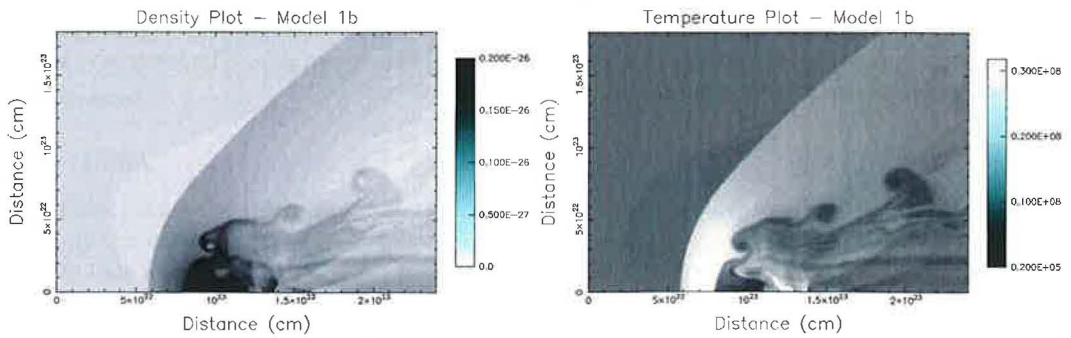

Figure 2.15: The density and temperature structure of the galaxy in 1 keV cluster. Note the dense streamers in the tail region. From Stevens et al. (1999)

Fujita & Nagashima (1999)

By means of a simple model of the evolution of molecular clouds, Fujita & Nagashima (1999) estimate the changes of star formation rate induced by the ram pressure from the ICM in a disk galaxy radially falling towards the cluster center. They note that as the galaxy approaches the cluster center with high density and deep potential well, the SFR increases to twice the initial value due to compression of the molecular gas content of the galaxy by the ram pressure. However, this increase does not affect the color of the galaxy significantly. Further, at distances lower than 1 Mpc from the cluster center, the initial enhancement of the SFR is followed by a rapid drop owing to the effect of the ram pressure stripping of outer parts of the galaxy. This makes the galaxies redden. In clusters with lower values of the central ram pressure, the SFR changes less significantly since both the HI compression and the stripping effect are not effective. They conclude that the recognized changes of the color and luminosity can explain the observed morphology and color distribution in clusters when assumed their formation by accretion of field spirals.

Abadi et al. (1999)

Performing 3D tree/SPH simulations, Abadi et al. (1999) study the stripping of spiral galaxies by operation of a constant flow of ICM particles homogeneously distributed in a simulation box of size 60 kpc × 60 kpc × 10 kpc with periodic boundary conditions.

A spiral galaxy with the rotation velocity of about 215 km s^{-1} undergoing the ram pressure in the range from about 300 to 30 000 $cm^{-3}km^2s^{-2}$ may be stripped of about 80 % of its ISM (see Fig. 2.16). A more detailed information is provided in Chapter 5.

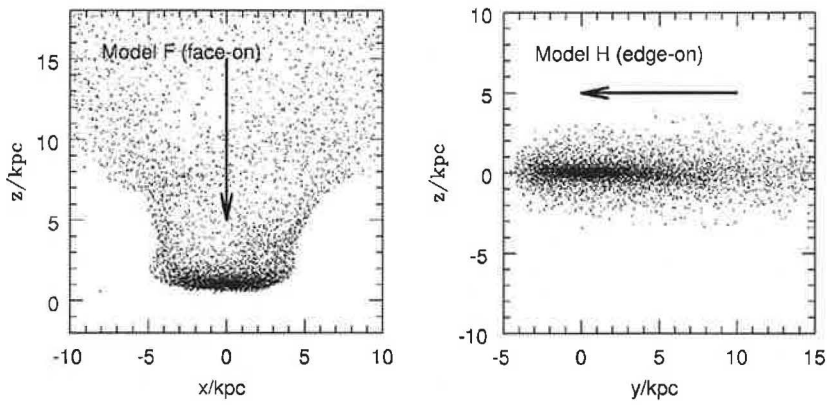

Figure 2.16: Positions of gas particles after $\sim 10^8$ yr of evolution under effect of face-on and edge-on ICM wind. From Abadi et al. (1999)

Mori & Burkert (2000)

First hydrodynamical simulations of the ram pressure stripping in dwarf galaxies were performed by Mori & Burkert (2000). They use axisymmetric two-dimensional finite-difference hydrodynamical simulations at high resolution to study the interaction between the ICM and an extended gas component of dwarf galaxies confined by a surrounding cold dark matter halo.

Their results show that the gas within the CDM halo of dwarf galaxies can be totally stripped in a typical galactic cluster (see Fig. 2.17), which shows the prime role of the ram pressure stripping in the chemodynamical evolution of dwarf galaxies in galactic clusters. During the interaction, a development of the forward shock propagating through the gas of dwarf galaxy, and of the reverse shock propagating through the ICM is observed. Consequently, the gas in the galaxy is strongly compressed. At later times, Kelvin-Helmholtz instabilities are observed at the contact discontinuity.

Mori & Burkert (2000) further describe the interaction analytically and suggest an alternative criterion for the instantaneous stripping of spherical galaxies to Gunn & Gott (1972) criterion. They state that the CDM halo of the galaxy is stripped completely if the ram pressure exceeds its central thermal pressure:

$$\rho_{ICM} v_{gal}^2 > \frac{GM_0 \rho_{g0}}{3r_0}, \tag{2.6}$$

where M_0 and ρ_{g0} is the core mass and density of the CDM halo.

They neglect the self-gravity of the gas that is assumed to be in hydrostatic equilibrium with the constant temperature. Further they neglect the effects of the self-gravity of the gas, radiative cooling, the heating by supernovae and stellar winds from massive stars, and the photoionization by UV radiation background.

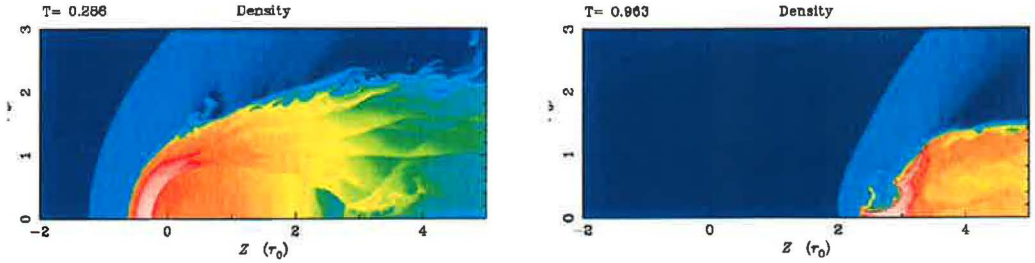

Figure 2.17: Stripping of a dwarf galaxy with core mass of 10^7 $M_\odot$ by the ICM wind of density 10^{-4} cm^{-3} and velocity 1000 km s^{-1}. Time is in 10^8 yr. From Mori & Burkert (2000)

Quilis et al. (2000)

In their simulations employing a high resolution 3D Eulerian code with a fixed grid based on high-resolution (512^3) shock-capturing method, Quilis et al. (2000) follow the interaction between the hot ICM and the cold ISM. The code includes turbulent and viscous stripping. The stellar and DM components are evolved using a particle-mesh code.

They find that the ram pressure stripping may be enough effective to remove all the interstellar material out of the disk and that this effect can explain the existence of S0 galaxies in nearby clusters and observed rapid truncation of the star formation. A more detailed information is provided in Chapter 5.

Vollmer et al. (2001a)

Investigating the role of the ram pressure stripping in the Virgo cluster, Vollmer et al. (2001) employ a method of sticky particles for modeling the warm neutral clouds of the ISM. Their model spiral galaxy with a constant rotation curve of $\sim$ 140 km s^{-1} feels the effect of the ram pressure that is included only analytically as an additional acceleration on the clouds located at the windward side of the gas distribution. But, contrary to most simulations discussed in this section, the ram pressure with temporal profiles instead of a constant ICM wind is introduced.

Their find that the stripping efficiency depends on the galaxy orbit, i.e., on the maximum approach to the cluster center, the maximum galaxy velocity, and the inclination of the disk. For low inclination angles they observe a reaccreting material falling back to the disk. They conclude that the scenario of the ram pressure stripping of the HI galaxy content is consistent with HI observations of the Virgo population (see Fig. 2.18). A more detailed information is provided in Chapter 5.

The same numerical code is used by Vollmer et al. (2001b) to model the dynamical state of the Coma galaxy NGC 4848, a highly HI deficient galaxy with detached CO emission regions. A model with a galaxy with the rotation velocity $v_{rot} \sim 250$ km s^{-1} and inclination angle of the disk $i = 20°$ moving through the ram pressure peak $p_{ram} = 2\,800$ cm^{-3}km^{2}s^{-2} reproduces best the

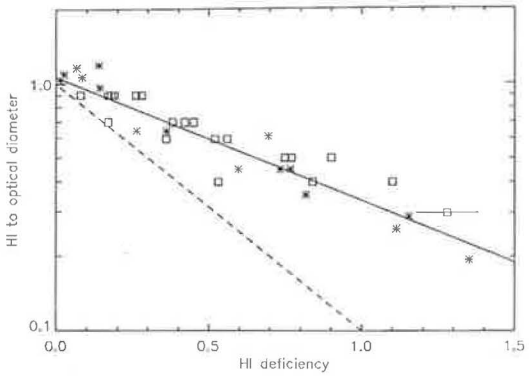

Figure 2.18: Comparison of simulation results of Vollmer et al. (2001a) (stars) with observations of Cayatte et al. (1994) (squares). From Vollmer et al. (2001a)

observations. They conclude, that the compression of the neutral gas due to reaccretion of the gas that was shifted out of the disk but not stripped by the ram pressure, leads to a phase transition from atomic to molecular gas and to star formation activity.

Schulz & Struck (2001)

The model dwarf galaxy in 3D HYDRA (SPH-AP^{3}M) simulations of Schulz & Struck (2001) is placed in a cubical grid with 100 kpc edge.

As a result of the ram pressure stripping, they get from simulations annealed galaxies with a ring of compressed ISM at the truncation radius. There, enhanced star formation can proceed - see e.g. NGC 4580 (Kenney et al. 2004). This ring is a consequence of a gravitational instability induced by a slight shift of the stellar disk in the wind direction. Then different ram pressures and restoring forces at the front and back sides of the ISM disk induce a tidal squeezing of the disk, Toomre's Q increases, and spiral arms at the outer disk region form. A crucial role in this effect plays the presence of the cooling in their simulations.

Schulz & Struck (2001) reveal that not all the gas stripped from the disk escape immediately from the galaxy but linger for times of order 10^8 yr. They show that the gravitational force of the halo galactic component can exceed the ram pressure force, and bind the gas to a region substantially offset from the initial disk. Its component in the wind direction is

$$F_h = \frac{GM(r)m_{cl}}{r^2}\frac{z}{r} = \frac{m_{cl}v_c^2 z}{r^2}, \tag{2.7}$$

where $M(R)$ is the halo mass within radius r, m_{cl} is the mass of the cloud, and v_c its local circular velocity. When this force balances the ram pressure force, a curve of r versus z corresponding to the boundary of the region where $F_h < F_{ram}$ can be derived:

$$\frac{z}{r} = \frac{\rho_{ICM} r v_{ICM}^2 \Delta A}{m_{cl} v_c^2}. \tag{2.8}$$

Although Schulz & Struck (2001) have a constant flow of the ICM they note that rapid traversal of the core can end the stripping on a time-scale shorter than the annealing time.

Piontek & Stone (2001)

Using simulation technique and galaxy model closely similar to Quilis et al. (1999), Piontek & Stone (2001) study the effect of varying mass of the gaseous and stellar disk, as well as the orientation of the galaxy with respect to the ICM wind. Their galaxy model has the total mass of the disk and halo of 5.8 10^{10} $M_\odot$ and 26 10^{10} $M_\odot$, respectively. It corresponds to the rotation velocity of

about 230 km s^{-1}. The ICM has initially the temperature of 10^8 K, a velocity of 2000 km s^{-1}, and density 2.6 10^3 cm^{-3}. The corresponding sound speed is 1060 km s^{-1}. Following Quilis et al. (1999), they include a central hole of radius of 2.5 kpc in the HI disk.

Varying the mass of the gas disk in a range (0.5 – 1) 10^{10} $M_\odot$, they perform a set of simulations and follow the mass of the gas contained within a cylinder of radius 25 kpc and thickness 2.5 kpc, centered on the stellar disk. The galaxy retains from 0 to 30 % of the initial gas mass after $\sim$ 200 Myr period of a constant operation of the ICM wind. If the mass of the gas disk is M_{gas} = 1 10^{10} $M_\odot$, it retains $\sim$ 15 %, while for M_{gas} = 0.5 10^{10} $M_\odot$, all the gas is stripped within 100 Myr. Changing the disk orientation can double the amount of the retained gas.

Hidaka & Sofue (2002)

Hidaka & Sofue (2002) investigate effects of the ram-pressure of the ICM wind on inner parts of the disk of spiral galaxies. They use 2D hydrodynamical simulation (PPMLR method) with 256×256 resolution. They neglect the self gravity of the gas and radiative heating/cooling. They model a galactic disk with a static axisymmetric potential and a non-axisymmetric, rotating bar potential. The ram-pressure acceleration per unit mass is given by (cf. Tosa 1994)

$$a_{ram} = C\, n_{ICM} |v_{ICM} - v_{rot}| (v_{ICM} - v_{rot}). \tag{2.9}$$

They adopt three values for the ICM density n_{ICM}: 1 10^4 cm^{-3} (corresponding to the intergalactic density), 5 10^{-4} cm^{-3}, and 1 10^{-3} cm^{-3}, and three values for the ICM velocity v_{ICM}: 530, 1000, and 1500 km s^{-1}.

From their simulations follows that the orbits of the inter-arm ISM are disturbed even if the ICM wind is not strong enough to strip the gas disk, and that the disturbed inter-arms ISM causes highly asymmetric molecular arms in the inner few kpc of the disk (see Fig. 2.19).

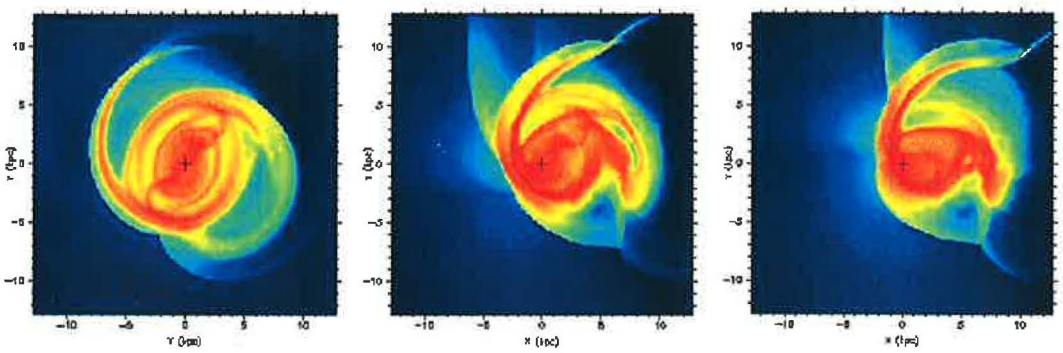

Figure 2.19: Effect of the ICM wind (blowing from left to right) on the orbits of the diffuse interarm gas. From Hidaka & Sofue (2002)

They further estimate analytically the effect of the ICM-ISM interaction: The ram force component parallel to the disk plane exerted on an ISM element corresponds to

$$f_{ICM} \sim \rho_{ICM}\, \Delta A\, \delta v^2 \cos\alpha \sin\alpha, \tag{2.10}$$

where ΔA is the surface area of the element, α is the angle between the ICM wind direction and the galactic plane, and δv is the local relative ISM-ICM velocity. The element is bound to the galaxy by a restoring force

$$f_{ISM} \sim \rho_{ISM}\, d\, \Delta A\, v_{rot}^2 r^{-1}, \tag{2.11}$$

where d is the vertical disk size, and r is the galactocentric radius of the element. The ratio of the two forces is

$$\eta = \frac{f_{ICM}}{f_{ISM}} \sim \frac{n_{ICM}}{n_{ISM}} \frac{r}{d} \left(\frac{\delta v}{v_{rot}}\right)^2 \cos\alpha \sin\alpha, \tag{2.12}$$

where n_{ICM} and n_{ISM} are the number densities of the ICM and ISM, respectively. When $\eta < 1$, the ISM motion is little affected, but if it exceeds unity, the ram force disturbs the ISM motion.

The analytic calculation for an ICM wind with $n_{ICM} \sim 10^{-4}$ cm^{-3}, $v_{ICM} = 1000$ km s^{-1} and the inner part ($r < 5$ kpc) of a galaxy with $d \sim 100$ pc, rotating at $v_{rot} \sim 200$ km s^{-1} shows, that the ISM is tripped if $n_{ISM} \ll 1$ cm^{-3}. Hidaka & Sofue (2002) estimate that for values of about 1 cm^{-3} the gas is not stripped but the ram pressure can indeed strongly disturb the interarm gas in the inner disk and result in deformed galactic shock waves that can be asymmetric due to different values of the δv in different parts of the disk. This mechanism can explain the asymmetric CO gas distributions in the central regions of observed Virgo spirals.

Okamoto & Nagashima (2003)

Performing N-body cosmological simulations in combination with a semianalytic galaxy formation model, Okamoto & Nagashima (2003) study the environmental effects – hot gas stripping, the ram pressure stripping of cold disk gas, major mergers, and minor mergers – on the evolution of bright cluster galaxies in a ΛCDM universe. Since the code enables them to calculate orbits of galaxies in the simulated cluster, a realistic effect of the ram pressure stripping of cold gas can be incorporated.

Results of the simulations surprisingly indicate that the ram pressure stripping is not important for colors and SFRs of galaxies in the cluster core because the star formation can be sufficiently suppressed by consumption of the cold gas in the disks.

Acreman et al. (2003)

Acreman et al. (2003) present results of a parameter study of 2D hydrodynamical simulations of an elliptical galaxy radially falling into a cluster. They follow the effects of the event on the galaxy and the impacts on observable properties. They assume a pre-existing gas halo surrounding the galaxy out to r_{200} distance. The duration of the initial phase of the ram pressure stripping depends on the halo initial mass, but after this phase, all runs have a similar behavior, i.e. after ~ 4 Gyr (which corresponds to the time of the second passage of the cluster core) the signatures of the initial gas content are no longer present.

Schindler et al. (2005)

Schindler et al. (2005) present numerical simulations including the galactic winds and ram pressure stripping and study the transfer of the metal-enriched ISM into the ICM. They create metalicity maps, which are directly comparable to those obtained from X-ray observations and find that ram pressure stripping is more efficient than quiet galactic winds in the redshift interval between 1 and zero.

As the enriched ISM is stripped from the galaxy, it is not mixed immediately with the ICM but inhomogeneities and even stripes of higher metalicity behind the galaxy can be seen. The ram pressure yields centrally concentrated metal distributions of the metals, while the galactic winds result in an extended metal distribution.

Domainko et al. (2006)

Using the numerical code of Schindler et al. (2005), Domainko et al. (2006) show that ram-pressure stripping can account for $\sim 10\%$ of the overall observed level of enrichment in the ICM within a radius of 1.3 Mpc. The level of enrichment drops quite fast at larger radii from the cluster center. The resulting distribution of metals in the ICM shows a complex pattern with stripes and plumes of metal-rich material. Since each stripping mechanism results in a characteristic distribution of metal rich material, such metalicity maps can be used to trace the underwent interactions between the ICM and cluster galaxies.

Roediger & Hensler (2005)

By varying galaxy properties and using a large range of ICM conditions, Roediger & Hensler (2005) perform a parameter study of the ram pressure stripping of face-on disk galaxies, using a 2D Eulerian simulations.

Their spiral medium and massive galaxy models with rotation velocities of about 150 km s^{-1} and about 200 km s^{-1} experience a constant ram pressure in the range from 10 to 10 000 cm^{-3} km^2 s^{-2}. They recover three phases of stripping. A more detailed information is provided in Chapter 5.

2.5.1 Summary

In Table 2.1, we propose a short summary of selected papers mentioned in this section. We compare first the used simulation method and its resolution (in the case of finite difference simulations) or the number of ICM particles (in the case of SPH methods). Then the model galaxy is compared – either the rotation velocity v_{rot} or the total mass M_{gal} are given. It is followed by the range of used values of the ram pressure p_{ram} and by its character (constant vs. changing). In the case of SPH simulations, the ratio of individual ICM vs. ISM particles is stated. Finally, a note whether given simulation deals with inclined cases, and some additional information are added.

paper	hydro-method	resolution, N_{ICM} (cells)	v_{rot}, M_{gal} (km s^{-1}, $M_\odot$)	p_{ram} ($cm^{-3}(km/s)^2$)	effect of RP	$\frac{m_{ICM}}{m_{ISM}}$	inclin.	further
Lea & De Young (1976)	2D finite diff.	41×100	$1\ 10^{11}$	140 – 1100	constant	–	no	–
Farouki & Shapiro (1980)	3D direct sum.	–	$2\ 10^{11}$	1500 – 7300	constant	–	yes	no hydro
Takeda et al. (1984)	2D finite diff.	32×42	$1\ 10^{12}$	130 – 500	changing	–	no	–
Gaetz et al. (1987)	2D finite diff.	–	$4.4\ 10^{11}$	2200	constant	–	no	many processes
Balsara et al. (1994)	2D finite diff.	–	$1.2\ 10^{10}$	...	constant	–	no	cool.,repl.,*form.
Stevens et al. (1999)	2D finite diff.	240×180	$1.2\ 10^{12}$	$100 - 3\ 10^4$	constant	–	no	mass repl.,*form.
Abadi et al. (1999)	3D tree/SPH	16 000	210	$300 - 3\ 10^4$	constant	0.1	yes	–
Mori & Burkert (2000)	2D finite diff.	100×...	$10^7\ M_\odot$	$10 - 10^3$	constant	–	no	–
Quilis et al. (2000)	3D finite diff.	512×512×512	220	260 – 5200	constant	–	no	disk holes
Vollmer et al. (2001)	sticky-particle	–	140	$10^3 - 10^4$	changing	–	yes	–
Schulz & Struck (2001)	SPH - HYDRA	80 000	$6.6\ 10^{10}$	70 – 150	constant	0.1	yes	rad. cooling
Hidaka & Sofue (2002)	2D finite diff.	256×256	200	140 – 2250	constant	–	edge-on	inter-arm ISM
Acreman et al. (2003)	2D finite diff.	800×400	$(1 - 4)\ 10^{12}$	~ 900	changing	–	no	mass replenish.
Roediger & Hensler (2005)	2D finite diff.	650× 650	200, 150	$10 - 10^4$	constant	–	yes	–

Table 2.1: Overview of selected existing simulations.

Chapter 3

Model

Models of galaxies and galaxy clusters introduced in this chapter will be employed in both analytical description of the ram pressure stripping in Chapter 6, and numerical simulations of galaxies orbiting through galaxy clusters in Chapters 5, 7, and 8. The model galaxy consists of a stellar disk and bulge, a dark matter halo, and a gaseous disk. For simulations with galaxies in the face-on orientation, we provide four galaxy models: LM, Lm, EM, and Em, differing in the total mass and the bulge-to-disk ratio. The rotation curves corresponding to the massive and low-mass galaxy models are at levels of 250 km s^{-1}, and 160 km s^{-1}, respectively. Non-face-on inclinations are further studied with the LM galaxy model.

3.1 Galaxy model

Our model galaxy is in a standard three-component disk/bulge/halo configuration with stellar and dark matter parts represented with collisionless particles. The bulge can be approximated as the spherical and centrally condensed component partially stabilizing the disk. Its fairly simple model can be represented by a spherically symmetric Plummer potential. The dark matter around inner parts of galaxies forming galactic halo keeps the rotation curve roughly flat in the outer regions. It can be modelled by the Plummer potential, as well. The density profiles of the bulge and halo components are then

$$\rho_{b,h}\,(r) = \rho_0 \frac{a_{b,h}^5}{(r^2 + a_{b,h}^2)^{5/2}}, \tag{3.1}$$

where r is the spherical galactocentric radius, and a_b, a_h are radial scale lengths of the bulge and halo component. The central density $\rho_0 = 3M_{b,h}/4\pi a_{b,h}^3$, where M_b, M_h are the respective total masses.

Particles of the axially symmetric disk component follow a Toomre-Kuzmin infinitely thin profile, multiplied by $\mathrm{sech}^2 z$ term defining its isothermal vertical profile

$$\rho_d\,(R,z) = \rho_0 \frac{a_d^3}{(R^2 + a_d^2)^{3/2}}\,\mathrm{sech}^2(z/z_0), \tag{3.2}$$

where (R, z) are the galactocentric cylindrical coordinates, and a_d and z_0 denote the scale radius and the scale height, respectively. The central density is determined by $\rho_0 = M_d/4\pi a_d^2 z_0$ with M_d corresponding to the total mass of the disk.

Although the bulge and halo components are not in our present simulations influenced by the cluster environment and thus could be treated only analytically, in future we plan to study the tidal effects invoked by the cluster potential. Therefore, we model all three galactic components using the particles.

We introduce model spiral galaxies varying in their types: late-type (L) or early-type (E), and alike Roediger & Hensler (2005) we subdivide the models according to their total mass: massive (M) and medium (m). L-types have a very low bulge-to-disk mass ratios, typically 10 - 20 %, compared to E-types, and M-types have a massive halo component compared to m-types. Thus, we employ four model galaxies: LM, Lm, EM, and Em. The values of model parameters are given in Tab. 3.1, where $r_{...}^{tr}$ and $M_{...}^{tr}$ stand for the radius at which the particle distribution of a given component is truncated, and the corresponding mass within the truncation radius. The scale height of the disk $z_0 = 0.25$ in all models.

		LM	**Lm**	**EM**	**Em**	
disk:	M_d	8.6	4	3	1.5	(10^{10}M$_\odot$)
	a_d	4	4	6	6	(kpc)
	R_d^{tr}	16	16	16	16	(kpc)
	M_d^{tr}	6.5	3	2	1	(10^{10}M$_\odot$)
bulge:	M_b	1.3	0.5	7.3	3.6	(10^{10}M$_\odot$)
	a_b	0.4	0.15	1.5	1.5	(kpc)
	r_b^{tr}	4	4	5	5	(kpc)
	M_b^{tr}	1.3	0.5	6	3	(10^{10}M$_\odot$)
halo:	M_h	42	14	49	16	(10^{10}M$_\odot$)
	a_h	20	20	25	25	(kpc)
	r_h^{tr}	40	40	40	40	(kpc)
	M_h^{tr}	30	10	30	10	(10^{10}M$_\odot$)
total:	M_b/M_d	0.15	0.13	2.4	2.4	
	M_{tot}	51.9	18.5	59.3	21.1	(10^{10}M$_\odot$)
	M_b^{tr}/M_d^{tr}	0.2	0.17	3	3	
	M_{tot}^{tr}	37.8	13.5	38	14	(10^{10}M$_\odot$)

Table 3.1: Summary of the disk, bulge and halo parameters for Late (L) or Early (E), massive (M) or low mass (m) type model of a spiral galaxy used in simulations.

Our standard galaxy model is the LM type. Fig. 3.1 displays its rotation curve including contributions of individual galactic components. The rotation velocity of the LM galaxy at 20 kpc radial distance is about 250 km s^{-1}. For other galaxy models Lm (see Fig. 3.1, right panel), EM, and Em, the rotation velocity is about 160 km s^{-1}, 220 km s^{-1}, and 150 km s^{-1}, respectively.

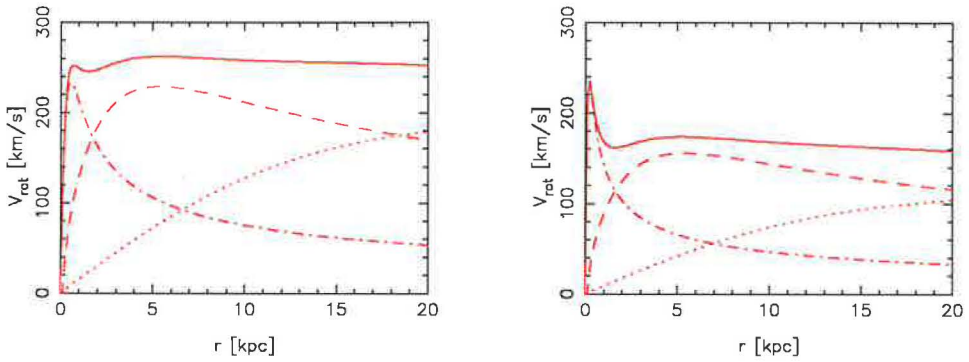

Figure 3.1: Left: Rotation curve of the LM galaxy model (solid) with the contributions of the halo (dotted), of the bulge (dash-dotted), and of the disk (dashed). Right: Rotation curve of the Lm galaxy model.

3.1.1 Gravitational restoring force

We assume that the ISM initially follows the density distribution (3.2), including about 9% of the total disk mass, i.e. the total mass of the stellar disk is ten times higher than that of the ISM. The

ISM surface density Σ_{ISM} is plotted as a function of the galactocentric distance for four galaxy types in Fig. 3.2, left panel. As will be discussed in Chapter 4, the ISM is in simulations treated as SPH particles with a constant temperature of $\sim 10^4$ K.

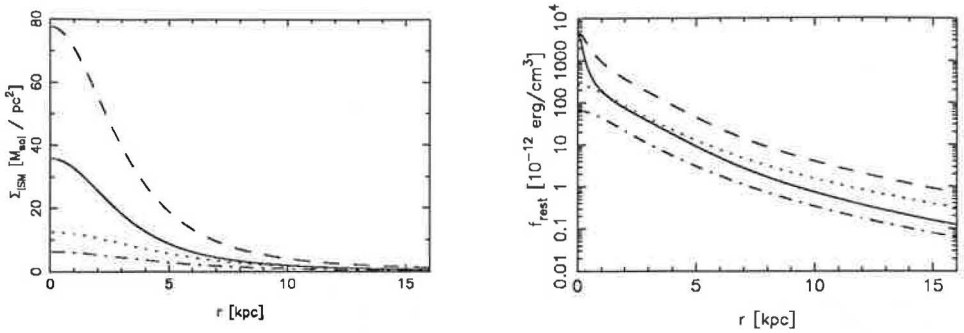

Figure 3.2: Left: Surface density of the ISM, Σ_{ISM}, as a function of the galactocentric distance r for the four adopted galaxy models: LM (dashed), Lm (full), EM (dotted), and Em (dash-dotted). Right: The maximum over z of the restoring force as a function of the galactocentric distance r for the four galaxy models.

Elements of the ISM are attracted towards the galaxy symmetry plane by the gravitational restoring force $f_{rest} = (\partial\Phi/\partial z)\Sigma_{ISM}$ per unit surface, where $\Phi(r,z)$ is the total gravitational potential of the galaxy including all its components, i.e. the disk, bulge, and halo. The restoring force is the force attracting an element towards the galaxy symmetry plane, where $f_{rest} = 0$. As described in detail e.g. by Roediger & Hensler (2005), the restoring force is a function of the vertical distance z from the disk plane. Fig. 3.3 shows the restoring force in the model galaxy LM as a function of z for 16 values of r within 16 kpc. It can be seen that f_{rest} is steeply growing when receding from the plane $z = 0$ and at any given r it has a maximum at some distance z. This maximum is more and more distant from the disk plane and its values decreases with the increasing distance r. In Fig. 3.2, right panel, we plot the maxima of the restoring force as a function of r for different galaxy types. LM galaxy has a massive disk and massive halo which gives the highest restoring force compared to other galaxy types. Both, disk and halo are less massive in Lm type, consequently the restoring force is smaller, only in the central part, where the very concentrated bulge dominates, the restoring force increases rapidly. Bulge is much more massive and extended in EM type galaxy, consequently the restoring force in the outer galaxy parts overcomes the Lm type. In the interval of r from 1 to 4 kpc, galaxy models Lm and EM show very similar run of the maxima with r, but they are at lower z-distances in Lm type comparing to EM type. The smallest restoring force has the Em galaxy, where disk and halo have lower masses compared to other types.

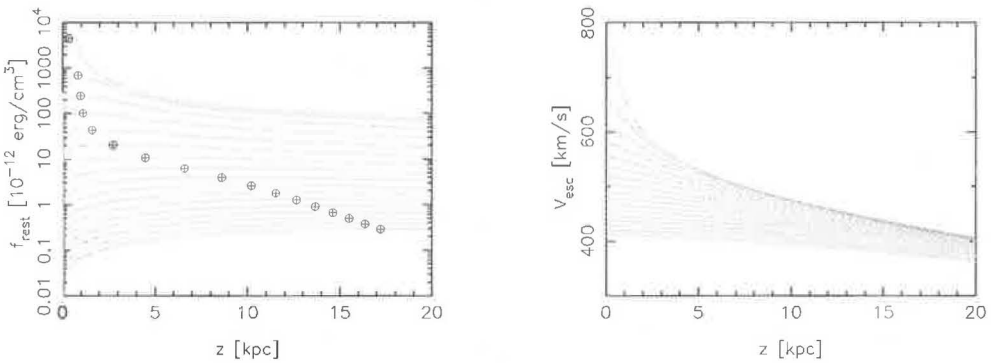

Figure 3.3: Left: The gravitational restoring force in the model LM as a function of z for 16 values of r starting with $r = 1$ kpc (top curves) with a step 1 kpc, circles denote the maxima at given distance r. Right: The escape velocity as a function of z for the corresponding distances r.

Fig. 3.3, right panel, displays the escape velocity of the LM model. The escape velocity is obtained as a function (r, z) from the potential: $v_{esc} = \sqrt{2|\Phi(r,z)|}$, snd it has always the maximum in the symmetry plane $z = 0$.

The restoring force as a function of (r, z) is displayed for the four model galaxies in Fig. 3.4. It depicts one quadrant of the plane that is perpendicular to the disk and going through its center. There the disk center is in the lower left corner and the disk plane coincides with the horizontal axis. Levels of the restoring force behind the disk plane are shown. The curves of marks "x" follow the positions of the restoring force maxima in the (r, z) plane. They are summarized in Fig. 3.5. It is clear that for early-type models the maxima are closer to the disk plane at inner disk radii than in the case of Late-types, which is due to more massive and extended bulges in the early-type models.

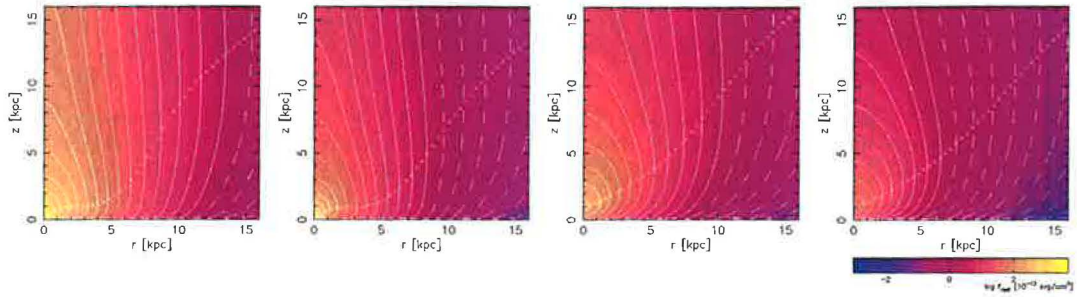

Figure 3.4: Levels of the restoring force as a function of (r, z) for model galaxies LM, Lm, EM, and Em (from left to right). In this configuration, the center of the disk is in the lower left corner, and the disk plane coincides with the horizontal axis. The positions of the maximum values of the restoring force at different radii are marked with x's.

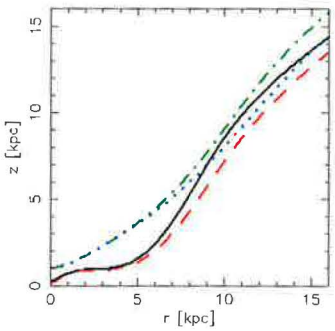

Figure 3.5: Positions of the maximum values of the restoring force behind the disk plane at different radii for the four galaxy models LM (full), Lm (dashed), EM (dot-dashed), and Em (dotted).

3.1.2 Restoring force in various disk potentials

In the following subsection we give a short study of the gravitational restoring forces in various disk potentials. It is motivated by a complexity of the analytic derivation of the formula in the Toomre-Kuzmin-sech$^2 z$ potential (3.2) which we need for our analytical estimates in Chapter 6.

Kuzmin potential

Potential of the infinitely thin Kuzmin disk is

$$\Phi_d\ (R,z) = -\frac{M_d}{\sqrt{R^2+(a_d+|z|)^2}}, \tag{3.3}$$

where R is the cylindrical radius, and z the vertical height. To this potential corresponds the following surface density:

$$\Sigma\ (R) = \frac{M_d a_d}{2\pi}\frac{1}{(R^2+a_d^2)^{3/2}}. \tag{3.4}$$

Vertical gradient of the potential is than

$$\frac{\partial\Phi_d}{\partial z}\ (R,z) = \frac{M_d(a_d+|z|)}{[R^2+(a_d+|z|)^2]^{3/2}}, \tag{3.5}$$

and the vertical profile of the restoring force taking into account contributions of the Plummer bulge and halo (3.1) is:

$$\begin{aligned} f_{rest}\ (R,z) &= \frac{\partial\Phi_{d+b+h}}{\partial z}\,\Sigma_{ISM}(R) \\ &= \left(\frac{M_d(a_d+|z|)}{[R^2+(a_d+|z|)^2]^{3/2}} + \frac{M_b\,z}{(r^2+a_b^2)^{3/2}} + \frac{M_h\,z}{(r^2+a_h^2)^{3/2}}\right)\Sigma_{ISM}, \end{aligned} \tag{3.6}$$

where Σ_{ISM} has the form of eqn.(3.4) but corresponding only to the ISM mass fraction of the disk mass $M_{d,ISM}$, and $r=\sqrt{R^2+z^2}$ is the spherical radius. First panel of Fig. 3.6 displays the restoring force (3.6) for 16 radii within 16 kpc with 1 kpc step. Note that a) in the disk plane ($z=0$) values are not zero but have some finite values (due to the term (a_d+z)), and b) positions of maxima do not recede to higher z's for increasing inner radii.

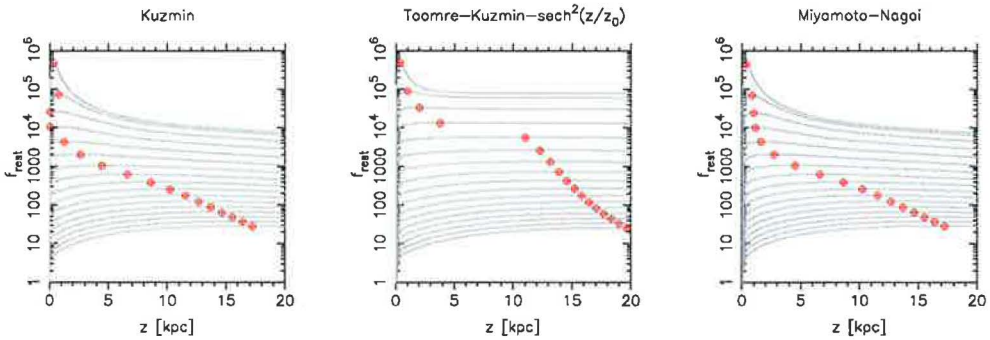

Figure 3.6: Restoring force as a function of z at radii increasing from 0 to 16 kpc with 1 kpc step (curves from top to bottom) in galaxies with different disk potentials. Red marks indicate positions of the maximum force for a given radius.

Toomre-Kuzmin-sech$^2(z/z_0)$

The surface density corresponding to the Toomre-Kuzmin-sech$^2(z/z_0)$ disk density profile (3.2) is equal to the Kuzmin surface density

$$\Sigma\ (R) = \frac{M_d\,a_d}{4\pi\,(R^2+a_d^2)^{3/2}}\,\frac{1}{z_0}\int_{-\infty}^{+\infty}\mathrm{sech}^2(z/z_0)\,dz = \frac{M_d\,a_d}{2\pi}\,\frac{1}{(R^2+a_d^2)^{3/2}}, \tag{3.7}$$

since

$$\int_{-\infty}^{\infty}\mathrm{sech}^2(z/z_0)\,dz = z_0\,\tanh\left(\frac{z}{z_0}\right)\Big|_{-\infty}^{+\infty} = 2z_0, \tag{3.8}$$

and $\tanh(z) = -\tanh(-z)$.

The Toomre-Kuzmin-sech$^2(z/z_0)$ disk is isothermal which means that the vertical velocity dispersion σ_z is independent of z. The vertical profile sech$^2(z/z_0)$ follows from solution of the Poisson equation in the z-direction, decoupled from (x, y). This can be done providing an infinite thin disk that is subject only to gravitation. Then, using the equation of hydrostatic equilibrium, $\nabla P = -\rho \nabla \Phi$, where the pressure of the velocity dispersion is $P = \rho \sigma_z^2$, the Poisson equation has form:

$$\frac{d}{dz}\left(\frac{1}{\rho}\frac{d\rho}{dz}\right) = -\rho\, 4\pi \frac{G}{\sigma_z^2}, \tag{3.9}$$

and its solution gives the above sech$^2(z/z_0)$ vertical profile of the density $\rho = \rho_0(z = 0)\text{sech}^2(z/z_0)$ with

$$z_0 = \sqrt{\frac{\sigma_z^2}{\pi G \Sigma}}, \tag{3.10}$$

where Σ represents the surface density. From that follows that $\sigma_z^2 = \pi G z_0 \Sigma$ and from equation of hydrostatic equilibrium we get the vertical gradient of the disk potential:

$$\begin{aligned}
\nabla_z \Phi_d &= -\frac{\nabla_z P}{\rho} = -\frac{\sigma_z^2}{\rho}\frac{d\rho}{dz} \\
&= -\frac{M_d\, a_d\, z_0}{2(R^2 + a_d^2)^{3/2}} \frac{4\pi\, z_0 (R^2 + a_d^2)^{3/2}}{M_d\, a_d} \cosh^2(z/z_0)\, \frac{d\rho}{dz} \\
&= -2\pi\, z_0^2 \cosh^2(z/z_0)\, \frac{M_d\, a_d}{4\pi\, z_0 (R^2 + a_d^2)^{3/2}} \frac{-2\sinh(z/z_0)}{z_0 \cosh^3(z/z_0)} \\
&= \frac{M_d\, a_d}{(R^2 + a_d^2)^{3/2}} \tanh(z/z_0)
\end{aligned} \tag{3.11}$$

Thus, the restoring force per unit surface for the gas in the vertical direction is

$$f_{rest}\,(R, z) = \left(\frac{M_d\, a_d}{(R^2 + a_d^2)^{3/2}} \tanh(z/z_0) + \frac{M_b\, z}{(r^2 + a_b^2)^{3/2}} + \frac{M_h\, z}{(r^2 + a_h^2)^{3/2}}\right) \Sigma_{ISM}, \tag{3.12}$$

where again $r = \sqrt{R^2 + z^2}$.

Second panel of Fig. 3.6 depicts the restoring force (3.12) and compares it with the restoring force of the Kuzmin disk (3.6). In the disk plane $z = 0$ the f_{rest} is zero, which is in agreement with our expectations due to galaxy components symmetry, but another problem occurs: when going to higher vertical distances z, the gravitational force due to the disk does not diminish but tends to $M_d\, a_d/(R^2 + a_d^2)^{3/2}$ (see Fig. 3.7). This is caused by the assumption of the infinite extent of the disk.

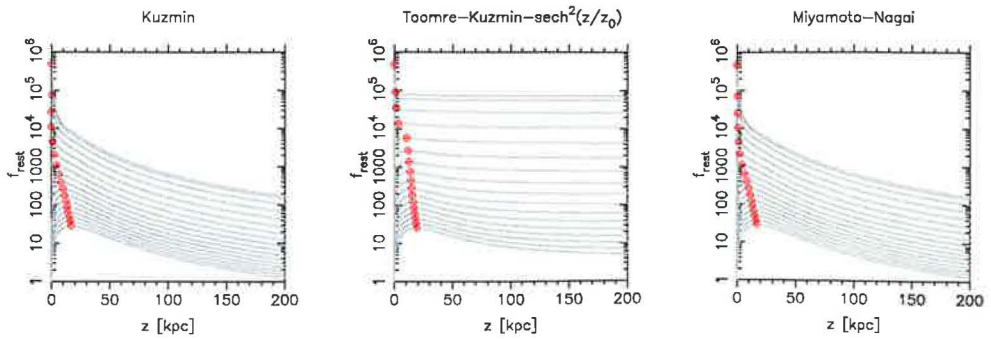

Figure 3.7: Same as in Fig. 3.6 but for distances up to 200 kpc behind the disk plane. One notes that the restoring force of the Toomre-Kuzmin-sech$^2(z/z_0)$ disk component at high vertical distances does not diminish (central panel).

From density profile (3.2) we derive the distribution of mass:

$$\begin{aligned} M(R,z) &= 2\pi \int_0^R \int_{-z}^{z} \rho\, R\, dR\, dz \\ &= \frac{2\pi M_0 a_d}{4\pi z_0} \int_0^R \frac{R}{(R^2+a_d^2)^{3/2}} \int_{-z}^{z} \operatorname{sech}^2 \frac{z}{z_0}\, dz\, dR \\ &= \frac{M_0 a_d}{2} \left(\tanh \frac{z}{z_0} - \tanh \frac{-z}{z_0} \right) \int_0^R \frac{R}{(R^2+a_d^2)^{3/2}} \\ &= M_0 \left(1 - \frac{a_d}{(R^2+a_d^2)^{1/2}} \right) \tanh \frac{z}{z_0}. \end{aligned} \tag{3.13}$$

Miyamoto-Nagai

In both figures Fig. 3.6 and 3.7, the above derived formulae for the restoring force are compared with the case of the Miyamoto-Nagai disk for which we know the analytic potential and thus the calculation of the restoring force is straightforward. The potential has a form:

$$\Phi_d(R,z) = -\frac{M_d}{\sqrt{R^2 + \left(a + \sqrt{z^2+b^2}\right)^2}}, \tag{3.14}$$

and the vertical restoring force is then

$$\frac{\partial \Phi_d}{\partial z}(R,z) = M_d \frac{z\left(a+\sqrt{z^2+b^2}\right)}{[R^2+(a+\sqrt{z^2+b^2})^2]^{3/2}\sqrt{z^2+b^2}}. \tag{3.15}$$

Miyamoto-Nagai density profile is:

$$\rho_d(R,z) = \frac{M_d b^2}{4\pi} \frac{aR^2 + (a+3\sqrt{z^2+b^2})(a_d+\sqrt{z^2+b^2})^2}{(R^2+(a+\sqrt{z^2+b^2})^2)^{5/2}(\sqrt{z^2+b^2})^3}, \tag{3.16}$$

Modified Toomre-Kuzmin-sech$^2(z/z_0)$

In order to make decrease the restoring force (3.12) for high z's, we tried to replace the cylindrical radius R in the disk term by the spherical radius r. Then

$$f_{rest}(R,z) = \left(\frac{M_d\, a_d}{(r^2+a_d^2)^{3/2}} \tanh(z/z_0) + \frac{M_b\, z}{(r^2+a_b^2)^{3/2}} + \frac{M_h\, z}{(r^2+a_h^2)^{3/2}} \right) \Sigma_{ISM}. \tag{3.17}$$

Fig. 3.8 displays the result of the modified formula (3.17). Now the restoring force is both zero in the disk plane, and falls down for high distances behind the disk plane. Therefore, formula (3.17) has a convenient properties and we will use it in our analytic calculations in Chapter 6.

3.2 Cluster model

The large scale distribution of the ICM in clusters is described with a β-profile (Cavaliere & Fusco-Femiano, 1976):

$$\rho_{ICM} = \rho_{0,ICM} \left(1 + \frac{R^2}{R_{c,ICM}^2} \right)^{-3\beta_{ICM}/2}, \tag{3.18}$$

where ρ_{ICM} denotes the ICM volume density at the distance R from the cluster center, $\rho_{0,ICM}$ the central volume density of the ICM, $R_{c,ICM}$ a core radius determining the ICM central concentration, and β_{ICM} the slope parameter. The β-profile enables deprojection of the observed quantities – the X-ray emission that is proportional to the projection of the squared density of the hot gas, and the optical observations that simply correspond to the projection of the optical galaxy density

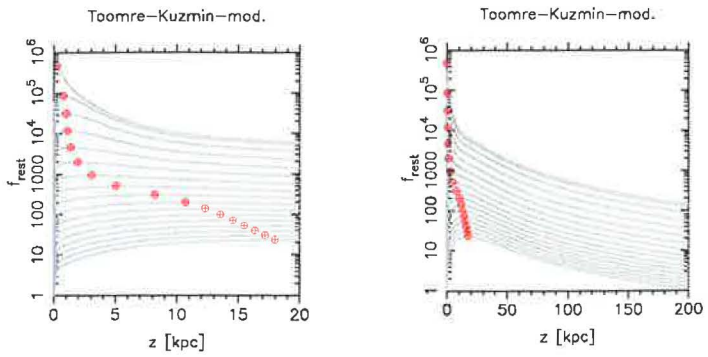

Figure 3.8: Restoring force for the Toomre-Kuzmin-sech$^2(z/z_0)$ profile with a modified term (3.17) assuring that it diminishes for large z's.

– to operate with comparable spatial densities (Schindler et al. 1999, Cavaliere & Fusco-Femiano 1976).

The gravitational potential of a galaxy cluster corresponds to dark matter (DM) distribution plus the ICM distribution described with (3.18). The DM is introduced through another β-profile, with this time ρ_{DM} denoting the DM volume density at the distance R from the cluster center, $\rho_{0,DM}$ the central volume density of the DM, $R_{c,DM}$ a parameter of DM central concentration, and β_{DM} the slope parameter. Tab. 3.2 gives values of the β-profile parameters of both the ICM and DM distributions.

	R_c (kpc)	ρ_0 (cm^{-3})	β
ICM	13.4	4 10^{-3}	0.5
DM	320	1.6 10^{-2}	1

Table 3.2: Standard values of the β-profile (3.18) parameters of the ICM and DM cluster components.

Having in mind the Virgo cluster, we set the cluster parameters listed in Tab. 3.2 to correspond to the Virgo northern subclump about the galaxy M87 (Schindler et al, 1999; Vollmer et al, 2001). The difference in the steepness of the gas and galaxy density profiles (β_{ICM} vs. β_{DM}) corresponds well to the observations, with the ICM density being steeper than the galaxy distribution in the inner part of the subclump, and vice-versa in the outer parts. Vollmer et al (2001) introduces the value of 4 10^{-2} cm^{-3} for the central ICM density, but following Schindler et al (2005) and others we adopt the above stated ten-times lower value of 4 10^{-3} cm^{-3}.

Our standard model of the cluster corresponds to the values given in Tab. 3.2. The density profiles of both the ICM and DM components are compared in Fig. 3.9, left panel. To model a rich galaxy cluster with a lot of hot ICM, or a poor cluster just with a central peak of the ICM, we vary the values of $R_{c,ICM}$ and $\rho_{0,ICM}$ relative to the standard values stated in Tab. 3.2. When studying the face-on flights of galaxies through clusters in Chapter 5, we use combinations of 0.25, 0.5, 1, 2, and 4 multiples of them. Thus we obtain a set of twenty-five simulations with galaxies flying through various clusters (see below in detail).

Fig. 3.9, central panel, illustrates the effect of the varying parameter $R_{c,ICM}$ for above mentioned five values. While the central density $\rho_{0,ICM}$ is fixed on the standard value, the width of the density peak grows with increasing $R_{c,ICM}$. To the multiples 0.25, 0.5, 1, 2, and 4 of $R_{c,ICM} = 13.4$ kpc, the following half-widths of the peaks correspond: 8.2 kpc, 16.4 kpc, 33 kpc, 66 kpc, and 132 kpc. These values are superior to $2R_{c,ICM}$ since the β-profile exponent β_{ICM} is lower than 1.

As the galaxy flies through the cluster, it encounters certain amount of the ICM. Fig. 3.9, right panel, depicts five clusters with such combinations of the ($R_{c,ICM}$, $\rho_{0,ICM}$) parameter pair that the traversing galaxy crosses a constant amount of the ICM. Shape of the peaks changes from

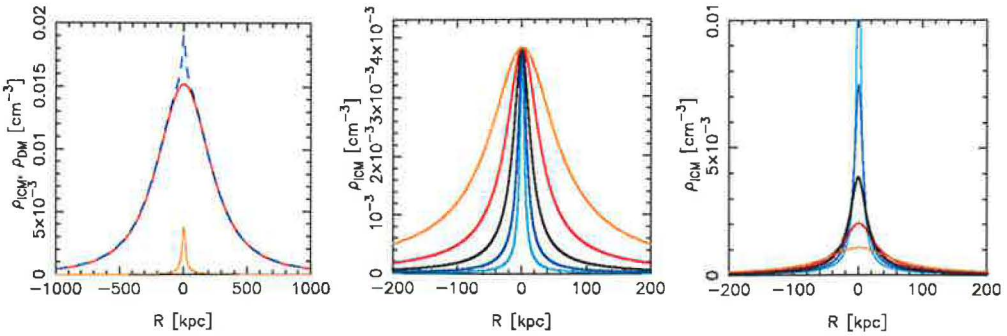

Figure 3.9: Left: Density profiles of the cluster components: ICM (orange), and DM (red). Total density (blue) is displayed, as well. Center: Central view of the ICM distribution with various widths, i.e. values of the $R_{c,ICM}$ parameter: 3.4 kpc (cyan), 6.7 kpc (blue), 13.4 kpc (black), 26.8 kpc (red), and 53.5 kpc (orange). Right: Peaks of the ICM density distribution with various combinations of the parameters $R_{c,ICM}$, $\rho_{0,ICM}$, but a constant amount of the encountered ICM at a radial orbit.

narrow and high to wide and low as the pair of parameters exceeds (0.25,3.82), (0.5,1.95), (1,1), (2,0.53), and (4,0.28) multiples of the standard values.

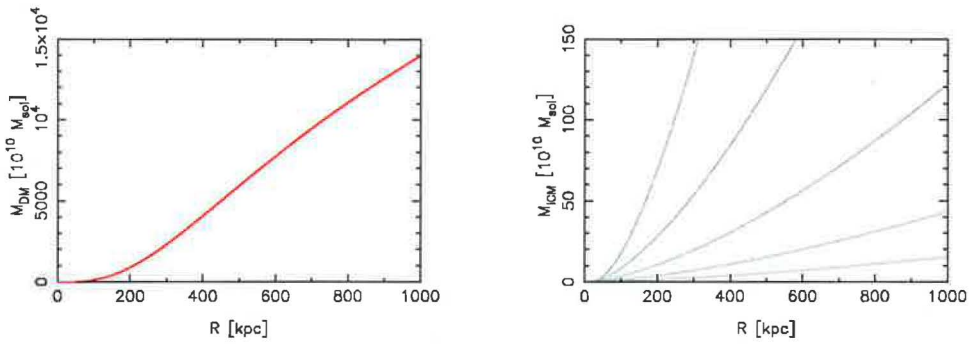

Figure 3.10: Mass profiles of the DM (left) and the ICM (right) as functions of the distance R from the cluster center. Curves of the ICM mass correspond to five values of the $R_{c,ICM}$ parameter: 3.4 kpc, 6.7 kpc, 13.4 kpc, 26.8 kpc, and 53.5 kpc (from bottom to top).

Since our main objective in this work is to follow the effects of the ISM-ICM interaction, only the intracluster medium is treated selfconsistently using SPH particles, and gravitational effect of the cluster dark matter and of other member galaxies is introduced analytically. To easily include the gravitational effect of the cluster DM into the numerical code, we present a formula for the DM mass:

$$\begin{aligned} M_{DM}(R) &= 4\pi \int_0^R R'^2 \rho_{DM}(R')\, dR' = 4\pi\rho_{0,DM} \int_0^R \frac{R'^2}{\left(1+\frac{R'^2}{R_{c,DM}^2}\right)^{3/2}}\, dR' \\ &= 4\pi\rho_{0,DM} R_{c,DM}^3 \left[-\frac{R}{(R^2+R_{c,DM}^2)^{1/2}} + \ln \frac{R+(R^2+R_{c,DM}^2)^{1/2}}{R_{c,DM}} \right]. \end{aligned} \quad (3.19)$$

For the ICM distribution an exact formula for the mass profile cannot be analytically expressed:

$$M_{ICM}(R) = 4\pi \int_0^R R'^2 \rho_{ICM}(R')\, dR' = 4\pi\rho_{0,ICM} R_{c,ICM}^{3/2} \int_0^R \frac{R'^2}{(R'^2+R_{c,ICM}^2)^{3/4}}\, dR'. \quad (3.20)$$

Fig. 3.10 shows the mass profiles of the DM and the ICM as functions of R. In the case of the

ICM, the curves correspond to five values of the $R_{c,ICM}$ parameter: 3.4 kpc, 6.7 kpc, 13.4 kpc, 26.8 kpc, and 53.5 kpc.

3.3 Initial conditions

From observations follows that the most preferable orbits in galaxy clusters are the radial ones (see Vollmer et al 2001 and references therein) leading the galaxies through the cluster center regions. The effect of the ram pressure is strongest in those regions, where both the ICM density, and the orbital velocities of galaxies are maximum. Further, as will be discussed in Chapter 8, galaxies on non-radial orbits change during their orbital motion the inclination of the disk plane with respect to the direction of motion. This of course affects the stripping results. Therefore, we firstly consider a simply free-fall of galaxies from the cluster periphery directly towards and through the center. Initially, the model galaxy is located at 1 Mpc distance from the cluster center, with zero velocity. Consequently, the galaxy starts to fall towards the center, passes it at the orbital time $T = 0.5$, and afterwards reaches the second apocenter at $T = 1$.

With the gravitational potential corresponding to ICM + DM mass distributions given with formula (3.18), in our analytical calculations we can solve the equations of motion and get an orbit of the galaxy in the cluster. Thus, we obtain $(R, v)_{gal}$ as a function of time, where v_{gal} always means the galaxy radial velocity in the cluster. R_{gal} is denoted as R throughout the rest of this text.

Contrary to the majority of recent simulations, we treat both the model galaxy and the intracluster filling of the cluster with particles. The galaxy model consists of 12 000 particles for the stellar disk, 6 000 for the bulge, and 12 000 for the halo component. The total mass of the individual components is divided to equally massive particles with the distribution initially following the density profiles (3.1) and (3.2). Individual components are cut off at 40 kpc, 4 kpc, and 16 kpc, in the case of halo, bulge, and disk, respectively (see Tab. 3.1). The ISM is represented with 12 000 SPH particles of the total mass equal to 9% of the total disk mass. Their initial distribution follows the density profile of the disk (3.2).

Fig. 3.11 depicts the initial configuration of the system. The galaxy is located at the cluster periphery at 1 Mpc distance from the center, $\boldsymbol{R} = (x, y, z) = [0, 0, 1]$ Mpc, with no systematic velocity. Consequently, it freely falls towards the cluster center, along the dashed line, being attracted by the gravitational force of the DM and the ICM.

The ICM of the cluster is modelled with 120 000 SPH particles following the β-profile (3.18) with a cut off at $R = 140$ kpc from the cluster center. Originally, we planned to spread the ICM particles throughout the cluster up to 1 Mpc radius so that the galaxy flied all its orbital time through the medium. Abadi el al (1999) warn that too massive ICM particles may become bullets punching holes into the ISM disk, and recommend at least to equalize mutual masses of individual ICM versus ISM particles. With this assumption and the number of ISM particles set to 12 000, the sphere of 1 Mpc radius of the cluster would need about 2 millions particles of the ICM. Consequently, the calculations would be very time-consuming, and the output data files large. Although we do not accord with the warning of Abadi et al (1999) (see Chapter 4) we restrict the active sphere of the ICM distribution to central regions of the cluster, where the effect of the ICM-ISM interaction is strongest. We fill up the central cluster sphere to such a radius at which the outskirts of the galaxy arriving from the cluster periphery start to be affected by the steeply arising ram pressure of the ICM. According to our standard model, the cut-off radius is set to 140 kpc, outside which the gravitational effect of the ICM to the galaxy is treated only analytically.

Free fall of the galaxy from the cluster periphery to the edge of the ICM distribution lasts about 1.53 Gyr, while to the very cluster center about 1.63 Gyr. When the profile of the ICM density is changed, the amount of the gravitating mass changes, as well. Although clusters are dominated by the dark matter, the effect of the ICM in the case of large distributions is not negligible and the galaxy adapts its motion. Tab. 3.4 summarizes the characteristic time instants of the basic radial orbit depending on the setting of the ICM distribution.

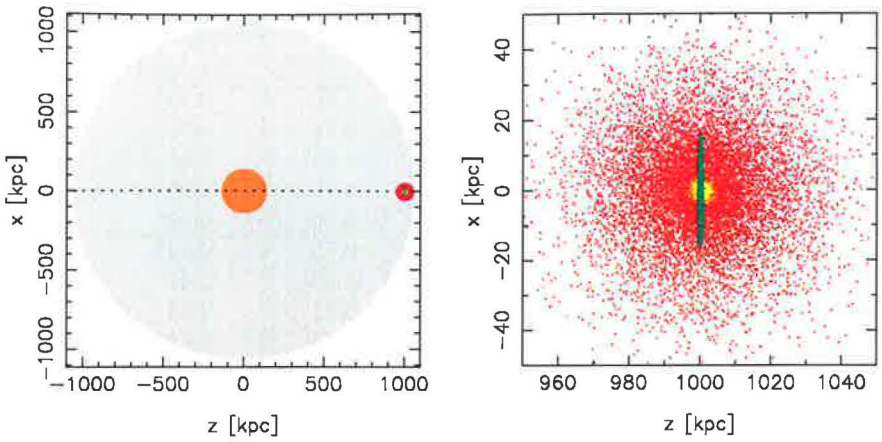

Figure 3.11: Initial conditions of our simulations. Left: Starting position of a galaxy falling face-on to the cluster center (dashed trajectory). SPH particles of the ICM are distributed about the cluster center up 140 kpc distance (orange), outside this region the ICM influences the galaxy only gravitationally. Right: Zoom on the initial configuration of the galaxy with the disk (green), bulge (yellow), and halo (red) components.

Although the ISM-ICM interaction occurs only after more than 1.5 Gyr, we let the galaxy evolve from the very beginning. Thus instabilities and spiral arms form and the ICM enters a developed galaxy.

The approximation that the ICM is considered only in the central regions can be defended by the fact that the ram pressure is steeply peaked and thus effect of the stripping proceeds mainly there.

3.4 Supersonic motion

Domainko et al (2005) state that a galaxy flying through the ICM with a velocity relative to the embedding medium higher than the local speed of sound, the classical Gunn & Gott (1972) approach has to be modified since such galaxies form bow shocks in front of them and the stripping criterion should be applied to the conditions behind these bows shocks. Landau & Lifshitz (1959) explain that when the velocity of a moving fluid becomes comparable with or exceeds that of sound, effects due to the compressibility of the fluid govern the behavior of the fluid. The nature of the flow of a gas is entirely different depending on whether its velocity is subsonic, or supersonic. If a gas receives a slight perturbation, then, if the flow velocity is greater than that of sound, the perturbation is propagated relative to the gas with velocity c only downstream within a cone with the aperture angle of 2α, where $sin\,\alpha = c/v$, and the angle α is called the Mach angle. Then, depending on local thermodynamic quantities and the local velocity of sound, the Mach surface cuts the flow at any point at the Mach angle. If the flow velocity is subsonic, the perturbation propagates isotropically. Thus, the difference in these two cases is that in a supersonic flow the effect of an obstacle extends only downstream and the oncoming gas has no knowledge of it.

As the gas crosses the surface of discontinuity, the related quantities change discontinuously. Rankine-Hugoniot conditions describe the behavior of a shock wave perpendicular to the oncoming flow. It provides the mass, momentum, and energy conservation:

$$\rho_1 v_1 = \rho_2 v_2 \tag{3.21}$$

$$p_1 + \rho_1 v_1^2 = p_2 + \rho_2 v_2^2 \tag{3.22}$$

$$v_1(p_1 + \rho_1 u_1 + \frac{1}{2}\rho_1 v_1^2) = v_2(p_2 + \rho_2 u_2 + \frac{1}{2}\rho_2 v_2^2), \tag{3.23}$$

where we subscript with 1 the gas into which the shock wave moves, and 2 that which remains behind the shock. Then the side of the shock towards the gas 1 is the front of the shock, and that

R_c (kpc)	ρ_0 (10^{-3}cm^{-3})	$M_{ICM}^{R<1\,Mpc}$ (10^{11}M$_\odot$)	$M_{ICM}^{R<140\,kpc}$ (10^{11}M$_\odot$)	$\Sigma_{ICM}^{R<1\,Mpc}$ (M$_\odot$/pc^2)	$\Sigma_{ICM}^{R<140\,kpc}$ (M$_\odot$/pc^2)	p_{ram}^{max} (cm^{-3}km^{2}s^{-2})
3.4	1	0.38	0.02	0.40	0.38	1612
	2	0.77	0.04	0.79	0.76	3231
	4	1.53	0.08	1.59	1.53	6453
	8	3.07	0.16	3.17	3.05	12949
	16	6.14	0.32	6.35	6.10	25900
6.7	1	1.08	0.06	0.78	0.74	1615
	2	2.17	0.11	1.56	1.47	3233
	4	4.34	0.22	3.11	2.94	6480
	8	8.67	0.44	6.23	5.87	13014
	16	17.34	0.89	12.45	11.76	26229
13.4	1	3.06	0.15	1.51	1.39	1618
	2	6.12	0.30	3.03	2.78	3245
	4	12.23	0.61	6.05	5.56	6524
	8	24.47	1.21	12.11	11.13	13182
	16	48.94	2.43	24.21	22.26	26894
26.8	1	8.60	0.39	2.91	2.56	1625
	2	17.19	0.78	5.81	5.12	3272
	4	34.39	1.57	11.62	10.25	6631
	8	68.77	3.14	23.24	20.50	13608
	16	137.54	6.28	46.49	40.99	28604
53.6	1	23.92	0.90	5.47	4.52	1641
	2	47.83	1.80	10.94	9.04	3336
	4	95.67	3.61	21.87	18.08	6888
	8	191.34	7.21	43.74	36.16	14637
	16	382.67	14.42	87.48	72.29	32722

Table 3.3: Values of quantities characterizing the set of twenty-five simulation runs with various combinations of the $R_{c,ICM}$ and $\rho_{0,ICM}$ parameters. $M_{ICM}^{R<1\,Mpc}$ and $M_{ICM}^{R<140\,kpc}$ correspond to the mass of the ICM within 1 Mpc, or 140 kpc about the cluster center, respectively. $\Sigma_{ICM}^{R<1\,Mpc}$ and $\Sigma_{ICM}^{R<140\,kpc}$ mark the column density of the ICM encountered by a galaxy radially passing the cluster within 1 Mpc, or 140 kpc distance about the cluster center, respectively. Finally, p_{ram}^{max} gives values of the maximum ram pressure occurring in the cluster center for strictly radial orbits of galaxies freely falling from 1 Mpc distance.

towards the gas 2 the back. In this notation the gas 1 corresponds to the ICM and the gas 2 to the ISM. Note the three components of the energy flux: mechanical work, internal energy, and kinetic energy. Defining the mass flux density at the surface of discontinuity $j = \rho_1 v_1 = \rho_2 v_2$ and the specific volumes $V_1 = 1/\rho_1$ and $V_2 = 1/\rho_2$, we get

$$j^2 = (p_2 - p_1)/(V_1 - V_2). \tag{3.24}$$

For the velocity difference $v_1 - v_2$ in front of and behind the shock we obtain

$$v_1 - v_2 = \sqrt{(p_2 - p_1)(V_1 - V_2)}. \tag{3.25}$$

Further derivation leads to the formula showing relations between the thermodynamic quantities on the two sides of the surface of discontinuity:

$$u_1 - u_2 + \frac{1}{2}(V_1 - V_2)(p_1 + p_2) = 0. \tag{3.26}$$

During the shock the entropy increases, which means that the motion is irreversible, i.e. energy is dissipated. For the increasing entropy, the following inequalities have to hold:

$$p_2 > p_1;\ v_2 > c_1;\ v_2 < c_2;\ V_1 > V_2;\ \text{and}\ v_1 > v_2. \tag{3.27}$$

R_c (kpc)	ρ_0 (10^{-3}cm^{-3})	$T_{140\,\mathrm{kpc}}$ (Myr)	$T_{0\,\mathrm{kpc}}$ (Myr)	$T_{-140\,\mathrm{kpc}}$ (Myr)	$v_{0\,\mathrm{kpc}}$ (km/s)
3.4	1	1532	1638	1745	1299
	2	1531	1638	1745	1299
	4	1531	1638	1744	1300
	8	1530	1637	1743	1301
	16	1528	1635	1742	1303
6.7	1	1531	1638	1745	1300
	2	1531	1637	1744	1300
	4	1529	1636	1743	1302
	8	1527	1634	1740	1304
	16	1523	1629	1735	1309
13.4	1	1530	1637	1743	1301
	2	1528	1635	1742	1302
	4	1526	1632	1738	1306
	8	1519	1625	1731	1312
	16	1507	1612	1717	1326
26.8	1	1527	1634	1743	1303
	2	1523	1629	1743	1308
	4	1514	1620	1743	1316
	8	1497	1602	1743	1333
	16	1465	1567	1743	1367
53.6	1	1520	1626	1732	1310
	2	1508	1613	1718	1321
	4	1485	1589	1692	1342
	8	1442	1543	1644	1383
	16	1367	1463	1558	1462

Table 3.4: Time instants of the galaxy's arrival to the ICM distribution ($T_{140\,\mathrm{kpc}}$), to the cluster center ($T_{0\,\mathrm{kpc}}$), and to the "rear" edge of the ICM distribution ($T_{-140\,\mathrm{kpc}}$). The rightmost column gives maximum orbital velocities when passing the cluster center.

It means that when the gas passes through the shock wave, it is compressed, the pressure and density increasing. Since the shock wave moves supersonically relative to the gas ahead of it, no perturbations starting from the shock can penetrate into that gas.

Shock waves are geometrical surfaces with non-zero thickness. It can be shown that shocks in which the discontinuities are small are in reality transition layers with finite thickness. The thickness diminishes as the magnitude of the discontinuities increases. In determining the structure of the layer, the effects of viscosity and thermal conductivity of the gas have to be taken into account. Then if the finite thickness of the transition layer is considered, the Rankine-Hugoniot conditions must be written not as the equality of the quantities on the two sides of the discontinuity but as their constancy through the thickness of the layer. The condition of mass conservation stays unchanged, but in the other two conditions additional fluxes of momentum and energy, due to internal friction and thermal conduction, must be included. It can be shown that the thickness of a strong shock is of the same order of magnitude as the mean free path of the gas molecules.

Domainko et al (2005) further say that for supersonic galaxies the ram pressure stripping is less efficient than the classical Gunn & Gott (1972) approach would suggest. They say that in the case of very fast galaxies, the ram pressure is by a factor of 4 lower behind the galactic bow shock than in front of it.

Roediger & Hensler (2005) precise that for Mach numbers of 1.423 and 2.53 at the upstream side of the shock the velocity at the downstream side is reduced by factors of 0.62 and 0.36, respectively. For a polytropic gas one can derive the following useful formulae expressing the ratios of densities, pressures and temperatures in a shock wave in terms of the Mach number $M_1 = v_1/c_1$ (Landau &

Lifshitz (1959):

$$\frac{\rho_2}{\rho_1} = \frac{v_1}{v_2} = \frac{(\gamma+1)}{(\gamma-1)}\frac{M_1^2}{M_1^2+2} \tag{3.28}$$

$$\frac{p_2}{p_1} = \frac{2\gamma M_1^2}{(\gamma+1)} - \frac{(\gamma-1)}{(\gamma+1)} \tag{3.29}$$

$$\frac{T_2}{T_1} = \frac{[2\gamma M_1^2 - (\gamma-1)][(\gamma-1)M_1^2+2]}{(\gamma+1)^2 M_1}. \tag{3.30}$$

The Mach number M_2 is given in terms of M_1 by

$$M_2^2 = \frac{2+(\gamma-1)M_1^2}{2\gamma M_1^2 - (\gamma-1)}. \tag{3.31}$$

In our model the ICM is treated adiabatically with

$$u_{init} = \frac{1}{\gamma-1}\frac{k}{m_H}T \tag{3.32}$$

It means that the galaxy moves strongly supersonically and thus a shock wave in front of the disk forms. Fig. 3.12 shows the speed of sound c_s of the ICM as a function of cluster radius.

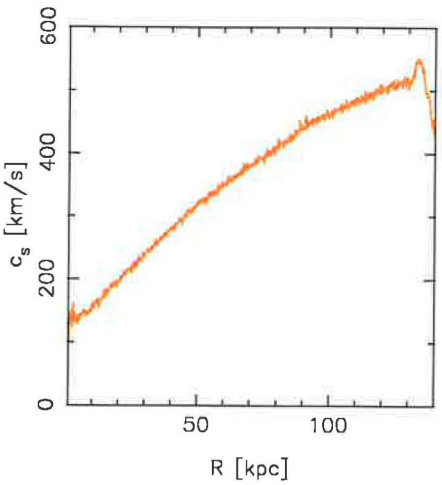

Figure 3.12: Profile of the speed of sound c_s in the ICM with the cluster radius. It shows that all galaxies move strongly supersonically and thus form a bow shock.

Rasmussen et al. (2006) notice that while the ram pressure itself is reduced at the shock, $P_{th} + \rho v^2$, where P_{th} is the thermal ICM pressure behind the shock, remains conserved for an inviscid fluid. Thus, the reduction of the ram pressure behind the shock is balanced by an increase in static thermal pressure. Therefore, the force per unit area acting on a disk normal to the flow is thus close to the pre-shock ram pressure.

Chapter 4

GADGET,
GAlaxies with Dark matter and Gas intEracT

In this chapter, we present primarily a description of the numerical code GADGET (Springel et al. 2001) by means of which we have performed our simulations of the ram pressure stripping phenomenon, whose results will be discussed in Chapters 5, 7, and 8. Here, firstly, the method of Smoothed Particle Hydrodynamics for treating the gasdynamical calculations, and its implementation into GADGET is introduced. Further, a short description of tree-based algorithms for effective calculations of gravitational interactions of collisionless particles follows. Finally, the modifications that we have made into GADGET, and their consequences are commented.

Nowadays, several code packets for solving selfgravitating hydrodynamical N-body problems are freely available. Based on various numerical approaches to both the gravitational and hydrodynamical effects, they provide treatment for different astrophysical problems. We have decided to use one of them rather than develop a new one. As the aim of our study is namely to describe the dynamical consequences of transits of cluster galaxies through the cluster core, we have chosen the three-dimensional N-body/SPH code GADGET developed by Volker Springel (Springel et al. 2001) on the basis of the TreeSPH code (Hernquist & Katz, 1989). This code employs the hierarchical tree method for solving the gravity and the Smoothed Particle Hydrodynamics (SPH) method for treating the hydrodynamics. Tree algorithms, contrary to various mesh-based methods do not cast a mesh over the computational area but arrange particles into a hierarchy of groups ordered from the smallest ones containing only one particle, over more extensive, up to the biggest one embracing the whole system. Then gravitational field at the position of a given particle is computed as a summation of multipole expansions of relevant groups. The computational cost is on the $O(N \log N)$ level. In SPH all hydrodynamical properties are calculated directly at the places of the particles that represent the fluid elements and the key idea is to define an effective radius of every such particle within which hydrodynamical interactions with neighboring particles are realized. Then the particles are not longer point masses but are smoothed out and local hydrodynamical properties are interpolated from the local mass distribution. A fixed number of neighboring particles is kept to achieve adaptive spatial resolution over an inhomogeneous system.

Both the tree algorithm and SPH are of the Lagrangian nature which is fully exploited in inhomogeneous systems with large dynamical range in the density distribution, where traditional grid-based methods encounter a problem. This property is in fact the most attractive feature of the SPH method. Thus, tree/SPH methods are well-suited for cosmological simulations mapping the gravitational growth of structures, automatically increasing the resolution in the regions of high particle density. Our simulations were performed with GADGET in version 1.1, but actually version 2.0 is available (see Springel et al. 2005). As described in detail in Chapter 3, our simulations contain two gaseous components, the very hot intra cluster medium (ICM), and the

warm interstellar gas, respectively. For both components, the use of SPH method is suitable. Therefore, only minor changes had to be made into the original GADGET code. In our future work we plan to employ version 2.0 of GADGET and implement the effects described in Chapter 9.

4.1 Smoothed Particle Hydrodynamics

Traditionally, the hydrodynamical effects in astrophysics were in their analytic treatments restricted to problems with high degree of symmetry. To simulate nonaxisymmetric three-dimensional phenomena, Lucy (1977) and Gingold & Monaghan (1977) independently invented the method of Smoothed Particle Hydrodynamics. Contrary to grid codes that cast over the computational area a mesh at which they solve the hydrodynamical equations using the finite-difference methods, SPH is a particle method that does not need a grid and thus is flexible to adapt to any given geometry.

Selfgravitating fluids can be represented by a set of fluid elements. Although real fluids are composed of an infinite number of such elements, limitations evoked by numerical simulations enable only a finite number of them to be selected. In SPH, these elements are represented by particles moving with the fluid according to the governing conservation equations. The selection of the fluid elements proceeds in such a way that the particle mass density follows the mass density of the fluid. The fundamental idea of SPH is to define an effective radius h of every particle. It means, that the particles are no longer point masses but are smoothed out by a kernel function, and local hydrodynamical properties are interpolated from the local mass distribution by summing the contributions of all particles within two smoothing radii. The contributions of each particle to a given property are weighted according to their distance from the particle of interest. This is governed by the kernel function W (see later). A fixed number of neighboring gaseous particles is kept to achieve a constant mass resolution over inhomogeneous system. It corresponds to assigning each particle its own smoothing length and allowing it to vary with time. Then the resolution automatically adapt itself depending on local conditions – in very dense regions with many particles being close together the smoothing length is small, while in regions with low density the particles are rare and h is large. Thus, in the former case the spatial resolution is high, while in the latter case low.

The SPH equations do not take a unique form and a number of different versions of them can be derived. Together with many existing recipes for force symmetrization (see later), the smoothing lengths determination, and forms of the artificial viscosity, the accuracy of a given implementation has to be studied.

The important disadvantage of SPH is that it has to rely on an artificial viscosity causing it tends to smear out shocks and contact discontinuities to a much greater extent than grid-based schemes.

SPH plays a role similar to tree-codes in self-consistent gravitational simulations of non-collisional systems. It is widely used in many astrophysical problems and is applied in many other physical fields as well. Due to its Lagrangian nature, SPH can be easily extended to simulate several non-mixing fluids, simply using the fact each particle can be initially assigned its type of phase and these marks do not change with time (see Ott & Schnetter 2003 for details).

4.1.1 Gasdynamics

Equations governing the hydrodynamical flow of a viscous fluid of varying density and temperature have the following form

- Continuity equation:

$$\frac{\mathrm{d}\rho}{\mathrm{d}t} + \rho\nabla\cdot\boldsymbol{v} = 0,$$

otherwise:

$$\frac{\partial\rho}{\partial t} + v_j\frac{\partial\rho}{\partial x_j} = -\rho\frac{\partial v_j}{\partial x_j}.$$

This equation expresses the conservation of mass.

- Euler equation (equation of motion):

$$\frac{\mathrm{d}v}{\mathrm{d}t} = -\frac{\nabla P}{\rho} - \nabla\Phi,$$

otherwise:

$$\rho\frac{\partial v_i}{\partial t} + \rho v_j\frac{\partial v_i}{\partial x_j} = \rho F_i + \frac{\partial P_{ij}}{\partial x_j},$$

where F_i is the i-th component of whatever external force acting on the fluid, and P_{ij} is the stress tensor.
This equation can be rewritten as:

$$\frac{\partial}{\partial t}\int_V \rho v_i d\tau = \int_V \rho F_i d\tau + \int_S P_{ij} dS_j - \int_S \rho v_i v_j dS_j,$$

which expresses the conservation of momentum. The rate of change of the momentum contained in a fixed volume V of the fluid is equal to the volume integral of the external forces acting on the elements of the fluid plus the surface integral of the normal stresses acting on the bounding surface S of V minus the rate at which momentum flows out of V across the boundaries of V by the motions prevailing on S.

- Energy equation:

$$\frac{\mathrm{d}u}{\mathrm{d}t} = -\frac{P}{\rho}\nabla\cdot\boldsymbol{v} + \frac{X(u,\rho)}{\rho},$$

where u is the thermal energy per unit mass, and $X(u,\rho)$ a function describing sinks or sources of heat for the gas. This function represents global sources of heat whereas the equation describes local changes of energy.

- Here we use the Lagrangian time derivatives:

$$\frac{\mathrm{d}}{\mathrm{d}t} = \frac{\partial}{\partial t} + \boldsymbol{v}\cdot\nabla$$

4.1.2 Brief thermodynamic discursion

Since temperature of the *ICM* is very high and its density is low, it can be treated using the approximations offered by the ideal gas thermodynamics (see previous chapter for review of the ICM properties).

Just to remind, an ideal gas is a hypothetical gas consisting of identical particles of negligible volume, with no intermolecular forces, and with the constituent atoms or molecules undergoing perfectly elastic collisions with the walls of the container. Of course, real gases do not exhibit exactly such properties, although the approximation is often good enough to treat them as ideal gases. At a temperature much higher than the critical temperature and at low pressures, the ideal gas law is a very good model for gas behavior. However, when dealing with gases at low temperature and at high pressure, correction has to be made. One of the common corrections made to the ideal gas law is the van der Waals's equation that approximates the behavior of real fluids taking into account the nonzero size of molecules and the attraction between them.

The ideal gas law (the equation of state of a simple ideal gas):

- for isothermal gases:

$$P = \frac{\rho kT}{\mu m_H}$$

- for adiabatic gases:

$$P = (\gamma - 1)\rho u,$$

where γ is the adiabatic exponent, $\gamma = 5/3$ for a monatomic ideal gas, μ is the mean molecular weight, k the Boltzmann constant, and m_H the hydrogen mass.

The internal energy of an ideal gas consists of translational, rotational and vibrational energy of its particles. Each degree of freedom contributes by $(1/2)kT$ to the total energy of a system. Particles of a monoatomic gas can exert only 3 translational motions consisting entirely of the translational kinetic energy of its particles. The total internal energy of a monatomic ideal gas is therefore simply:

$$u = (3/2)nRT = (3/2)NkT, \tag{4.1}$$

where n is number of particles in moles, R ideal gas constant, T absolute temperature, N number of particles, and k the Boltzmann constant. The probability distribution of particles by velocity or energy is given by the Boltzmann distribution.

The ideal gas law is an extension of experimentally discovered gas laws. While, strictly speaking, only an ideal gas obeys these gas laws exactly, at low density and high temperature, real fluids roughly approximate the behavior of a classical ideal gas. However, at lower temperature or higher density, a real fluid deviates strongly from the behavior of an ideal gas, particularly as it condenses from a gas into a liquid or solid. These deviations are often approximated through quantum-mechanical statistical methods.

In our simulations, we treat the ICM adiabatically since the approximation of only slow thermodynamical changes within the cluster is convenient for it. Further, we suppose mono-atomic gas and take $\gamma = 5/3$. The adiabatic sound speed is then:

$$c^2 = \gamma \frac{P}{\rho}.$$

On the contrary, due to its much higher density, compared to the ICM, we treat the ISM of the galaxy isothermally.

4.1.3 SPH methodology

Generally, an arbitrary physical field $A(r)$ can be interpolated by

$$\langle A(\mathbf{r}) \rangle = \int A(\mathbf{r}') W(\mathbf{r} - \mathbf{r}'; h) \mathbf{dr}', \tag{4.2}$$

where the integration runs over the entire space, and a smoothing kernel function $W(\mathbf{r}; h)$ specifying the extent of the interpolating volume is introduced. The kernel is chosen to have a sharp peak about $\mathbf{r} = 0$ and to satisfy the following two conditions:

$$\int W(\mathbf{r} - \mathbf{r}', h) \mathbf{dr}' = 1 \tag{4.3}$$

and

$$\lim_{h \to 0} W(\mathbf{r} - \mathbf{r}', h) = \delta(\mathbf{r} - \mathbf{r}'). \tag{4.4}$$

The former condition represents the normalization and the latter the requirement that $\langle A(\mathbf{r}) \rangle \to A(\mathbf{r})$ as $h \to 0$. For the rest of this subsection we will substitute the notation of the interpolant $\langle A(\mathbf{r}) \rangle$ by the actual function $A(\mathbf{r})$.

In numerical implementation, when values of $A(\mathbf{r})$ are known only at locations of a selected finite number of particles which are distributed with number density $n(\mathbf{r}) = \sum_j \delta(\mathbf{r} - \mathbf{r}_j)$, the equation (4.2) gets shape

$$A(\mathbf{r}) = \int A(\mathbf{r}') \frac{n(\mathbf{r}')}{\langle n(\mathbf{r}') \rangle} W(\mathbf{r} - \mathbf{r}'; h) \mathbf{dr}' \approx \sum_j \frac{A(\mathbf{r}_j)}{\langle n(\mathbf{r}_j) \rangle} W(\mathbf{r} - \mathbf{r}_j; h), \tag{4.5}$$

and from the definition of the number density it can be rewritten as

$$A(\mathbf{r}) = \sum_j m_j \frac{A(\mathbf{r}_j)}{\rho_j} W(\mathbf{r} - \mathbf{r}_j; h), \tag{4.6}$$

where m_j and ρ_j are the mass and density of a fluid element j at the position $\mathbf{r}_j$, and A_j denotes value of the quantity A at the location $\mathbf{r}_j$. By (4.6), the integral interpolant is approximated by a summation interpolant.

When looking for a form of gradients of the local fluid properties, by definition (4.2) one gets

$$\nabla A(\mathbf{r}) = \int \nabla A(\mathbf{r}') W(\mathbf{r} - \mathbf{r}'; h) \mathbf{dr}'. \tag{4.7}$$

Integrating by parts leads to

$$\nabla A(\mathbf{r}) = \int A(\mathbf{r}') \nabla W(\mathbf{r} - \mathbf{r}'; h) \mathbf{dr}', \tag{4.8}$$

since the other term resulting from the integration $A(\mathbf{r}')W(\mathbf{r} - \mathbf{r}'; h)$ tends to zero as the kernel function rapidly vanishes when $|\mathbf{r} - \mathbf{r}'| \to \infty$. Then, in the summation interpretation, the gradient of function can be found from

$$\nabla A(\mathbf{r}) = \sum_j m_j \frac{A(\mathbf{r}_j)}{\rho_j} \nabla W(\mathbf{r} - \mathbf{r}_j; h). \tag{4.9}$$

It means that a differentiable interpolant of a function A can be constructed from its values at the positions of particles, by using a differentiable kernel function.

The error made in approximating $A(\mathbf{r})$ by the smoothed interpolant is of order $O(h^2)$ or better. It can be determined by expanding the integrand of (4.2) in series in h.

Since the kernel function is sharply peaked about $\mathbf{r} = 0$ and diminishes rapidly at $|\mathbf{r} - \mathbf{r}_j| > h$, only a small number of particles in fact contributes to the interpolation of function A. Then, the interpolant can be determined only from its values in the locations of the neighboring particles within the radius equal to the smoothing length h. The Lagrangian nature of SPH arises when the number of neighbors is kept constant.

Thus, in the following equations, the summations are over the neighboring particles $j = 1, N$, instead of all the particles occurring in the system, and the functions are evaluated in the position of a particle i. The density is then estimated as

$$\rho_i = \sum_j m_j W(\mathbf{r}_{ij}; h), \tag{4.10}$$

where ρ_i stands for $\rho(\mathbf{r}_i)$ and $\mathbf{r}_{ij}$ for the position vector $(\mathbf{r}_i - \mathbf{r}_j)$.

When following "the golden rule of SPH" proposed by Monaghan (1992), the formula for the gradient can be rewritten in the form with the density placed inside the operator:

$$\rho \nabla A = \nabla(\rho A) - A \nabla \rho. \tag{4.11}$$

Then, using (4.9), the gradient estimate becomes

$$\rho_i (\nabla A)_i = \sum_j m_j (A_j - A_i) \nabla_i W(\mathbf{r}_{ij}; h), \tag{4.12}$$

where $\nabla_i W(\mathbf{r}_{ij}; h)$ denotes the gradient of the kernel function with respect to the coordinates of particle i. Analogously, the divergence and vorticity of e.g. the velocity at particle i is given by

$$\rho_i (\nabla \cdot \boldsymbol{v})_i = \sum_j m_j (\boldsymbol{v}_j - \boldsymbol{v}_i) \cdot \nabla_i W(\mathbf{r}_{ij}; h), \tag{4.13}$$

$$\rho_i (\nabla \times \boldsymbol{v})_i = \sum_j m_j (\boldsymbol{v}_i - \boldsymbol{v}_j) \times \nabla_i W(\mathbf{r}_{ij}; h), \tag{4.14}$$

Two different concepts of evaluating the function A in the position of a particle i are possible: the "scatter" interpretation assumes that each particle of the system has a mass smoothed in

the space according to the kernel function W and chosen value of h. The value of the function A is then found by summing the contributions from the neighboring particles. On the contrary, in the "gather" interpretation, the local value of the function A is obtained by sampling the neighboring particles and weighting their contributions according to W. Of course, if the smoothing length h is constant for all particles the both approaches coincide, but if h is spatially varies, the distinction arises. In terms of the two concepts, the above summation interpolants employ the gather formulation of the smoothing.

Originally, SPH assumed a constant value of h for all particles throughout the system, varying only in time. But since the constant h produced relatively more accurate estimates in regions with a high number density of particles, and it is the smoothing length which determines the spatial resolution of the calculation, the SPH method was generalized to local, spatially variable smoothing lengths, which has increased the resolution substantially. However, such an improvement, either in gather or scatter scheme, had a significant drawback, the equations of motion transformed into the smoothed forms violated the third Newton's law. In order to conserve the total momentum of the system, the kernel has to be symmetrized in smoothing lengths of the two interacting particles i and j. A symmetrized kernel can be obtained by symmetrizing the used smoothing length, e.g. by substituting a simple arithmetic mean $(h_i + h_j)/2$ for h_i and h_j. Alternatively, Hernquist & Katz (1989) have introduced the symmetrizing of the two kernels themselves. In this approach both gather and scatter schemes are linearly combined. The old kernel function $W(\mathbf{r}_{ij}; h)$ is replaced with

$$\tilde{W}_{ij} = \frac{1}{2}[W(\mathbf{r}_{ij}; h_i) + W(\mathbf{r}_{ij}; h_j)]. \tag{4.15}$$

Further, the smoothed forms of the dynamical equations have to be derived. Following Monaghan (1992), instead of using the standard form (4.9) for the smoothed estimate of the pressure gradient, which introduces non-conserving linear and angular momenta, the following identity provides a symmetric expression

$$\frac{\nabla P}{\rho} = \nabla\left(\frac{P}{\rho}\right) + \frac{P}{\rho^2}\nabla\rho. \tag{4.16}$$

Then the gasdynamical acceleration from the Euler's equation is obtained

$$\frac{dv_i}{dt} = -\frac{1}{\rho_i}\nabla P_i + a_i^{visc} = -\sum_j m_j \left(\frac{P_i}{\rho_i^2} + \frac{P_j}{\rho_j^2} + \Pi_{ij}\right)\nabla_i \tilde{W}_{ij}, \tag{4.17}$$

where a_i^{visc} stands for the acceleration arising from artificial viscosity discussed later. Then the force contribution on SPH particle i from particle j laying within h_i is

$$\boldsymbol{f}_{ij} = -m_i m_j \left(\frac{P_i}{\rho_i^2} + \frac{P_j}{\rho_j^2} + \Pi_{ij}\right)\nabla_i \tilde{W}_{ij}, \tag{4.18}$$

and when $\boldsymbol{f}_{ij}$ is added to the force on particle i and $-\boldsymbol{f}_{ij}$ to the force on j, the momentum conserves. Hernquist & Katz (1989) propose another identity for the pressure gradient calculation:

$$\frac{\nabla P}{\rho} = 2\sqrt{P}\frac{\nabla\sqrt{P}}{\rho} \tag{4.19}$$

symmetrizing the pressure terms with a geometric mean $2\sqrt{P_i P_j}/(\rho_I \rho_j)$ instead of the arithmetic one $P_i/\rho_i^2 + P_j/\rho_j^2$. The dynamical evolution of the internal energy determined by the thermal energy equation can be smoothed in the following form, neglecting the heating and cooling processes

$$\frac{du_i}{dt} = \frac{1}{2}\sum_j m_j \left(\frac{P_i}{\rho_i^2} + \frac{P_j}{\rho_j^2} + \Pi_{ij}\right)(\boldsymbol{v}_i - \boldsymbol{v}_j)\cdot\nabla_i \tilde{W}_{ij}. \tag{4.20}$$

When trying to interpret the energy equation in any SPH form, using a Gaussian kernel, the thermal energy of particle i increases when a particle j approaches it. This effect represents the SPH equivalent of $\nabla \cdot \boldsymbol{v} < 0$.

To close the system of hydrodynamical equations, an equation of state must be added, i.e. by writing the ideal gas law as

$$P_i = (\gamma - 1)\rho_i u_i. \tag{4.21}$$

4.1.4 Artificial viscosity

The introduction of the artificial viscosity is required to capture the shocks in the flow, i.e. to convert relative motion into heat. The artificial viscosity in fact dampens post shock oscillations in the solution and prevents particle to interpenetrate in high Mach number collisions. The viscous contribution to the pressure gradient can have the following form (Monaghan, 1988) describing well the flow near shocks

$$\Pi_{ij} = \begin{cases} (-\alpha c_{ij}\mu_{ij} + 2\alpha\mu_{ij}^2)/\rho_{ij}, & \text{if } \boldsymbol{v}_{ij}\cdot\mathbf{r}_{ij} < 0 \\ 0, & \text{if } \boldsymbol{v}_{ij}\cdot\mathbf{r}_{ij} > 0, \end{cases} \tag{4.22}$$

where the viscosity vanishes when $\boldsymbol{v}_{ij}\cdot\mathbf{r}_{ij} > 0$ which corresponds to the condition $\nabla\cdot\boldsymbol{v} > 0$. The viscosity is zero for particles moving away from each other and positive for particles approaching each other. The first term, linear in the velocity differences, produces shear and bulk viscosity, and the second term suppresses particle interpenetration at high Mach number. c_{ij} stands for the sound speed in the form $(c_i + c_j)/2$ helping to limit the degree to which cold particles shock against dense clumps, and

$$\mu_{ij} = \frac{h_{ij}\boldsymbol{v}_{ij}\cdot\mathbf{r}_{ij}}{\mathbf{r}_{ij}^2 + \eta^2}. \tag{4.23}$$

Actual experiences show that the viscosity in the form (4.22) spreads shock fronts over $\sim 3h$. The value of α is typically near to 1, and the factor η is inserted to prevent numerical divergences. When $\eta^2 = 0.01h^2$, it means that smoothing of the velocity takes place only if the particles spacing is $< 0.1h$.

A number of forms have been proposed for the artificial viscosity

$$\widetilde{\Pi}_{ij} = \frac{1}{2}(f_i + f_j)\Pi_{ij}, \tag{4.24}$$

where

$$f_i = \frac{|(\nabla\cdot\boldsymbol{v})_i|}{|(\nabla\cdot\boldsymbol{v})_i| + |(\nabla\times\boldsymbol{v})_i|} \tag{4.25}$$

introduces a shear-correcting term (Balsara 1995, Steinmetz 1996) that limits the damping of shear flows.

To dissipate the energy added to the fluid from shocks, an artificial viscous pressure term is introduced into the momentum and energy equations. The omission of this term in the inviscid hydrodynamics equations results in large unphysical oscillations in the field variables in the wake of a shock.

4.1.5 Kernel function

The original SPH calculations of Gingold & Monaghan (1977) used a 1D Gaussian kernel

$$W(x;h) = \frac{1}{h\sqrt{\pi}}e^{-x^2/h^2}, \tag{4.26}$$

mimicking the delta function for $h \to 0$.

The smoothing kernel of Monaghan & Lattanzio (1985) based on spline functions in the following form

$$W(\mathbf{r};h) = \frac{8}{\pi h^3}\begin{cases} 1 - 6q^2 + 6q^3, & \text{if } 0 \le q \le 1/2 \\ 2(1-q)^3, & \text{if } 1/2 \le q \le 1 \\ 0, & \text{otherwise,} \end{cases} \tag{4.27}$$

where $q \equiv r/h$ is used in GADGET. Advantages of a spline kernel are its compact support with interactions diminishing for for $r > h$, continuous second derivative and consequent $O(h^2)$ error in the integral interpolant.

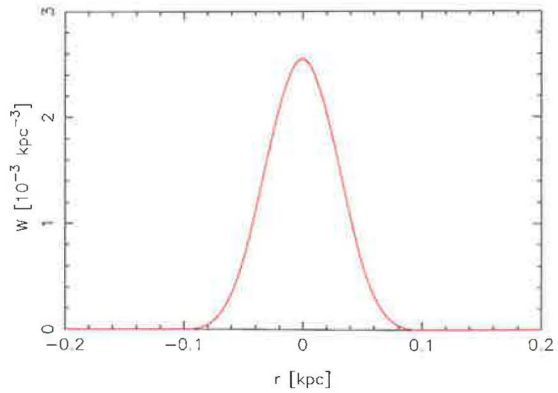

Figure 4.1: The smoothing kernel function (4.27) as function of r for $h = 0.1kpc$.

4.1.6 Smoothing sizes

As noted above, originally, the smoothing length varied in SPH calculations with time but was constant in space. Its value was determined from

$$h \propto 1/\langle\rho\rangle^{1/3}, \quad \text{where} \quad \langle\rho\rangle = \frac{1}{n}\sum_i \rho_i, \tag{4.28}$$

and n is the number of particles. Since the smoothing length determines the resolution and the number of neighbors, the computational efficiency would increased when h reflected the local particle density. The following subsection shows the way how to update the smoothing length such that the number of neighbors is kept roughly constant.

4.1.7 SPH in GADGET

As will be described lower, GADGET implements an integrator with completely flexible timesteps, i.e. the particles have individual timesteps. Therefore, only a small fraction of particles may require a a force walk through the tree at each timestep and a system of active and passive particles is introduced (see Springel et al. 2001 for details).

In GADGET, the SPH implementation proceeds in two phases. Firstly, for all active particles, new values of the smoothing lengths are determined. The prediction of the new smoothing length is based on the value h_i from the previous timestep, the number of neighbors N_i at that timestep, and the local divergence of the velocity:

$$\tilde{h}_i = \frac{1}{2}h_i\left[1 + (N_s/N_i)^{1/3}\right] + \dot{h}_i\Delta t, \tag{4.29}$$

where $\dot{h}_i = (1/3)h_i(\nabla \cdot \boldsymbol{v})_i$, and N_s is the desired number of neighbors. When the number of neighbors deviates from N_s, it is adapted with the first term. Further, for all active particles, the neighboring particles are found. As described above, the number of neighbors is desired to be constant which is achieved by varying the smoothing lengths. The h_i then adapts to the local number density of particles which yields into a constant mass resolution. When the neighbors are known, the density at positions of the active particles is computed using (4.10), together with divergence and vorticity (4.13). Density, internal energy, and smoothing lengths are predicted for passive particles from the values of the last update of those particles. The pressure at particles positions is computed from (4.21). In the second phase, the gasdynamical forces are computed from (4.17), and the change of the internal energy from (4.20), employing (4.24) form of the artificial viscosity.

Since GADGET implements an individual timestep scheme, when looking for neighbors of a particle i, one needs to find all particles with $|\mathbf{r}_{ij}| < \max(h_i, h_j)$ to estimate the hydrodynamical force on the particle i. The neighbor search is based on a method of geometric search tree, which in

fact employs the same tree algorithm constructed for the gravity calculations. The Barnes & Hut (1986) oct-tree can be successfully used (see below). Although we describe in detail the principle of construction and manipulation with the BH-tree in Section 4.2, here we give some brief information about its application to the SPH neighbors search. By walking the tree from the ground (trunk) enclosing the whole system to individual branches, one can finally arrive to cells encompassing only one particle lying inside the search radius, or to a whole node whose all particles satisfy the neighboring test. Then a list of all nodes and particles is constructed and thus the neighboring particles can be quickly sought out.

4.2 Tree algorithms

As an alternative to existing N-body methods for numerical treating of collisionless dynamics, like direct summation, Particle-Mesh, P^3M, or expansion methods, the hierarchical tree algorithm (Appel 1985, Barnes & Hut 1986) has been proposed. In their essence, hierarchical methods are similar to P^3M algorithms, since they equally use direct summation to compute attractions of close particles, but differ in treating remote particles interactions. The key idea of these methods is that from the view of a given particle, detailed internal structure of the remote groups of many particles can be ignored. Particles are organized into a hierarchic structure of groups and cells, resembling a tree with individual leaves related to the particles themselves, and branches joining together representing cells merging into greater and more complex groups. Then, when the force on given particle is evaluated, it is allowed to interact with various elements of the hierarchy. The influence of remote particles is obtained by evaluating the multipole expansion of the group. Such approach exploits the fact that higher-order multipoles of the gravitational field decay rapidly with respect to the dominant monopole term. Thus many similar particle–distant-particle interactions are replaced with a single particle–group interaction. It is possible to approximate the group's potential only by monopole term, or low-order corrections for the group's internal structure can be included as well. It is clear that with growing distance from a given particle, one can put together higher number of particles into still larger group. In this way, the computational cost of the force evaluation reduces and if the accuracy criterion determining how deeply the internal structure of a given group has to be analyzed is indirectly proportional to the distance from a given particle, i.e. the size of an unresolved group increases with the distance, the sum over N particles is replaced by a sum over $\log N$ interactions, and the cost scales as $O(N \log N)$.

The construction of the tree can be treated in several ways. The AJP method (Appel 1985, Jernigan 1985, Porter 1985) applies a method of recursive center of mass coordinate transformation. Given a list of N particles, the two which are closest together in physical space are chosen to form a first node. Then these two particles can be removed from the total list of particles and replaced by the center-of-mass node, leaving a list of $N - 1$ entities. In the next step, two other currently closest particles may form another node, or a single particle closest to the first node is joined together with it. This procedure is repeated until only one object, the root node, remains in the whole system. It has a mass of all the particles and is located at the center of mass of the system. Since the tree conserves the spatial relationship of particles and groups, it can be referred to as a mutually nearest neighbor tree.

Barnes & Hut (1986) introduced another technique based on hierarchical subdivision of the system space containing the particles, not only the particles themselves. The system is hierarchically divided into a sequence of cubes. Initially, a sufficiently large cubic volume encloses all particles. This root cell is consecutively subdivided into eight cubic subcells of equal volume which represent the first descendants of the root cell. Identical procedure is then repeated until each cell at the lowest level in the hierarchy contains either one ore none particle. Since each node has eight descendants, the resulting structure can be called the oct-tree. Each node of the tree carries an entry about the total mass of all particles within a given volume and their center-of-mass coordinates. The leaves of the tree always represent a volume containing exactly one particle because information about the empty cells is not stored in the tree. Compared to the AJP tree, the BH tree does not conserve spatial relationship of the particles and nodes since the boundaries of adjacent

subcells at a high level in the hierarchy can divide physically tightly close particles on completely different widely separated branches of the tree. Nevertheless, the way of the BH tree construction allows to create a cleaner and simpler tree structure than in the AJP scheme (Hernquist 1987) since the sizes and shapes of the nodes are uniform across a given level in the BH tree, but are completely arbitrary in the AJP algorithm.

Since GADGET employs the BH tree construction, the oct-tree structure is constructed in the computational space. During the tree construction process, a list of cells together with readings about the number of encompassed particles is being created. The root cell represents the trunk of the tree and individual cells with descending complexity the ramifying branches. The outer bounder of the tree is created by the leaves of which each represents precisely one particle. Thus, the number of leaves coincides with the total number of particles. Once the tree is completed, information about masses, center-of-mass positions, and multipole moments are append to each cell.

Then, by walking the tree and summing up appropriate force contributions from the nodes, the force on a given particle is computed. Standardly, the multipole expansion of a cell is used only if the following "opening" criterion is fulfilled

$$r > \frac{l}{\theta}, \tag{4.30}$$

where l is the size of the cell, r its distance from the particle, and θ a fixed tolerance parameter called opening angle. Then, the influence of all particles within the cell is computed as a single particle-cell interaction, i.e. the tree walk along the corresponding branch can be terminated. Otherwise, the cell is opened, and further subdivided until either the criterion is fulfilled or an elementary cell is reached. The opening criterion follows from comparison of the size of the quadrupole term, with the size of the monopole term and it is purely geometric criterion saying that if a cell is sufficiently small and remote from the particle, its internal structure may be neglected. The opening angle is a parameter typically less than unity, and it may be used to adjust the accuracy of the method. The smaller is its value, the more accurate results are yield because the precise structure of the cells is explored to greater extent. However, the computational expense grows since more direct particle-particle interactions are computed. Dubinski et al. (1996) have introduced a simple modification of the opening criterion: $r > l/\theta + \delta$, where δ is the distance of the cell's geometric center to its center-of-mass. This modification solves a fail of the criterion in its simple form (4.30) that can occur when a cell's center-of-mass lies too far from its geometric center. From cosmological simulations follows that for an unclustered particle distribution the opening criterion requires much smaller opening angle than for a clustered one, in order to achieve a similar force accuracy level.

In regions of high particle density, it can occur that a node fulfills the opening criterion and at the same time r is less than the gravitational softening length h. For the Newtonian gravity the multipole expansion of the potential of a collection of point particles in a bounded region is

$$\Phi(r) = -G\left(\frac{M}{r} + \frac{1}{2}\frac{\boldsymbol{r}\cdot\boldsymbol{Q}\cdot\boldsymbol{r}}{r^5}\right), \tag{4.31}$$

where the dipole term vanishes since the center-of-mass is used as the expansion center, M is the mass of the node of particles, and $\boldsymbol{Q}$ the traceless quadrupole tensor

$$Q_{ij} = \sum_k m_k(3x_{k,i}x_{k,j} - r_k^2\delta_{ij}). \tag{4.32}$$

To correctly handle the above mentioned situation with $r < h$, the multipole expansion of the softened potential has to be made. By deriving the spline-softened gravitational force from the normalized spline kernel used in the SPH formalism (4.27), the force due to a point mass m is replaced with the force exerted by the mass distribution $\rho(\boldsymbol{r}) = mW(\boldsymbol{r}; h)$. The exact potential of a node is then

$$\Phi(\boldsymbol{r}) = -G\sum_k m_k g(|\boldsymbol{x}_k - \boldsymbol{r}|), \tag{4.33}$$

where m_k and x_k are masses and coordinates of individual particles of the node, and the function $g(r)$ describes the softened force law; for Newtonian gravity $g(r) = 1/r$, and for the spline softened gravity

$$g(r) = -\frac{1}{h} W_2\left(\frac{r}{h}\right), \tag{4.34}$$

where h is the softening length and

$$W_2(q) = \begin{cases} \frac{16}{3}q^2 - \frac{48}{5}q^4 + \frac{32}{5}q^5 - \frac{14}{5}, & \text{if } 0 \le q < 1/2 \\ \frac{1}{15}q^{-1} + \frac{32}{3}q^2 - 16q^3 + \frac{48}{5}q^4 - \frac{32}{15}q^5 - \frac{16}{5}, & \text{if } 1/2 \le q < 1 \\ -q^{-1}, & \text{if } q \ge 1, \end{cases} \tag{4.35}$$

with $q = r/h$. For the spline softening the force becomes exactly Newtonian for $r > h$. The multipole expansion of the softened potential, assuming $|\boldsymbol{y}| \gg |\boldsymbol{x}_k - \boldsymbol{s}|$, where $\boldsymbol{y} = \boldsymbol{r} - \boldsymbol{s}$, and $\boldsymbol{s}$ is the center-of-mass, is then

$$\Phi(\boldsymbol{r}) = -G\left[Mg(y) + \frac{1}{2}\boldsymbol{y}^T\left(\frac{g''(y)}{y^2}\boldsymbol{Q} + \frac{g'(y)}{y^3}(\boldsymbol{P} - \boldsymbol{Q})\right)\boldsymbol{y}\right]. \tag{4.36}$$

The introduced tensors $\boldsymbol{Q}$ and $\boldsymbol{P}$ have the following form

$$\boldsymbol{Q} = \sum_k m_k(\boldsymbol{x}_k - \boldsymbol{s})(\boldsymbol{x}_k - \boldsymbol{s})^T \tag{4.37}$$

and

$$\boldsymbol{P} = \boldsymbol{I}\sum_k m_k(\boldsymbol{x}_k - \boldsymbol{s})^2, \tag{4.38}$$

where $\boldsymbol{I}$ stands for the unit matrix. Then, for the Newtonian gravity the expansion of potential reduces to (4.31). Corresponding derivation of the approximation of the softened gravitational field can be found in Springel et al. (2001).

GADGET employs the Barnes-Hut opening criterion (4.30) only to compute the very first force. Then, an alternative opening criterion is used and a tree node is opened if

$$Ml^4 > \alpha|\boldsymbol{a}_{old}|r^6, \tag{4.39}$$

where α stands for a fraction of the total force on the particle represented with the acceleration of the previous timestep. This criterion is based on the estimation of the multipole truncation error which should not exceed the fraction α of the total force. Since the multipole expansion is truncated at quadrupole order, the octupole or hexadecapole moments form the leading terms of the neglected part.

4.3 Dynamic tree updates & time integration

GADGET incorporates an individual time integration scheme. Then the prediction of all particles and reconstruction of the full tree at every time step is not necessary. As noted by McMillan & Aarseth (1993), the structure of the tree evolves only relatively slowly with time. Therefore, the reconstruction of the tree can be made only every few timesteps. A tree node is updated when its center-of-mass has moved by more than a small fraction of the node's side-length since the last reconstruction. The full tree is reconstructed whenever a total of about $0.1N$ force computations have been done since the last full update, to take into account the slow changes in the hierarchy. Finally, these procedures results in the time scales of $O(M \log M)$, where M is a small number of particles that are advanced in the given timestep.

GADGET offers several possible timestep criteria, see section 5.1 of Springel et al. (2001) for details. The used time integrator works in the following manner: each particle has a time step Δt_i and a current time t_i when its position, velocity and acceleration are stored. Consequently, the dynamical state of the particle can be predicted with first order of accuracy at times $t_i \pm 0.5\Delta t_i$. The next particle k to be advanced is the one with the minimum prediction time defined as

$\tau_p = \min(t_i + 0.5\Delta t_i)$. This time becomes the new current time of system. Then to advance the corresponding particle, positions of all particles at time τ_p are predicted:

$$\tilde{\boldsymbol{r}}_i = \boldsymbol{r}_i + \boldsymbol{v}_i(\tau_p - t_i). \tag{4.40}$$

From these positions, the acceleration of particle k at the middle of its timestep is

$$\boldsymbol{a}_k^{(n+1/2)} = -\nabla\Phi(\tilde{\boldsymbol{r}}_i)|_{\tilde{\boldsymbol{r}}_k}. \tag{4.41}$$

Position and velocity of particle k are then advanced as

$$\boldsymbol{v}_k^{(n+1)} = \boldsymbol{v}_k^{(n)} + 2\boldsymbol{a}_k^{(n+1/2)}(\tau_p - t_k), \tag{4.42}$$

$$\boldsymbol{r}_k^{(n+1)} = \boldsymbol{r}_k^{(n)} + \left[\boldsymbol{v}_k^{(n)} + \boldsymbol{v}_k^{(n+1)}\right](\tau_p - t_k), \tag{4.43}$$

and its current time can be updated to

$$t_k^{(\mathrm{new})} = t_k + 2(\tau_p - t_k). \tag{4.44}$$

Finally, a new timestep $\Delta t_k^{(\mathrm{new})}$ for the particle is estimated.

The particles are ordered according to their prediction times $t_i^p = t_i + (1/2)\Delta t_i$ and are not advanced one by one but in groups – the particle with the smallest t_i^p and all subsequent ones until the first with $\tau_p \leq t_i + (1/4)\Delta t_i$ is found. The size of the group that is advanced at a given timestep is only a small fraction of the total particle number.

4.4 GADGET modifications

In a hypothetical system with homogeneously distributed particles, smoothing lengths of all the particles are identical. N_b neighboring particles of each particle is enclosed within a volume of l^3. When the number of particles in the system is multiplied by a parameter α, the number density of particles changes by α, as well. If the number of neighbors ought to be constant, they have to be now enclosed in a reduced volume of l'^3, where $l' = l\ \alpha^{-1/3}$. If the smoothing length h corresponds to a radius within which N_b particles are enclosed, the $h' = h\ \alpha^{-1/3}$. It means, that to the density at a given point contributes an unchanged number of neighboring particles, but that are now located closer to the particle and are smaller. Since the kernel function smoothing out the particles is normalized by (4.3), the resulting value of the density in the point of interest does not change.

If the system is not homogeneous in density, in extreme it can be modelled either by a set of equal-mass particles whose positions follow up the density distribution of the system, or by a homogeneous particle distribution with the density profile realized by assigning different masses to the particles. The latter method is inconvenient in that way, that regions with different densities are represented with the same number of particles and so the spatial resolution of the model is not adaptive to the needs of the system. On the other hand, the former method would provide enough spatial resolution in the densest regions, but it would demand an immense number of particles in systems with a large range in the density. Therefore, a mean is a combination of the two extremes.

What than happens with particles that initially occur in a low density environment and later reach a density peak? Since the number density is in the initial location low, the particles are large in the SPH sense. As they get closer to a bunch of particles representing a density peak, they start to shrink since a fixed number of neighbors is used to the revaluation of their size. If the particle cluster has in its center a substantially higher number density than its surrounding, the arriving large particles shrink to their sizes and mutually interact only locally.

As mentioned above, GADGET can handle different types of particles in the gravitational part of the code, e.g. by assigning them different softening length values. On the contrary, it resolves only one gaseous phase in the version 1.1, which means that all the gaseous particles occurring in the system are hydrodynamically treated as a one group. The volume densities of the ISM in the

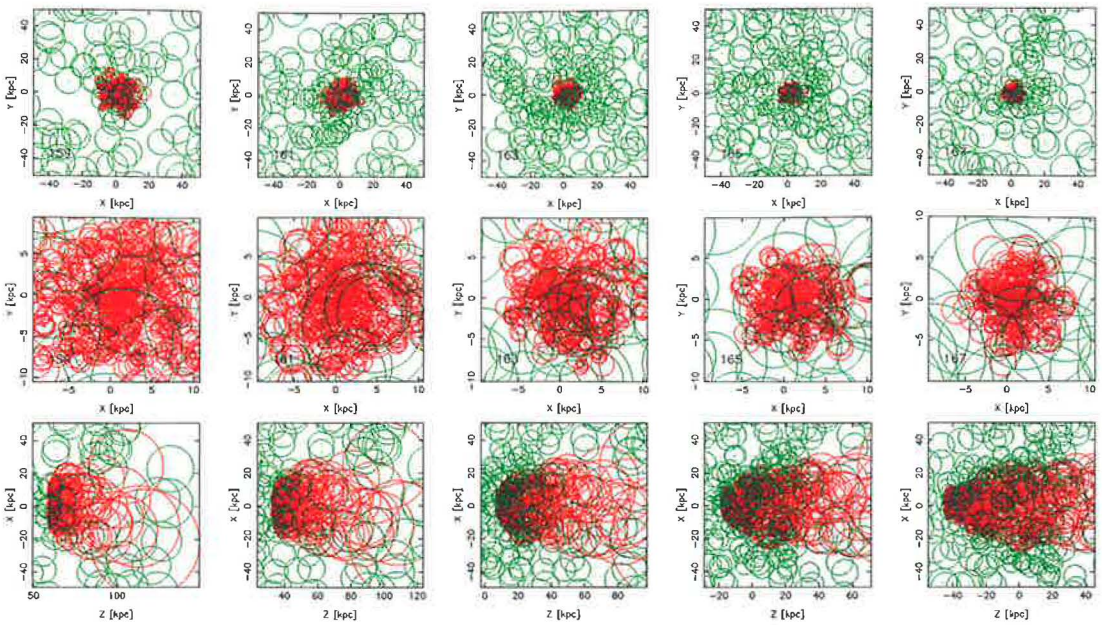

Figure 4.2: The SPH sizes of the ISM (red) and ICM (green) particles in five time instants as the galaxy flights through the cluster center. $N_{ICM} = 120\,000$, $N_{ISM} = 12\,000$. Upper row displays a face-on view of the galaxy surroundings with the ISM particles located within $\pm$ 2 kpc about the disk plane, and the ICM particles within $\pm$ 20 kpc about the disk plane. The middle row focuses to the central disk part, and the bottom row depicts the edge-on view of the situation with ICM particles located within $\pm$ 20 kpc about the disk in the line of sight direction. In all panels, only every tenth particle is displayed.

disk and of the surrounding ICM differ in several orders, as well as their temperatures. To treat correctly their interaction, the number density of the ICM particles, n_{ICM}, should not be lower than that of the ISM particles, n_{ISM}. Otherwise, the ICM particles located far from the galaxy would be larger in the SPH sense than the ISM particles, since the number of neighboring particles is kept constant throughout the system. When later approaching the disk, the size of these large ICM particles is revaluated from both the ICM and the ISM particles locally presented, and since $n_{ISM} > n_{ICM}$, the ICM particles shrink to the size of the ISM particles. Then the ICM particles do not cover completely the disk, but only small areas of it in their locations, and an effect of punching the holes into the disk mentioned by Abadi et al. (1999) can occur, further depending on the mass ratio of the individual ICM versus ISM particles. Of course, to achieve a similar number densities of both the gases, an immense number of ICM particles would be necessary.

Having in mind these constraints, we introduce a set of changes into GADGET related to the fact that we need to simulate two different gaseous phases (ICM, and ISM) with different spatial resolution. Firstly, the subroutine for searching the neighboring particles is adapted to distinguish between the two phases. Consequently, the smoothing radii h's of either ICM or ISM particles are calculated separately from the neighbors of a corresponding phase. Then, both the phases are treated separately, which allows us to employ a reasonably small number of ICM particles. These particles are then substantially larger than the ISM and their size does not change even in the vicinity of the disk. It assures that all the disk area is covered by the ICM particles. Secondly, the hydrodynamical interaction of the two phases proceeds. While in the previous step of evaluating the particle sizes, the ICM and ISM phases are searched separately in the sense that all neighboring particles of the second phase are omitted, and the search continues until N_b proper neighbors is found, now both phases are searched together to find all particles with $|r_{ij}| < \max(h_i, h_j)$. I.e., a given ISM particle interacts with all the ICM counterparts within whose smoothing radii it is contained. Further, the adiabatical, and isothermal treatment of the ICM, and ISM is implemented, respectively.

Fig. 4.2 shows snapshots of the galaxy flying through the cluster center in our standard simula-

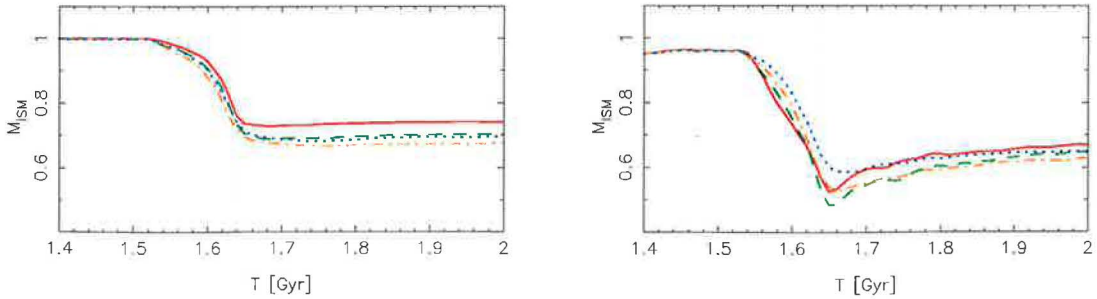

Figure 4.3: Results of the standard face-on flight of the LM galaxy through the cluster center, as will be discussed in the following chapter. Total amount of bound ISM (left panel), and amount of the ISM located within the disk radius of 16 kpc, and a layer of ±1 kpc height about the disk plane (right panel), as functions of the orbital time. Individual curves correspond to different number of ICM particles, N_{ICM}: 480 000 (full), 120 000 (dashed), 24 000 (dot-dashed), and 12 000 (dotted).

tion run with $N_{ICM} = 120\,000$ and $N_{ISM} = 12\,000$, as introduced in Chapter 3. SPH sizes of both the ISM (red) and ICM (green) particles in the galaxy surroundings are displayed. The upper row shows the face-on view of the disk, the middle one focuses on the disk central parts again in the face-on view, and the lower row shows the edge-on view of the situation. Only every tenth particle is displayed, which makes impression of voids occurring among particles. One can observe the difference in the ISM versus ICM particles sizes that is maintained in the disk area. As the galaxy gets to the cluster center, which corresponds to the third panel in the sequence (e.g. in the bottom row), the ICM particles get smaller since the ICM density grows. As will be described later, a bow shock of ICM particles forms around the galaxy. Within the shock the density is enhanced and sizes of the ICM particles are smaller (see in the last panel of the bottom row). Similarly, a decrease of the sizes of the ISM particles in the disk at lower radii is visible. As the ISM is stripped out of the disk, its density falls and the sizes of individual particles noticeably grow. In the tail of stripped particles, the h_{ISM} and h_{ICM} become then comparable.

4.4.1 Effect of varying number density

Since we have modified GADGET to a two-phase regime, the smoothing radii h's of either ICM or ISM particles are calculated separately from the corresponding phases. To achieve a sufficient spatial resolution in the disk, we fix the number of ISM particles N_{ISM} on an adequate value. Therefore, in all simulations, the resolution in the disk is the same. In Fig. 4.2 we saw the respective sizes of the ISM versus ICM particles in the standard run with $N_{ISM} = 12\,000$ and $N_{ICM} = 120\,000$. What happens when the number of ICM particles is varied? Then, since the number of SPH neighbors is kept constant, the smoothing sizes correspondingly adapt. As noted above, when N_{ICM} is multiplied by a parameter α, the smoothing radii evolve as $h' = h\ \alpha^{-1/3}$. What is the effect of the changing sizes of the ICM particles to the stripping results in which we are interested and which will be discussed in the following chapters?

We have performed a set of test runs of the LM galaxy flying through the $R_{c,ICM} = 13.4$ kpc, $\rho_{0,ICM} = 4\ 10^{-3}$ cm^{-3} ICM peak, differing in the total number of the ICM particles. This brings, apart from the varying sizes of the ICM particles, changing ratios m_{ICM}/m_{ISM} of individual ICM versus ISM masses. The ratios both superior and inferior to 1 are represented. Fig. 4.3 displays the results of these simulations – total amount of the ISM bound to the galaxy (left panel), and amount of the ISM located within the disk (right panel). Both quantities are displayed as functions of the orbital time. Details concerning the stripping results will be given in Chapter 5. The number of ICM particles varies like: $N_{ICM} = 480\,000$, 120 000, 24 000, and 12 000. Since the number of ISM particles is in all the simulations fixed at 12 000, the ratio m_{ICM}/m_{ISM} of individual particles of the two gaseous phases evolves from 0.26, 1, and 5.2, to 10.3.

Due to our modifications of GADGET described above, a fixed number of proper neighbors is searched separately for the two gaseous phases (ICM, and ISM). The smoothing sizes $h_{ISM}(r)$ of the ISM particles are with respect to a fixed N_{ISM} unchanged in the four cases, while the smoothing

radii of ICM particles are large in simulations with a low value of N_{ICM}, and get smaller when the N_{ICM} increases. Then calculation of gasdynamical forces between the SPH particles proceeds in that way that a particle i interacts with a particle j whenever the $|r_{ij}| < h_i$ or $|r_{ij}| < h_j$.

Three interesting things showed up in Fig. 4.3: Firstly, the instantaneous minima of the ISM mass within the disk (right panel) shortly after the cluster center passage (marked with vertical line) vary with growing number of ICM particles. From a shallow and wide shape in the case of $N_{ICM} = 12\,000$, it gets sharper and deeper with the N_{ICM} growing. But the minimum is not lowest for $N_{ICM} = 480\,000$, since the curve corresponding to this value is shifted above the $N_{ICM} = 120\,000$ curve. Secondly, the higher is the number of ICM particles, the steeper is the decline of the M_{ISM} as the galaxy plunges towards the cluster center. Thirdly, the final number of ISM particles is in all cases similar. The maximum difference in the final result is

The first two points are connected to the varying sizes of the ICM particles in individual runs. When h_{ICM}'s are large, the edge of the ICM distribution at 140 kpc is for the ISM particles in the arriving disk softened, since they feel the ICM particles sooner than the galaxy really enters the distribution.

The third finding is the most surprising one, since simulations differing forty-times in the N_{ICM}, i.e. about 3.4-times in the ICM particle sizes, lead to only slightly different results. With such a low number of ICM particles as in the case of 12 000, the difference between smoothing sizes of ICM versus ISM particles is huge. The ICM particles are so large, that every simple one of them can cover a substantial part of the whole ISM disk. That means that a group of close particles laying within a given ICM particle feel only pressure of the ICM but no pressure gradients, as it would be the case when the sizes of ICM and ISM particles were comparable. Then, in fact no detailed hydrodynamical effects can evolve and the ISM-ICM interaction loses its hydrodynamical character. But, Fig. 4.3 shows that when the ICM particles are smaller and thus the hydrodynamical interactions are treated in a better way, the result of the ISM-ICM interaction is similar. It therefore seems that a detailed hydrodynamical treatment of the interaction is not much important, and only the ram pressure plays a crucial role in the stripping.

4.5 Our simulation approach

Following the discussion in the previous section, we can try to characterize our approach to the stripping simulations and compare it with other existing methods. Since the study with varying number of ICM particles in Fig. 4.3 showed that the stripping results are determined primarily by the global ram pressure, we can use a reasonably low value of N_{ICM}. As described in Chapter 3, we distribute the ICM particles within radius of 140 kpc about the cluster center. The standard value of N_{ICM} is then set to 120 000 in all simulations discussed later.

As we omit the detailed hydrodynamics in the ISM-ICM interaction treatment, our approach resembles the method of Vollmer et al. (2001) who in their sticky-particle simulations include the effect of the ram pressure only analytically as an additional acceleration on the clouds located at the surface of the gas distribution. In our case, of course, the restriction of the interaction on the surface layer only is not introduced. What is more realistic than in Vollmer et al. (2001) is that we treat the ICM phase fully hydrodynamically. It means, that in the mutual interactions of the ICM particles is not restriction like in the case of ICM-ISM interactions. Therefore, as will be discussed later, we see in simulations a bow shock that forms in the ICM in front of the galaxy. Consequently, the incoming ICM particles are realistically deflected from their direction to flow around the disk. Moreover, when from the SPH point of view small ISM particles are stripped out of the disk, their number density falls and their size increases. In the tail of stripped particles, the sizes of both the ISM and ICM become then comparable, and the hydrodynamical treatment of the tail is correct.

Abadi et al. (1999) use a 3D SPH/tree code similar to GADGET in their simulations. They warn against too massive ICM particles punching holes into the ISM disk and thus introduce a simulation box of size 60 kpc × 60 kpc × 10 kpc homogeneously filled up with the ICM particles flowing with periodic boundary conditions. With N_{ICM} equal to 20 000 they reach the ICM number density of about 0.55 kpc^{-3}. In our standard simulation run, a mean number density of

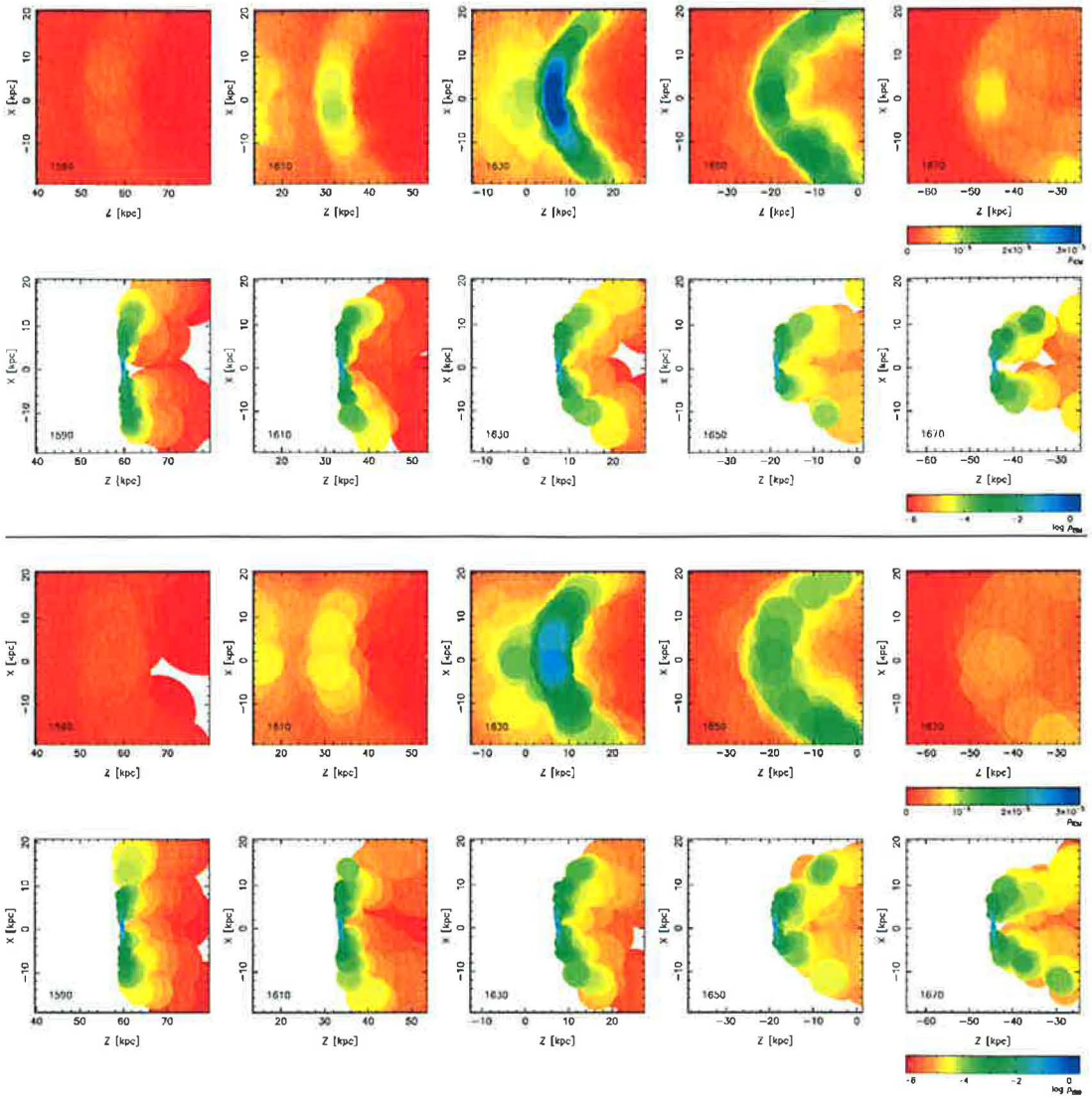

Figure 4.4: Top: $N_{ICM} = 480\,000$, bottom: $N_{ICM} = 120\,000$. In both cases $N_{ISM} = 12\,000$. Upper row in both figures displays the density (color scale) of the ICM in the surroundings of the galaxy at five time instants as the galaxy passes through the cluster center. Particles are displayed as filled circles with radii corresponding to their SPH radii h_i. Bottom row shows the density of the ISM particles, with a logarithmic scale in the wedge.

ICM particles within 10 kpc radius about the cluster center is about 0.2 kpc^{-3}. This difference corresponds to only 1.4-times smaller ICM particles in Abadi et al. (1999) compared to us.

Since the number of particles modelling the ICM distribution within the central radius of 140 kpc is kept constant in all simulations, the number density of the particles and thus their sizes in the very cluster center depend on the $\rho_{0,ICM}$ and $R_{c,ICM}$ parameters of the ICM peak. In clusters with a fixed value of the central density but varying in the $R_{c,ICM}$, the (central) number density of particles increases and the particles are smaller as the $R_{c,ICM}$ decreases. It means that in narrow clusters the ISM-ICM interaction is better treated in the hydrodynamical sense than in wide ones.

Fig. 4.4 shows edge-on views of the surroundings of the galaxy at five epochs of its passage through the cluster center. It compares two simulations with N_{ICM} equal 480 000 and 120 000, respectively. Upper rows show the ICM density, i.e. the density at positions of the ICM particles that are displayed as filled circles with radii corresponding to their SPH smoothing radii h_i.

Bottom rows analogously depict the ISM density. One notes three things: firstly, a difference in sizes of ICM particles in the two cases, secondly, a clearly visible bow shock forming in the ICM, narrower in the upper case with $N_{ICM} = 480\,000$, and thirdly, sizes of the ISM particles that are minuscule in the disk plane, and grow up as the particles are stripped from the disk and their number density falls.

We conclude that our approach combines a method introduced by Vollmer et al. (2001), who include only analytic transfer of momenta between the ICM and the ISM clouds located at the windward side of the disk, and a method of correct hydrodynamical treating of the intracluster material itself, leading to formation of bow shocks in front of galaxies and thus influencing the stripping of the ISM.

4.5.1 SPH versus grid methods

Agertz et al. (2006) put to test the SPH versus grid-based hydrodynamical codes to compare their ability to correctly simulate a system of interacting multiphase fluids. They show important differences in behalf of the grid methods that can resolve and treat dynamical instabilities (e.g. Kelvin–Helmholtz or Rayleight–Taylor), contrary to the SPH. The grid codes thus can treat better the high-resolution surface phenomena and destroy the dense cloud in tiny pieces, while SPH does not. Agertz et al. (2006) explain the difference with an artificial pressure forces on SPH particles in regions with steep density gradients.

However, in our simulations all these instabilities are below our resolution, and as will be shown in the following chapters, we discuss mainly the short duration of the stripping, while the above processes take a long time.

Chapter 5

Numerical simulations: Face-on radial stripping

After introducing models of both the galaxy and the cluster in Chapter 3, and describing the numerical code GADGET that we use for our simulations in Chapter 4, we discuss the simulation results obtained for the face-on interaction of galaxies with the ICM, here. Firstly, we follow the LM galaxy on a radial orbit leading it to the very center of the cluster and study the effects of the varying cluster setting, especially the width and height of the ICM density peak, to the stripping results. Further, we compare the fate of the LM galaxy with other galaxy models, the Lm, EM, and Em, on the same orbit. In the next chapter we will describe the face-on interaction analytically and compare the numerical results with the analytical predictions.

5.1 LM galaxy in the standard cluster

In Chapter 3 we have described in detail the initial conditions of the model galaxies LM, Lm, EM, and EM, as well as of the model clusters with varying parameters of the ICM density peak $R_{c,ICM}$ and $\rho_{0,ICM}$ that we will use in our numerical simulations. The model galaxy sets out from the cluster periphery at 1 Mpc distance with zero initial velocity. It causes its subsequent free fall towards the cluster center. Depending on the ICM density distribution, the galaxy reaches the center with a slightly varying velocity at a slightly different times (see Tab. 3.4). The initial configuration is shown in Fig. 3.11. We remind that the ICM particles are distributed only within central 140 kpc radius which corresponds in the case of the standard cluster to the distance at which the outer parts of the LM disk start to be influenced by the ram pressure.

Firstly, we study the crossing of the LM galaxy through the standard cluster with the ICM distribution parameters set to $R_{c,ICM} = 13.4$ kpc and $\rho_{0,ICM} = 4\ 10^{-3}$ cm^{-3}. The simulation shows how the ISM of the galaxy evolves under the influence of the evolving galactic gravitational field including the self-gravity of the ISM disk, the gravitational field of the cluster, which changes along the orbit, and under the influence of the ram pressure due to relative motion of the ISM and ICM.

Fig. 5.1 displays edge-on-view snapshots of the ISM disk at 30 time epochs starting at 1.5 Gyr after the beginning of the orbit. The ICM wind blows from the left. The color coding of the ISM particles corresponds to their radial distance in the disk – particles at higher radii are bluer, while those at lower radii are greener. The galaxy initially approaches the edge of the distribution of the ICM particles at 140 kpc, further passes through the center at ~ 1.64 Gyr, leaves the ICM at ~ 1.75 Gyr and continues towards the second apocenter. As noted above, when the galaxy enters the ICM distribution, the local value of the ram pressure is sufficient enough to influence only the outer disk regions. This can be observed at times 1.53 Gyr and 1.54 Gyr. Later on, the ISM from

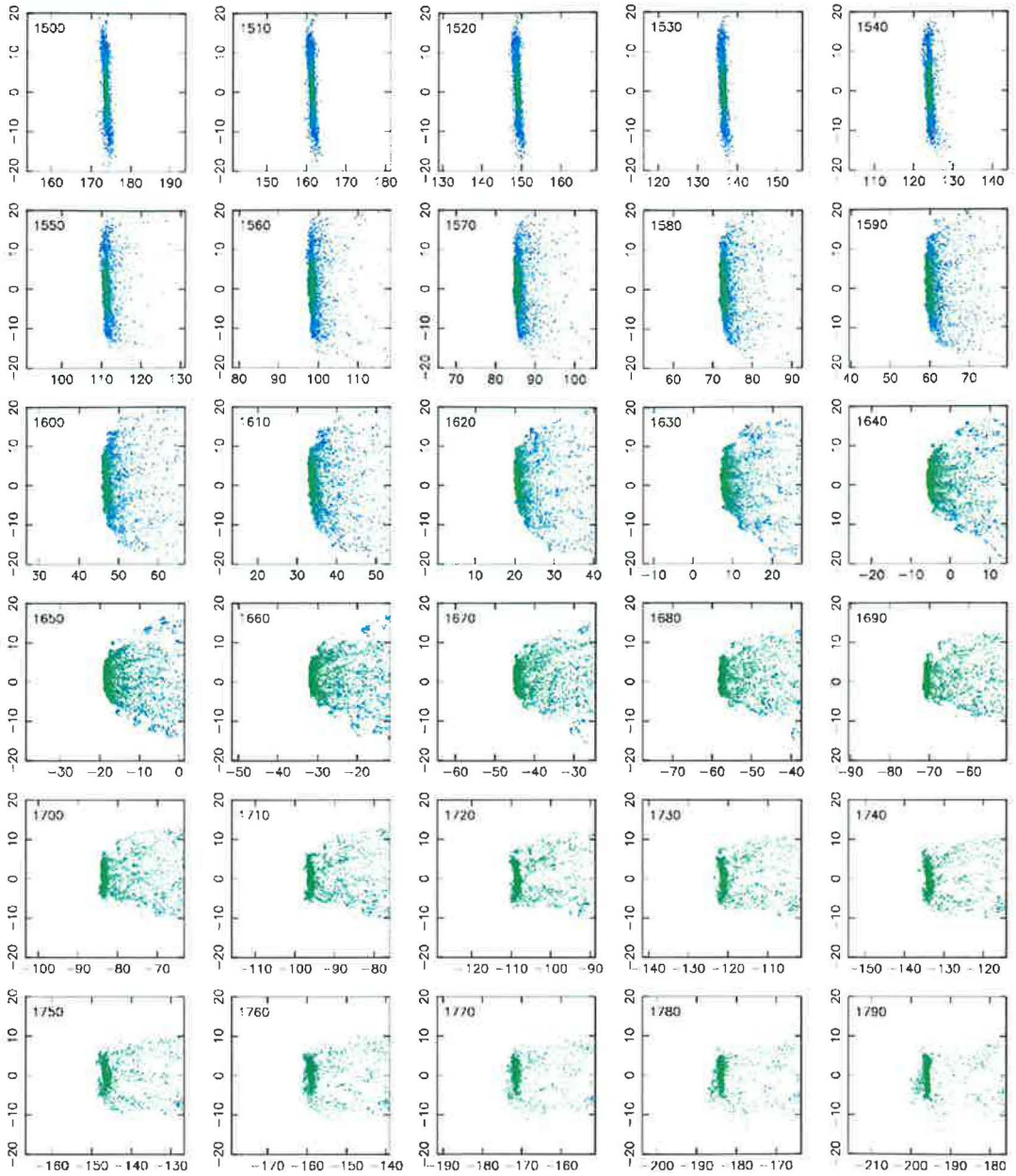

Figure 5.1: Face-on run of the model galaxy LM through ICM particles in the cluster center.

lower and lower radii is influenced by the increasing ram pressure and a tail of stripped particles form. At the cluster center the ram pressure is maximum, both due to the peak of the ICM density and the galaxy's maximum orbital velocity. At T =1.74 Gyr the ram pressure completely ceases and following evolution of the ISM disk is due to the underwent stripping event.

At $T \sim 1.73$ Gyr one firstly notes a clump of the material that appears on the windward side of the disk. It corresponds to the material that was shifted behind the disk by the strongest ram pressure and after its cease it has returned, oscillating about the disk plane. At the last panel, a number of ISM particles occurs on both sides of the disk and the stripping tail behind the disk gets feeble and tends to discontinue. Due to the strong ram pressure at the cluster center, the inner part of the disk is at times about $T = 1.66$ Gyr bowed in accordance with the ram pressure

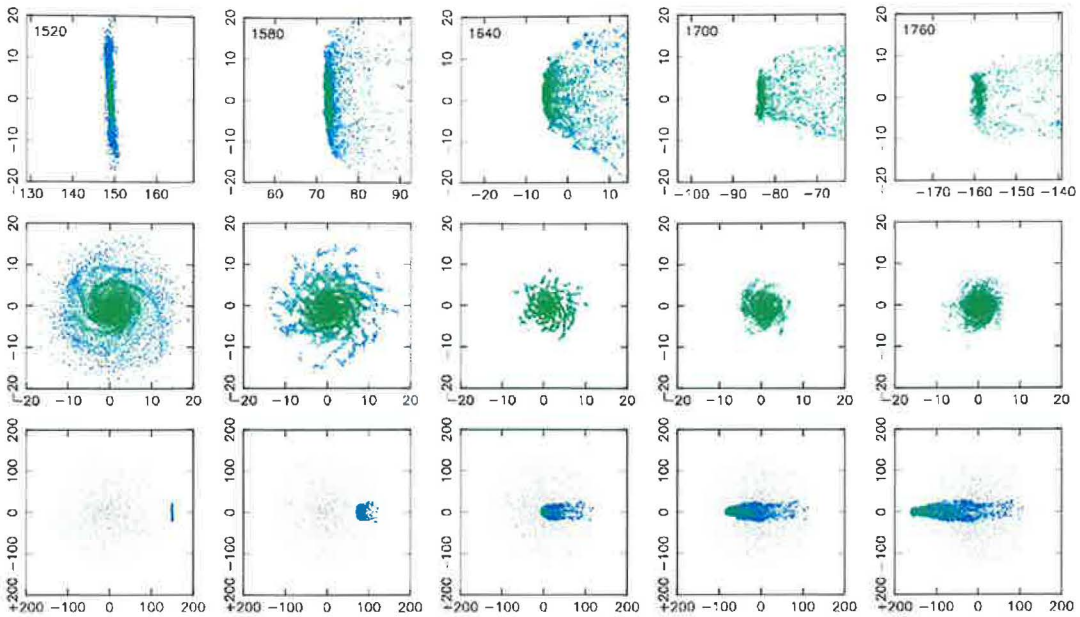

Figure 5.2: Face-on (top) and wide cluster center (bottom) view of selected snapshots of Fig. 5.1. Note the enhanced spiral structure of the ISM disk (second panel), and clearly visible tail of stripped particles.

direction with outer parts slightly shifted in the wind direction. As a reaction, the disk is found bowed to the opposite direction at times about $T = 1.72$ Gyr when the ram pressure has ceased.

During the most animated parts of the stripping event one can observe chains of stripped particles and clumps of the material stripped at once. All these effects are connected to the stripping of the ISM from the disk that has a complex spiral structure.

Further views of the standard stripping event are provided in Fig. 5.2. Central row shows from the face-on direction the ISM disk at times 1.52 Gyr until when the galaxy has evolved without hydrodynamical effect of the ICM, at times 1.58 Gyr, 1.64 Gyr, and 1.7 Gyr when the galaxy occurs under the action of the ICM wind when passing through the cluster center, and at time 1.76 Gyr when it relaxes after the fade-out of the wind, respectively. The second panel of the face-on view illustrates the effect described by Schulz & Struck (2001) that the stripping enhances the spiral structure of the disk since particles from positions of lower surface densities are more easily removed. Bottom row then offers a wider view of the whole central cluster region with visibly extending tail of the stripped material. Particles that were stripped from the disk at initial stages when the ram pressure was low, gain low output velocities from the disk and follow the track of the galaxy. Thus, at later times the tail of stripped particles is hardly visible at their original stripping locations.

As the ISM disk moves through the intracluster medium, a bow shock on the windward disk side forms. Fig. 5.3 displays the density of the ICM in the surroundings of the galaxy during its flight through the central cluster region. In this plot, the snapshot area is divided into 30×30 grid and the ICM density is calculated in every cell as an average value from all enclosed ICM particles. In Chapter 4, Fig. 4.4 shows the ICM density in the disk vicinity using individual ICM particles that are displayed filled circles with radii corresponding to their SPH radii h_i. The bottom row of Fig. 5.3 shows the velocity vectors of the ICM particles interacting with the ISM. One notes the evolution of the slope of the bow-shock cone due to the stripping of outer layers of the ISM. Domainko et al (2005) draw attention to the role of the bow-shock formation in the case of supersonic motions through the ICM. When the galaxy enters the ICM, particles located in front of the disk (in face-on case) are gathering on its front side, local density thus growing and relative velocity steeply dropping. Oncoming ICM particles are then forced to deflect from their original direction

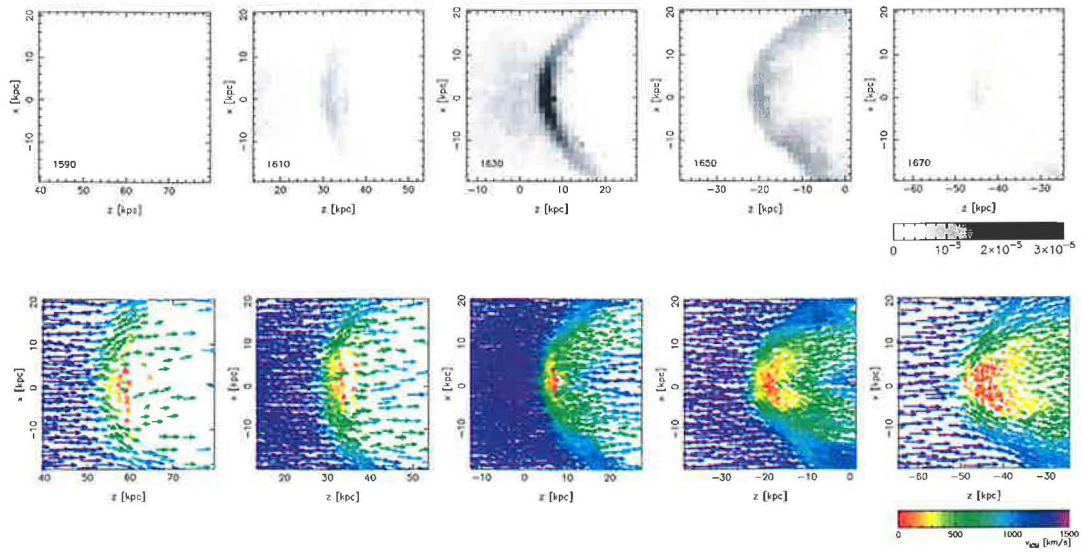

Figure 5.3: Vectors of relative velocity of ICM particles interacting with the ISM disk during the STD simulation run (top), and scan of the ICM density illustrating the creation of a bow-shock (bottom). Particles of the ISM are plotted in bottom panels as white points.

and flow along the bow shock. On head of the shock situated in front of the central parts of the disk ICM particles are decelerated and their relative velocities tend to zero values, i.e. they are catched by the disk and move with it. In both figures, particles occurring in the shadow area of the disk can be found. Particles in central disk parts are almost stopped by interaction with the ISM and thus may slowly pass through the disk with no effect on the ISM. At the outskirts, ICM particles may reach shadowed area by a turbulent motion. The effect is strengthened by complex structure of the disk with inter-arms spaces of lower density among spiral arms. It is interesting that initially the region behind the disk plane is of a low density compared to the environment in front of the disk, while at later times, when the galaxy again leaves the cluster center, the situation is reversed – i.e, the galaxy pulls some ICM out of the central cluster region.

In Fig. 5.4 we follow the number of ISM particles within different radii of the disk during its crossing of the cluster. Since all the ISM particles have the same mass, this number is equivalent to the ISM mass. Roediger & Hensler (2005) distinguish a cylindrical space about the disk, and a region copying the original flattened shape of the disk in which they follow the amount of the galactic ISM. Vollmer et al. (2001) define a space volume with the galaxy's radius of 20 kpc and a constant height of 1 kpc. In Fig. 5.4, we count the ISM particles within a layer $|z| < 1$ kpc about the disk plane and radii growing from 1 kpc to 16 kpc (dashed curves) with 1 kpc step. The upper blue full curve corresponds to the radius of 16 kpc. Before the galaxy enters the ICM zone at about 1.53 Gyr, no important changes in counts of the ISM particles within individual radii are observed. The blue curve does not initially equal to 1 which corresponds to the fact that the galaxy has relaxed and thus some particles (about 5 %) get out of the initial radius of 16 kpc. Once the galaxy reaches at T =1.53 Gyr the edge of the ICM distribution, particles at outer radii experience a growing ram pressure and are being shifted behind the disk, i.e. out of the $|z| < 1$ kpc layer. Thus, the increasing ram pressure gradually decreases the number of particles at lower and lower radii. Since the particles from outer radii are stripped, the upper curves consequently coincide with the lower ones corresponding to lower radii. At T ~1.64 Gyr, the galaxy gets to the very cluster center and with a small delay of about 20 Myr the number of particles inside the disk zone becomes minimum. Particles down to a radius $r_{min} \sim 4.5$ kpc are influenced.

After the moment when the ISM mass enclosed within the evaluation zone is minimum, a strong reaccretion of the material occurs. That concerns the material previously only shifted out of the disk by a short-term effect of the strongest ram pressure. From the minimum value of about 50

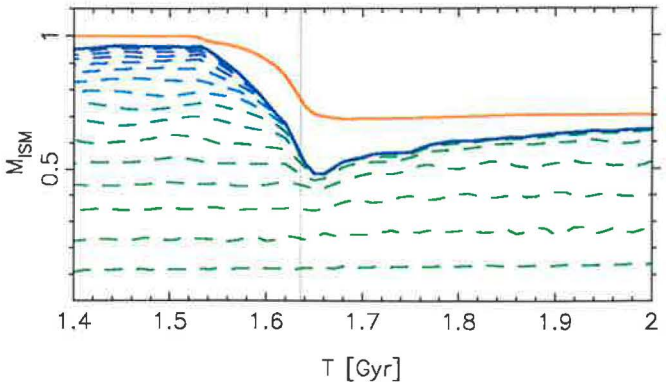

Figure 5.4: The standard simulation run: time evolution of the number of ISM particles (i.e. the ISM mass) within 16 different disk radii (1 – 16) kpc and $|z| < 1$ kpc layer (dashed curves). The uppermost curve corresponds to the ISM mass bound to the galaxy. The instant of crossing the cluster center is marked with the vertical line. The stripping of outer layers starts at 1.53 Gyr, the global minimum of the ISM mass in the evaluation zone occurs in time 1.65 Gyr, and the number of bound particles decreases till 1.68 Gyr. Note the bumps at 1.74 Gyr and 1.81 Gyr (i.e. a period of $\sim$ 70 Myr) corresponding to oscillations of reaccreted particles about the disk plane.

% of the total ISM mass, it grows to about 66 % at time $T = 2$ Gyr. Of course, the minimum value of the ISM mass, as well as its final value depend on the definition of the evaluation zone, especially on its extent in the z-direction. If the cylinder were higher in z, the reaccretion would be weaker since the minimum radius would be larger. At the same time as the shifted ISM reaccretes, almost no visible changes of the disk radius occur. The dashed curve corresponding to the radius of 4 kpc, in the minimum almost coincides with the blue full curve, while later the gap between them increases only slowly. It means, that when taking into account only the particles located within the evaluation zone, the disk radius increases after the maximum stripping only slightly. Therefore, the accumulated material originating at higher radii is deposited below the r_{min} and the surface density of the disk Σ_{ISM} increases.

The uppermost orange curve in Fig. 5.4 shows the number of all the ISM particles (i.e. the ISM mass, $M_{\rm bnd}$) that are bound to the galaxy potential, i.e. that have negative total energy. Initially, it includes all the ISM. When the ram pressure rises, the ISM from decreasing radii start to be released, and the amount of the bound material decreases even after the galaxy's passage through the cluster center. It means that particles are being released even after the ram pressure maximum. After that, their number stays constant and substantially higher than the number of particles enclosed within the cylinder. Even at the final time T =2 Gyr all the shifted but not released particles are not re-accreted to the disk.

Above we have stated that the fact that the ICM particles are distributed only within the radius of 140 kpc does not influence the stripping since the value of the ram pressure at this distance from the cluster center influences only the outermost radii of the disk. Looking carefully at Fig. 5.4, one notes that the decline of the dashed curves is not absolutely smooth but shows a small edge. It means that the outermost radii would start to be deflected from the disk at a little larger distance from the cluster center than at 140 kpc and thus Fig. 5.4 does not provide a complete view of the stripping event. Nevertheless, the limitation is only marginal. Further, it is possible that if the ICM particles were distributed to higher cluster radii, reaccretion of shifted ISM particles would start at a slightly later time. But no quantitative changes would occur since the number of released particles is clearly decided before the galaxy gets from the ICM distribution (see the orange curve). Therefore, the later stripping phases, as well as the subsequent reaccretion phase are described correctly.

To summarize the stripping event of the LM galaxy crossing the standard cluster (i.e. with $R_{c,ICM} = 13.4$ kpc and $\rho_{0,ICM} = 4\ 10^{-3}$ cm^{-3}) we determine the stripping radius and the final ISM mass. As will be discussed in more detail in Chapter 7, the determination of the stripping

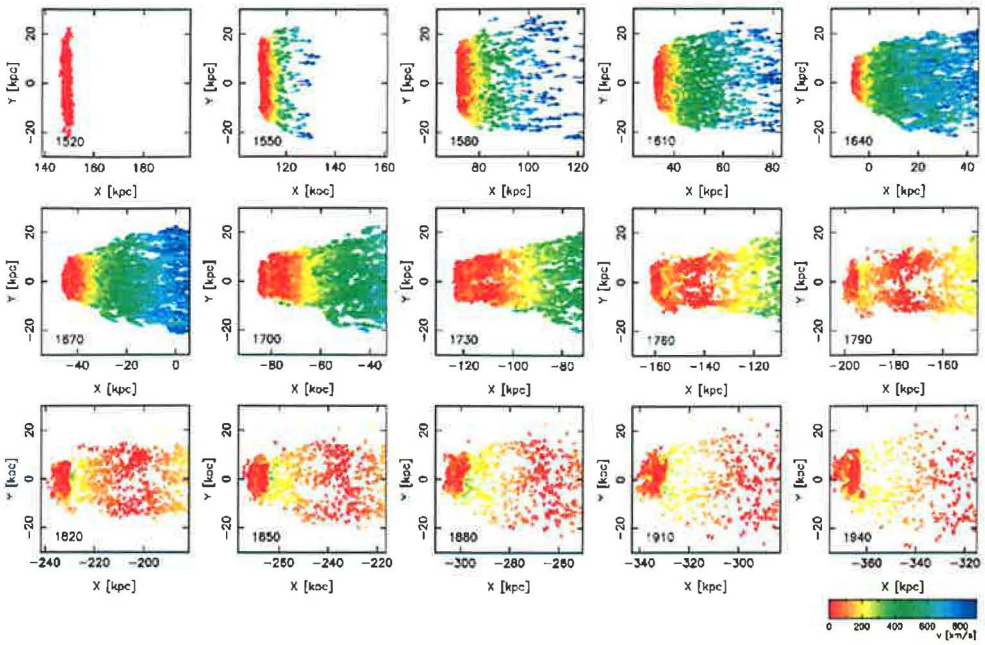

Figure 5.5: Velocity vectors (arrows) of the ISM particles. Colors correspond to the velocity components in the z-direction ranging from 0 to 800 km s^{-1}, times are in Myr.

radius r_{strip} is not a straightforward task. It can be defined as a radius at which the ISM surface density falls below certain value (see e.g. Roediger & Hensler 2005). Thus, one can choose a minimum value of the Σ_{ISM} that determines the stripping radius. But rather than the value itself, its maintenance for determining the radii in different simulation runs is important to obtain comparable results. Evaluating the surface density of the ISM in radial shells can be tricky, since a few of ISM particles with an insignificant total mass then determine the value of the radius whose slight variance can correspond to an essential change in the contained mass. Assuming a Σ_{min} = 0.01 x $\Sigma_{central}$, we determine the stripping radius to be R_{strip} = 6.3 kpc. Another possibility of the R_{strip} determination could consist in assuming that the ISM keeps the initial profile of the surface density and thus determining the stripping radius as a radius containing the final mass.

Contrary to the stripping radius, the final mass of the ISM can be easily determined from Fig. 5.4-type plots. We define the final mass M_{final} as the mass of the ISM that stays bound to the galaxy after the stripping event. In the case of Fig. 5.4 the final mass corresponds to the level of the orange curve at the final simulation time T = 2 Gyr: M_{final} = 0.71 x $M_{d,ISM}$. From the above definition of the final mass follows that it should be superior to the mass corresponding to that contained within the stripping radius since at the time T = 2 Gyr, not all shifted (but bound) ISM particles are already reaccreted.

With a constant flow of the ICM, Roediger & Hensler (2005) identify three phases of stripping: an instantaneous phase when the outer disk parts are bent in the wind direction but stay bound to the galaxy, a dynamic intermediate phase during which the bending breaks and a part of the ISM is stripped and another part falls back to the disk, and a quasi-stable continuous viscous stripping phase when the outer disk layers are peeled off by the Kelvin-Helmholz instability at a rate of $\sim$ 1 M$_\odot$ yr^{-1}. The time scale of the first phase is $\sim$ 20 – 200 Myr, while the following second phase is about ten-times longer. In our simulations, we observe a behavior similar to the first two phases, however, the evolution of the $M_{\rm bnd}(t)$ and $M_{|z|<1{\rm kpc}}(t)$ under the operation of a peaked ram pressure is different (see Fig. 5.4). Once the ram pressure rises, the outer disk layers are released, while the more inner ones are only shifted from the $|z|$ < 1 kpc zone. Although

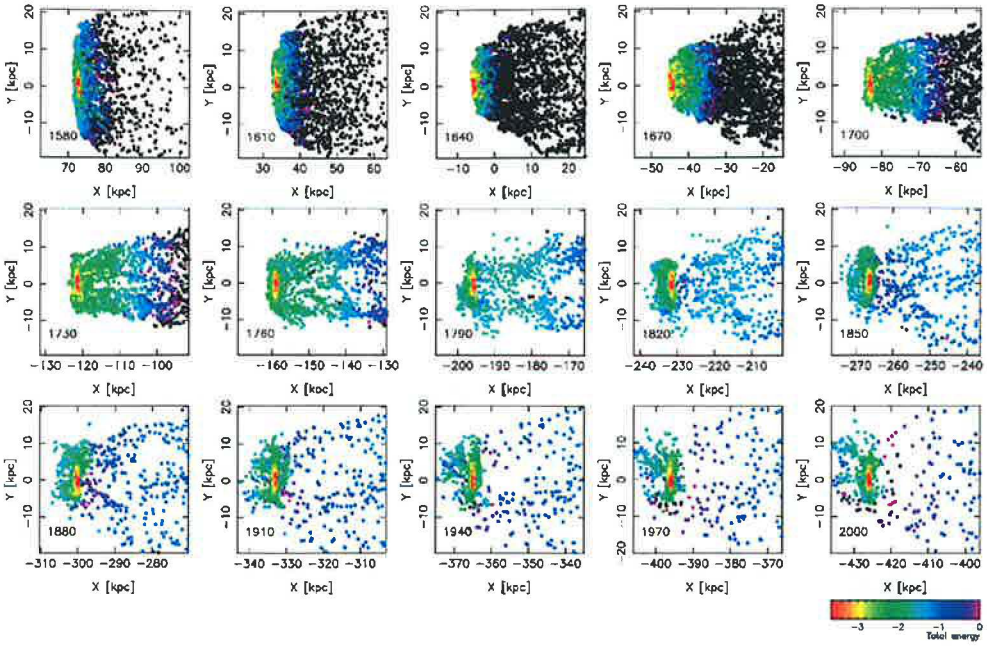

Figure 5.6: Snapshots of the standard simulation run with colors representing values of the total energy of ISM particles. Released particles are marked with black color. The release of particles is strongest when the galaxy approaches the cluster center.

the rate of the release is lower compared to the shifting, both effect occur simultaneously. When the ram pressure ceases, the shifted but bound ISM reaccretes. In our SPH simulations, the Kelvin-Helmholz instability cannot take effect.

To explore the face-on stripping event in more detail, we study the velocity field of the ISM particles with respect to the galaxy's rest frame in Fig. 5.5. Different colors correspond to the velocity components in the z-direction ranging from 0 to 800 km s^{-1}. Initially, as the galaxy plunges into the ICM distribution, the ISM from outer regions is being accelerated by the ram pressure. As the galaxy approaches the cluster center, an increasing number of ISM particles is shifted out of the disk and accelerated in the wind direction towards the escape velocities. The number of released elements grows fastest within central ~ 40 kpc (see Fig. 5.4). Up to time $T \sim 1.64$ Gyr, particles with zero (or low) velocities are distributed only in the plane of the disk, according to the fact that the ram pressure is high and thus accelerates the particles strongly. Later, as the ram pressure decreases, the ISM particles from the disk are only slowly shifted out of the disk and the distribution of low-speed (up to ~ 200 km s^{-1}) considerably extends. At time $T = 1.76$ Gyr the ram pressure has already ceased and particles of the tail close to the galaxy stop and start to fall back towards the disk. They can be accelerated up to ~ 300 km s^{-1} when reaching the disk. Further, note the evolution of the top angle of an imaginary cone enveloping the tail of stripped particles in Fig. 5.5. It gradually decreases to a value of $\sim 20°$ at $T = 1.73$ Gyr.

Fig. 5.6 displays the edge-on views of the ISM disk, with varying colors corresponding to particles with different total energy $E = E_{kin} + E_{pot}$. The released particles are marked with black points. According to Fig. 5.4, the particles are released from the galaxy only at phases when the galaxy approaches the cluster center, with a delay of about 20 Myr when already shifted particles reach the escape velocities. Therefore, after the passage through the center, a layer of the released ISM recedes to higher z-distances. It means, that the actual ram pressure is not efficient enough to release more particles, but only to shift them behind the disk plane. The first (outermost) particles are being released at about 3 kpc distance behind the disk plane, and further this distance grows to about 7 kpc for elements at lower radii, which correspond to the different profiles of the restoring

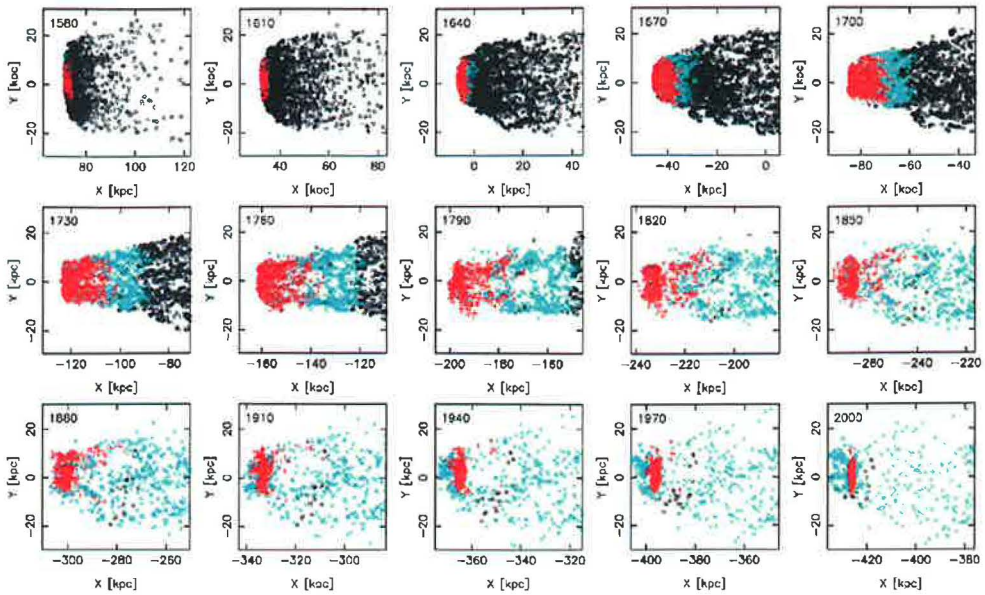

Figure 5.7: Tracing the origin of the ISM elements that are at the final simulation time $T = 2$ Gyr (lower right panel) bound to the galaxy (cyan crosses), and located within the disk (red pluses). Elements that are at the final time free are marked with black circles.

force at different radii.

Finally, Fig. 5.7 traces the fate of the ISM particles occurring at the final simulation time $T = 2$ Gyr in the disk plane. Therefore, these particles are identified at the final time (red signs) and further displayed their positions at previous times during the simulation. One sees, that the particles were shifted by the ram pressure up to 30 kpc behind the disk plane, and later reaccreted as the ram pressure ceased. Further, black points in Fig. 5.7 denote released particles, and cyan crosses the particles bound to the galaxy at time $T = 2$ Gyr but located outside the disk plane.

5.2 LM galaxy in various clusters

In the previous section, we have presented the results of the simulation run corresponding to the standard situation (see Chapter 3) with the LM galaxy flying face-on through the cluster with $R_{c,ICM} = 13.4$ kpc, and $\rho_{0,ICM} = 4\ 10^{-3}$ cm^{-3} parameter setting. Now, we are interested in stripping results of the LM galaxy flying through clusters with varying values of the $R_{c,ICM}$ and $\rho_{0,ICM}$ parameters. These parameters in fact correspond to the width and height of the ICM density peak. Therefore, a change of the $\rho_{0,ICM}$ parameter leads to a different maximum value of the ram pressure in the cluster center, and the effect is strengthened by a varying maximum orbital velocity of the galaxy that corresponds to the amount of the gravitational mass in the cluster. Since the cluster is dominated by the dark matter, the effect of the varying amount of the ICM to the orbital velocity is not important. Further, when changing the $R_{c,ICM}$ parameter, the maximum ram pressure stays almost unchanged, altered only by the above slight modification of the maximum orbital velocity. However, what changes in this case is the period over with the galaxy experiences the interaction with the intracluster medium. The orbit of the galaxy stays in the following study unchanged, i.e. a strictly radial one leading the galaxy directly through the cluster center. We again stress that this configuration has the advantage of preserving the inclination of the disk plane with respect to the orbital direction, which will be discussed in Chapter 7.

We complete the standard simulation (Fig. 5.4) with a set of additional 24 runs specified by varying values of the parameters $R_{c,ICM}$ and $\rho_{0,ICM}$. Combinations of 0.25, 0.5, 1, 2, and 4 multiples of the standard values $R_{c,ICM} = 13.4$ kpc and $\rho_{0,ICM} = 4\ 10^{-3}$ cm^{-3} are used. Profiles

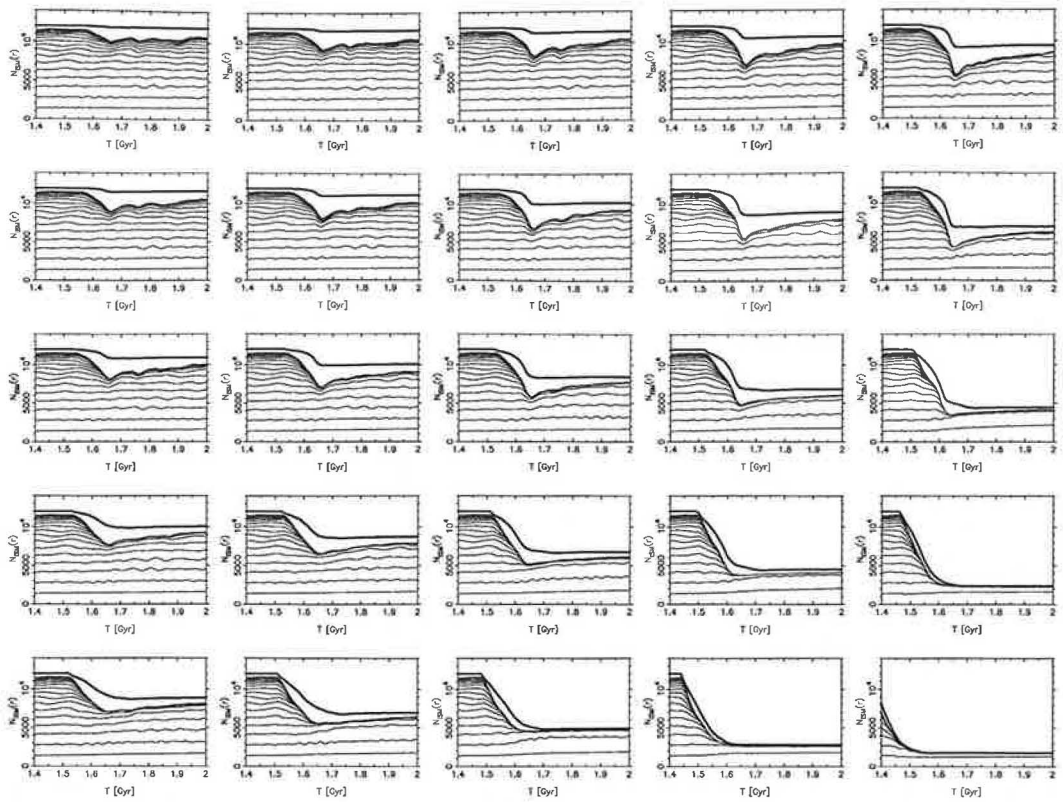

Figure 5.8: Set of plots of Fig. 5.4–type for twenty-five simulation runs of the LM–type galaxy crossing face-on central parts of clusters with varying ICM distribution. In every row, $R_{c,ICM}$ is constant, while $\rho_{0,ICM}$ varies: 0.25, 0.5, 1, 2, 4 × 4 10^{-3} cm^{-3} (from left to right); and in every column, $\rho_{0,ICM}$ is constant, while $R_{c,ICM}$ varies: 0.25, 0.5, 1, 2, 4 × 13.4 kpc (from top to bottom). The central panel corresponds to Fig. 5.4.

of the ICM density distributions with constant $R_{c,ICM}$ and varying $\rho_{0,ICM}$, and constant $\rho_{0,ICM}$ and varying $R_{c,ICM}$ are displayed in Fig. 3.9. Fig. 5.8 thus contains twenty-five panels showing the stripping results of the introduced set of simulations, with the central panel coinciding with the standard simulation (Fig. 5.4). Rows gather runs with constant $R_{c,ICM}$'s and varying $\rho_{0,ICM}$'s, while columns keep fixed $\rho_{0,ICM}$'s and vary the $R_{c,ICM}$. Evolution of the ISM mass (i.e. the number of equally mass ISM particles) enclosed within a layer $|z| < 1$ kpc about the disk plane and sixteen radii growing from 1 kpc with 1 kpc step, is followed as a function of the orbital time. The uppermost thick curves correspond to the ISM mass bound to the galaxy.

The main stripping event is in all displayed cases rather short, taking 100 – 200 Myr. When going in Fig. 5.8 from left to right, and from top to bottom, values of the parameters $\rho_{0,ICM}$ and $R_{c,ICM}$ increase, respectively. In both the directions, a visible expansion of the stripping extent into more and more inner parts of the disk occurs. It means, that both the increasing width, and height of the ICM density peak cause a stronger stripping. Nevertheless, the process of stripping itself is different when following either direction. For a fixed value of $R_{c,ICM}$, i.e. following a row, the minimum of the ISM mass that is contained within the evaluation zone, deepens with growing value of the central density (from left to right). It is the most markedly observable in the first row, where galaxies traverse very narrow ICM peaks with $R_{c,ICM} = 3.4$ kpc. Then, such a narrow but high ram pressure peak kicks abruptly the particles down to low radii, accelerating the outer of them directly to the escape velocities, and only shifting the others out of the disk plane. Since the ram pressure operates during a short time, the shifted particles then reaccrete. For a fixed value of

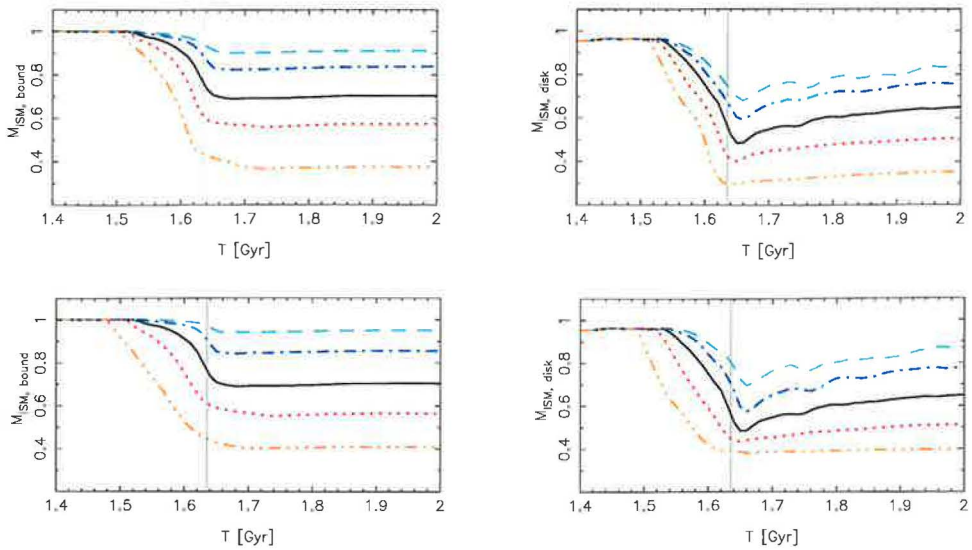

Figure 5.9: Evolution of the ISM mass bound to the galaxy (left) or staying within $r < 16$ kpc and $|z| < 1$ kpc about the disk plane (right) during the passage through central parts of clusters with (top) fixed $R_{c,ICM} = 13.4$ kpc and varying $\rho_{0,ICM}$: 0.25, 0.5, 1, 2, and 4 x 4 10^{-3} cm^{-3} (from top to bottom); and (bottom) fixed $\rho_{0,ICM} = 4\ 10^{-3}$ cm^{-3} and varying $R_{c,ICM}$: 0.25, 0.5, 1, 2, and 4 x 13.4 kpc (from top to bottom). Re-accretion of the stripped ISM is observable.

the central density, i.e. following a column, the stripping of the outer disk layers begins for wider clusters at earlier times, since a value of the ICM density that is sufficient to affect the outer ISM shifts to higher distances from the cluster center. Thus, the minimum of the ISM mass within the evaluation zone broadens.

Fig. 5.9 summarizes the results displayed in Fig. 5.8. In the first row, which corresponds to the central row of Fig. 5.8, the evolution of the ISM mass bound to the galaxy (left) or staying within $r < 16$ kpc and $|z| < 1$ kpc layer about the disk plane (right) is displayed for passages through the central parts of clusters with $R_{c,ICM} = 13.4$ kpc and $\rho_{0,ICM} = 0.25$, 0.5, 1, 2, 4 x 4 10^{-3} cm^{-3}. The second row corresponds to the central column of Fig. 5.8 with $\rho_{0,ICM} = 4\ 10^{-3}$ cm^{-3} and $R_{c,ICM} = 0.25$, 0.5, 1, 2, 4 x 13.4 kpc. From this comparison clearly follows a general trend that galaxies flying through wider and higher ICM density peaks lose a growing amount of the ISM, and in addition the reaccretion weakens. Further, the stripping of the ISM from outer disk radii begins within a close time span in clusters with varying central densities but constant widths, while it occurs much earlier in wide than narrow clusters with constant central densities. It corresponds firstly to the fact that galaxies fall faster towards the center in wide clusters where the amount of the gravitating ICM is higher, and secondly to a larger extent of higher densities of the ICM in wide clusters (cf. Fig. 3.9)

In Figs. 5.8 and 5.9 one notes that the wider and/or higher is the ICM density peak, the steeper is the fall of the disk's ISM mass. Having in mind our initial configuration of the ICM particles that are spread only within the central 140 kpc, one guesses that the stripping would start earlier than displayed if the ICM would range to larger distances from the cluster center. As will be discussed in more detail in Chapter 8, this artificial cut-off causes a slightly underestimated stripping results from large clusters but the difference is not important.

Tab. 5.1 summarizes the stripping results of the 25 simulation runs. As stripping results we read the following quantities: the stripping radius R_{strip} of the ISM disk, the final mass of the ISM staying bound to the galaxy M_{final}, the mass of the stripped ISM M_{strip}, the minimum ISM mass within the evaluation zone M_{min} occurring in the cluster center, the mass of the reaccreted material M_{accr}. The data are further completed with values of the maximum ram pressure p_{ram}^{max} occurring

$R_{c,ICM}$ (kpc)	$\rho_{0,ICM}$ (10^{-3} cm^{-3})	r_{strip} (kpc)	M_{final} (%)	M_{strip} (%)	M_{min} (%)	M_{accr} (%)	p_{ram}^{max} (km^2/s^2/cm^3)	Σ_{ICM} (M$_\odot$/pc^2)
3.4	1	13.8	99.2	0.8	84.0	15.2	1 612	0.397
	2	12.8	98.0	2.0	77.7	20.3	3 231	0.793
	4	11.8	95.0	5.0	70.0	25.0	6 453	1.587
	8	10.3	88.3	11.7	59.0	29.3	12 949	3.173
	16	7.5	78.3	21.7	48.0	30.3	25 900	**6.347**
6.7	1	12.3	96.8	3.2	75.0	21.8	1 615	0.778
	2	11.2	93.2	6.8	67.5	25.7	3 233	1.556
	4	8.7	85.5	14.5	57.2	28.3	6 480	3.113
	8	7.1	74.0	26.0	47.0	27.0	13 014	**6.225**
	16	4.5	59.4	40.6	36.0	23.4	26 229	12.450
13.4	1	10.8	91.2	8.8	68.2	23.0	1 618	1.513
	2	8.4	83.9	16.1	59.0	24.9	3 245	3.027
	4	6.3	70.5	29.5	48.7	21.8	6 524	**6.054**
	8	4.1	57.1	42.9	40.0	17.1	13 182	12.107
	16	2.6	37.3	62.7	29.2	8.1	26 894	24.214
26.8	1	8.8	83.7	16.3	64.0	19.7	1 625	2.905
	2	7.0	72.6	27.4	54.7	17.9	3 272	**5.811**
	4	5.0	56.3	43.7	43.5	12.8	6 631	11.622
	8	2.8	37.6	62.4	31.2	6.4	13 608	23.243
	16	2.5	19.8	80.2	19.8	0.0	28 604	46.486
53.6	1	7.7	73.8	26.2	59.0	14.8	1 641	**5.468**
	2	5.0	57.7	42.3	46.5	11.2	3 336	10.936
	4	3.5	40.8	59.2	38.0	2.8	6 888	21.871
	8	2.9	23.5	76.5	23.5	0.0	14 637	43.742
	16	2.4	14.8	85.2	14.8	0.0	32 722	87.484

Table 5.1: Summary of stripping results of the set of twenty-five simulations from Fig. 5.8. Stripping radius r_{strip} of the ISM disk, final mass of the ISM bound to the galaxy M_{final}, mass of the stripped ISM M_{strip}, minimum mass of the ISM within the evaluation zone, and reaccreted ISM mass M_{accr} are stated. $M_{strip}+ M_{min}+ M_{accre} = 100$ %.

on the orbits in the cluster center, and the column density Σ_{ICM} of the ICM encountered by galaxies during their flights through clusters. The amount of the reaccreted material corresponds to the difference between the ISM minimum disk mass in the cluster center and the final mass, i.e. to the amount of the ISM that falls back to the evaluation zone after the stripping maximum.

In a small (low and narrow) cluster, poor in the ICM, where $\rho_{0,ICM} = 10^{-3}$ cm^{-3}, and $R_{c,ICM} = 3.4$ kpc, strip the LM type model galaxy of less than 1 % of its ISM only. On the other hand, a large (high and wide) cluster with a lot of ICM, where $\rho_{0,ICM} = 1.6\ 10^{-2}$ cm^{-3}, and $R_{c,ICM} = 53.6$ kpc, the stripping of about 85 % of the ISM is achieved. If the pulse of the ram pressure is high enough, like in the case with $R_{c,ICM} = 3.4$ kpc, and $\rho_{0,ICM} = 1.6\ 10^{-2}$ cm^{-3}, about 52 % of the ISM particles move out of the evaluation zone $|z| < 1$ kpc. But more than half of them, $\sim$ 30 % of the original ISM mass, remains gravitationally bound. This means that a certain fraction returns to the $|z| < 1$ kpc zone later. It may be seen in Fig. 5.8 as a deep notch with the deepest notch at $T \sim 1.65$ Gyr. On the other hand, if the peak is not so high, as seen in the case of $R_{c,ICM} = 3.4$ kpc, and $\rho_{0,ICM} = 10^{-3}$ cm^{-3}, most of the ISM particles stay in the evaluation zone. Only about 12 % of them have been shifted out of it due to the ram pressure pulse, but almost all of them stay gravitationally bound to the galaxy. The wiggles seen in Fig. 5.8 reflect oscillations of the reaccreting ISM about the disk plane. Broad clusters with $R_{c,ICM} = 54.6$ kpc are not only much more effective in removing the ISM outside the evaluation zone, but the more extended ram pressure pulses in their cases are also able to accelerate the ISM and release it from the galaxy.

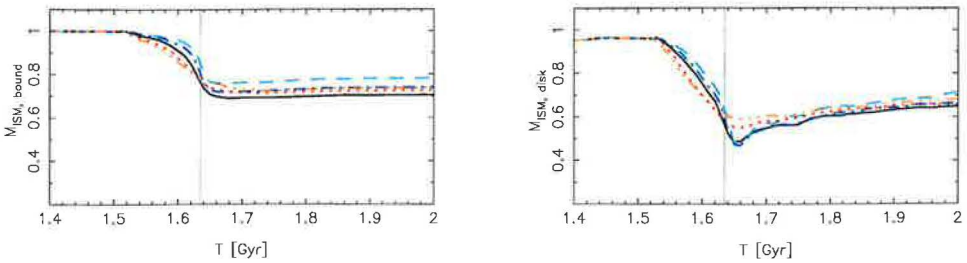

Figure 5.10: Evolution of the ISM mass bound to the galaxy (left) or staying within $r < 1$ kpc and $|z| < 1$ kpc layer about the disk plane (right) during the passage of the galaxy through central parts of clusters with the following combinations of the $(R_{c,ICM}, \rho_{0,ICM})$ parameter pair: (3.4,16) – dashed, (6.7,8) – dot-dashed, (13.4,4) – full, (26.8,2) – dotted, and (53.6,1) – dot-dot-dashed in [kpc,10^{-3} cm^{-3}] units. Such combinations lead to a similar value of the encountered ICM column density ~ 6 M$_\odot$/pc^2. Vertical line indicates the instant of the galaxy's passage through the center of cluster with $R_{c,ICM} = 13.4$ kpc, $\rho_{0,ICM}$ 4 10^{-3} cm^{-3}.

5.2.1 Comparison with the criterion of Gunn & Gott

When we focus in Tab. 5.1 on values of the column density of the ICM encountered by the galaxy during its crossing of different clusters, we note that clusters with e.g. the combinations (3.4, 16), (6.7, 8), (13.4, 4), (26.8, 2), and (53.6, 1) of the $(R_{c,ICM}, \rho_{0,ICM})$ parameter pair with units (kpc, 10^{-3} cm^{-3}), have a similar value of the $\Sigma_{ICM} \sim 6$ M$_\odot$/pc^2. It is caused by the shape of the ICM density profile modelled with the β-profile. When the galaxy encounters a similar amount of the ICM, does it mean that the stripping results will be similar, as well, no matter if the peak is low and wide or high and narrow? As shown in Fig. 5.10, both the final masses and the ISM masses enclosed within the evaluation zone are similar. However, the stripping history differs: in the case of a narrow and high cluster, there is a lot of ISM mass shifted out of the $|z| < 1$ kpc zone, which is reaccreted later ($M_{accr} \sim 30$ % in 3.4 kpc, 1.6 10^{-2} cm^{-3} case). In the case of a wide and low cluster, much more particles remain near the galaxy symmetry plane ($M_{accr} \sim 15$ % in 53.6 kpc, 1 10^{-3} cm^{-3} case). The two extreme cases substantially differ in the value of the peak ram pressure, almost of a factor 16. Gunn & Gott (1972) criterion

$$p_{ram} > \left|\frac{\partial \Phi}{\partial z}\right|_{max} \Sigma_{ISM}, \tag{5.1}$$

comparing the peak ram pressure $p_{ram} = \rho_{0,ICM} v^2_{max}$ with the restoring force would predict a completely different amount of stripping in these two cases. However, as we shall argue later, the final stripping depends on column density of the encountered ICM, which is similar in both the discussed cases.

Stripping radii r_{strip} and final masses M_{final} resulting from the set of twenty-five simulations are depicted in Fig. 5.11. Signs of different types correspond to groups with a fixed value of the $R_{c,ICM}$ parameter: 3.4 kpc – pluses, 6.8 kpc – open circles, 13.4 kpc – full circles, 26.8 kpc – open squares, and 53.6 kpc – crosses. The R_{strip} and M_{strip} are shown as functions of the peak ram pressure p_{ram} occurring in the cluster centers and makes clearly visible indications of Fig. 5.8: the amount of stripping strongly depends on the $R_{c,ICM}$ parameter. Such a dependence is completely missing in Gunn & Gott (1972) criterion which gives a single curve for all values of the $R_{c,ICM}$ (black).

For lower values of the central density, Gunn & Gott (1972) determines a stronger stripping than indicate simulations with any of the used values of the $R_{c,ICM}$ parameter, while for densities $\gtrsim 10^4$ cm^{-3}(km/s)^2 it overlaps with results of $R_{c,ICM} = 53.6$ kpc or 26.8 kpc. As will be discussed in the next chapter, Gunn & Gott (1972) criterion that takes into account only the peak value of the ram pressure, should constitute stripping limits to which should converge the results from large ICM distributions in which the maximum amount of the ISM is stripped since the operation of the ram pressure is approximately constant.

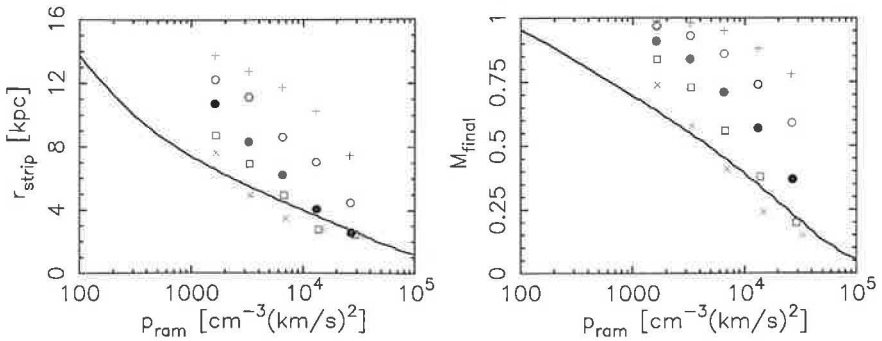

Figure 5.11: Comparison of stripping radii r_{strip} (left) and final ISM masses M_{final} (right) resulting from twenty-five simulation runs described above with predictions of Gunn & Gott (1972) – black. Signs of different types correspond to groups with a fixed value of the $R_{c,ICM}$ parameter: 3.4 kpc – pluses, 6.8 kpc – open circles, 13.4 kpc – full circles, 26.8 kpc – open squares, and 53.6 kpc – crosses. The r_{strip} and M_{final} are shown as functions of the peak ram pressure occurring when galaxies pass the cluster center.

Fig. 5.12 shows the dependence of the R_{strip} and M_{final} on the extent of the ICM distribution in the cluster. For increasing $R_{c,ICM}$ the degree of stripping becomes less and less dependent on the width of the ICM distribution, that is characterized by the $R_{c,ICM}$ parameter itself, and approaches a constant, which depends on the value of $\rho_{0,ICM}$. This depends on whether or not the ISM is accelerated during the ram pressure pulse to the escape velocity. The critical size of the active region ΔR_c is $\Delta R_c = v_{esc}\, v\, \Sigma_{\rm ISM}/p_{\rm ram}^{\rm eff}$, where $p_{\rm ram}^{\rm eff}$ is an effective value of the ram pressure. Here we take $p_{\rm ram}^{\rm eff} = p_{\rm ram}^{\rm max}/2$. With $\Sigma_{\rm ISM} = 10^{21}$ cm^{-2}, $v_{\rm esc} = 400$ km s^{-1}, $p_{ram}^{\rm max} = 6000$ cm^{-3} km^2 s^{-2} and $v = 130$ km s^{-1} we get $\Delta R_c \approx 60$ kpc. This nicely corresponds to $R_{\rm c,ISM} = \Delta R_c/2 = 30$ kpc (see Fig. 5.12), where $M_{\rm final}$ loses its dependence on $R_{\rm c,ISM}$ and converges to Gunn & Gott (1972) prediction given with Eqn. 5.1. Thus, our results give much less stripping compared to Gunn & Gott (1972) in clusters with a narrow ICM peak, while converge to its predictions in extended ICM clusters (see Fig. 5.11).

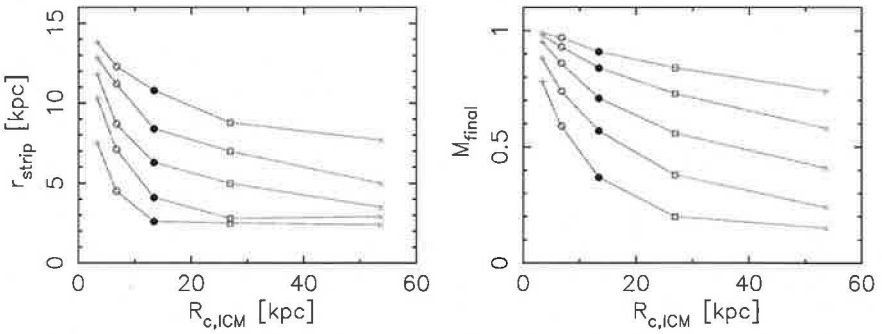

Figure 5.12: Stripping radii (left) and final ISM masses (right) as a function of $R_{c,ICM}$ for the LM-type galaxy. The lines correspond to different values of the $\rho_{0,ICM} = 0.25$, 0.5, 1, 2, and 4 x 4 10^{-3} cm^{-3} (from top down).

5.3 Stripping of galaxies of various types

In the following section, we show the stripping results of various galaxy-types, that were introduced in Chapter 3: LM, Lm, EM, and Em. The models mimic late-type (L) or early-type (E), and massive (M) and mow-mass (m) spiral galaxies. L-types have a massive disk compared to E-types with low mass disks, M-types have a massive halo compared to m-types with low-mass halo. The values of the model parameters are given in Tab. 3.1.

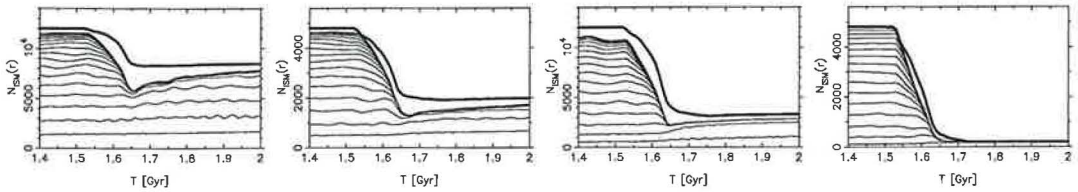

Figure 5.13: Evolution of the stripping in the LM, Lm, EM, and Em galaxy types (from left to right) during their flight through central parts of the standard cluster $R_{c,ICM} = 13.4$ kpc and $\rho_{0,ICM} = 4\ 10^{-3}$ cm^{-3}.

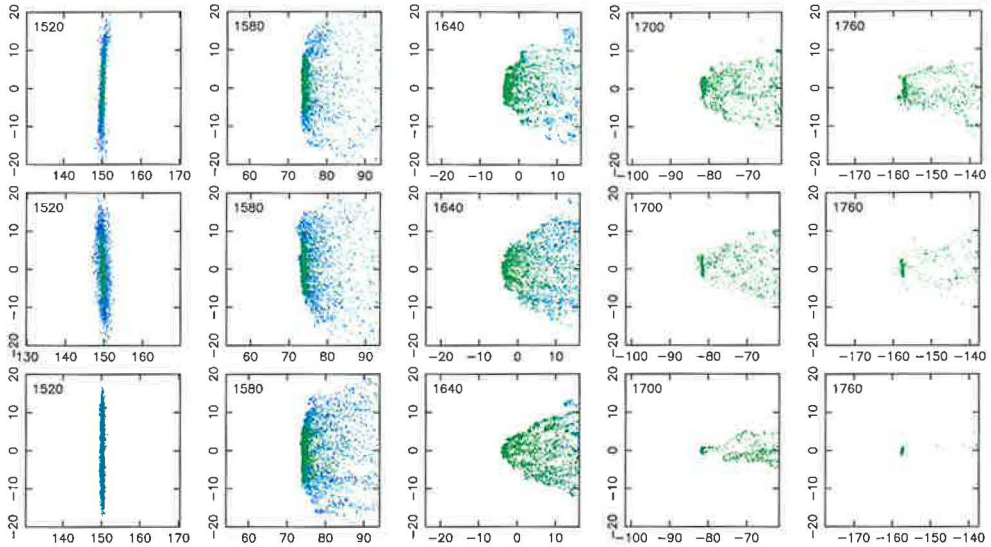

Figure 5.14: Snapshots of the Lm, EM, and Em galaxies flying through central parts of the standard cluster.

A comparison of the models LM, Lm, EM, and Em in a standard cluster with $\rho_{0,ICM} = 4\ 10^{-3}$ cm^{-3} and $R_{c,ICM} = 13.4$ kpc is shown in Fig. 5.14. Again, evolution of the mass of the ISM contained within $|z| < 1$ kpc layer about the disk plane and sixteen radii from 1 kpc, with a step of 1 kpc, together with the mass of the ISM that is bound to the galaxy, are displayed. The LM-type galaxy has a stripping radius of about 6 kpc, and loses about 29 % of its original ISM. For Lm, and EM-types the stripping radii move closer to the galaxy center to about 3.9 kpc, and 2.9 kpc, respectively. The Em-type galaxy is stripped almost completely. As summarized in Tab. 5.2, the LM, Lm, EM, and Em galaxy types lose during the face-on motion through the cluster with standard ICM distribution about 29 %, 59 %, 69 %, and 96 % of its original ISM.

When comparing the profiles of the maximum restoring force as a function of galactic radius in Fig. 3.2, one notes that except the innermost radii, the maximum restoring force is larger for the EM galaxy comparing to the Lm type, however in the range of radii about (1 – 4) kpc, the maxima are almost equal. Further, as displayed in Fig. 3.2, the surface density of the ISM is lower in the EM type than in the Lm galaxy, and the escape velocity is in the EM galaxy on the contrary higher, due to its higher mass. Therefore, one would expect that the amount of stripping would be higher in the case of the EM galaxy. As we shall see in the next chapter, neither the combination of a lower escape velocity and higher Σ_{ISM} in the Lm type explain its less stripping compared to the EM.

As is observable in Fig. 3.5, the maxima of the restoring force over z-direction occur substantially closer to the disk plane in the case of Lm galaxy, especially at lower galactic radii, while, as stated above, the values of the maxima are similar. Therefore, the rise of the restoring force behind the disk is much steeper in the Lm galaxy than in the EM model. Both the galaxies fly

Gal. type	R_{strip} (kpc)	M_{strip} (%)	M_{min} (%)	M_{accr} (%)
LM	6.3	29	49	22
Lm	3.9	59	27	14
EM	2.9	73	18	9
Em	0.2	96	4	0

Table 5.2: Stripping results of the Lm, EM, and Em galaxy types after their flights through the standard cluster with $R_{c,ICM} = 13.4$ kpc and $\rho_{0,ICM} = 4\ 10^{-3}$ cm^{-3}. Values of the stripping radius R_{strip}, and stripping mass M_{strip}, together with the minimum amount of the ISM enclosed in the disk M_{min}, and the mass of the reaccreted ISM M_{accr}, are stated.

through a narrow cluster with $R_{c,ICM} = 13.4$ kpc. Consequently, ISM elements of the Lm galaxy are by the short ICM wind gust shifted only "slowly" out of the disk, and therefore less of them is accelerated to the escape velocity. On the contrary, ISM elements of the EM galaxy are by the ram pressure more easily shifted to higher z's which means that they are accelerated during a longer time and thus more of them reach the escape velocity.

A further explanation of the stripping results of the Lm versus EM galaxies can follow from hydrodynamical effects: the higher density of the ISM can lead to creation of a larger and stronger bow shock, better protecting the ISM against the incoming ICM, that is more effectively deflected to the sides, causing the ISM in the Lm galaxy gets less ICM momenta compared to the EM.

Fig. 5.14 displays five snapshots of the Lm, EM, and Em galaxies during their crossing the central parts of the standard cluster. A noticeably higher amount of the reaccreting particles is observable at time $T = 1.76$ in the case of the Lm galaxy, compared to the EM galaxy. The ISM disk of the EM–type galaxy is due to its higher bulge-to-disk mass ratio remarkably thicker than that of the Lm–type. This brings another possible explanation of the more effective stripping of the EM galaxy: its thicker disk is more vulnerable to the ram pressure.

5.4 A comparison to existing simulations

Abadi et al. (1999)

Using a 3D SPH/N-body simulation code, Abadi et al. (1999) study the stripping of spiral galaxies by operation of a constant flow of ICM wind in a simulation box of size 60 kpc × 60 kpc × 10 kpc homogeneously filled up with the ICM particles flowing with periodic boundary conditions. Their model is a spiral galaxy with a spherical Plummer bulge, a non-spherical halo, and exponential stellar and gaseous disks. The masses of respective components are: 1.7, 21.3, 4.5, and 1.1 x 10^{10} $M_\odot$; the characteristic scale lengths are $a_d = 3.5$ kpc, $z_0 = 0.35$ kpc for both the stellar and gaseous disk, $a_b = 0.5$ kpc, and $a_h = 24.5$ kpc, $b_h = 3.5$ kpc. The corresponding rotation curve is flat with rotation velocity at 16 kpc of about 215 km s^{-1}. The galaxy receives the wind of 1000 km s^{-1}, 2000 km s^{-1}, or 3000 km s^{-1} of two various densities: $\rho_c = 3.37\ 10^{-3}$ cm^{-3}, and $\rho_v = 0.1\rho_c$, corresponding to the central densities of the Coma and Virgo cluster, respectively. The ram pressure then ranges from about 300 to 30 000 cm^{-3}km^{2}s^{-2}.

Abadi et al. (1999) state that the analytic Gunn & Gott criterion provides a good approximation to their stripping results. However, they emphasize the importance of the potential contribution of the bulge at small radii to the restoring force. For the wind corresponding to the Coma-like cluster center, they estimate the stripping radius of a spiral galaxy to 4 kpc, i.e. to about 80 % loss of the galaxy's diffuse gas mass. They find the time-scale of the stripping to be only a fraction of the crossing time, $\sim$ 100 Myr. They estimate that galaxies orbiting through poorer clusters, or with inclined disk, lose significantly less gas. They conclude that the ram pressure alone is insufficient to account for the rapid and widespread truncation of star formation observed in cluster galaxies, or the morphological transformation of Sab galaxies to S0 types.

Although Abadi et al. (1999) use a similar numerical approach as we do, the main difference

compared to present simulations is that their ram pressure is constant over time and is treated with a periodic boundary condition.

Quilis et al. (2000)

In their simulations employing a high resolution 3D Eulerian code with a fixed grid based on high-resolution shock-capturing method, Quillis et al (2000) follow the interaction between the hot ICM and the cold ISM. The stellar and DM components are evolved using a particle-mesh code. They model a luminous spiral galaxy similar to the Milky Way or Andromeda galaxy with the rotational velocity of the disk ~ 220 km s^{-1}. The galaxy has a spherical bulge, a non-spherical DM halo, and exponential stellar and gas disks. The characteristic scales are the same as in Abadi et al. (1999). The total masses of the bulge, halo, stellar and gas disk components are: 1.7, 26.5, 5.6, and 0.5 $\times$ 10^{10} M$_\odot$. The diffuse ISM disk has temperature $T_{\rm ISM} = 10^4$ K. The ICM is modelled as a uniform medium with temperature $T_{\rm ICM} = 10^8$ K and constant densities $\rho_c = 2.6\ 10^{-3}$ cm^{-3}, and $\rho_v = 0.1\rho_c$. Both the ICM and ISM are treated adiabatically. The ISM disk is modelled as a) a uniform smooth disk, or b) as the previous disk but with a central hole of 2 kpc radius, or c) as an inhomogeneous disk with small holes of radii 300 pc and an increased density within central 5 kpc radius. The galaxy moves through the ICM wind at velocities of 1000 km s^{-1}, or 2000 km s^{-1}.

Only their run with the uniform disk crossing at $v = 2000$ km s^{-1} the ICM with $\rho_c = 2.6\ 10^{-3}$ cm^{-3} is comparable to our models. Quilis et al. (2000) estimate the stripping radius in this case to ~ 3 kpc. In the cases with a hole in the disk, the ISM is completely stripped.

Vollmer et al. (2001a)

Investigating the role of the ram pressure stripping in the Virgo cluster, Vollmer et al. (2001a) employ a method of sticky particles modelling the warm neutral clouds of the ISM. The effect of the ram pressure is included only analytically as an additional acceleration on the clouds located at the windward side of the gas distribution. Contrary to other simulations discussed in this section, they introduce temporal ram pressure profiles instead of a constant ICM wind.

Their model galaxy includes an analytical gravitational potential of a spherical halo and bulge, and a Miyamoto-Nagai disk. The total masses of the respective components are 8.6, 0.56, and 2.6 x 10^{10} M$_\odot$. The characteristic scales are $a_h = 12$ kpc, $a_b = 0.4$ kpc, and $a_d = 2.7$ kpc and $z_0 = 0.25$ kpc. It corresponds to a constant rotation curve of about 140 km s^{-1}.

Vollmer et al. (2001a) use the same β-model of the DM and ICM distribution as in present simulations but with ten times higher central density $\rho_{0,\rm ICM} = 4\ 10^{-2}$ cm^{-3}. Their model galaxy moves through the cluster on slightly elliptical orbits with the closest approach to the cluster center in the range of (70 – 200) kpc. Thus, the galaxy does not traverse directly through the cluster center. Then the maximum encountered ICM density $\rho_{\rm ICM} < \rho_{0,\rm ICM}$, and since the ICM distribution is narrow with $R_{\rm c,ICM} = 13.4$ kpc, the fall-off of the density when receding from the center is steep: at the distance $R = R_{\rm c,ICM}$, it equals to $\rho_{\rm ICM} \sim 0.6\rho_{0,\rm ICM}$, and at $R = 2R_{\rm c,ICM}$ it drops to $\rho_{\rm ICM} \sim 0.3\rho_{0,\rm ICM}$.

Another effect of the non-central passages through an ICM peak is that the galaxy effectively encounters a wider than $R_{\rm c,ICM}$ ICM peak. Fig. 5.15 shows vertical slices of the ICM density profile at five distances from the cluster center: 20, 40, 60, 80, and 100 kpc (black curves). For comparison, profiles with the same peak values of the $\rho_{\rm ICM}$ but corresponding to completely radial orbits through ICM distribution with the original value of the width: $R_{\rm c,ICM} = 13.4$ kpc (red curves) are displayed. One notes that the slices are much wider than the profiles of completely radial orbits.

The analytically modelled peaks of the ram pressure reach in their simulations maximum values ranging from 1 000 to 10 000 cm^{-3} km^2 s^{-2} corresponding to several simulations with different orbital parameters. Vollmer et al. (2001a) show that in some cases a strong reaccretion of the atomic gas occurs after the stripping event. Comparing the HI observations and the results of their simulations, they show that the HI deficiency depends strongly on the shape of galaxy orbit. They conclude that the ram pressure stripping scenario may be consistent with all HI 21 cm observations in the Virgo Cluster.

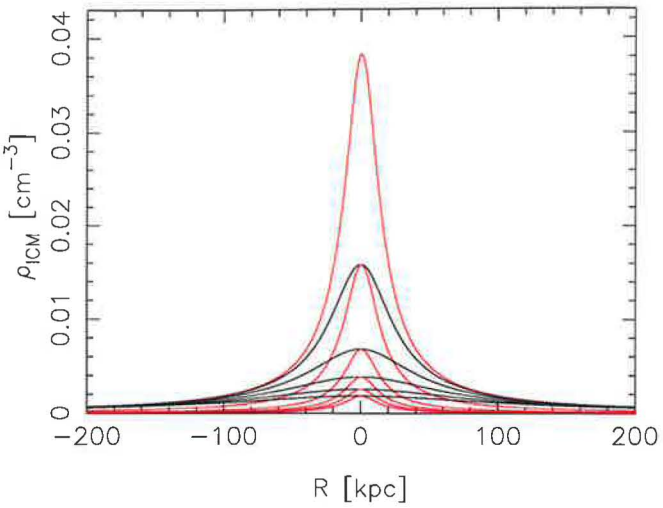

Figure 5.15: Vertical slices through the ICM density peak with $R_{c,ICM} = 13.4$ kpc and $\rho_{0,ICM} = 4\ 10^{-2}$ cm^{-3} at five distances from the cluster center: 20, 40, 60, 80, and 100 kpc (black curves). Profiles with the same peak values of the ρ_{ICM} but corresponding to completely radial orbits through the ICM distribution with $R_{c,ICM} = 13.4$ kpc are plotted (red curves). The uppermost red curve covers the uppermost black curve.

By its impulse character, and time-dependent ram pressure profiles, the model of Vollmer et al. (2001a) is the model closest to ours. However, their model galaxy is much lighter than our LM–type, and as shown in Fig. 5.15, it moves through effectively wider clusters when compared to our simulations, and thus it better approaches to Gunn & Gott (1972) predictions. In addition, they use no hydrodynamical treatment in the simulations.

Schulz & Struck (2001)

Model dwarf galaxy in 3D HYDRA (SPH-AP^{3}M) simulations of Schulz & Struck (2001) is placed in a cubical grid with 100 kpc edge. The masses of individual components of the model galaxy are 8.7 10^9 M$_\odot$ for the disk, and 6 10^{10} M$_\odot$ for the dark matter in a spherical halo. The gas mass represents 50 % of the total disk mass. This corresponds to the total galaxy mass of 6.57 10^{10} M$_\odot$. The galaxy is surrounded with 80 000 uniformly distributed ICM particles. The temperature of the ICM is $T_{ICM} = 4.6\ 10^5$ K, and the density of the wind is $\sim 7.3\ 10^{-5}$ cm^{-3}.

In their face-on models, the galaxy moves with a velocity of 1000 km s^{-1}, and 2000 km s^{-1}. Then, the stripping radii measured from their Figs. 2 and 14 are ~ 7.2 kpc and ~ 5.2 kpc.

Roediger & Hensler (2005)

By varying galaxy properties and using a large range of ICM conditions, Roediger & Hensler (2005) perform a parameter study of the ram pressure stripping of face-on disk galaxies, using a 2D Eulerian simulations. They introduce two galaxy models with exponential stellar and gaseous disks, and spherical bulge and halo. They differ in the total mass: a) a massive model with $M_* = 8\ 10^{10}$, and $M_{gas} = 8\ 10^9$ M$_\odot$, $M_b = 2\ 10^{10}$ M$_\odot$, and $M_h(40kpc) = 2.8\ 10^{11}$ M$_\odot$, and b) a medium model with $M_* = 3\ 10^{10}$, and $M_{gas} = 3\ 10^9$ M$_\odot$, $M_b = 8\ 10^9$ M$_\odot$, and $M_h(40kpc) = 1.8\ 10^{11}$ M$_\odot$. The scaling radii are a) $a_* = 4$ kpc, $b_* = 0.25$ kpc, $a_{gas} = 7$ kpc, $b_{gas} = 0.4$ kpc, $a_b = 0.4$ kpc, and $a_h = 23$ kpc, and b) $a_* = 3$ kpc, $b_* = 0.25$ kpc, $a_{gas} = 7$ kpc, $b_{gas} = 0.4$ kpc, $a_b = 0.15$ kpc, and $a_h = 15$ kpc. Except the gaseous disk, all components are treated analytically, providing only the gravitational potential. The ICM densities range in their simulations from 10^{-5} to 10^{-3} cm^{-3}, and the resulting ram pressure covers a range from 10 to 10 000 cm^{-3}km^{2}s^{-2}. Roediger & Hensler (2005) conclude that gas disks of galaxies in high density environments can be heavily truncated or even completely stripped.

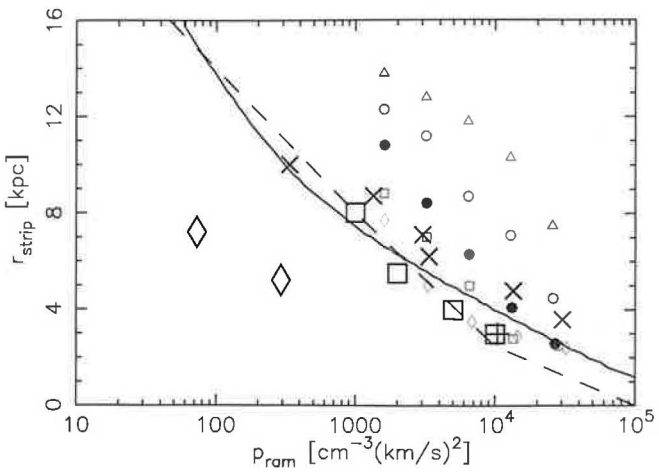

Figure 5.16: The r_{strip} versus the peak ram pressure p_{ram}^{max}: a comparison with simulations by Abadi et al. (1999) – large X, Quilis et al. (2000) – large plus, Vollmer et al. (2001a) – large squares, Schulz & Struck (2001) – large diamonds, models of Roediger & Hensler (2005) – dashed line. Our simulations: $R_{c,ICM}$ = 3.4 kpc – triangles; 6.7 kpc – circles; 13.4 kpc – filled circles; 26.8 kpc – squares; 53.6 kpc – diamonds. Solid line shows the prediction using Gunn & Gott (1972) formula. In the case of Roediger & Hensler (2005) we display results corresponding to their massive galaxy model.

5.4.1 Summary

The above different simulations are listed in Tab. 5.3 and a comparison is shown in Fig. 5.16. All the models shown, except Schulz & Struck (2001), use comparable spiral galaxy models, the galaxy of Vollmer et al. (2001a) has rotation velocity of only 140 km s^{-1} compared to 250 km s^{-1} of our LM–type galaxy. Abadi et al. (1999), Quilis et al. (2000) and Roediger & Hensler (2005) show high stripping efficiency close to the Gunn & Gott (1972) prediction, which is due to a constant ICM density adopted. There is no difference in the stripping radius and M_{final} from 2D and 3D hydrodynamical simulations and SPH. It seems that the global stripping effect on the galaxy does not depend on the details of the hydrodynamical approach.

Author	Method	ICM flow	galaxy
Abadi	SPH	constant	spiral
Quilis	3D finite diff.	constant	spiral
Vollmer	sticky particle	changing	spiral
Schulz	SHP	constant	dwarf
Roediger	2D finite diff.	constant	spiral
Jáchym	SPH	changing	spiral

Table 5.3: The list of compared simulations.

The results of Schulz & Struck (2001) show the same stripping efficiency at lower ram pressures (see Fig. 5.16), which is, in accordance to Gunn & Gott (1972), due to lower disk restoring force in the case of dwarf galaxies.

Our models with small values of $R_{c,ICM}$ show less stripping. This is mainly due to the effect of changing strength and finite duration of the ram pressure peak. For large values of $R_{c,ICM}$ in large clusters with long interaction times our models approach the Gunn & Gott (1972) prediction and results of other models. It demonstrates that our SPH approach gives similar results to SPH simulations of others and to 2D and 3D Eulerian codes.

Simulations by Vollmer et al. (2001a) use the changing ram pressure force acting on sticky particles showing results close to Gunn & Gott (1972) prediction. However, with a similar dependence of the ram pressure on time, we get less stripping. However, their galaxy is less massive compared

to our LM–type and its interaction region with the ICM is effectively wider in the above discussed sense. Simulations with sticky particles thus may overestimate the stripping efficiency, since this kind of simulations disregards such hydrodynamical effects as formation of the bow shock in the ICM in front of the galaxy. It actually shields the galaxy reducing the efficiency of stripping.

Chapter 6

Ram pressure stripping

After we have tackled in the previous chapter the ram pressure stripping of the interstellar content of galaxies moving in galaxy clusters from the view of numerical simulations, we focus on the analytical problem in this chapter. We describe the dynamical processes that occur in galaxies interacting in the face-on configuration with the intracluster material and further the successive stripping of their interstellar material proceeding on the long-term time scales of their orbital motions. In existing papers, no attention is paid to the galactic orbital history that might influence results of the ICM-ISM interaction, and it is commonly thought that only the maximum value of the ram pressure occurring on a given orbit is the critical parameter for the stripping result. Our intention is to show that different galactic orbits produce unequal stripping, and we look for an analytic approach determining overall stripping results based on parameters of the cluster, galaxy, and orbit.

6.1 Classical Gunn & Gott's approach

In existing literature dealing with the environmental effects of galaxy clusters on the interstellar material of member galaxies, Gunn & Gott (1972) criterion is generally used to determine stripping results. Gunn & Gott (1972) estimated for the first time what part of the ISM could be stripped out of a typical spiral galaxy during its flight through an intracluster medium of density $\geq 5\ 10^{-4}$ cm^{-3}. They assumed that the interstellar material is held in the disk plane by a force per unit area

$$F_{rest} = 2\pi G\, \Sigma_* \Sigma_{\mathrm{ISM}}, \tag{6.1}$$

where Σ_* is the star surface density and Σ_{ISM} the gas surface density on the disk of the galaxy. According to this criterion, a disk element is stripped out of the disk when its restoring gravitational force is exceeded by the ram pressure of the incident intracluster medium:

$$p_{ram} > F_{rest}. \tag{6.2}$$

In the following text, we adopt the notation Gunn & Gott (1972) for the above criterion with the restoring force in the original form (6.2). The criterion has two following limitations: firstly, the restoring force in the form (6.1) takes into account only a contribution of the disk galactic component, and secondly, the face-on orientation of the disk with respect to the ICM wind direction is assumed.

The restoring force acting on the disk elements located at different galactic radii differs due to the internal distribution of the mass in the galaxy and is stronger for elements at lower radii. Therefore, a given level of the ram pressure can remove elements downwards to some minimum radius at which it is balanced by the restoring force. The stronger is the ram pressure, the lower is this stripping radius. Following that logic, it should be the maximum value of the ram pressure

occurring on a galactic orbit that is crucial for the stripping extent. For radial orbits, the maximum ram pressure occurs in the cluster center regions determining thus, from the view of Gunn & Gott (1972), the final stripping radius of the galaxy.

Therefore, Gunn & Gott (1972) criterion for a given galaxy-cluster configuration depends only on the maximum value of the ram pressure and the maximum values of the restoring force of individual disk elements. However, it does not take into consideration the shape of the galaxy's orbit through the cluster, i.e. its orbital history. It only picks the moment of the maximum ram pressure and denotes the supposed stripping radius. By using this criterion, one could obtain identical results for two galaxies moving on totally different orbits but with incidentally the same value of the maximum ram pressure. Such a situation is possible since besides the ICM density, the ram pressure is a function of the galactic orbital velocity. Then a suitable combination of the two quantities can lead to coincident values of the ram pressure. More precisely, the approach of Gunn & Gott (1972) would provide the same results for galaxies spending different times to pass through the peak of the ICM density.

Although Gunn & Gott (1972) assumed only a contribution of the disk to the restoring force (6.1), effect of all the galactic components have to be taken into account (Abadi et al. 1999, and others). The restoring force per unit area in the direction of the ICM wind is then

$$f_{rest}(z,r) = \frac{\partial \Phi}{\partial z}(z,r)\Sigma_{\rm ISM}(r), \tag{6.3}$$

where z notes the direction perpendicular to the disk plane, coinciding with the ICM wind direction, and Φ is the galactic potential. As was shown in Chapter 3, the restoring force is a function of the vertical distance z behind the disk plane. Fujita (1999) and others expand the restoring force in the following way:

$$F_{rest} = 2\pi G\,\Sigma_*\Sigma_{\rm ISM} = v_{rot}^2 R^{-1}\Sigma_{\rm ISM}, \tag{6.4}$$

where the rotational velocity v_{rot} of the galaxy takes into account the contribution of all galaxy components, including the halo and bulge.

A modified version of Gunn & Gott (1972) criterion employing formula (6.3) for the restoring force is then

$$p_{ram} > \left|\frac{\partial \Phi}{\partial z}\right|_{\rm max}\Sigma_{\rm ISM}, \tag{6.5}$$

where at every disk radius the maximum value of the gravitational force occurring behind the disk plane is assumed. We adopt the notation "Gunn & Gott's criterion" for (6.5).

6.2 ISM versus ICM interaction

In the following text, let us focus on a galaxy in the face-on configuration freely falling from an initial distance R_{init} towards the center of a galaxy cluster filled with the intracluster material distributed with a β-profile (3.18). These initial conditions are described in Section 3.3. The galaxy starting at the cluster periphery initially moves through a tenuous medium. As it accelerates towards the center, an external ram force $F_{ram} = \Delta A\, p_{ram}$ of the oncoming ICM starts to act on an ISM disk element with surface ΔA located at a galactocentric radius r of the face-on disk. During the orbit, the galaxy encounters an increasing amount of the ICM. Here we neglect hydrodynamical effects like formation of the bow shock in front of the disk, which was observed in simulation results in the previous chapter.

Due to symmetry, the restoring force is zero in the disk plane (see Fig. 3.3) and the rising ram force shifts the element out of it. The element is in every moment pushed to such a distance z where the local restoring force is balanced by the actual ram pressure. Rate of this process of shifting to higher z's depends on the change of the ram pressure with the orbital time, i.e. on the time derivative of the ram pressure $\dot{p}_{ram}$. This derivative competes with the gradient of the restoring force in the z direction, $\nabla_z f_{rest}$.

If we assumed that the element accumulated the incoming ICM, the restoring force would, on top of the fact that it changes as the element shifts in z, evolve due to the mass accumulation and it would stop to correspond to Fig. 3.3. The restoring force would then become a function of time

$$\begin{aligned} f_{rest}(z,t) &= \frac{\partial \Phi}{\partial z}\left[\Sigma_{\rm ICM}(t) + \Sigma_{\rm ISM}\right] \\ &= f_{rest}(z)\left(\frac{\Sigma_{\rm ICM}}{\Sigma_{\rm ISM}} + 1\right). \end{aligned} \tag{6.6}$$

However, as noted e.g. by Abadi et al. (1999) and as is visible in present simulations, the ICM does not accumulate on the ISM disk but is rather deflected along the bow shock formed in front of the disk, and flows around the galaxy. Therefore, we can maintain the idea of the time derivative of the ram pressure $\dot{p}_{ram}$ competing with the gradient of the restoring force $\nabla_z f_{rest}$, rather than with the time derivative of a time-varying restoring force $\dot{f}_{rest}$. But if we realize, that during the ISM-ICM interaction the ISM is swept out from the disk, the restoring force is a function of time, anyway. The change invoked by the stripping is however not important since the contribution of the ISM disk to the gravitational restoring force of the galaxy is small.

Of course, the steepness of the $\dot{p}_{ram}$ differs for galaxies moving in clusters with varying β-profile of the ICM distribution, which is caused by changing parameters $R_{c,ICM}$ and $\rho_{0,ICM}$ themselves, and by different orbital velocity of the galaxy corresponding to the altered gravitational effect of the cluster DM + ICM.

6.2.1 Wide clusters

To measure the width of a cluster and resolve whether it is wide or narrow, we can compare the $R_{c,\,ICM}$ parameter with some characteristic scale parameter of the galaxy. In the face-on case, such a parameter could be a "mean vertical distance" $\langle z \rangle$ behind the disk plane at which the restoring force is maximum. In the case of the LM model galaxy, maxima of the restoring force for elements at radii lower than 16 kpc are closer to the disk plane than about 15 kpc. Then, if the galaxy orbits through a cluster whose ICM density peak is much wider than $\langle z \rangle$, the ram pressure rises early after the galaxy sets out and the $\dot{p}_{ram}$ grows gradually along its orbital motion towards the cluster center. Since growth of both the galactic velocity and the ICM density is gradual, the element ΔA is deflected from the disk plane only slowly, all the time being kept in the maximum possible elongation of an imaginary gravitational spring drawing it back to the disk plane.

Then the ISM elements are pushed towards vertical distances z_{max} of the maximum restoring force corresponding to their galactic radius. The elements that reach this position during the entering phase of the orbit, can be released from the galaxy since still growing ram pressure easily surpasses their – at that time decreasing – restoring force. Then the stripping radius of the disk coincides with that radius at which elements get over their z_{max} position right at the moment of the cluster center passage. It means that all the "strip-able" elements, i.e. elements with maximum restoring force lower than the maximum ram pressure will be released, which in fact exactly corresponds to the Gunn & Gott's conception.

What would be the result, if we again assumed the accumulation of the ICM? The element ΔA accumulates in a time interval Δt a mass $\Delta A \Delta t \rho_{ICM}(t) v(t)$, while the value of the ram pressure changes with time as $\rho_{ICM}(t) v^2(t)$. Thus the effect of the growing mass depending on $v(t)$ which intensifies the bound to the galaxy is less important than that of the growing ram pressure depending on $v^2(t)$. The latter shifts the element to higher z's and endeavors to push it through the maximum value of the restoring force. Then, the element accumulating an increasing amount of the ICM has a chance to advance to higher vertical distances but more slowly and eventually to lower maximum elongations than if we neglected the accumulation. During the long flight through a wide ICM peak, the disk would accumulate a substantial amount of the ICM. This would cause the restoring force to stop to correspond to Fig. 3.3 and to become a function of time. Then, a simplest improvement of Gunn & Gott (1972) criterion would consist in taking into account the accumulation:

$$\rho_{ICM} v^2 > \left.\frac{\partial \Phi}{\partial z}\right|_{max} \left(\Sigma_{\rm ISM} + \Sigma_{\rm ICM}\right), \tag{6.7}$$

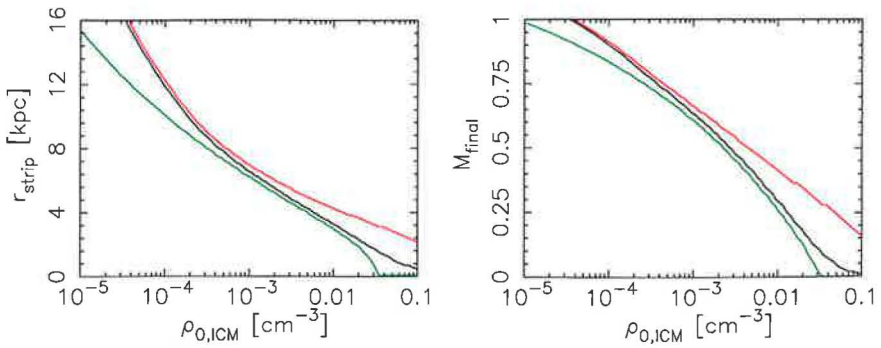

Figure 6.1: Stripping radius and final ISM mass as functions of the central ICM density, determined using the classical (black) and modified (red) Gunn & Gott's criterion (eqns. 6.5, and 6.7). Passage through cluster with $R_{c,ICM} = 53.6$ kpc is assumed. The original form of the criterion (6.2) completes the figure (green).

where the column density of the accumulated intracluster medium, Σ_{ICM}, should be added at the moment of the galaxy's passage through the cluster center.

Fig. 6.1 displays the stripping radius r_{strip} and the corresponding final mass M_{final} as functions of the central ICM density $\rho_{0,ICM}$ for the above mentioned galaxy falling towards the cluster center from 1 Mpc distance. The stripping radii and final masses are in Fig. 6.1 calculated using Gunn & Gott criterion in the original form (6.2) – green, the modified form including the restoring force of all the galaxy components (6.5) – black, and the above version (6.7) assuming the mass accumulation – red. It shows that the difference implied by the above modification would be important only for clusters with high central densities of the ICM where the galaxy encounters a large amount of the ICM. The comparison of (6.2) and (6.5) is interesting, showing that the former overestimates the stripping in clusters with low or high central densities. In Fig. 6.1, $R_{c,ICM} = 53.6$ kpc.

If the central cluster density $\rho_{0,ICM}$ is low, an element of the galaxy crossing a wide cluster slowly deflects from the disk plane only to low z's since the restoring force is too high. Then the element may not reach the position z_{max}, behind which the restoring force would decline, and after the cluster center passage it falls back to the disk plane. But if the central ICM density is substantially high, it is shifted upwards more easily and may win the fight with the growing restoring force and release from the galaxy.

What could be then a real scenario of evolution of the restoring force and its time derivative acting on a disk element during the plunge of the galaxy to a wide cluster? Initially, the $\dot{f}_{rest}$ follows the $\dot{p}_{ram}$ since the restoring force itself has close to the disk plane a steeply growing profile, and thus it controls the $\dot{p}_{ram}$ growth. Approaching the cluster center, the element is shifted near the z-distance of the maximum restoring force. $\dot{f}_{rest}$ starts to fall down, while the $\dot{p}_{ram}$ keeps growing. At the z_{max} position, $\dot{f}_{rest} = 0$ and the element easily continues to higher z's as it is accelerated by still high value of the ram pressure. Shortly behind the cluster center, the element is released.

Thus, in very wide clusters, the effect of the ram-pressure is nearly constant, which means that the classical Gunn & Gott's criterion should constitute an upper limit of the stripping efficiency. In other words, the long-lasting duration of the ram pressure effect in wide clusters can be simply represented as a sufficiency of time to really strip all elements that are "strip-able", i.e. all the elements whose maximum restoring force is inferior to the maximum ram pressure occurring in the cluster center. As implies Fig. 6.1, if (even a small fraction of) the encountered ICM were accumulated, it would make the ISM elements more strongly bound to the galaxy and thus stripping would decrease. Of course, no hydrodynamical processes that would certainly affect the stripping are taken into account here.

It is evident that the long-lasting effect of the ram pressure reflects an importance of the orbital

history of the galaxy to stripping results.

6.2.2 Narrow clusters

In clusters with narrow ICM distributions, growth of the ram pressure is much steeper. It is due to a high concentration of the ICM about the cluster center and thus higher entering velocities of the galaxy to the ICM peak at locations closer to the cluster center than in the case of wide clusters. Even if we assumed the mass accumulation, in the case of narrow clusters it would be very low. What is different from the situation in wide clusters is that the ram pressure peak has a very short duration. Thus, an element ΔA that is by an abrupt rise of the ram pressure strongly pushed to higher z's early loses the driving force, slows down and falls back to the disk plane.

Thus, when we look apart from the fact that the width of the ICM peak influences only slightly the orbital velocity of the galaxy by presence of a higher amount of the ICM, it is evident that the narrower is the cluster, the steeper is the ram pressure time derivative, but on the other hand, it arises considerably later than in wide clusters of the same $\rho_{0,ICM}$. The tendency is strengthened since the galaxy reaches the ICM density peak with a much higher velocity. Pushing of ISM elements to higher z-distances is therefore much faster than in wide clusters. But, another important factor is the duration of the ram pressure operation determining whether an element has enough time to be accelerated to the escape velocity and be stripped out of the galaxy or not. Therefore, in narrow clusters, a strong re-accretion of the ISM pulled out of the disk but staying bound to the galaxy, should be observed.

In narrow clusters, besides the effect of the ICM peak width, the rate of the element's shifting out of the disk depends on the profile of the restoring force. Fig. 3.5 illustrates that positions of the maxima of the restoring force behind the disk plane differ in our late and early-type galaxies. In late–type galaxies, due to their smaller bulges, the maxima are closer to the disk plane, especially at lower galactic radii, compared to the early-types. Then the same peak of ram pressure shifts the elements of a late-type galaxy to distances lower than in the case of early-type galaxies.

Contrary to the case of wide clusters, where all strip-able elements have enough time to be stripped, in narrow clusters the peak of the ram pressure can cease before such elements are accelerated to the escape velocity, and thus stay bound to the galaxy and fall back to the disk.

6.2.3 Clusters with constant $\Sigma_{\rm ICM}$

In the above subsections we have discussed the stripping effects of clusters with either wide or narrow distributions of the ICM. It is clear that in narrow clusters the amount of the stripped ISM would be lower than in wide clusters, and the simulation results from Chapter 5 confirmed that.

But the present simulations have further shown, that the stripping level is similar if galaxies cross clusters with similar total amount of the encountered intracluster material. Five runs with LM-type galaxy crossing clusters with the following values of the parameter pair ($R_{c,ICM}$, $\rho_{0,ICM}$) = (3.4, 1.6 10^{-2}), (6.7, 8 10^{-3}), (13.4, 4 10^{-3}), (26.8, 2 10^{-3}), and (53.6, 1 10^{-3}) [kpc, cm^{-3}] show close stripping radii and final masses (see Fig. 5.10). How is it possible, that the effect of a narrow and high cluster on one side is the same as the effect of a wide and low cluster on the other side?

Already the simulations propose an answer. In the former case, the peak value of the ram pressure is high but it operates only very shortly. Thus the ISM elements receive an abrupt shock of the ram pressure and are pushed out of the disk, the outer of them being accelerated to the escape velocity. However, the ram pressure early ceases and most of the shifted elements stay bound to the galaxy and fall back to the disk. In the latter case, the peak ram pressure is low but its action is long enough to really strip all potential elements. Only a small fraction of shifted particles then reaccretes to the disk.

A galaxy can encounter a constant amount of the ICM by several ways. It may cross

- clusters with different ICM distribution on a fixed orbit,
- the same cluster on different orbits,
- a non-relaxed cluster with several clumps of the dense ICM.

6.3 Analytic approach

In this section we consider the interaction of the galactic ISM with the intracluster medium from an analytic point of view. We describe the trajectory of an individual ISM element originally sitting in the disk plane, as it moves under the influence of the cluster gravity forces, the restoring force of the galaxy, and the ICM pressure force.

As follows from the previous sections, Gunn & Gott (1972) criterion does not take into account the orbital history of the galaxy and thus generally overestimates the stripping. Elements of the disk specified by this criterion as strip-able can overpass the maximum restoring force location z_{max} and withal stay bound to the galaxy. Therefore, we look for a more realistic analytical description of the stripping, i.e. an enhanced Gunn & Gott formula taking into account the orbital history of the galaxy and other processes mentioned above.

6.3.1 Equation of motion of an ISM element

As shown in the simulations, a bow shock forms when the oncoming ICM arrives to the galaxy. Consequently, the ICM decelerates at the shock, transferring part of its momentum to the galaxy, and flows along the shock envelope around the disk. The disk itself feels the pressure of the bow shock and thus the ISM is pushed out of the disk plane, against the galaxy restoring force.

Disregarding the above hydrodynamical effects, the equation of motion (EOM) describing the trajectory of the ISM element is

$$\frac{d\left(v_{out}\Sigma_{\mathrm{ISM}}\right)}{dt} = \rho_{\mathrm{ICM}}(v - v_{out})^2 - \frac{\partial\Phi}{\partial z}\Sigma_{\mathrm{ISM}}, \tag{6.8}$$

where v stands for the galaxy's orbital velocity with respect to the cluster center, and the rightmost term for the gravitational restoring force at the z-position of the ISM element, with Φ denoting the galactic potential. In the EOM in the above form the ISM element is accelerated to the velocity v_{out} with respect to the galaxy's rest frame and neglects the gravitational effect of the cluster. In the case of face-on interaction, v_{out} points in the z-direction which coincides with the wind direction.

The v_{out} is initially zero and the element sits in the disk plane. The ram pressure term in (6.8) is positive since it contributes to the element's output velocity, while the restoring force operates in the opposite direction. When numerically solving this equation we compute a two-body problem of the cluster center and the galaxy and get the corresponding orbit. The equation of motion in the form (6.8) describes correctly the evolution of the element as long as it is bound to the galaxy, but once the binding weakens and the element releases, it feels no other external force since the cluster gravitational effect is neglected. Thus the EOM should be rearranged in the following form:

$$\frac{d\left(v_e\,\Sigma_{\mathrm{ISM}}\right)}{dt} = -\rho_{\mathrm{ICM}}\,v_e^2 - \frac{\partial\Phi_g}{\partial z}\Sigma_{\mathrm{ISM}} - \frac{\partial\Phi_{cl}}{\partial r}\Sigma_{\mathrm{ISM}}, \tag{6.9}$$

where v_e represents the element's velocity relative to the cluster center, the negative sign in the ram pressure term expresses the fact that it slows down the element with respect to the cluster center. The rightmost term introduces the gravity of the cluster. Then the motion of the element is described well even after its release from the galaxy. In both equations, the restoring force has to be evaluated in the element's actual position z behind the disk.

The criterion of stripping is then

$$v_{out}\,(t) > v_{esc}\,(r, z), \tag{6.10}$$

where the local value of the escape velocity corresponds to Fig. 3.3.

Since the orbital velocity of the galaxy v is not a constant, but it decreases towards the second apocenter, the quantity v_{out} in the case of a released element brings misleading values at final orbital times since the element moves with some velocity v_e far away behind the galaxy, while the galaxy itself stops.

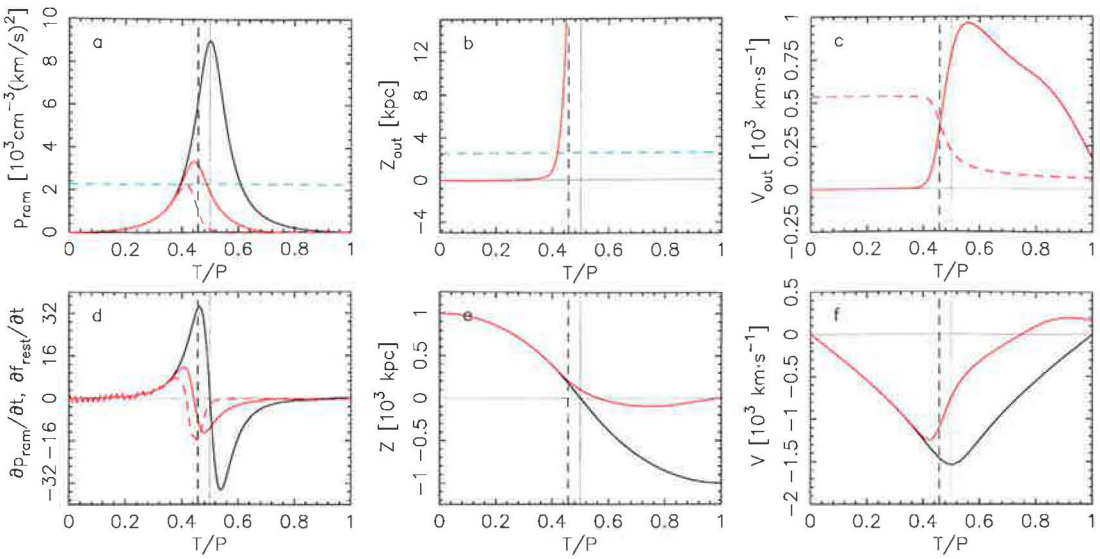

Figure 6.2: Numerical solution of the equation of motion (6.9) of an ISM element of the disk at 6 kpc radius. The galaxy crosses a cluster with very wide ($R_{\rm c,ICM}$ = 250 kpc) ICM distribution. The element is by the ram pressure stripped from the disk. The following quantities are displayed as functions of the orbital time: a) ram pressure p_{ram} of the ICM as felt by the disk (black) and by the element (red), compared with the element's local restoring force $f_{rest}(z)$ (dashed), b) actual z-distance of the element behind the disk plane, c) speed of the element v_{out} relative to the galaxy (red) compared with the local escape velocity (dashed), d) time derivatives of the ram pressure $\dot{p}_{ram}$ as felt by the galaxy (black) and by the element (red), plus time derivative of the element's local restoring force $\dot{f}_{rest}$ (dashed), e) distance of the galaxy (black) and the element (red) from the cluster center, f) velocity of the galaxy (black) and the element (red) with respect to the cluster center. Dashed verticals indicate the instant of the element's release, solid verticals the time instant T = 0.5. In panels a) and b) the dashed horizontals show the maximum restoring force of the element, and its distance z_{max} behind the disk, respectively.

6.3.2 Solving the EOM

Figs.6.2 and 6.3 show two illustrative solutions of Eqn. 6.9 for cases when the tracked element gets stripped, or stays kept by the disk, respectively. Each figure displays the following quantities: a) comparison of the ram pressure in the galaxy's and element's position with the local restoring force acting on the element, b) vertical distance z_{out} of the element from the disk plane, c) element's velocity v_{out} with respect to the disk, d) time derivatives $\dot{p}_{ram}$ in the galaxy's and element's position and $\dot{f}_{rest}$ in the element's position, e) distance of the galaxy and the element from the cluster center, and f) velocity of the galaxy and the element relative to the cluster center.

To be the situation more obvious, in both cases the galaxy crosses very wide clusters with $R_{c,ICM}$ = 250 kpc. In Fig. 6.2 the ram pressure is high enough (due to $\rho_{0,ICM} = 4\ 10^{-3}$ cm^{-3}) to strip the element, while in Fig. 6.3 the element stays bound since the central ICM density is lower by a factor of 3. In the former case, one notes how the element shifts from the disk plane and since the ram pressure easily exceeds the maximum restoring force, it is accelerated towards the escape velocity. As the element shifts from the disk, its velocity relative to the ICM wind decreases, and thus it experiences a maximum ram pressure that is much smaller than the peak ram pressure acting on the disk. The element is released before the galaxy passes through the cluster center, it further decelerates due to ongoing ram pressure, stops a step behind the cluster center, and falls backwards. In panel c) of Fig. 6.2, the effect of the galaxy slowing down towards the orbital apocenter influences the profile of the element's velocity relative to the galaxy v_{out}.

As noted above, the actual value of the ram pressure experienced by the element is different (lower) from that in the disk plane, since the element is stripped far ahead of the cluster center. When the value of the central ICM density decreased, the instant of the release would shift to later times, closer and behind the cluster center. At the same time, the values of the ram pressure

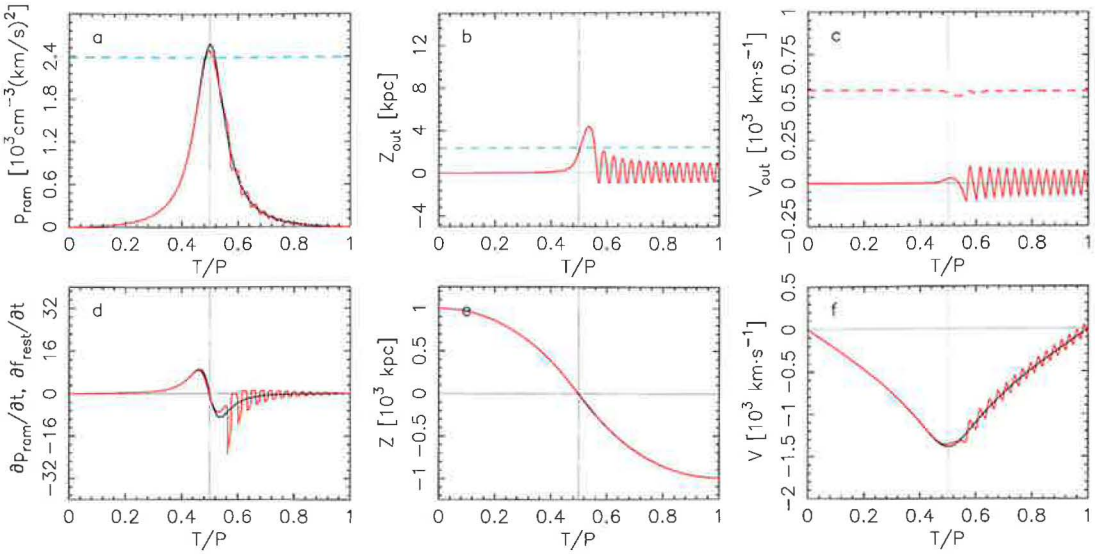

Figure 6.3: Same as in Fig. 6.2 but for a case when the element stays kept by the galaxy because of the central ICM density lower by a factor of about 3. In panel a) the vertical scale is changed.

felt by the disk and the element would get closer since the element would hold closer to the disk plane. The same process would have elements at decreasing galactic radii in a constant cluster distribution. Let's note that Gunn & Gott (1972) criterion takes into account only the peak ram pressure felt by the disk, but in fact, this value would strip the innermost possible elements.

In the case when the element survives the effect of the ram pressure bound to the galaxy (Fig. 6.3), one notes that the element starts to be pulled from the disk plane only shortly ahead of the cluster center, is shortly accelerated so it gets over the z-position of the maximum restoring force, but then the ram pressure decreases and the element falls back to the disk, oscillating about the disk plane. The oscillation persists in the analytic calculation.

Let us note what would happen if we assumed that the ISM elements accumulated a fraction of the encountered ICM. Then the restoring force would be supported by the accumulation and it would grow above the initial maximum value. Then even the elements whose original maximum restoring force would be exceeded by the ram pressure (i.e. elements fulfilling Gunn & Gott 1972) could stay bound to the galaxy.

Solution of the equation of motion (6.9) for the disk elements at different radii of the LM–type galaxy orbiting face-on in a standard cluster is displayed in Fig. 6.4. Panel (a) shows the time instants τ when elements gradually shifted by the ram pressure from different radii of the disk exceed the local escape velocity and are released. One notes that inner elements at radii up to $\sim$ 7.5 kpc stay bound to the galaxy till the end of the simulation, which is indicated by the value $\tau = 1$. Going from the disk outskirts towards the center, elements are stripped at only slightly later times. The most dramatic delay have elements just above the the stripping threshold, i.e. the stripping radius. Panel (b) shows vertical deflections of the elements at instants of their release, or at the final time when staying bound. For increasing radii, the more closer to the stripping radius, elements are by the peaked ram pressure deflected to higher z-distances and after it ceases, the elements return to the disk, strongly oscillating about the disk plane. In this analytic calculation, the oscillations persist undamped till the and of the simulation. The dashed curve in panel (b) corresponds to the z-positions of the maximum restoring force at given radius. Panel (c) gives velocities v_{out} of elements again at instants of their release, or at the final time. The dashed curve shows the local escape velocity at times tau. Above the stripping radius, the output velocity $v_{out}(\tau)$ firstly grows and about radius $r \sim 9$ kpc again decreases. That corresponds to the vertical

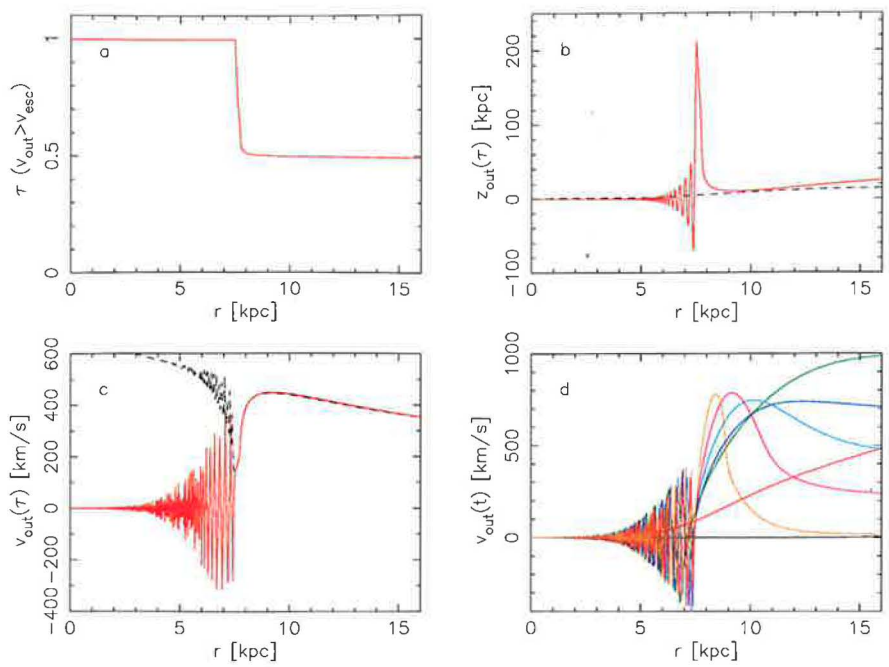

Figure 6.4: Solution of the equation of motion (6.9) for ISM elements of the LM–type galaxy crossing the STD cluster: a) time instants $\tau < 1$ when elements at different radii exceed the local escape velocity – elements at radii with $\tau = 1$ stay bound to the galaxy; b) vertical position z_{out} of elements at different radii at respective times τ's of their release (or at final time in the case of bound elements); c) velocity v_{out} of elements at different radii relative to the disk plane at times τ; d) comparison of velocities v_{out} of elements at different radii at several orbital times: 0.4, 0.5, 0.6, 0.7, 0.8, 0.9, and 1 (from red to orange). It is clear that elements at radii lower than about 7.5 kpc stay bound to the galaxy, strongly oscillating at radii close to the threshold.

distance, at which the corresponding radii were released. In panel (d) velocities of elements v_{out} relative to the disk are shown at several orbital times: 0.4, 0.5, 0.6, 0.7, 0.8, 0.9, and 1. At the time $t = 0.4$ (black), elements are still in the disk plane since the galaxy did not yet enter the ICM peak. At the time $t = 0.5$ (red), elements at outer radii accelerate, but still staying bound to the galaxy. At later times, the effect of slowing down of the galaxy flying towards the second apocenter at final orbital times reflects. The effect is the most observable at the outer radii since the elements were stripped earliest.

Using the EOM (6.9) and the stripping criterion (6.10), we can reproduce a series of snapshots of the galaxy experiencing the effect of the ram pressure along its orbit, analogous to the outputs from our numerical simulations. Fig. 6.5 shows the evolution of the infinitely thin ISM disk of the LM–type galaxy model moving through a standard cluster with $R_{c,ICM} = 13.4$ kpc on a completely radial orbit from 1 Mpc distance. Edge-on views of one half of the disk are displayed in 15 epochs about the cluster center, at orbital times 0.4 – 0.6. Fig. 6.6 then shows a similar evolution but corresponding to crossing a wide cluster with $R_{c,ICM} = 53.6$ kpc. Figs. 6.5 and 6.6 show how the outer parts of the disk are deflected from the disk plane when the ram pressure rises. As the galaxy approaches the cluster center, elements from lower and lower radii are affected. In the wider cluster the elements are deflected earlier and more strongly, compared to the narrow one. One notes how changes the envelope of the deflected elements when the galaxy crosses the cluster center: from a bowed shape with a rounded connection to the disk, to a straight, sharp profile. Further, one may compare the evolution of the opening angle of the "tail" of stripped elements in the two cases. At bottom rows, the ram pressure fades and individual elements falling back towards the disk plane are visible.

The bottom rows show the ISM elements that were shifted out of the disk plane but stayed bound and after the ram pressure decreased, they reaccrete to the disk, oscillating about the plane.

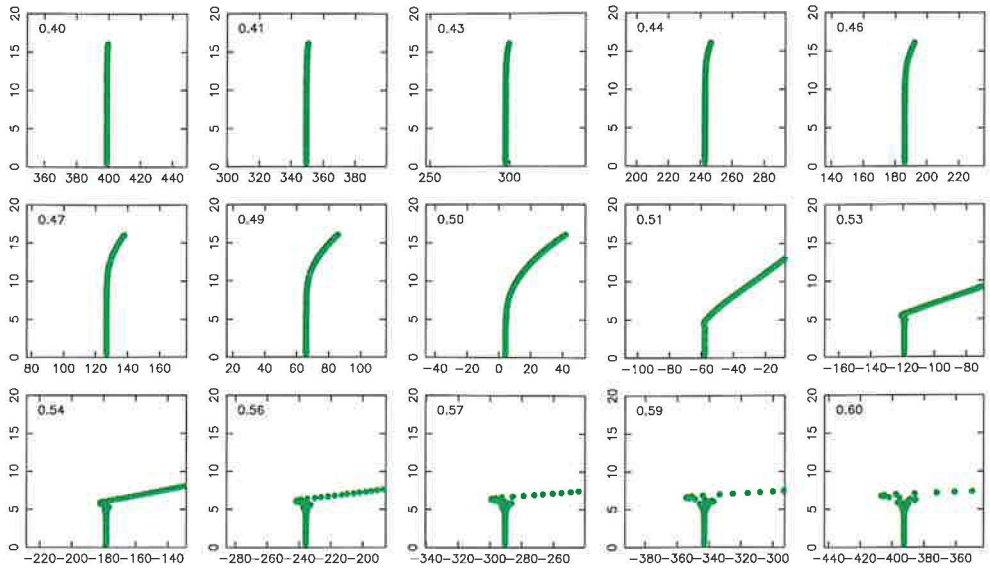

Figure 6.5: Evolution of the ISM disk calculated from the EOM (6.9) for the standard cluster and a potential of the LM–type galaxy. The orbital time is given in the upper left corner.

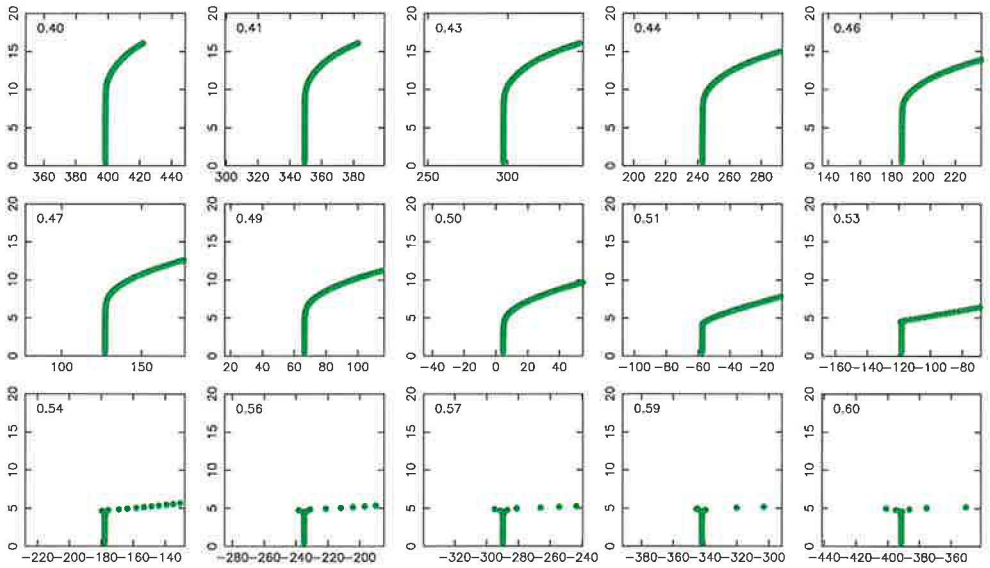

Figure 6.6: The same as in Fig. 6.5 but for a wide cluster with $R_{c,ICM} = 53.6$ kpc.

Finally, we use the EOM (6.9) to estimate the stripping radii of the four galaxy types LM, Lm, EM, and Em introduced in Chapter 3, crossing a wide range of clusters with both the $R_{c,ICM}$ and $\rho_{0,ICM}$ parameters varying from 0.25 to 8.25 $\times$ their standard values $R_{c,ICM} = 13.4$ kpc, $\rho_{0,ICM} = 4\ 10^{-3}$ cm^{-3}. Fig. 6.7 shows the results. One notes that the Em–type is almost completely stripped in all clusters, except the smallest ones. The most resistant is the LM–type due to its strongest restoring force (see Fig. 3.2). As discussed in Chapter 5, the numerical simulations show that the EM–type galaxy is stripped more than the Lm–type, despite of the restoring force profiles in Fig. 3.2. Even the EOM does not provide an explanation to these results, and determines the EM–type to be less vulnerable to the ram pressure in all clusters. Thus, effects

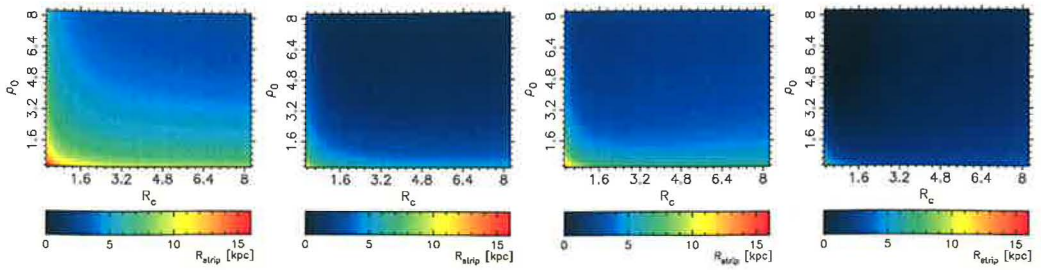

Figure 6.7: Map of the stripping radius r_{strip} for galaxies having passed through clusters with combinations of ρ_0 and R_c parameters in range of $(0.25, 8.25)$ of their standard values.

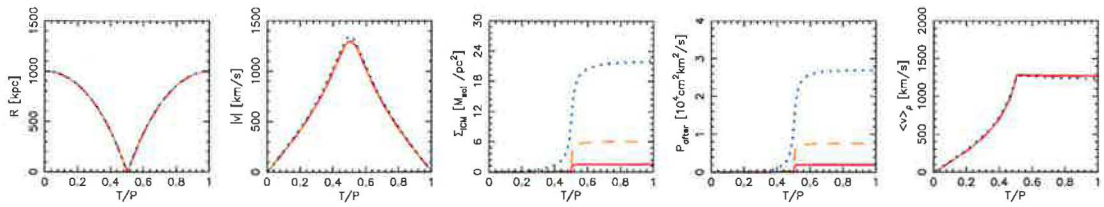

Figure 6.8: Orbital characteristics and quantities occurring in formula (6.13) as functions of the orbital time. From left to right: distance R and velocity v of the galaxy relative to the cluster center, column density $\Sigma_{\rm ICM}$ of the encountered material, surface density P_{after} of the accumulated momentum, and averaged velocity $\langle v \rangle_{\rho_{ICM}}$. Solid, dashed, and dotted curves correspond to three values of the $R_{c,ICM}$ parameter: 3.4 kpc, 13.4 kpc, and 53.6 kpc, respectively.

proposed in Section 5.3 taking into account the hydrodynamics of the ISM-ICM interaction and the differences in the vertical disk profiles of the two types, provide the likely explanation.

6.3.3 Impulse approximation

To determine the stripping results using Eqn. 6.8 is not a trivial task since it contains the speed of the ISM element with respect to the galaxy's rest, v_{out}, on its both sides. Since our principal intention is not to follow the fate of the stripped elements but only to identify them and obtain the stripping radius (or the final mass), let us introduce an approximative solution of the EOM.

A first order solution, if we consider only the regions where the gas is clearly stripped from the galaxy disk, is to use the momentum conservation. Neglecting the restoring force of the disk in these outer regions, the momentum gained by the stripped gas, of surface density $\Sigma_{\rm ISM}$, and velocity v_{after} is

$$P_{after} = v_{after}\Sigma_{\rm ISM} = \int \rho_{\rm ICM} v^2 dt, \tag{6.11}$$

If we note that the momentum P_{after} accumulated per surface area of the ISM element can be considered as the integrated history of the ram pressure, it can be arranged in the following way:

$$P_{after} = \Sigma_{\rm ICM} \frac{\int \rho_{\rm ICM} v^2 dt}{\int \rho_{\rm ICM} v dt} = \Sigma_{\rm ICM} \langle v \rangle_{\rho_{\rm ICM}}, \tag{6.12}$$

where $\Sigma_{\rm ICM} = \int \rho_{\rm ICM} v dt$ is the column density of the encountered ICM, and $\langle v \rangle_{\rho_{\rm ICM}}$ is the averaged velocity v along the galaxy's orbit weighted with the local volume density ρ_{ICM}. Then Eqn. 6.11 gets shape

$$v_{after} = \langle v \rangle_{\rho_{\rm ICM}} \frac{\Sigma_{\rm ICM}}{\Sigma_{\rm ISM}}. \tag{6.13}$$

Of course, the restoring force f_{rest} can only be neglected in the stripped outer parts of the galaxy.

Fig. 6.8 shows in detail how quantities occurring in formula (6.13) evolve with the orbital time in three clusters with varying value of the $R_{c,ICM}$ parameter. From left to right the following quantities are displayed: distance R and velocity v of the galaxy relative to the cluster center, column density $\Sigma_{\rm ICM}$ of the encountered material, surface density P_{after} of the accumulated momentum (6.11), and averaged velocity $\langle v \rangle_{\rho_{\rm ICM}}$ (6.11). One notes that the orbital velocity of the galaxy varies only slightly when changing the width of the ICM distribution. With growing value of the $R_{c,ICM}$, the ICM distribution gets wider and the galaxy encounters more ICM material. Accumulated momentum P_{after} grows, as well. Then value of $\langle v \rangle_{\rho_{\rm ICM}}$ at the orbital times $T > 0.5$ after the passage of the cluster center, is due to the ICM concentration almost constant or only slightly declining in clusters with large $R_{c,ICM}$, where the velocity gets more weight compared to sharply peaked clusters. Thus, the final velocity v_{after} does not change much at the second part of the orbit.

If the $R_{c,ICM}$ parameter were fixed but $\rho_{0,ICM}$ varied, the orbital velocity determined mainly by the cluster DM distribution would again stay almost unchanged. Amount of the encountered ICM would be in clusters with higher $\rho_{0,ICM}$ larger, but more or less corresponding to values displayed in Fig.6.8, since a change of the $R_{c,ICM}$ or $\rho_{0,ICM}$ parameters by the same value causes almost the same variation of total ICM mass (as discussed in the previous chapter). Consequently, the other quantities have similar profiles as in the above case.

If the galaxy started its radial orbit from a larger initial distance from the cluster center, it would reach higher central orbital velocity and would encounter a larger amount of the ICM.

If we compared orbits through clusters with standard ICM distribution ($R_{c,ICM} = 13.4$ kpc, $\rho_{0,ICM} = 4\ 10^{-3}$ cm^{-3}) but differing in the central DM density $\rho_{0,DM}$, galaxies would feel an unequal gravitational effect and reach different velocities. Thus, the accumulated momentum P_{after} would be different, while the amount of the encountered material $\Sigma_{\rm ICM}$ would stay constant. Then, the $\langle v \rangle_{\rho_{\rm ICM}}$ velocity is higher in clusters with higher DM amount.

A better approximation of the EOM than (6.13) is to take into account at least the maximum value over z of the restoring force. The acceleration of the ISM out of the galaxy then starts only when the ram pressure exceeds this maximum. At a given radius,

$$v_{after} = \frac{\int (\rho_{\rm ICM} v^2 - \frac{\partial \Phi}{\partial z}|_{\rm max}\, \Sigma_{\rm ISM})\, dt}{\Sigma_{\rm ISM}}, \tag{6.14}$$

where the integration proceeds during a time interval (t_1, t_2) when $p_{ram} > f_{rest,max}$, i.e. when Gunn & Gott (1972) criterion (6.5) is fulfilled. This obviously overestimates the binding of an element to the galaxy plane, since the actual value of the restoring force at the position (r, z) is less compared to its maximum value. Eqn. 6.14 then in fact represent a derivation of Gunn & Gott (1972) formula along the galaxy's orbit.

Since $\Sigma_{\rm ISM}$ is a function of the galactocentric radius r, the v_{after} velocity varies with r. If v_{after} exceeds the value of the escape velocity at the disk plane $v_{esc}(r, z = 0)$, the ISM from the given radius can be removed. Thus, we obtain the condition for stripping

$$v_{after} > v_{esc}(r). \tag{6.15}$$

The escape velocity at the galaxy symmetry plane is obtained as a function of r from the potential in the plane of the disk: $v_{esc}(r) = \sqrt{2|\Phi(r)|}$. This potential includes all components of the galaxy and its value is always the largest compared to other values at given z.

6.4 Numerical versus analytical estimates

Fig. 6.9 compares the predictions of the equation of motion (Eqn. 6.9) with the results of numerical simulations in r_{strip} vs. p_{ram} and $M_{\rm final}$ vs. p_{ram} plot, where p_{ram} corresponds to the peak value of the ram pressure occurring on the completely radial orbit in the cluster center. One notes that the analytic curves match very well the simulation marks in the case of narrow clusters with $R_{\rm c,ICM} = 3.4$ kpc, 6.7 kpc, and 13.4 kpc. When going to wider clusters, the analytic curves firstly

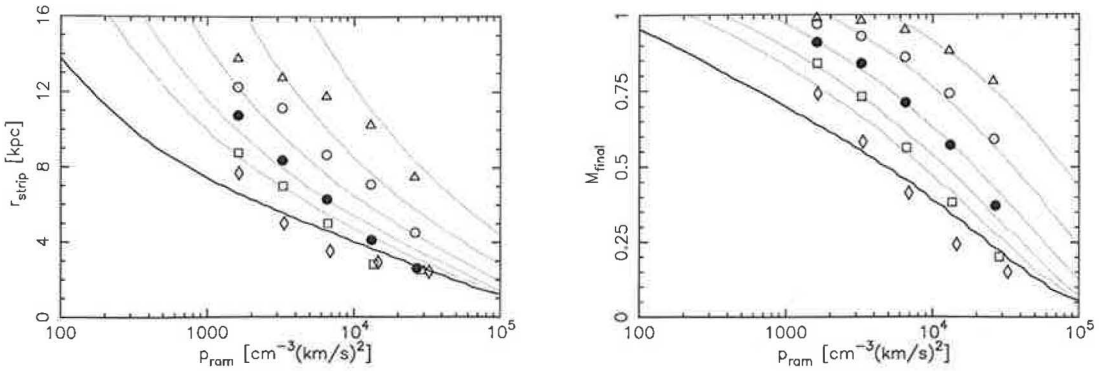

Figure 6.9: Numerical results (markers) versus analytic predictions of Eqn. 6.9 (light curves) of stripping radius r_{strip} (left) and final mass fraction of the remaining gas $M_{\rm final}$ after the stripping events (right) as functions of the maximum value of the ram pressure p_{ram}. Results for five groups of clusters with various values of the $R_{c,\rm ICM}$: 3.4 kpc (triangles), 6.7 kpc (circles), 13.4 kpc (filled circles), 26.8 kpc (squares), and 53.6 kpc (diamonds) are displayed. The thick solid line corresponds to Gunn & Gott (1972), Eqn. 6.5.

depart from the simulations in dense clusters, and in the case of $R_{\rm c,ICM} = 53.6$ kpc they completely underestimate the stripping. It can be caused by several reasons: a) we neglect the deformation of the stripped ISM disk contributing to the restoring force, b) in analytical calculations we assume an infinitely thin disk, c) Eqn. 6.8 does not take into account any hydrodynamical effects occurring in the simulations.

Fig. 6.9 further shows that the analytic curves approach the estimate of Gunn & Gott (1972) at high values of $R_{\rm c,ICM}$ and $\rho_{0,\rm ICM}$, but never cross it. This corresponds to the fact that Gunn & Gott (1972) assume a constant operation of the peak value of the ram pressure and compare it with the maximum restoring force. Therefore, as described earlier, at all radii of the disk, where the (peak) ram pressure exceeds the maximum restoring force, all the ISM elements can be accelerated to the escape velocities. On the contrary, in the EOM, the fact that an ISM element crosses the z-distance of the maximum restoring force needn't mean that this element is released, since the ram pressure is peaked and can cease before the element is accelerated to v_{esc}.

Worse agreement in the case of the stripping radius may be caused by process of relaxation underwent by the disk before it entered the ICM distribution. Consequently, the initially sharp edge of the disk at 16 kpc dissolves and it becomes difficult to define the R_{strip}. But due to low ISM density at the disk outskirts, the outer disk regions enclose only a small fraction of the total mass and thus correspondence of the M_{final} is not affected. Therefore, we state that the quantity of the final mass M_{final} provides a better tracer of the final after-stripping state.

If we assumed in Eqn. 6.8 that the ISM accumulates the incoming ICM, the restoring force acting on the elements would grow with time, and the v_{out} velocities of shifted elements would decrease. But as discussed above, and as seen in simulations, formation of the bow shock prevents such a behavior.

Fig. 6.10 shows a comparison of the simulation results and the approximations of Eqns. 6.13 (left) and 6.14 (right), which are expected to bracket the actual equation. The final mass M_{final} is determined as an ISM mass enclosed within the stripping radius, according to the profile (3.2). The stripping radius r_{strip} is a radius above which $v_{after}(r)$ exceeds the value of the escape velocity in the $z = 0$ plane. One notes that the curves of Eqn. 6.13, which neglects the restoring force, overestimate the stripping, while curves corresponding to Eqn. 6.14, which keep only the maximum restoring force, underestimate the stripping. The departures from simulations are in the case of Eqn. 6.14 larger than with the predictions of the EOM (Eqn. 6.9), displayed in Fig. 6.9. However, curves of Eqn. 6.13 correspond better to the simulations in large clusters with $R_{c,ICM} = 26.8$ kpc and 53.6 kpc and high values of the central density $\rho_{0,ICM}$.

Of course, comparing numerical simulations with analytic predictions may have several caveats.

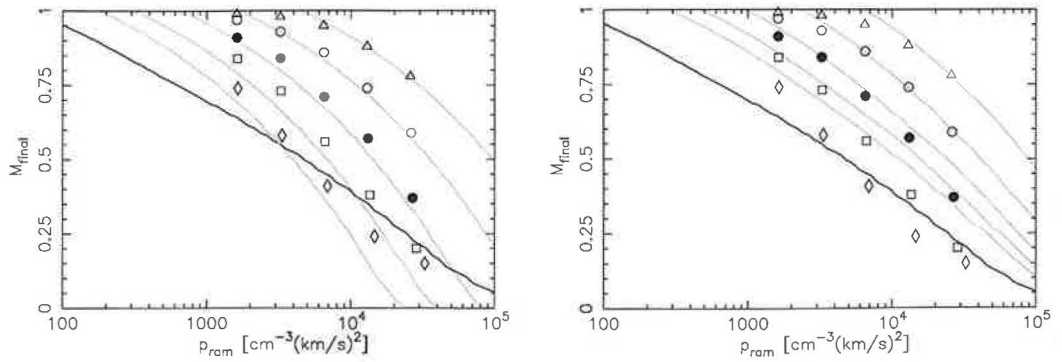

Figure 6.10: Numerical results versus analytic predictions of Eqns. 6.13 (left) and 6.14 (right) of final remaining gas mass fraction $M_{\rm final}$ after the stripping events as functions of the maximum value of the ram pressure p_{ram}. The symbols for individual simulations are the same as in Fig. 6.9. The thick solid line corresponds to Gunn & Gott (1972), Eqn. 6.5.

The most important is that the hydrodynamical processes, such as the effect of the bow-shock and size of the galaxy shadow, are disregarded in the solution describing the dynamics of an individual ISM element. Further, in analytic calculations, a fixed profile of the ISM, coincident with the initial distribution (Eqn. 3.2) is assumed. However, in simulations, processes of relaxation and formation of spiral arms, as well as the progressive stripping, can change the surface density profile of the ISM disk. Such changes of course consequently affect the restoring force, and the escape velocity profiles.

On the other hand, it is surprising that the simple conservation of momentum (Eqn. 6.13), on one side neglecting the actual effect of the restoring force and the element's shifting out of the disk, and on the other side overestimating the escape velocity and changes of the ISM disk due to stripping, can give a good order of magnitude of the stripping, when the variable ICM density along the orbit is to be taken into account. The Gunn & Gott (1972) formula, computed only from the maximum ICM density along the orbit, of course overestimates the stripping. However, in cases with large values of $R_{\rm c,ICM}$ and $\rho_{0,\rm ICM}$ the simulations show even larger stripping as compared to Gunn & Gott (1972) estimate. This may be a consequence of uneven gas distribution in the galaxy disk where spiral arm inhomogeneities contribute to the ISM removal as also shown by Quilis et al. (2000).

6.4.1 EOM: restrictions and possible improvements

In the form (6.9), the equation of motion of the ISM elements has a number of restrictions and simplifications. Especially, it

- completely neglects hydrodynamical processes occurring during the ISM-ICM interaction, including the formation of a bow shock in front of the galaxy visible in numerical simulations in Chapter 5.
- assumes all the ISM laying in the $z = 0$ plane,
- neglects the changes of the ISM disk morphology due to the ram pressure stripping,
- does not take into account the inhomogeneity of the disk with spiral arms–structure. Consequently, in inter-arm spaces the surface density Σ_{ISM} is lower than in positions of the arms themselves (Schulz & Struck 2001, Quilis et al. 2000).
- assumes the restoring force and the escape velocity corresponding to a smooth, unperturbed ISM disk, while it is strongly modified by the two above effects,
- ignores self-gravitation of the ISM elements,

- it forgets vertical velocity dispersion of ISM elements $\sigma_z = \sqrt{\pi G z_0 \Sigma_d}$, which could support, or on the contrary impede the stripping, depending on the actual direction of the dispersion velocity of an ISM element with respect to the ICM wind, especially in narrow clusters.

Further, the equation of motion (6.9) cannot be simply used to study more general cases of the ISM-ICM interaction, including those with different inclination angles of the disk with respect to the orbital direction. Then, the rotation of the disk should be taken into account.

6.4.2 Effect of oscillations

The initial value of the ram pressure acting on the galaxy at its starting position R_{init} depends on the width of the ICM distribution. What would be a consequence of an abrupt entry of the galaxy into a distribution of the ICM, e.g. a clump of the intracluster material? Following an element of the disk, the initial shock of the ram force causes that the disk element bounces forward in the ICM wind direction and gets to a higher vertical distance with a superior value of the restoring force. Consequently, the element is drawn back as a body on a spring and goes backwards. Then it is re-catched by the ram pressure pulse, now stronger as the galaxy gets deeper into the cluster (clump) and the situation repeats. Thus, the element oscillates about a mean trajectory.

For comparison, when the galaxy enters smoothly into an arising ram pressure pulse, the element is all the time in equilibrium with the growing ram force and thus it is held at the maximum elongation possible at any moment and does not oscillate.

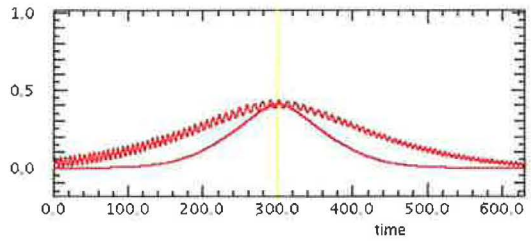

Figure 6.11: Vertical trajectory of a disk element of the galaxy entering smoothly (lower curve), or abruptly to an ICM distribution, calculated using the equation of motion (6.9). The yellow vertical indicates the instant of the peak ram pressure.

Fig. 6.11 shows the difference between the two described trajectories. When fitted together, the element from the former case would oscillate about the trajectory of the element from the latter case. The initial oscillations can arise on condition that the ram pressure grows slowly to have the element enough time to be drawn back from its actual elongated position, to oscillate. In the analytic calculation, the oscillations are not damped.

Further, we study the effects of possible initial vertical oscillations of the ISM elements corresponding e.g. to their dispersion motions. In the above sections describing the ISM-ICM interaction from an analytic point of view, we have provided the ISM elements laying in the $z = 0$ plane with zero initial vertical velocity. Fig. 6.12 illustrates an element that is in the case of its location in the $z = 0$ plane not released from the galaxy after the passage through the ram pressure peak, but as a consequence of an initial vertical motion it can reach the escape velocity. The horizontal axis shows the orbital time, at $t = 30$ units the galaxy experiences the maximum ram pressure (yellow line). The vertical axis displays the vertical position of the element with respect to the $z = 0$ plane. Vertical motion of the element for two initial positions (1 kpc above and below the $z = 0$ plane with respect to the ICM wind direction) and a set of values of the initial vertical velocities is calculated numerically using Eqn. 6.9. The element initially oscillates around the disk plane and as it gets to the area of the ram pressure peak it is sooner or later accelerated to the escape velocity, depending on the initial value of the velocity.

Fig. 6.13 then displays dependence of the vertical motion of an element located in the $z = 0$ plane on its initial velocity. If it is higher than about $0.5 v_{esc}$, the element is released, while with

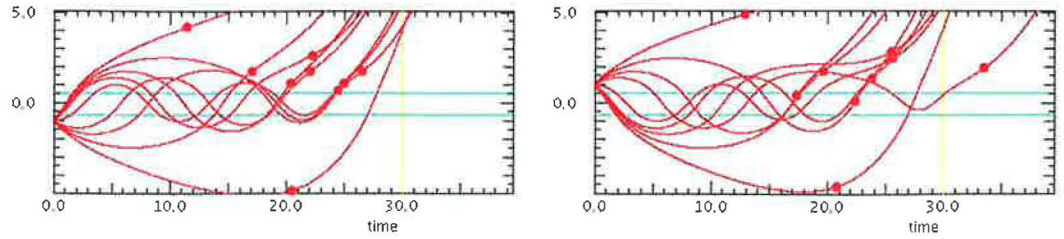

Figure 6.12: Vertical trajectories of a disk element initially located at 1 kpc distance on the windward (left), or leeward (right) side of the disk, and with various initial vertical velocities. The element is released from the galaxy potential for all displayed initial vertical velocities: -0.7, -0.6, -0.5, -0.4, 0, 0.4, 0.5, 0.6, and 0.7 $\times$ v_{esc}. Negative velocities point against the wind direction. Note that if located in the $z = 0$ plane with zero vertical velocity, the element would stay bound. Cyan lines show the position of the maximum restoring force.

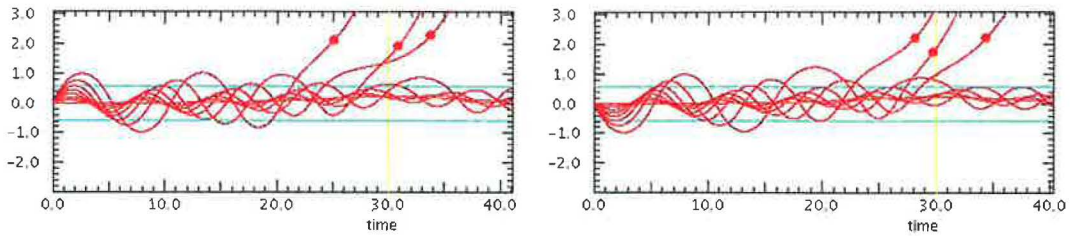

Figure 6.13: Vertical motions of an element initially located in the $z = 0$ plane with varying value of the vertical velocity, either in the sense coincident (left), or opposite (right) to the ICM wind direction. Velocities of 0, 0.1, 0.2, 0.3, 0.4, 0.5, 0.6, and 0.7 $\times$ escape velocity are displayed. For initial velocities higher than about $0.5v_{esc}$ the element is released. Cyan lines show the position of the maximum restoring force.

velocities lower it survives the passage of the ram pressure peak bound to the galaxy.

Chapter 7

Numerical simulations: Edge-on and inclined radial stripping

In the previous chapter, we have studied the consequences of the ISM-ICM interaction in galaxies flying through galaxy clusters on radial orbits with disks in the face-on orientation with respect to the orbital direction. Of course, probability of such a configuration is very low and generally inclined galaxies have to be taken into account. Roediger & Brüggen (2006) recently focused on inclined galaxies interacting with a constant flow of the intracluster material using a grid-based hydrodynamical code. Previously, Abadi et al. (1999), Quillis et al. (2000), and Schulz & Struck (2001) touched the problem of the ram pressure stripping of inclined galaxies concluding that the stripping efficiency significantly changes only for nearly edge-on cases and stay almost unchanged for higher inclinations. Vollmer et al. (2001), who by means of a Lorenzian profile modelled a realistic time profile of the ram pressure acting on galaxies with HI clouds treated as sticky-particles, studied together with the face-on galaxies also the inclined cases. They found interesting nontrivial consequences. In the following text we stay concerned by the radial orbits and study in detail the inclined stripping events, comparing the results with the above mentioned papers.

7.1 Inclined ISM-ICM interaction

A general orientation of a galaxy with respect to the direction of its orbital motion is characterized by three angles – the plane of the disk can be firstly inclined about an axis perpendicular to the orbital direction, and then slew about the other two axes. If we confine to cases when the galaxy moves along a completely radial orbit and the disk is only inclined about the first axis, a single parameter describes the orientation – the inclination angle i (see Fig. 7.1). We define it in such a way that $i = 90°$ corresponds to the face-on case, and $i = 0°$ to the edge-on orientation of the disk, respectively. In the next chapter we will deal with galaxies moving about the cluster center on non-radial orbits. There, since the plane of the galactic disk keeps its orientation in space, galaxies have time-varying inclinations and it must be studied which part of their orbit through the intracluster medium has the most important stripping effect on the ISM disk and what inclination angle the disk contains at that time.

In interacting an inclined disk with the intracluster medium, the role of the galactic rotation arises. In the face-on case its effect is hidden since the rotational velocity v_{rot} is at every disk location perpendicular to the ICM wind direction. Its only observable effect confines to a twisted structure of the tail of stripped ISM elements. Fig. 7.1 illustrates the geometry of an inclined disk with respect to the instantaneous direction of the oncoming ICM. In the case of a completely radial orbit leading through the cluster center, this direction is fixed and the main axis (AC) about which

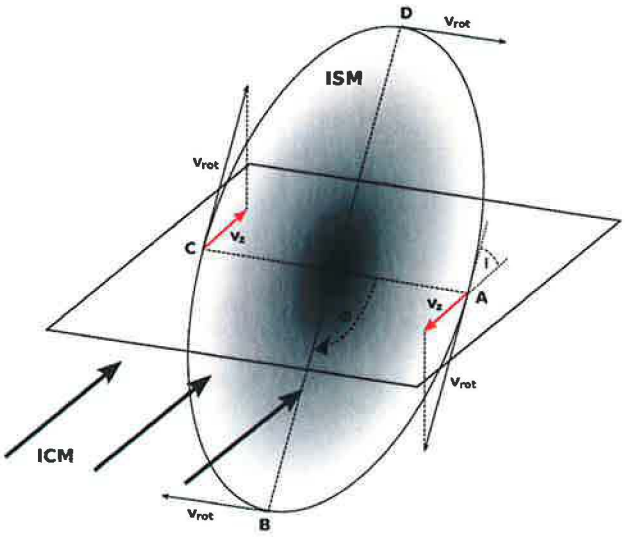

Figure 7.1: Scheme of an inclined configuration of the disk with respect to the oncoming ICM. The disk rotates with a rotational velocity $v_{rot}(r)$ whose projection into the ICM wind direction is maximum at lateral positions A and C, and zero at B and D. The angles i and ϕ stand for the inclination and azimuth.

the disk is inclined keeps its orientation perpendicular to the cluster center direction. As the disk is inclined, the contribution of the rotational velocity to the orbital direction becomes non-zero. Its value depends on the position in the disk and is maximal at the axis of inclination AC. In our LM–type galaxy model, the rotational curve is flat with velocity of about 250 km s^{-1}. Then if the inclination is e.g. 45°, the maximal contribution to the orbital direction in the position A is $\sqrt{2}/2\ v_{rot} \sim 176$ km s^{-1}. Since the ram pressure $p_{ram} = \rho_{ICM} v^2$, its maximum value in the center of the standard cluster increases due to the rotation by a factor of about 1.3, from $\sim 6\,500$ to $\sim 8\,500$ cm^{-3} km^2 s^{-2}. On the contrary, elements at the axis (BD), perpendicular to the axis of inclination, have the rotational velocity vector perpendicular to the ICM wind direction and thus, similarly to the face-on case, the effect of the disk rotation is there completely hidden. In our notation, the point A has azimuth $\phi = 0°$, the point B $\phi = 90°$, etc. (see Fig. 7.1). The maximum contribution of the rotational velocity ($v_{rot} \cos i$) is then at the azimuth 0°, or 180°, and diminishes when going to higher azimuths of 90° or 270°, i.e. the axis BD). At one side of the disk (sector DAB), the disk rotation increases the relative velocity of the ICM wind and thus supports the ram pressure, while on the other side (sector BCD), it counterworks the ram pressure. If the disk were not only inclined but also slewed about another axis, the projection of the rotational velocity at various azimuthal angles would not be symmetric as in the above case.

Besides the ram pressure due to the galaxy's orbital motion through the ICM, the ISM experiences a "lateral" pressure due to the rotation into the "static" surrounding material. This pressure is active even in the face-on case, however, its value is small (~ 260 cm^{-3} km^2 s^{-2} in the LM–type galaxy) and the disk itself shields its parts. But this marginal ram pressure could affect the ends of disk spiral arms that are not shielded by an homogeneous disk. Another thing is the effect of this "rotational" ram pressure on elements stripped from the disk and forming the tail whose surface density drops.

Similarly to the face-on case discussed in the previous chapter, let us look at the problem from an analytic point of view. Originally perpendicularly acting ram pressure on a disk element ΔA sees in an inclined case only a projected cross-section of the element, $\Delta A \sin i$. Then the ram force gets shape

$$F_{ram} = \rho_{ICM}\, v_{rel}^2 \sin i\, \Delta A, \tag{7.1}$$

where ρ_{ICM} is the density of the ICM stream, i is the inclination angle, and v_{rel} denotes the

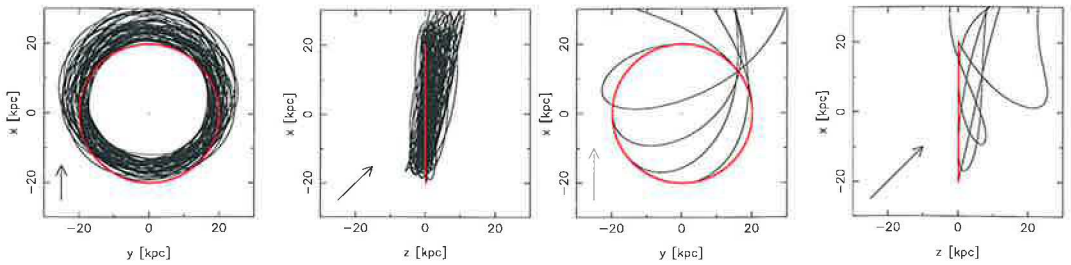

Figure 7.2: Trajectories of six ISM test elements at $r = 20$ kpc radius and different azimuths in the potential of the LM–type galaxy and under the influence of the ram pressure operating from $i = 45°$ direction (arrows). When the ram pressure is low, the elements are only shifted on disturbed excentric orbits (left), while when it is strong enough, the elements are stripped at rates depending on their original azimuths. The orbits of shifted elements (left) fill up the displayed annuloid in about 6 Gyr.

relative velocity of the ICM wind with respect to the disk. As discussed above, the projection of the disk rotational velocity to the wind direction depends on the azimuthal angle ϕ of a given ISM element in the disk plane. Elements located with $\phi = 0°$ and $\phi = 180°$ at the inclination axis have the maximum contribution of the rotational velocity to the wind direction, $v_z = v_{rot}\, cos\, i$, where the velocity is denoted with z since we assume that the galaxy moves in the z-direction towards the cluster center. As the azimuthal angle grows towards the axis perpendicular to the inclination axis, the component of the rotational velocity in the ICM wind direction decreases: $v_z = v_{rot}\, cos\, i\, cos\, \phi$. Thus, the relative velocity looks like

$$\boldsymbol{v}_{rel} = \boldsymbol{v}_{ICM} + \boldsymbol{v}_z = \boldsymbol{v}_{ICM} + \boldsymbol{v}_{rot}\, cos\, i\, cos\, \phi, \tag{7.2}$$

where again $\boldsymbol{v}_{ICM}$ stands for the vector of the wind velocity of the ICM.

On one side of the disk the rotation increases the relative velocity v_{rel}, while on the second side it reduces it. This could mean that the overall effect balances. But, this depends on the duration of the ram pressure operation. When the galaxy passes through a narrow ICM peak, the ram pressure operates only shortly, on time scales much shorter than the rotational period of the galaxy. In this case, indeed the compensation of the two disk sides applies, since during a short ICM peak the ISM from one disk side should be stripped slightly less, when compared to the strictly face-on orientation, while at the other side the stripping should be by the same factor stronger. But when the ICM peak is wide, the ram pressure operates during a long time and the ISM from more or all azimuths gradually gets by the rotation to the disk side that supports the stripping. Thus the final stripping efficiency should increase, compared to the strictly face-on case. In the LM–type galaxy the rotational period at the radius of 10 kpc is about 310 Myr. It means that when the ISM-ICM interaction lasts during a comparable or longer period, the ISM from all azimuths finally gets to the sector of enhanced stripping, and the galaxy should reach a symmetric final shape.

Thus, in clusters with narrow ICM distribution the elements at different azimuths do not have enough time to get to the disk side where the ram pressure is supported by the disk rotation. The ram force then depends on the azimuth:

$$F_{ram} = \rho_{ICM}\, (v_{ICM} + v_{rot}\, cos\, i\, cos\, \phi)^2\, sin\, i\, \Delta A, \tag{7.3}$$

while in wide clusters where all elements subsequently get to the sector of the strongest ram pressure and thus the dependence on the azimuthal angle vanishes:

$$F_{ram} = \rho_{ICM}\, (v_{ICM} + v_{rot}\, cos\, i)^2\, sin\, i\, \Delta A. \tag{7.4}$$

However, one thing is the value of the ram pressure, and another thing is the momentum of the ISM elements. At the sector DAB of the disk in Fig. 7.1, the ram pressure is indeed increased by the rotation but the elements rotate against the wind direction and thus are more difficult to be

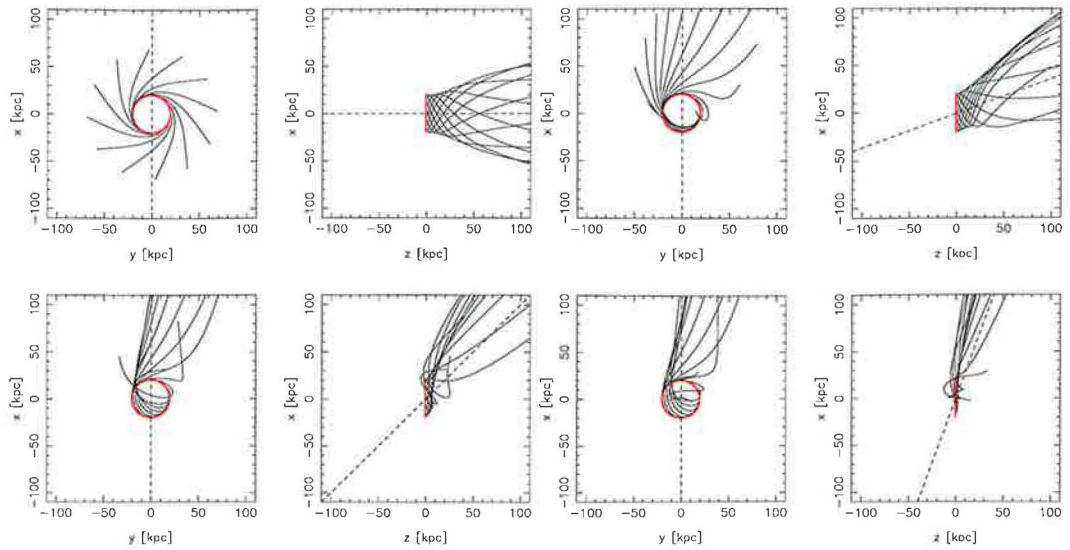

Figure 7.3: Trajectories of twelve elements of the ISM disk located at $r = 20$ kpc and various azimuthal angles under the operation of the ram pressure from different directions (dashed lines): $i = 90°$, $70°$, $45°$, and $20°$ with respect to the disk plane. The duration of interaction is about 600 Myr. The elements are treated as test particles in the potential of the LM–type galaxy.

stripped. On the other side (sector BCD), the ram pressure is weakened since the relative velocity is lower, but elements move due to the rotation in the wind direction and thus they become easier to be accelerated to the escape velocity. Therefore, one has to revalue the above image of stripping which takes into account only the projected rotational velocity to the wind direction.

Then the elements most susceptible to the stripping are those that originate in Fig. 7.1 from positions about the point B, since their projected rotational velocity will during the next half-orbital period coincide with the wind direction and they thus can be most easily accelerated in the wind direction. Then a marginal ram pressure that is not sufficient to strip the elements from a given radius of a face-on disk can be enough to remove the elements originating from the leading side of an inclined disk (about point B), and not from the positions of an enhanced ram pressure about point A. This behavior is confirmed by our simulations presented in the next section.

How change the orbits of the ISM elements of an inclined disk under the influence of a ram pressure? Fig. 7.2 shows trajectories of six ISM test elements located at $r = 20$ kpc radius with different azimuths in the LM–type galaxy potential under the influence of a constant ram pressure operating from $i = 45°$ direction. If the ram pressure is low enough (left), all the elements stay bound to the galaxy potential but their orbital trajectories change: the circular orbits turn into excentric non-planar roseta-like orbits. After a long period (~ 6 Gyr displayed), these trajectories fill up an annulus that is shifted about 5 kpc in the x-direction and about $20°$ inclined with respect to the disk plane. When the ram pressure is stronger, it strips the elements (right). The process of stripping of individual elements depends on their original azimuth: those whose projected rotational velocity vector coincides with the wind direction first get to higher radii since their orbits prolong, while those with v_{rot} that points against the wind get to lower radii as their orbits are distorted (compressed).

Fig. 7.3 again shows trajectories of test elements located at $r = 20$ kpc radius with various azimuths in the potential of the LM–type galaxy but under operation of constant ram pressure operating from different directions: $i = 90°$, $70°$, $45°$, and $20°$. It shows that in the face-on case the shifted elements get due to the galactic rotation to higher (galactocentric cylindrical) radii. However, in our numerical simulations such a strong expansion of the tail is not observed. This may correspond to several things: first, the swept elements rotate "into" the surrounding static ICM and interact with the bow shock occurring along the tail, which prevents the expansion. Further,

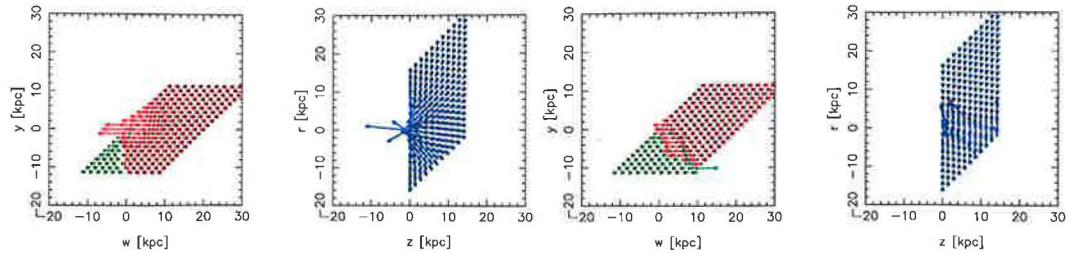

Figure 7.4: A two-dimensional grid of locations where the restoring force on stripped ISM elements is calculated in the $i = 45°$ case. First panel shows the grid in the coordinate system of the ICM wind, second panel in the galactic coordinate system. Clearly, along the lines of nodes parallel with the wind direction both r and z changes. First panel shows contribution of the restoring force in the wind direction (green, or red in locations with coincident, or opposite sense, respectively), second panel the restoring force. The right pair of panels illustrates the situation when the galactic rotation is taken into account.

in simulations the ISM particles are treated self-consistently and thus can gravitationally interact. From the above reason follows, that the assumption of elements shifting on constant radii is a good approximation.

On the contrary, in an inclined configuration, one can see in Fig. 7.3 that the galactic rotation plays a more important role: the tails again follow the wind direction (marked with a dashed line), however the trajectories closely behind the disk plane are more complicated and depend on the original azimuths of the elements.

Therefore, one cannot say that the elements of an inclined disk are simply shifted out of the disk in the wind direction, but must take into account the conservation of angular momentum. Consequently, the profile of the restoring force acting on a given element along its trajectory is not a simple projection to the wind direction.

Roediger & Brüggen (2006) think about the situation in the disk plane ($z = 0$). They note that at any radius of the galactic disk the radial gravitational force is in balance with the centrifugal force. Then only the projected vertical component of the gravitational force known from the face-on case contributes to the restoring force (per unit surface) in the ICM wind direction:

$$f_{rest} = \frac{\partial \Phi}{\partial z} \sin i \, \Sigma_{ISM}, \tag{7.5}$$

and since the ram pressure in the wind direction (Eqn. 7.1) is a function of $\sin i$ as well, the dependence of the ISM-ICM interaction on the inclination vanishes.

However, as discussed above, an element originally rotating at some galactic radius is shifted out of the disk plane and due to rotation it gets to a different radius where it feels a different gravitational force. Thus Eqn. 7.5 can describe well the situation in narrow clusters where the ISM-ICM interaction is rapid and a given element can be stripped before it gets to a different galactic radius. On the contrary, in wide clusters the process of stripping takes a long time and a change both of the radius and of the vertical distance of the elements takes effect and the above assumption of the restoring force fails. Then its actual value in the wind direction at some galactic radius and vertical distance behind the disk plane can be written as

$$\boldsymbol{F}_{rest} = \frac{\partial \Phi}{\partial w} \hat{\boldsymbol{w}} + \frac{v_{rot}^2}{r} \cos i \, \hat{\boldsymbol{w}}, \tag{7.6}$$

where $\hat{\boldsymbol{w}}$ is the direction of the wind, and the right-handed term is the projection of the centrifugal force.

If we are interested by how the restoring force in the wind direction looks behind the inclined disk, we numerically calculate its values at a non-cartesian grid of positions lying in the plane that is parallel with the wind direction, perpendicular to the inclination axis and crosses the galaxy center. Fig. 7.4 shows in its leftmost panel such a grid for the inclination angle of 45°. The

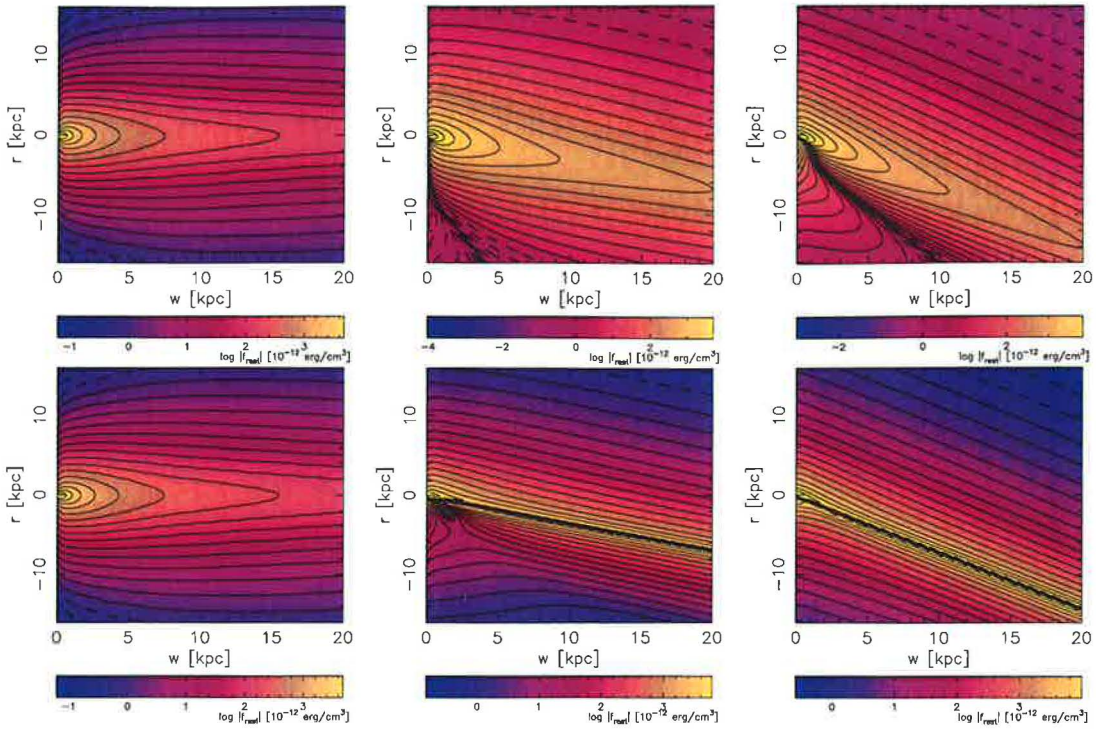

Figure 7.5: Projection of the gravitational restoring force of inclined galaxies as a function of distance w behind the inclined disk to the ICM wind direction for different projected radii. In upper row only gravitational force of the disk+bulge+halo components is taken into account, in lower row the effect of galactic rotation is included, while assuming that the ISM elements are by the ram pressure shifted out of the disk strictly in the wind direction and that they preserve their original rotational velocity from the disk plane.

horizontal axis of the grid coincides with the ICM wind direction, and the second axis is parallel with the disk seen edge-on. Second panel of Fig. 7.4 depicts the grid in the galactic coordinate system. At every position, the gravitational force is evaluated and its component in the wind direction is determined and indicated by arrows. The positions where the sense of the projected gravitational attraction coincides with the wind direction are marked with green, the others with red color.

When the centrifugal force due to the galactic rotation is taken into account, the area behind the leading side of the inclined disk where the restoring force coincides with the wind direction enlarges (right-handed pair of panels in Fig. 7.4). The effect of the rotation is included in such a way that at all positions behind a given galactic radius r in the wind direction $\hat{\boldsymbol{w}}$, we take the value of the centrifugal force corresponding to this radius r. Of course, we have seen that ISM elements do not shift out of the disk directly in the wind direction, but depending on their initial azimuth, they continue to move on disturbed orbits. Nevertheless, we can assume that the situation in the third panel of Fig. 7.4 corresponds to the time about half-period after the ram pressure have risen when elements originating from the "top" radii (as seen in the panel) have moved along compressed orbits to lower radii at the bottom positions, and the elements from "bottom" radii have moved to higher radii in the top positions of the panel along elongated orbits – c.f. Fig. 7.2.

Fig. 7.5 shows the restoring force in the positions behind the disk calculated by the above described approach. In the upper row it depicts the restoring force of the galaxy in the wind direction when neglecting the galactic rotation for inclinations of 90°, 70°, and 45°. The lower row displays the restoring force including the effect of rotation for the same inclinations. It must be stressed that the panels in non-face-on cases should be tilted by the inclination angle since they depict the restoring force at locations behind the inclined disk along the wind direction. In the case of

face-on orientation ($i = 90°$), the effect of rotation diminishes and the restoring force is symmetric along the disk rotational axis which coincides with the wind direction. For inclined orientations the restoring force is asymmetric. The axis of maximum values strongly deflects from the wind direction, but neither coincides with the disk rotational axis. At the leading side of the inclined disk the sense of the projected restoring force coincides with the wind direction. Since Fig. 7.5 displays the restoring force in a logarithmic scale, negative values are taken in absolute values. Then the area where the force coincides with the wind direction is from the rest separated by a cutting of values tending to zero. Size of this area expands as the inclination diminishes towards the edge-on orientation. Further, when the disk rotation is taken into account, the area of negative forces extends and the border between negative and positive values shifts towards the axis of maximum restoring force.

When studying the ISM-ICM interaction in the case of face-on galactic configuration in Chapter 6, we have described the stripping of ISM elements using the equation of motion (EOM). Since effect of the galactic rotation was hidden, the EOM was a simple one-dimensional differential equation. When the disk is inclined, the rotation cannot be neglected and motion on an individual ISM element becomes three-dimensional. Therefore, the equation of motion has to be solved in three dimensions, as well. For an element originating at a radius r and azimuth ϕ the EOM is

$$\frac{d(\boldsymbol{v}_e \Sigma_{\mathrm{ISM}})}{dt} = \rho_{\mathrm{ICM}} v_{e,w}^2 \hat{\boldsymbol{w}} + \frac{v_{rot}^2}{r} \hat{\boldsymbol{r}} \Sigma_{\mathrm{ISM}} + (\frac{\partial \Phi_g}{\partial r} \hat{\boldsymbol{r}} + \frac{\partial \Phi_g}{\partial z} \hat{\boldsymbol{z}}) \Sigma_{\mathrm{ISM}}, \tag{7.7}$$

where $\boldsymbol{v}_e$ is the velocity of the element with respect to the galaxy's rest, $v_{e,w}$ its component in the wind direction, v_{rot} the element's original rotational velocity, and $\hat{\boldsymbol{w}}$ the unit vector in the wind direction. Thus, we assume that the element keeps its original rotational velocity even when stripped out of the disk plane.

7.2 Existing simulations

History of numerical simulations studying inclined ram pressure stripping events is not very long. Up to day, only about a dozen papers deal with such stripping events. Bellow, we propose a short summary of them.

Farouki & Shapiro (1980) – they performed one non-face-on stripping simulation with $i = 45°$ and found out that the gas was stripped on a longer time scale than in the face-on case but noted the same thickening of the disk and unperturbed appearance of the nucleus.

Kritsuk (1984) – except the above mentioned simulation of Farouki & Shapiro (1980), he studied for the first time the effect of inclination on the gas stripping. It is shown that although dense molecular clouds have a low probability to be stripped, diffuse HI clouds are readily swept out and the efficiency of the sweeping decreases with increasing degree of concentration of mass toward the center of the galaxy. They cover both the stripping and pushing of gas compared to the local gravitational binding and show a strong coupling of between the disc rotation and the wind in highly inclined cases.

Phookun & Mundy (1995) – in their in fact observational paper study high-resolution VLA images of the Virgo Cluster spiral NGC 4654 which has a strongly asymmetric HI distribution with a compressed edge on one side and a long tenuous tail on the other. They speculate whether this structure is a result of the ram pressure or of a tidal interaction with the neighboring NGC 4639. They introduce a term of "ram pressure pushing" when ram pressure acts on a cloud of gas and tends to push it out of its former orbit. According to Kritsuk (1983) they note that if ram pressure is not efficient enough to strip the gas, the force perpendicular to the disk plane cannot do much, but the component in the disk plane can combine with rotation and create asymmetries in the disk. For origin of the tail of HI gas extended in one quadrant on the southwestern side of the galaxy they propose a scenario of the edge-on flight of the galaxy through a weak ICM wind. Then the ram pressure is greater for clouds on the disk side moving due to rotation against the wind, than

on clouds moving on the opposite side with the wind. If the speed of the wind is much higher than the rotational velocity of a gas cloud, the direction of the ram force practically coincides with that of the wind. Thus, the ram force and the gravitational force are approximately perpendicular at lateral sides of the disk, and parallel or antiparallel at the front or rear disk side. If $F_{ram} \simeq -F_g$ near the rear of the disk, the ISM there are approximately free of the radial force and stream out tangentially forming a tail in the quadrant of the disk where the gas flows against the wind. This tail is a long-lasting feature since it is a kind of density wave supported by gas in modified orbits resulting from an equilibrium between the ram pressure and gravity. They derive a formula for the bounding radius of un-stripped gas in a galaxy moving edge-on through the ICM:

$$\frac{\rho_{ICM}\, v_{\rm ICM}^2}{\Sigma_{\rm ISM}} \simeq \frac{v^2}{r}, \tag{7.8}$$

where $\Sigma_{\rm ISM}$ is the surface density of a HI cloud. Phookun & Mundy (1995) conclude that the asymmetric gas distribution of NGC 4654 is caused by ram pressure pushing in the disk plane.

Hidaka & Sofue (2002) – using 2D finite difference hydro-simulation with 256×256 resolution, they investigate the effects of the ram pressure of the ICM wind on inner parts of the disk of spiral galaxies. Their galaxy has a galactic disk with a static axisymmetric potential and a non-axisymmetric rotating bar potential. The ram pressure acceleration per unit mass is introduced analytically as

$$\boldsymbol{a}_{ram} = C\, n_{ICM} |\boldsymbol{v}_{ICM} - \boldsymbol{v}_{rot}| (\boldsymbol{v}_{ICM} - \boldsymbol{v}_{rot}). \tag{7.9}$$

Their simulations show that even weak ram pressures can disturb the orbits of the inter-arm ISM (see Fig. 2.19 in Chapter 2). Consequently, highly asymmetric molecular arms in the inner few kpc of the disk can form. Hidaka & Sofue (2002) further estimate analytically the effect of the ICM-ISM interaction: the ram force on an ISM element in the direction parallel to the disk plane is

$$f_{ICM} \sim \rho_{ICM}\, \Delta A\, \delta v^2 \cos\alpha \sin\alpha, \tag{7.10}$$

where ΔA is the surface area of the element, α is the angle between the ICM wind direction and the galactic plane, and δv is the local relative ISM-ICM velocity. Since the element is bound to the galaxy by a restoring force

$$f_{ISM} \sim \rho_{ISM}\, d\, \Delta A\, v_{rot}^2 r^{-1}, \tag{7.11}$$

where d is the vertical disk size, and r is the galactocentric radius of the element, the ratio of these two forces is

$$\eta = \frac{f_{ICM}}{f_{ISM}} \sim \frac{n_{ICM}}{n_{ISM}} \frac{r}{d} \left(\frac{\delta v}{v_{rot}}\right)^2 \cos\alpha \sin\alpha. \tag{7.12}$$

n_{ICM} and n_{ISM} are the number densities of the ICM and ISM, respectively. Then, when $\eta < 1$, the ISM motion is little affected, but if it exceeds unity, the ram force disturbs the ISM motion.

Abadi et al (1999) – completing their face-on simulations with two inclined cases, the edge-on and $i = 45°$ case, they noted that their model galaxy lost due to the constant effect of ram pressure in the edge-on configuration about 50% less ISM than in the face-on case. Their Fig. 6 and 7 show that the edge-on stripping event is more efficient than the 45° one.

Quilis et al. (2000) – using a finite difference code with high resolution, Quilis et al. (2000) study the interaction between the hot ICM and the cold ISM of a luminous spiral galaxy similar to the Milky Way. They model the ISM disk as an uniform exponential disk, or as an inhomogeneous disk with either a central hole of 2 kpc radius or with small holes of radii 300 pc. The uniform disk is in the $v_{\rm ICM} = 2000$ km s^{-1}, and $\rho_{\rm ICM} = 2.6\ 10^{-3}$ cm^{-3} stripped to a radius of ~ 3 kpc, while the inhomogeneous disk is stripped completely. Exploring different orientations of the galaxy they show that galaxies inclined twenty degrees to the direction of motion suffer as much stripping as face-on encounters and conclude that except of the edge-on case, the inclination has only a little

effect.

Vollmer et al. (2001a) derive a quantitative relation between the orbit parameters and the resulting HI deficiency containing explicitly the inclination angle. They define the inclination angle between the disk and the orbital plane in such a way that 0° means edge-on stripping and 90° face-on stripping. For the simulations with time-dependent ram pressure profile, they varied the inclination of 0°, 20°, 45°, and 90°. The ram pressure is included only analytically as an additional acceleration of HI clouds in the direction of the galaxy motion. Clouds on the surface of the disk are assumed to shield the clouds located inside the disk. In their edge-on run, the stripping begins at the disk side where the rotational velocity is parallel to the wind direction leading to an armlike structure parallel to the wind direction. A much weaker arm forms at the opposite disk side. When the ram pressure ceases, the dynamics is determined by rotation and re-accretion. Finally, the gas forms a leading $m = 1$ structure.

They found that the stripping takes effect in the face-on configuration before the ram pressure reaches its maximum, whereas for edge-on orientation only after the maximum (see Fig. 7.13). They state that at the initial stages of the ISM-ICM interaction, galaxies with $i < 30°$ may be due to compression highly asymmetric. For low ram pressure maxima and low inclination angles a considerable amount gas accretes back during 200 - 300 Myr. In the case of edge-on stripping the reaccretion achieves a rate of ~ 1 $M_{\odot}yr^{-1}$ and more than 50 % of stripped gas falls back to the disk (contrary to only few percents in the face-on case). They derived an approximative relation for the re-accreted amount as a function of the maximum ram pressure and the inclination angle:

$$M_{accr} \sim 6 \left(p_{ram}^{max}\, sin^2\left[0.9\,(i + 10°)\right]\right)^{-0.7}. \tag{7.13}$$

Concerning the evolution of the central surface density, they note that it decreases in the case of nearly-face-on events, and rises and reaches a maximum (and eventually after $\sim$ 300 Myr a secondary maximum) for nearly-edge-on inclinations. They give another formula determining the amount of the HI deficiency depending on the maximum ram pressure and the inclination angle:

$$\frac{M_{HI}^{in}}{M_{HI}^{fin}} = 0.25\, p_{ram}^{max}\, sin^2[0.9\,(i + 10°)] + 0.84, \tag{7.14}$$

where M_{HI}^{in}/M_{HI}^{fin} corresponds to the fraction between the final and initial total mass. The value of the p_{ram}^{max} in Eqns. 7.13 and 7.14 is normalized by $p_0 = 100$ cm^{-3} (km/s)^2.

Vollmer et al. (2001a) conclude that the amount of stripping depends besides other orbital parameters on the inclination of the disk with respect to the orbital plane. Using a realistic temporal ram pressure profile they observe a phase of re-accretion in which the gas that has not been accelerated to the escape velocity falls back to the galaxy. For weak ram pressures and low inclination angles, the central gas surface density can increase up to a factor of 1.5 within a few 10^7 yr leading to an increase of the local star formation rate up to a factor of 2. Since asymmetries of the HI disk were observed after the closest approach to the cluster center, they speculate that majority of galaxies with a peculiar HI distribution are in the orbital phase after the cluster core passage.

Vollmer et al. (2001b) – using their numerical code from Vollmer et al. (2001a) they show that the observed state of the HI–deficient galaxy NGC 4848 in the Coma cluster can correspond to the operation of a peak ram pressure $p_{ram} \sim 2\,800$ cm^{-3} km^2 s^{-2} during the passage through the cluster center about 4 10^8 yr ago. The gas shifted out of the galaxy during this $i \sim 20°$ ISM-ICM interaction recently reaccretes to the disk and compresses the neutral gas which leads to a phase transition from atomic to molecular gas and to star formation activity.

Schulz & Struck (2001) – performed several simulations with inclined disks and found that such galaxies are stripped on longer timescales and that they are annealed by a stronger loss of angular momentum causing a contraction of galaxies and their further resistance against stripping. They examine the evolution of the angular momentum of the gas disk as another tool for understanding the complex dynamics. They describe two simulation results with 40° and 60°

inclinations of the disk from the z-axis. It corresponds in our notation to inclinations of 50° and 30°. In comparison with their standard model they note several differences: a) after 5.6 10^8 yr much less stripped material remains between the disk and the tail, i.e. the tail is disconnected, b) the ISM particles forming at time of 3 10^8 yr the tail originate from a strong spiral arm appearing in the disk plane at time $\sim$ 3 10^8 yr and being stripped as it rotates into a position where it is moving against the wind. They note an asymmetric distribution of temperatures in the bow shock. When plotting the z-velocity contours on the disk plane projection they see a normal pattern o projected rotation within inner disk parts. Outside this ring the asymmetries are large, c) the initial mass loss in the 40° case is not as rapid as in the face-on orientation, but at the end of the run the stripped amount is comparable (about 25%), d) the 60° run is similar to the 40° one, however it shows a narrower bow shock, and is slightly less effective.

Further, Schulz & Struck (2001) discover that the process of stripping proceeds through the same sequence of phases almost regardless of the disk inclination and value of ram pressure. In inclined cases, more shifted material stays bound to the galactic halo potential and hang up behind the disk. Moreover, in inclined models, more angular momentum for a given amount of mass removal is lost which explains why inclined models appear to have more compact annealed structure.

Marcolini et al. (2003) – run several hydrodynamic simulations of ram pressure stripping in disky dwarf galaxies located in small groups and found that the inclination of the disk plays a role as long as the central disk pressure is comparable to the ram pressure, where for stronger pressures the disk is stripped completely. For the edge-on configuration, they estimate the stripping radius by assuming only the Kelvin-Helmholz instability as the decisive process for the stripping result, provided that ISM rests at radii where the galaxy's gravity can suppress the KH-instability.

Roediger & Brüggen (2006) – they present 3D hydrodynamical simulations of the ram pressure effect on massive galaxies in inclined orientation moving in clusters. They use a constant flow of the ICM characterized by a corresponding ram pressure value, regulated by the varying ρ_{ICM}, while a constant $v_{ICM} = 800$ km s^{-1}. Their standard run is a subsonic flight with $M = 0.8$, completed with several supersonic cases. They state that the evolution of the retained mass and the disk radius are remarkably similar for face-on, 60°, and 30° runs. The face-on and 60° runs are almost identical. They distinguish three phases of stripping in all but edge-on cases: the instantaneous stripping during which the outer parts of the disk are pushed in the wind direction; the intermediate phase characterized by $M_{bnd} > M_{disk}$; and the continuous stripping. The basic point in all aspects is that the stripping process is nearly independent of inclination as long as the inclination is not close to edge-on.

7.3 Simulation results

In this section we use the initial conditions consistent with those in the face-on simulations in Chapter 5: a model galaxy freely falling from 1 Mpc distance towards the cluster center, about which the intracluster medium is distributed within 140 kpc. During its arrival to the ICM distribution, the galaxy evolves. The number of particles of both gaseous types stays unchanged, $N_{ICM} = 120\,000$, $N_{ISM} = 12\,000$. In all simulations in this chapter we have used the LM–type galaxy.

7.3.1 Edge-on case

First, we repeat the standard simulation run through the cluster with $R_{\rm c,ICM} = 13.4$ kpc and $\rho_{\rm 0,ICM} = 4\ 10$ cm^{-3}, but now with the disk in the edge-on configuration. The galaxy passes exactly the same orbit as the face-on galaxy, with its arrival towards to the edge of the ICM distribution at 1.52 Gyr, reaching the cluster center at 1.64 Gyr, and subsequent leaving the ICM at 1.75 Gyr. The fate of the galaxy is followed during 600 Myr, up to the time of 2 Gyr when it occurs at a distance of about 400 kpc from the cluster center, with the ICM ram pressure having ceased long before.

Fig. 7.6 displays face-on-view snapshots of the ISM disk at 25 epochs starting at 1.52 Gyr after

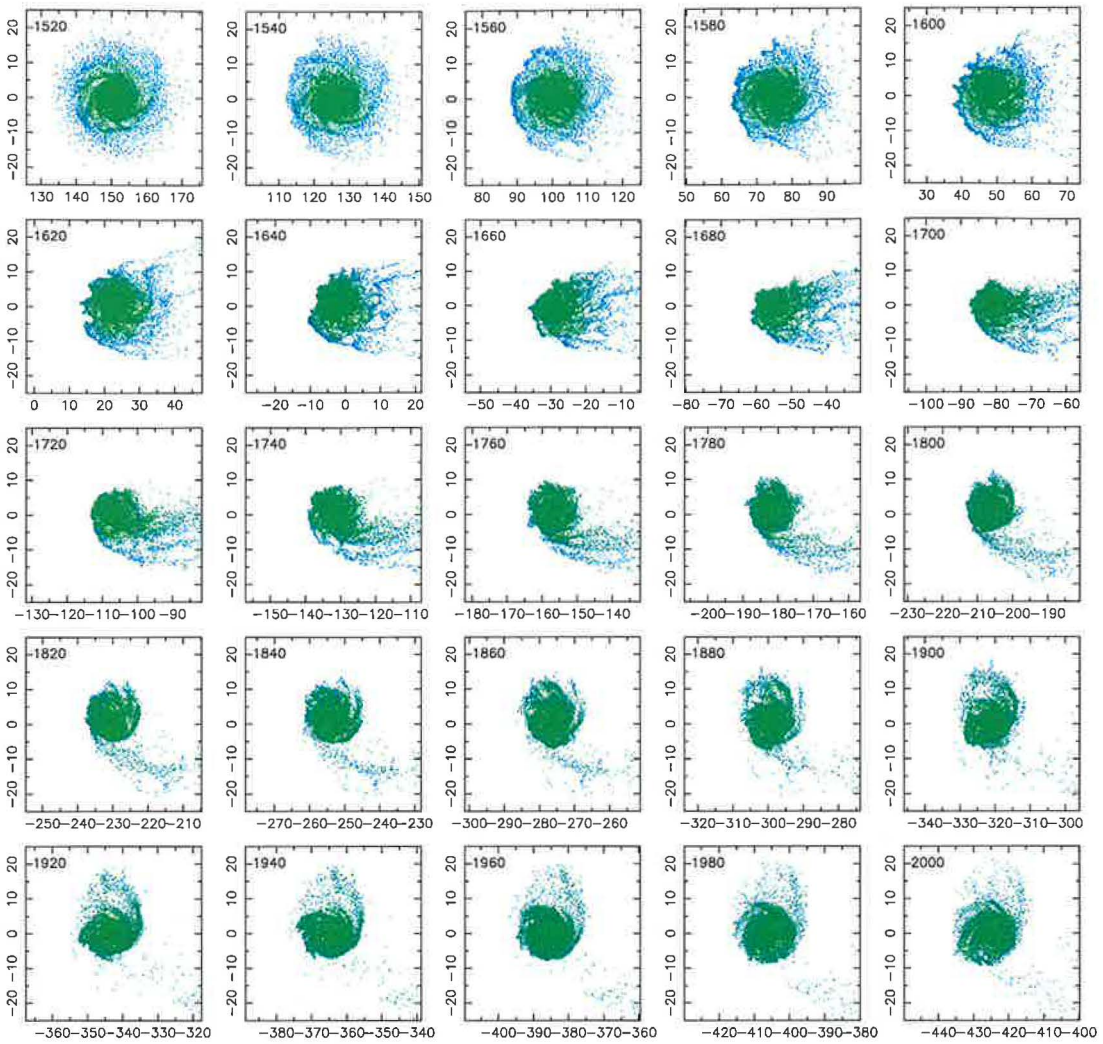

Figure 7.6: Snapshots of the ISM disk of the LM model galaxy flying through the standard cluster with $R_{c,ICM} = 13.4$ kpc and $\rho_{0,ICM} = 4\ 10\ \mathrm{cm}^{-3}$ in the edge-on configuration. At time 1.53 Gyr the galaxy enters the particles of the ICM distribution, and at 1.64 Gyr it passes through the cluster center.

the galaxy's start from the cluster periphery, when it approaches the edge of the ICM distribution, and ending at 2 Gyr, when the galaxy have passed through the ICM and got away to a distance of about 400 kpc from the cluster center. The snapshots reveal that early after the entry of the galaxy into the ICM, the windward (front) side of the disk starts to be compressed by the rising ram pressure, while the rear side is shielded from the ICM influence. This leads to a strongly asymmetric shape of the disk with respect to the axis intersecting the disk center perpendicularly to the wind direction.

As the ram pressure increases, a toothed profile at the front disk side appears at positions of the spiral arms endings, where the ISM is denser and thus more resistant to the stripping than in the inter-arm areas. Due to the rotation, the side of the disk where sense of the rotational velocity coincides with the wind direction (upper side at snapshots view) is more easily stripped which can be further observed in Fig. 7.7 which shows the velocity field of the ICM particles in the surroundings of the galaxy. There, supersonic motion of the galaxy forms a bow shock in the front disk side and the effect of rotation makes the shock envelope asymmetric with respect to the axis going through the disk center in the wind direction. The bow shock is more pronounced at

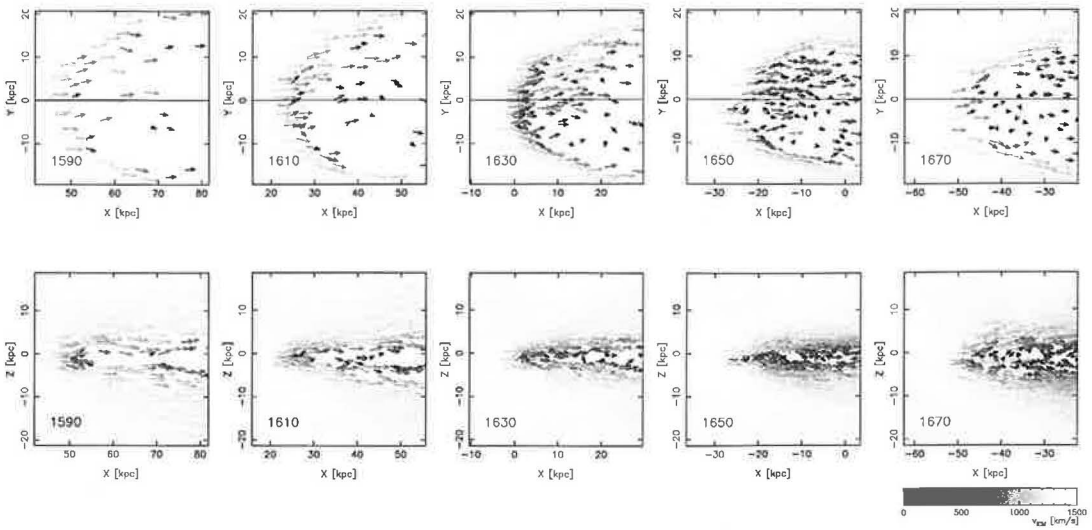

Figure 7.7: Velocity field of the ICM particles at five time instant about the edge-on galaxy's passage through the cluster center. A clear bow shock forms at the location of the windward edge of the disk. Due to galaxy rotation, the bow shock gets asymmetric with respect to the axis passing through the disk center in the wind direction. face:+-2kpc, edge:+-10kpc

the counter-rotating side of the disk, whereas more smoothed at the opposite side. Nevertheless, a sharp entering edge forms in the ISM which is visible in Fig. 7.6.

Shortly after the disk traverses the very cluster center, the windward side gets almost rectangular shape with two straight edges containing almost right angle. This effect could be evoked by a very narrow distribution of the ICM with $R_{c,ICM} = 13.4$ kpc. Then even on scales of the disk diameter, different parts of the disk feel unequal ram pressure. Consequently, the front disk edge is during the passage of the very cluster center quickly compressed, while the material located at that time at the bottom (counter-rotating) side of the disk is not, and when it later gets by the rotation to the front position, the ram pressure has already dropped. It invokes a rectangular shape which thus is a consequence of the short-lasting operation of the strong ram pressure.

During the galaxy's interaction with the ICM, elements from the co-rotating side of the disk are the most affected by the ram pressure since they are the most easily accelerated by the ICM wind. Elements at outer disk radii are directly stripped and released from the galaxy, while those at smaller radii are accelerated in the wind direction. Later, about the time 1.68 Gyr, as the strong ram pressure ceases, the tail of shifted ISM elements starts to be winded up around the disk, it gets narrower and subsequently shifts to locations behind the counter-rotating part of the disk. Finally, the shifted elements accumulate in a one-armed structure. As these elements start about the time 1.8 Gyr to fall back to the disk, they accelerate to velocities that are slightly higher than the rotational velocity at the outer disk radius where the tail is connected, and they overshoot to the co-rotating "upper" disk sector where they accumulate. This loop-like structure then about the time 1.9 Gyr disconnects and the elements fall to the disk (see Fig. 7.6).

As noted above, the rotational time of the LM galaxy is about 300 Myr, which means that in the above cluster configuration, the galaxy rotates roughly 0.8 times during the operation of the ram pressure. And of course, peak of the strong ram pressure is even much shorter and thus not all parts of the disk pass through the region of the strongest (by rotation supported) stripping.

Fig. 7.8 shows velocity field of the ISM particles. The color scale is displayed under the last snapshot, coding velocities from 0 to 800 km s^{-1}. In the first panel, the front part of the disk just entering the ICM distribution shows a narrow strip of particles accelerated by the arising ram pressure. In the next step, these particles are pushed to lower radii as the disk is compressed, and their velocities again lower. But due to the disk rotation, these first witnesses of the ICM interaction are in following $\sim$ 100 Myr released, anyway. Another mark of the disk rotation can be

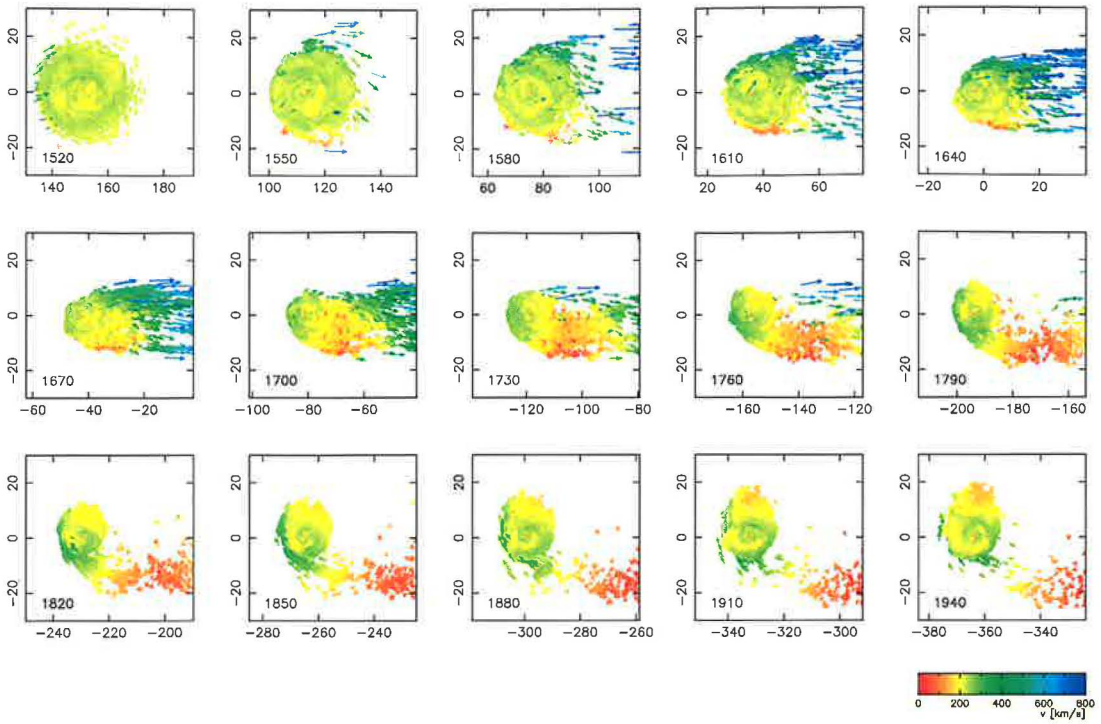

Figure 7.8: Snapshots of the ISM velocity field. Particles firstly accelerated by the ram pressure and supported by the disk rotation are further stripped out or only shifted from the disk. The latter again decelerate and reaccrete to the disk. Asymmetry of the tail of stripped particles is clearly visible.

observed at the same time, when on the counter-rotating side a band of almost staying elements forms, while on the opposite disk side, a zone filled with accelerated elements occurs. About 100 Myr after the galaxy's entry into the ICM, when it passes through the cluster center, a visually rich tail of stripped particles exists. The displaced particles are being accelerated and some of them released. Thus the tail grows and gets longer. Further, when the ram pressure weakens, the region behind the disk becomes filled with particles moving with velocities similar to the rotational speed of the disk (about the time 1.7 Gyr). As the stripping ceases, the tail gets narrower due to the rotation. It is interesting to observe how at $\sim$ 1.76 Gyr the tail starts to disconnect in velocities at the distance of about 20 kpc from the disk center. Elements that decelerate or stop there start to re-accrete on the disk. Consequently, at the region of the disk where the arm of stripped particles is connected, occurs a velocity discontinuity when particles rotating in the disk are joined by much faster reaccreted particles of the tail. The effect of overshooting the reaccreted ISM described above is the best visible at the time 1.85 Gyr when along the whole front disk side elements have higher that rotational velocities and consequently form a bunch of particles at the "upper" side of the disk. Due to the disk rotation, this asymmetry ceases with time.

As described above, at later interaction times the tail of stripped particles is due to the disk rotation wound up and compressed to a form of narrow spiral arm attached to the disk at its rear co-rotating side (with respect to the wind direction). Origin of the ISM forming the tail can be deduced from the corresponding snapshots. Fig. 7.9 focuses on the time instant of 1.82 Gyr when the tail looks the most pronounced, and traces its composition. At this epoch, we identify in the tail the ISM particles that are bound or released from the galaxy, according to their total energy. Three different colors are denoted to the particles – black to the released ones, cyan to the bound ones, and red to the bound and forming the tail ones, respectively. It reveals that the tail is up to $\sim$ 60 kpc distance from the galaxy center composed of bound particles, while at larger distances of released particles. Fixing the corresponding colors to the particles, snapshots back to the initial epochs can be displayed. Then original positions of particles of each group can be traced.

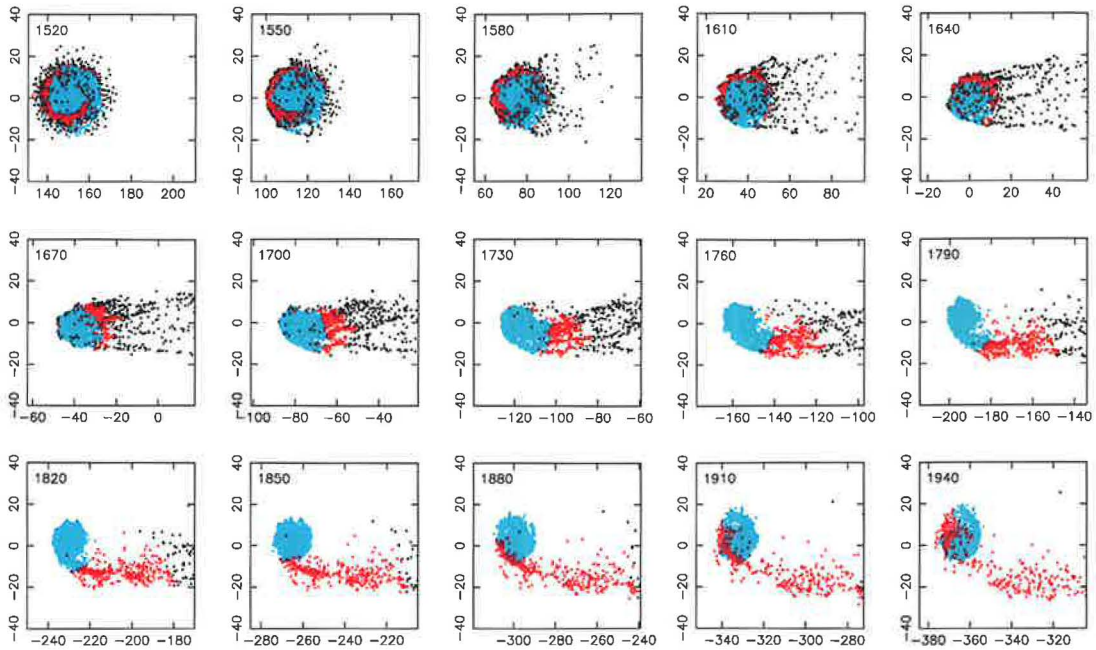

Figure 7.9: Snapshots of the edge-on run tracing the origin of the tail of bound particles at the time 1.82 Gyr. Released, bound, and bound and forming the tail at 1.82 Gyr time instant particles are displayed as black, cyan, and red points, respectively.

Fig. 7.9 confirms what we have expected – at the time 1.82 Gyr bound particles originate from the inner parts of the disk, and released particles from the outskirts of the disk, especially from its front side. Interestingly, the red particles later forming the tail are not distributed symmetrically in the disk, but form an outer disk ring with the most particles at the front side and in the counter-rotating region which gets to the windward edge in about 60 Myr.

Leftmost panel of Fig. 7.10 shows the evolution of the number of ISM particles enclosed within a layer of $|z| < 1$ kpc about the disk plane and sixteen galactic radii from 1 to 16 kpc, with the orbital time. Similarly to the Chapter 5, all ISM particles have the same mass, which implies that their number corresponds to the ISM mass. The upper thick curve gives the total number of particles bound to the galaxy. The number of bound particles slightly decreases right after the galaxy passes at the time $t = 1.63$ Gyr through the cluster center. It is clear that the stripping efficiency of the edge-on configuration in the standard cluster is very low – the fraction of ISM mass remaining bound to the galaxy after the event is 95.3 %, in comparison to $M_{after} = 70.5$ % in the face-on configuration from Chapter 5. Following the curves of the ISM mass within individual radii, the initial compression of the front side of the disk can be traced: at about 1.6 Gyr, a growing tendency of curves corresponding to the radii superior to about 4 kpc is visible.

Due to the recognized asymmetric shape of the disk including a strong arm of shifted particles at one disk side, it is not obvious how to measure the instantaneous radius of the galaxy. Even in Fig. 7.10, the curves of ISM mass within individual radii count in the ISM elements forming at later times the narrow arm of stripped material. Therefore, the profiles do not show any strong evolution, although the snapshots in Fig. 7.6 display a dramatic changes in the disk. It means that the curves do not take into account the strong galactic asymmetry and cannot be used as an indicator of the disk radius. Roediger & Brüggen (2006) study radial profiles of the ISM density, rotational velocity, and projected surface density using twelve radial directions in the disk where they measure the quantities. Then, they define a mean disk radius and the maximum and minimum radii measured in the above mentioned twelve directions. We introduce a similar method, which will be described in the following section.

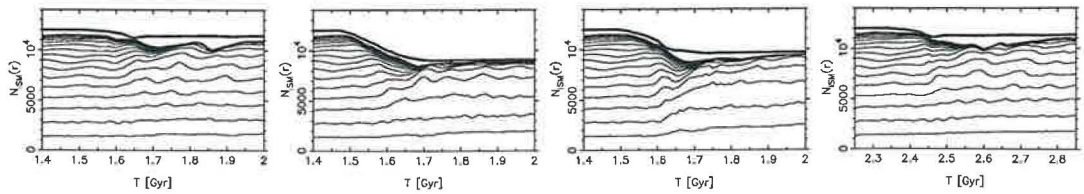

Figure 7.10: Comparison of stripping events for the edge-on disk configuration in clusters with pairs of parameters ($R_{c,ICM}, \rho_{0,ICM}$) equal to: (13.4 kpc, 4 10^{-4} cm^{-3}), (53.6 kpc, 4 10^{-4} cm^{-3}), and (13.4 kpc, 16 10^{-4} cm^{-3}) with the LM galaxy initially freely falling from 1 Mpc distance. Last panel corresponds to the standard (13.4 kpc, 4 10^{-4} cm^{-3}) cluster but with the galaxy starting at 1.5 Mpc distance. Note the compression corresponding to the growing central surface density.

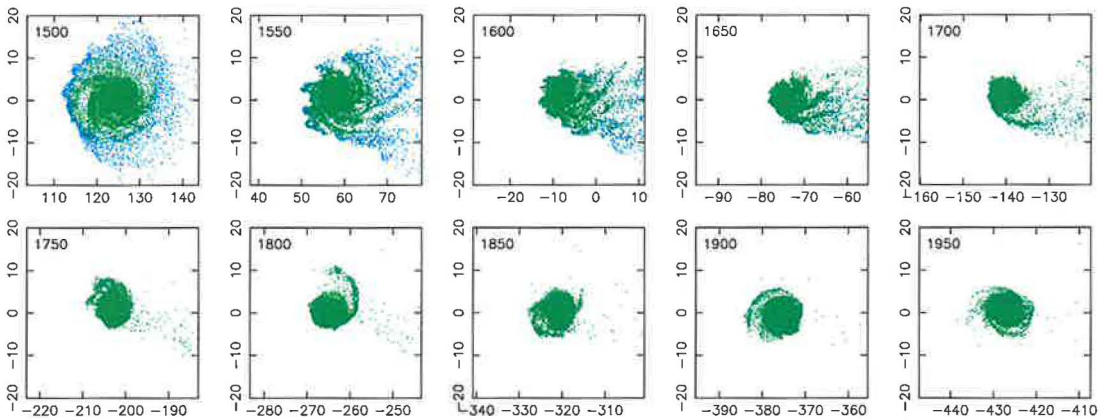

Figure 7.11: Snapshots of the ISM disk of the LM model galaxy in edge-on configuration flying through a wide cluster with $R_{c,ICM}$ = 53.6 kpc. The central density $\rho_{0,ICM}$ = 4 10 cm^{-3}. The galaxy enters the ICM distribution at time 1.48 Gyr, and passes through the cluster center at 1.59 Gyr.

Besides the results of the edge-on run through the standard cluster described above, Fig. 7.10 shows three further edge-on simulations with varying cluster and orbital parameters. The first run corresponds to the LM galaxy flying through a wide distribution of ICM with $R_{c,ICM}$ = 53.4 kpc and $\rho_{0,ICM}$ = 4 10^{-4} cm^{-3}). It is evident that the stripping is substantially more effective, with the final mass fraction of 76 %. Also the compression of the disk is in this case much more pronounced. It is interesting that the number of bound particles in fact coincides with the number of particles within 16 kpc radius. It would indicate that there is no re-accretion of material outside 16 kpc from the galaxy center. But this is only the effect of the disk asymmetry that stays hidden in plots of Fig. 7.10 type. When analyzing the disk at different azimuths, the result could change. See Fig. 7.11 which depicts ten snapshots of this run. Note a narrow arm of particles at 1.8 Gyr and a "curly" structure of the veil of stripped ISM at 1.55 and 1.6 Gyr.

Further simulation was run in a narrow, but highly peaked cluster with $R_{c,ICM}$ = 13.4 kpc and $\rho_{0,ICM}$ = 16 10^{-4} cm^{-3}). The stripping is slightly weaker than in the previous case, but the compression reaching the innermost radii is much more important. As noted by Vollmer et al. (2001a) and Fujita et al. (1999) such compression of the central gas can lead to an short-term increase of the local star formation by a factor of 2. The last simulation leads the LM–type galaxy again to the standard cluster with $R_{c,ICM}$ = 13.4 kpc and $\rho_{0,ICM}$ = 4 10^{-4} cm^{-3}), but it now starts its free-fall orbit at higher a distance: R_{init} = 1.5 Mpc. Thus, the orbital velocity when traversing the cluster center is higher and the ram pressure increases as well. Its peak value is higher by a factor of about 1.33. However, no substantial difference in comparison with the standard case is visible. Table 7.1 summarizes the stripping results of the above four edge-on simulations.

$R_{c,ICM}$ (kpc)	$\rho_{0,ICM}$ (10^{-3} cm^{-3})	R_{init} (Mpc)	M_{final} (%)
13.4	4	1	95
53.6	4	1	76
13.4	16	1	81
13.4	4	1.5	94

Table 7.1: Stripping results of the LM–type galaxy crossing in the edge-on configuration clusters with varying parameters.

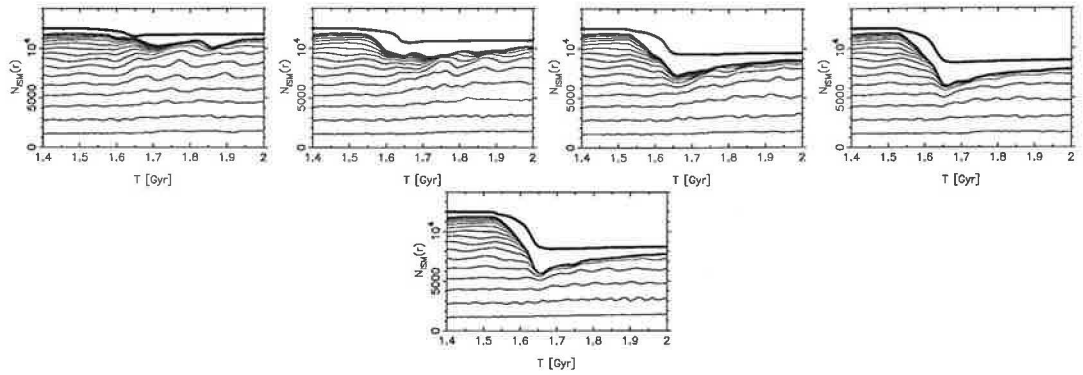

Figure 7.12: Comparison of stripping events for variously inclined LM galaxies. Upper row shows four diagrams of evolution of the number of ISM particles (i.e. the ISM mass) with the orbital time for 0° (edge-on), 20°, 45°, and 70° inclinations of the disk. Second row corresponds to the standard LM face-on run discussed in Chapter 5.

7.3.2 Other inclinations

Further, we have performed three additional simulations of the same system configuration but with varying inclination angles of the disk. Table 7.2 summarizes the stripping results of runs with 0° (edge-on), 20°, 45°, and 70° disk inclination. The process of stripping with orbital time is shown in Fig. 7.12 for $i = 0°$, 20°, 45°, and 70°. The results are compared with the face-on stripping event (lower row). The curves again correspond to the ISM masses enclosed within disk radii in the range of (1 – 16) kpc and within ±1 kpc layer settled on the disk plane. The upper curve represents the total mass of the ISM gravitationally bound to the galaxy. One notes that the stripping efficiencies in the case of $i = 70°$ and in the face-on case are similar. The same trend is described by Roediger & Brüggen (2006).

Table 7.2 gives information following from plots of Fig. 7.12. The final mass M_{final} is the fraction of the bound ISM at the final simulation time of 2 Gyr. Near the cluster center, the fraction of the ISM particles within the evaluation zone is minimum. This value gives the quantity M_{min}. Then the fraction of the ISM that falls back to the disk is M_{accr}, and the fraction of the stripped ISM is M_{strip}. The last column gives the value of the M_{strip} of the face-on galaxy multiplied by sinus of the inclination angle: $M_{strip}(i) = M^{90°}_{strip} \sin i$. When compared to values of the M_{strip} measured in individual simulations, one notes a good agreement with this simple formula.

Fig. 7.13 extracts results from the plots of Fig. 7.12. It shows the total mass of the ISM bound to the galaxy as a function of the orbital time for the above five inclinations ($i = 0°, 20°, 40°, 70°$, and 90°). The difference between the face-on case and $i = 70°$ orientation is of course the minimum. Further, the ISM mass within 16 kpc distance from the galaxy's center and ±1 kpc about the disk plane is shown for the same inclinations. It can be noted that in the face-on or $i = 70°$ case, the displacement of elements out of the evaluation cylinder starts about 50 Myr earlier than in the edge-on case. While the edge-on shift of ISM elements is very slow and gradual with a minimum value far behind the cluster center passage, in the $i = 20°$ orientation the ram pressure pushes the

i (°)	M_{final} (%)	M_{strip} (%)	M_{min} (%)	M_{accr} (%)	$sin\, i$	$M^{90°}_{strip} \cdot \sin i$ (%)
0 (*edge-on*)	95.4	4.6	86.8	8.6	0.00	0.0
20	90.9	9.1	75.3	15.6	0.34	10.0
45	82.0	18.0	61.8	20.2	0.71	20.9
70	72.9	27.1	52.8	20.1	0.94	27.7
90 (*face-on*)	70.5	29.5	48.7	21.8	1.00	29.5

Table 7.2: Stripping results of the LM–type galaxy crossing the standard cluster on a completely radial orbit with different inclinations of the galactic disk: 0°, 20°, 45°, 70°, and 90°.

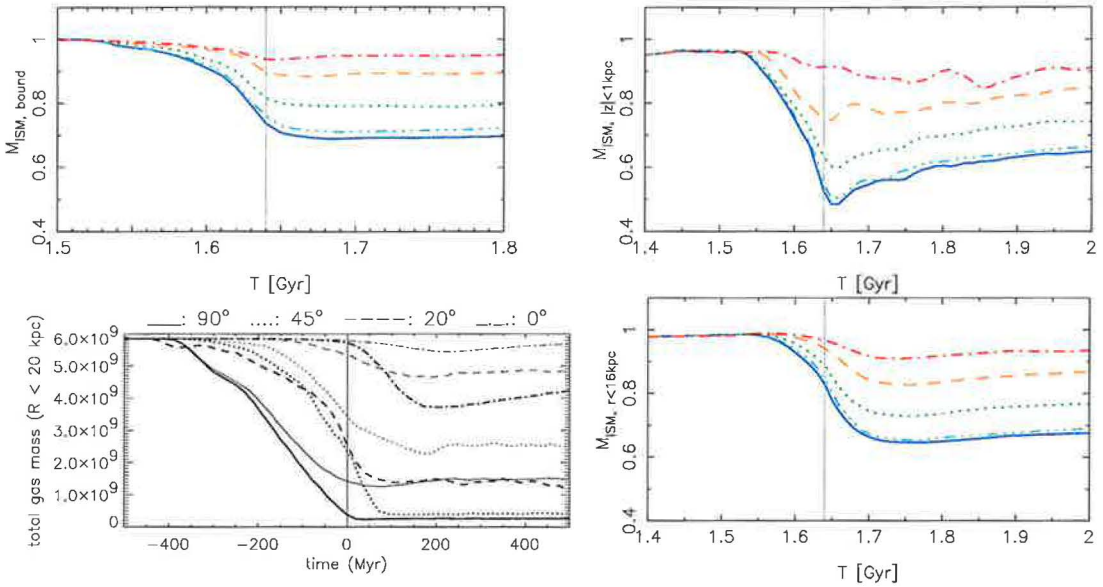

Figure 7.13: Total mass of the bound ISM (first panel), mass of the ISM within a cylinder of 16 kpc radius from the galaxy center and ±1 kpc height about the disk plane (second panel), and mass of the ISM within 16 kpc sphere about the galaxy center (fourth panel) as functions of the orbital time. Curves correspond to various inclinations: face-on (blue solid), 70° (cyan dot-dot-dashed), 45° (green dotted), 20° (orange dashed), and edge-on (red dot-dashed). For comparison, Fig. 13 of Vollmer et al. (2001) showing the total gas mass within the galaxy's radius $r = 20$ kpc and a constant height of 1 kpc is shown (third panel). Vertical lines show the instant of galaxy's passage through the cluster center.

ISM out of the disk area faster and the epochs of the minimum value of the ISM coincides with the cluster center passage. Results of our simulations are compared with Fig. 13 of Vollmer et al. (2001) which displays the total gas mass within the galaxy's radius $r = 20$ kpc and a constant height of 1 kpc. In this figure, Vollmer et al. (2001) show that effects of the ram pressure on the ISM appear earlier for higher inclination angles. In their face-on run through a maximum ram pressure of 10 000 $cm^{-3}km^2s^{-2}$, the stripping begins about 300 Myr before the maximum, while for a maximum of 2000 $cm^{-3}km^2s^{-2}$ and the edge-on orientation stripping begins about 50 Myr after the maximum is reached. Vollmer's figure can be compared to the second panel of Fig. 7.13 but as they display results from runs with different maximum values of the ram pressure (stronger in the face-on case, and weaker in the edge-on case), while we keep the configuration unchanged in all the cases, the comparison is not straightforward. Generally speaking, the trend described by Vollmer et al. (2001) seems to be similar in our simulations but we cannot say that the edge-on stripping begins after the passage through the cluster center, only later than the face-on stripping.

We note that the time delay of the edge-on stripping with respect to more inclined cases

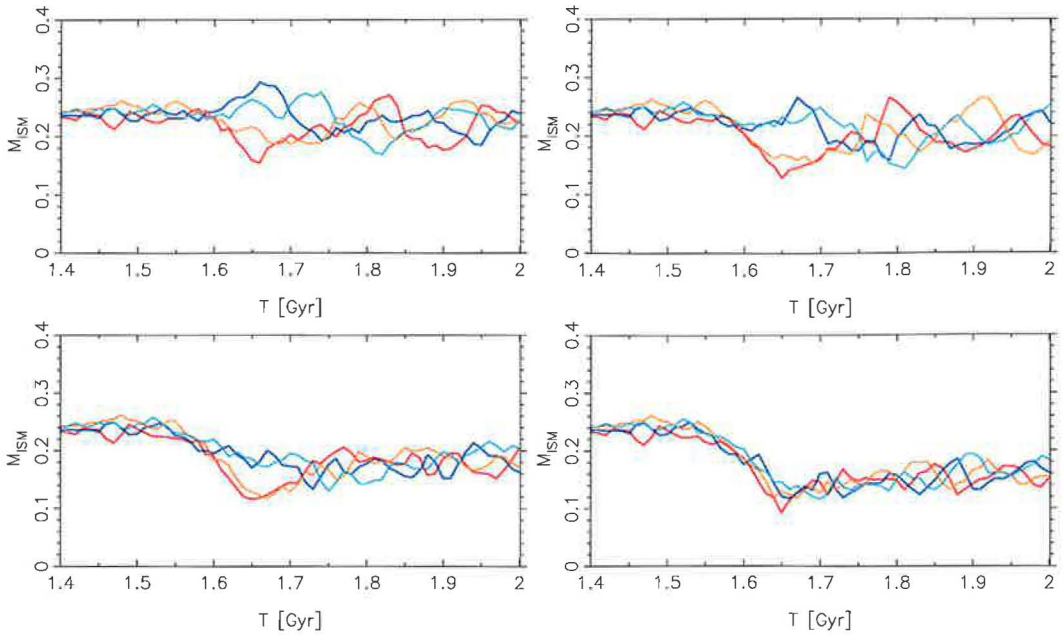

Figure 7.14: Mass of the ISM in different sectors of a fixed cylinder of radius 16 kpc and height ±1 kpc centered on the disk plane. The cylinder is divided into quadrants along the disk axes perpendicular and parallel to the wind direction. The sectors in the edge-on orientation are: the front counter-rotating (red), the front co-rotating (orange), the rear co-rotating (blue), and the rear counter-rotating (cyan). Panels from left to right and top to bottom correspond to edge-on, 20°, 45°, and face-on inclinations.

corresponds to the shape of the evaluation zone, which may be disadvantageous for the edge-on and low-i cases. In the face-on orientation the elements have to surpass only about 1 kpc distance to leave the evaluation layer, but in the edge-on case the shifted elements have to pass (depending on their azimuth) a larger distance which may be comparable to the radius of the evaluation zone. Of course, the elements that are affected by the ram pressure but pass through the disk towards the edge of the zone cannot be identified by this method. Thus, in the third panel of Fig. 7.13, we depict the total ISM mass enclosed within a sphere of 16 kpc radius about the galaxy center.

Another problem of the above evaluation zone enclosing the original disk is that it gives only an averaged information corresponding to each galactic radius. As described above, the stripped disks are in inclined cases highly asymmetric with structures like tails of stripped elements or the arms of re-accreted ISM. These features stay hidden in plots of Fig. 7.12–type. In Fig. 7.14, the evaluation cylinder of 16 kpc radius and ±1 kpc of height settled on the disk is therefore divided into four sectors along the main disk axes perpendicular and parallel to the wind direction. With respect to the ICM wind, the front counter- and co-rotating quadrants of the disk in the edge-on orientation correspond to the red and orange curves, and the rear co- and counter-rotating quadrants to the blue, and cyan curves, respectively. Then, asymmetries of the disk are easily visible. Initially, all sectors possess roughly the same amount of the ISM. As the ram pressure grows, the front parts loose the material, unequally due to the rotation. The accelerated material shifts to rear parts of the disk and corresponding curves increase. Later, the tail of shifted elements is wound up to the disk and the rear counter-rotating sector profits by the re-accretion. The returned elements than get to all sectors and the disk almost symmetrizes. When going to higher inclinations, the curves get closer, and in the face-on case they follow each other, including the central cluster period.

As noted above, Roediger & Brüggen (2006) define twelve radial directions in which they follow the values of characteristics that depend on galactic radius. To determine the stripping radius of the galaxy at the final simulation time we firstly employ a method similar to Roediger & Brüggen (2006) – we divide the disk plane into twelve sectors and measure the number of ISM particles in

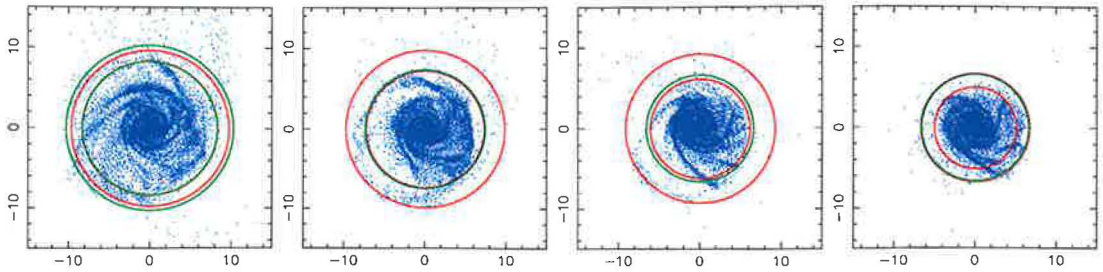

Figure 7.15: Determination of the stripping radius at final simulation time of 2 Gyr using two different methods described in text for galaxies with $i = 0°$, 20°, 45°, and 70° inclinations.

radial shells. The outermost shell of a given sector in which the number drops under certain low value, is declared as the stripping radius of the sector. Then, the maximum and average radius is found from all the twelve sectors and the stripping radius is set either to the average, or to the maximum value.

The second method is based on searching in what radius of the disk a fraction of the finally bound ISM is enclosed. Applying it to the edge-on case, radii containing 90 and 95 % of the M_{final} roughly correspond to the average, and maximum radius from the former method, respectively.

In both the mentioned methods a number of particles is followed in ±1 kpc thick layer about the disk plane. As galaxies move through the ICM, the ram pressure shifts the ISM elements out of the disk roughly in the wind direction. Then, elements staying bound but shifted from the face-on galaxies reach high off-disk distances, while elements from the edge-on galaxies stay almost all in the disk plane. This in fact geometrical effect of the disk inclination therefore affects the above counting methods since edge-on galaxies have almost all the ISM within the evaluation layer, contrary to the face-on galaxies. Only at very later time when all the shifted elements would fall back to the disk plane, one could determine the stripping radii of variously inclined galaxies using either method. But the process of re-accretion takes a long time, and meanwhile, it is not clear how to distinguish whether the outer ISM in an edge-on galaxy is already reaccreted or not.

Thus, the instantaneous radii of galactic disks are dependent on the inclination not only from the point of view of the stripping efficiency but also from the geometrical reasons, and their determination is not fully consistent. Fig. 7.15 depicts the face-on views of the ISM disks of galaxies with $i = 0°$, 20°, 45°, and 70° inclinations. The concentric circles correspond to the radii determined using the two above methods – the average and maximum radii at which the ISM density falls below some low value (red), and the radii within which 90 and 95 % of the bound mass is enclosed (green), respectively. In all cases with inclination higher than 0°, the 95%–radius is not shown since the whole disk does not contain 95% of the bound ISM.

In the edge-on, 20°, and 45° case, the 90%–radius coincides with the average radius, whereas in the 70° (and face-on) case with the maximum radius. This corresponds to the geometrical effect described above. Table 7.3 summarizes the results of Fig. 7.15.

Fraction of the total bound ISM mass enclosed within increasing galactic radii and ±1 kpc height about the disk plane is shown in Fig. 7.16 for the five different disk inclinations. Finding the intersection of the curves with the line of 0.9 M_{bound} in this figure in fact illustrates the principle of the second method of the radius determination.

Fig. 7.17 displays snapshots of the runs with $i = 0°$, 20°, 45°, and 70° at five orbital epochs in the range of (1.52 – 2) Gyr from the beginning of the free fall from the cluster edge. Face-on and edge-on views are depicted. The first thing to note is the decreasing asymmetry of the stripped disk at $t = 1.64$ Gyr when going to higher inclinations. Such asymmetry of course causes a torque on the disk. The front edge of the inclined disks is under the operation of the ram pressure compressed and visibly rough since the ISM of uneven density is differently stripped from spiral arms and inter-arms positions of the disk. After passing the cluster center, the process of reaccretion of bound particles starts. In an inclined configuration, the shifted ISM reaccretes in the way described earlier – the tail of bound particles is wound up to the disk due to the galactic

i (°)	R_{avg} (kpc)	R_{max} (kpc)	$R_{90\%}$ (kpc)	$R_{95\%}$ (kpc)
0	8.3	9.7	8.3	10.3
20	7.3	9.8	7.4	–
45	6.1	9.2	6.6	–
70	5.1	6.7	5.6	–

Table 7.3: Stripping radii of galaxies with four different inclinations of the disk determined at the final simulation time of 2 Gyr by two different methods (see text).

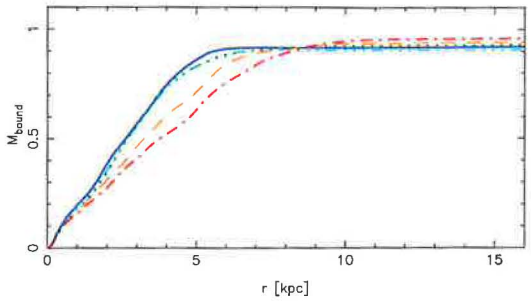

Figure 7.16: Fraction of the ISM mass bound to the galaxy at the final simulation time of 2 Gyr as a function of the galactic radius. Situation for five inclination is displayed: face-on (solid), 70° (dot-dot-dashed), 45° (dotted), 20° (dashed), and edge-on (dot-dashed).

rotation, later it disconnects when the elements closer to the disk start to fall back to the galaxy, while the more distant particles of the tail are only decelerating. The reaccreting ISM then falls to the disk along the tail connection to the disk and accelerates to velocities superior to the rotation velocity. Consequently, they get again to higer radial positions on the co-rotating side of the disk where they form a loop-like feature. Especially in the $i = 20°$ case, clumps of the ISM are clearly visible in the loop. In real galaxies, such density condensations could become places of observable star formation.

It is interesting that this loop-like structure of the reaccreted material (best visible about the time 1.88 Gyr), forms at the identical position in cases of all inclinations, but gets weaker when going towards the face-on orientation. At the final simulation time ($t = 2$ Gyr), this loop has changed into an off-axis ring best visible in the $i = 20°$ case (see Fig. 7.19). When comparing the snapshots in the final simulation time, it shows that galaxies with higher inclinations ($i = 20°$, 90°) have almost symmetrical disks, while in lower inclination cases, it would need a longer time to pass the above described features and symmetrize the disk.

We conclude, that in all displayed cases one can follow similar features that however fade when going from the edge-on orientation to cases with higher inclinations.

Shapes of the tails of stripped material are compared for the discussed cases in Fig. 7.18. It is clear that the higher the inclination, the broader the tail. In the case of $i = 20°$, the tail is visibly narrower at higher distances behind the disk, while in higher inclinations, it extends. Further, in higher inclinations, the envelope of the tail seems to be more pronounced compared to less inclined disks. It is interesting to follow a clumps of gravitationally bound particles in the tails.

Fig. 7.19 focuses on the above mentioned interesting annular structure that forms in the 20° inclination case at the final simulation time. The circle of ISM particles lies in the disk plane at the front disk side (with respect to the wind direction) and its center does not coincides with the galactic center but is shifted about 2 kpc aside. Right panel displays velocity field of the situation. Particles forming the annulus were originally shifted from the disk while staying bound.

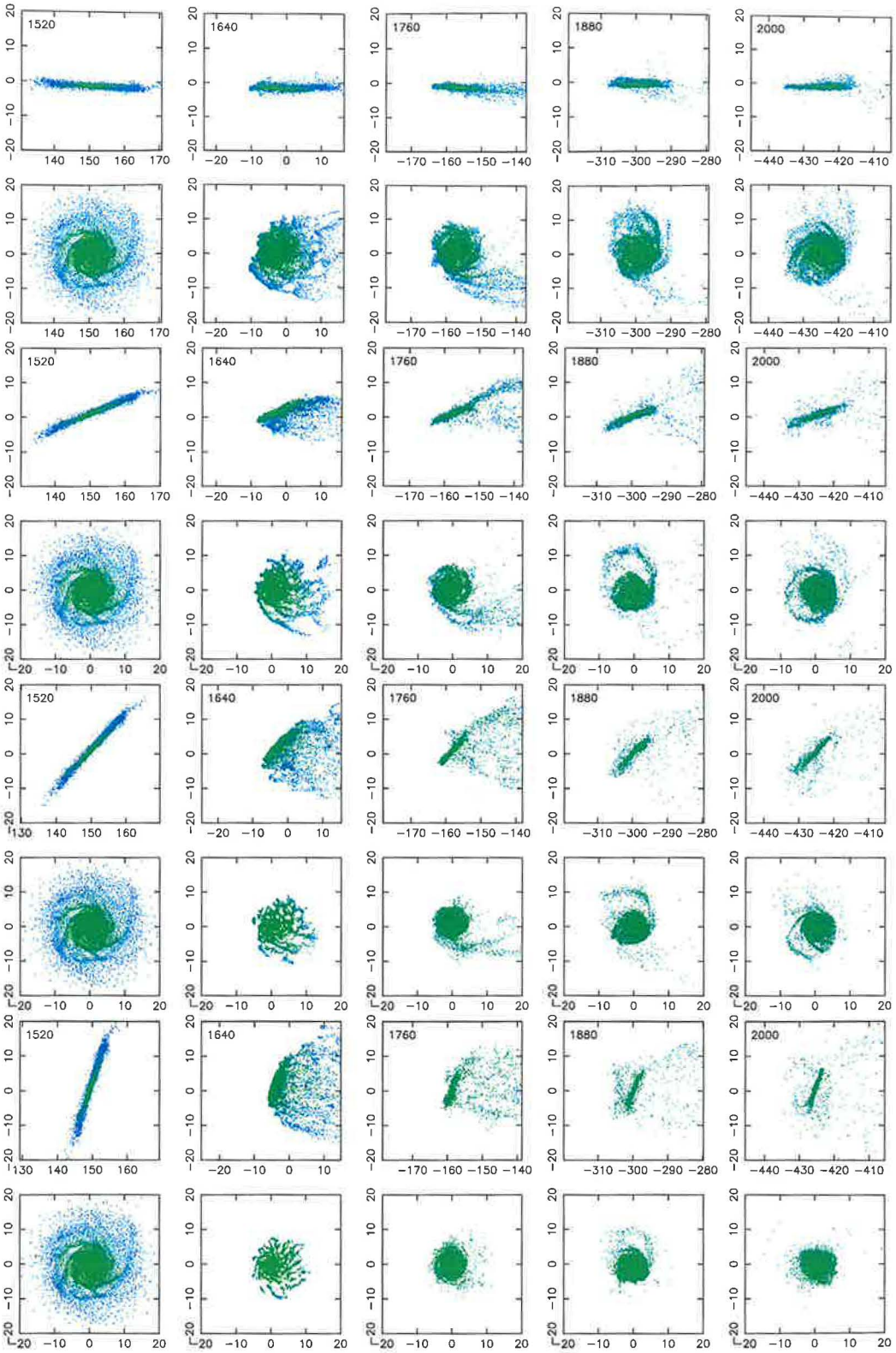

Figure 7.17: Edge-on and face-on snapshots of the LM–type galaxy crossing the standard cluster with different orientation of the disk: $i = 0°$, $20°$, $45°$, and $70°$.

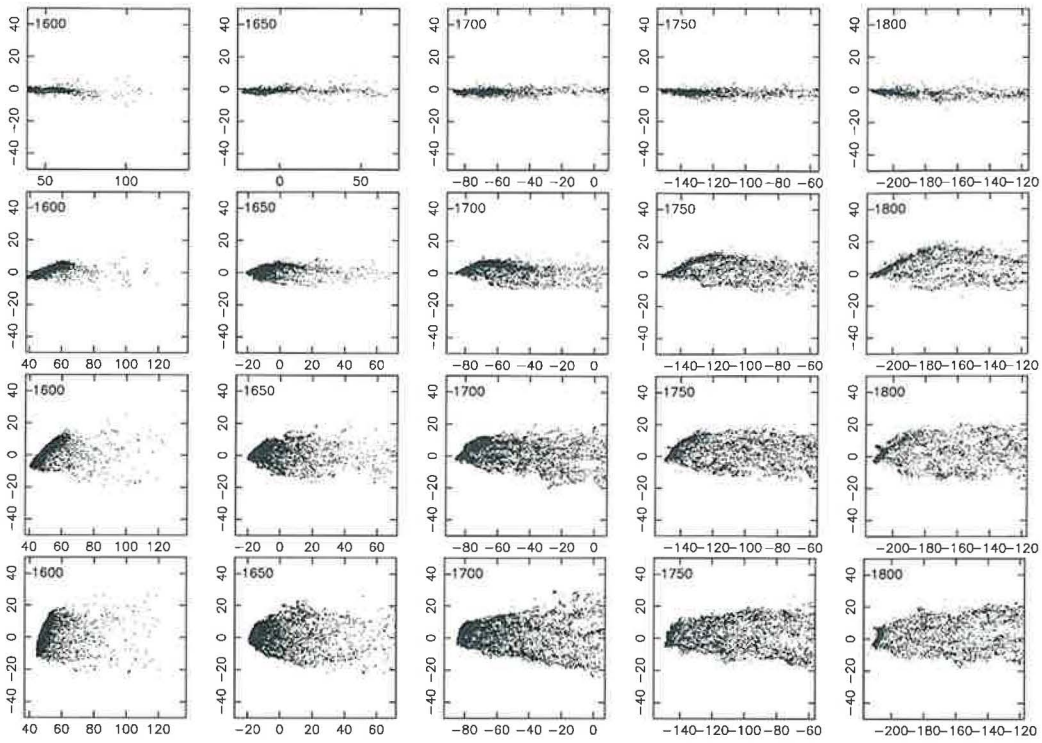

Figure 7.18: Tails of stripped material in the case of $i = 0°$, $20°$, $45°$, and $70°$ galaxies (from top to bottom).

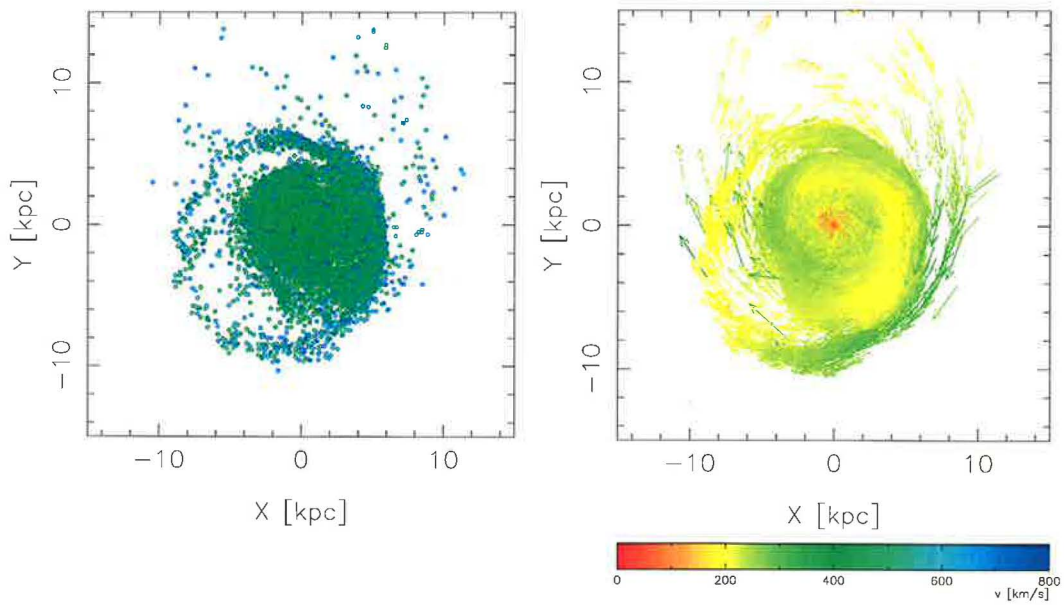

Figure 7.19: Detail of the annular structure having formed in the $20°$ inclined galaxy about 350 Myr after its passage through the cluster center.

Chapter 8

Numerical simulations: General cases

So far, we have been concerned with galaxies interacting with the intracluster medium of galaxy clusters when moving on strictly radial orbits leading the galaxies to the very cluster center. Chapter 5 focused on galaxies with the face-on orientation of the disk with respect to the direction of the orbital motion, and chapter 7 on galaxies with disks of various inclinations, but again on radial orbits leading through the densest cluster regions. However, it is clear that members of galaxy clusters move on general orbits with various ratios of apocentric to pericentric distances. Such orbits brings them to cluster regions with different ICM densities, while moving at supersonic speeds near the pericenter and at subsonic speed when leading to the apocenter regions. What is the distribution of orbital shapes in real clusters and how it depends on different cluster populations?

8.1 Orbits of cluster galaxy populations

The problem of recognizing the distribution and kinematics of galaxies populating the galaxy clusters is closely connected to the question of the determination of the mass distribution in clusters. Already in thirties, Zwicky (1933, 1937) estimated using the virial theorem the total masses of the best known clusters, the Virgo and Coma clusters. It provided the first evidence of dark matter. Zwicky considered the cluster member galaxies to be tracers of the cluster potential, what remains the key assumption in using galaxy kinematics to derive the gravitational potential of the dark matter. But, since galaxies constitute only a small fraction of the total cluster mass, their velocity distribution could differ from that of the dark matter, although in the standard scenario, galaxies form at centers of dark matter halos and thus are likely to have their orbital distribution connected to that of the dark matter.

At the same time, knowledge of the orbital characteristics of member galaxies can provide information about formation and evolution of clusters themselves. Since clusters are still accreting galaxies, their orbits are not relaxed and can be random. Such galaxies which are probably on their first approach to the central dense core of the cluster then become subjects to the ram pressure stripping. On the contrary, early–class galaxies were probably part of the clusters at the time of their formation, and due to relaxation, their orbits have isotropized.

Since different cluster populations show different distribution, the assumption that the orbital distribution is connected to that of the dark matter is unlikely. The orbital distribution of galaxies remains a major source of uncertainty in determining the mass profiles from the cluster dynamics.

Pryor & Geller (1984) constrain the orbits of HI-deficient galaxies by assumption that they had to cross the cluster core regions to be stripped of their gas. Merrifield (1998) suggests to determine the galaxy orbits using the observations of radio or X-ray trails in the ICM.

Introducing a parameter of the orbital anisotropy:

$$\beta(r) \equiv 1 - \frac{\langle v_t^2 \rangle (r)}{\langle v_r^2 \rangle (r)}, \tag{8.1}$$

where $\langle v_t^2 \rangle (r)$ and $\langle v_r^2 \rangle (r)$ are the mean squared components of the radial and tangential velocity. Then, an isotropic velocity distribution corresponds to $\beta = 0$, radial orbits have $0 < \beta < 1$, and tangential orbits $-\infty < \beta < 0$.

Benatov et al. (2006) examine to what extent the intracluster medium and member galaxies can trace the potential of clusters. They combine the method of gravitational lensing, and results of the temperature and surface brightness X-ray observations, for the determination of the mass distribution. Using the measured galaxy velocities, they solve the anisotropic Jeans equation which applies to collisionless, spherically symmetric systems of particles, and obtain a formula for the orbital anisotropy parameter β. In their sample of five clusters, they find a variety of orbits – two of the nearby clusters appear to have mainly tangential orbits in the region out to 1 Mpc distance, whereas another shows mostly radial orbits. On the contrary, distant clusters are dominated by radial orbits.

Biviano & Katgert (2004) deal with the cluster galaxies from the ESO Nearby Abell Cluster Survey. They divide the cluster galaxies into several types, and estimate the mass density profile of the "ensemble cluster". Among the galaxies located outside recognized substructures they distinguish four galaxy classes, according to their projected phase-space distributions: the brightest ellipticals, the other ellipticals together with the S0's, the early-type spirals (Sa-Sb), and the late-type spirals and irregulars (Sbc-Irr). Based on the shape of the velocity distribution, the early-type galaxies are assumed to be on isotropic orbits. Data for the early spirals confirm their isotropic orbits, except a radial anisotropy at $0.45r_{200}$. On the other hand, the data for the late spirals reject the isotropic orbits and these are found on mildly radial orbits. The fact that early galaxies follow isotropic orbits is consistent with the assumption that they form the oldest cluster populations. The density profile of late galaxies shows that they almost avoid the inner $0.2 - 0.3r_{200}$ cluster region. This supports the idea that late galaxies are on their first infalling orbits.

Vollmer et al. (2001a) state that the strength of all stripping mechanisms possible depends crucially on orbits of galaxies. Radial orbits bring the cluster member galaxies deeper into the cluster, where the ICM density substantially increases, together with other galaxy spatial density, and the galactic orbital velocity. Further they note that both the observations of HI-deficient galaxies, and numerical simulations support radial orbits. Ghigna et al. (1998) studied the properties of dark matter haloes hierarchically formed in rich galaxy clusters using high-resolution simulations. Following about 150 halos, they estimate the median ratio of apocentric to pericentric radii to 6:1. The orbital distribution is close to isotropic, with circular orbits being rare, and radial orbits common. About 20 % of all formed halos pass within central 200 kpc, i.e. $0.1R_{200}$. Vollmer et al. (2001) model the M87 subcluster of the Virgo cluster in the presence of the gravitational potential of the giant elliptical galaxy M86. The latter brings into the system a perturbation affecting both the trajectory of the test galaxy, and the motion of the M87. The orbit of the test galaxy consequently changes from a planar one with a constant pericentric distance to the cluster center, to a complex 3D trajectory with a variation of the impact parameter and the maximum velocity for each cluster center approach. Concerning the shape of the orbits of observed HI-deficient galaxies in the Virgo cluster, Vollmer et al. (2001) refer to their simulations showing that spiral galaxies on radial orbits, and thus sufficient level of the ram pressure corresponding to the observed HI-deficiency, cannot occur at observed positions in the radial velocity vs. projected distance plot. They suggest another explanation related to the presence of the M86 subcluster that infalls to the M87. If the M86 originally entered the M87 with its own population of spiral galaxies, these could have been captured on orbits very different from the settled ones in the M87 cluster. Then a special galaxy population can arise with high radial velocities at large projected distances, as observed in the case of HI-deficient galaxies.

In conclusion, the velocity distribution of member galaxies depends on the cluster population: that of the early–types is virialized and that of the late–types is non-Gaussian with a broader distribution. Fig. 14 of Boselli & Gavazzi (2006) shows the velocity distribution of member galaxies of A1367, Coma, and Virgo clusters with the above mentioned profiles. It suggests that late–type galaxies are free falling into the cluster. In the Virgo cluster, two clouds of spiral galaxies belonging to the subclump A are observed with significantly different velocity distributions, which could indicate that they are falling onto the subclump A at velocitites at about 500 km s^{-1} (Gavazzi et al. 1999).

8.2 Existing non-radial simulations

It is clear that the stripping efficiency is related to the shape of the orbit since two crucial parameters affecting the stripping change during the flight on the orbit: density of the ICM, and galactic velocity. Moreover, since the disk plane keeps its orientation in space, its inclination with respect to the orbital direction varies with time. Such a dependence of the inclination angle is important for the stripping history since it is its value in the pericentric parts of the orbit, when the galaxy moves fastest and through the densest ICM, that affects the stripping result.

Vollmer et al. (2001) perform numerical simulations described already in Chapters 7, and 2. They deal with galaxies on non-radial orbits including the ram pressure as an additional analytic force acting only on outer layer of the disk. The time varying profile of the ram pressure corresponding to the orbital motion of the galaxy on an orbit is approximated by a Lorenzian profile of the analytic external force. Then, the ram pressure has a realistic evolution with time, but the effect of varying inclination angle along the orbit is not taken into account.

Toniazzo & Schindler (2001) use an Eulerian three-dimensional hydrodynamical code including cooling. They study the interaction of elliptical galaxies with the intracluster medium during their motion on non-radial orbits with pericentric-to-apocentric ratios of 1 : 2.8, and 1 : 2.3 leading them to about 300 kpc minimum distance to the cluster center. The gas dynamic evolution differs in different parts of the orbit: near the pericenter the galaxy's velocity exceeds the sound speed of the ambient medium and the ram pressure is effective. They note that a major stripping occurs if the kinetic pressure grows rapidly to a value of the order of the galactic central thermal pressure, over a time smaller than the sound crossing time of the ISM. Otherwise, the stripping is more gradual. On the contrary, near the apocenter the orbital velocity is subsonic, and the gas dynamics evolution is dominated by another physical phenomena – the gas–mass replenishment, radiative cooling, Kelvin-Helmholz instability etc.

8.3 Simulation results

According to radial orbits recognized for late-type galaxies in galaxy clusters, what was discussed in the previous section, we perform a set of simulations with the LM model galaxy moving on orbits differing from the strictly radial one. The motion is confined to planar orbits characterized by a single parameter α. This parameter determines with what fraction of the circular velocity the galaxy sets out from its starting location in the direction of the circular motion. Only the velocity component perpendicular to the cluster center direction is thus non-zero. Then, $\alpha = 1$ corresponds to the circular motion of the galaxy about the cluster center, and $\alpha = 0$ sends the galaxy on the radial orbit passing through the very cluster center. Therefore, when $\alpha \neq 0$, the galaxy does not freely fall directly towards the cluster center, as it was the case in Chapters 5 and 7, but gets to off–center regions with lower values of the ICM density. Fig. 8.1 shows shapes of orbits with $\alpha = 0.1$ (blue), 0.3 (cyan), 0.5 (green), 0.7 (orange), and 1 (red). The starting point is common for all the orbits and lies at 1 Mpc distance in the z-direction. At each orbit, labels indicate the orbital time elapsed from the starting point, with step of 0.5 Gyr. One circular orbit takes to the galaxy about 7.6 Gyr. With growing α, the ICM density declines at pericentric stages of orbits and the maximum orbital velocity decreases. Thus the maximum ram pressure acting on

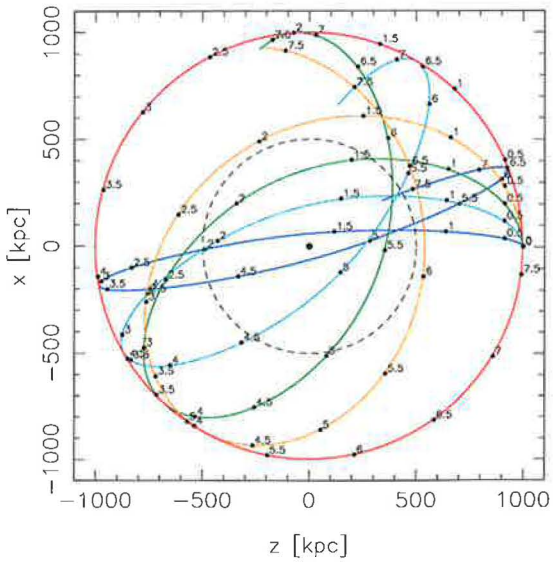

Figure 8.1: Shapes of galaxy orbital trajectories used in simulations of non-radial stripping events. The starting point at 1 Mpc distance is common for all the orbits differing in value of the parameter α which determines the fraction of the radial velocity that is assigned to the initial v_x-velocity component: 0.1 (blue), 0.3 (cyan), 0.5 (green), 0.7 (orange), and 1 (red). The dashed circle defines the area filled up with the ICM particles. The gravitational potential of the cluster corresponds to the standard DM distribution and $R_{c,ICM} = 53.6$ kpc and $\rho_{0,ICM} = 4\ 10^{-3}$ cm^{-3} (see Chapter 3).

the galaxy diminishes.

Fig. 8.2 illustrates orbital characteristics of trajectories depicted in Fig. 8.1, completed with the strictly radial case $\alpha = 0$. Second to sixth panel show the following quantities as functions of the orbital time: radial distance r from the cluster center, inclination angle i of the disk plane with respect to the instantaneous orbital direction, orbital velocity v, density of the ICM ρ_{ICM} along the orbit, and profile of the ram pressure p_{ram} along the orbit. As mentioned above, when $\alpha \neq 0$, the inclination of the disk is not constant during the galaxy's flight through the cluster. Assuming that the galaxy starts with the disk plane oriented perpendicularly to the cluster center direction, its initial inclination with respect to the orbital direction is edge-on. As the component of the orbital velocity in the cluster center direction (z) becomes non-zero, the inclination increases, exceeds 90°, and when approaching the second apocenter, it reaches 180°. From the point of view of the ram pressure stripping, the critical is the inclination when passing through the densest cluster regions. In the case of $\alpha = 0.1$ orbit, this central inclination is almost face-on, but the more is the orbit getting circular, its value decreases.

Orbital characteristics of all the trajectories are summarized in Table 8.1. The pericentric-to-apocentric ratio, together with the maximum orbital velocity at the pericentric position, and the peak ram pressure value are stated. Clearly, the maximum orbital velocity decreases with growing α towards the value of the circular velocity. This decrease, together with a strong fall of the ICM density, evokes a drop of the ram pressure from the central to outer cluster regions by a factor 200.

Similarly to Toniazzo & Schindler (2001), who follow the stripping effects in galaxies moving on orbits with pericentric-to-apocentric ratios of roughly 1:3, and 1:2, we choose for our simulations three orbits characterized with $\alpha = 0.1$, 0.3, and 0.5, in Fig. 8.1 corresponding to blue, cyan, and green curves. The first value corresponds to an extremely radial orbit with the pericentric-to-apocentric ratio of 1:17, while the latter two to mildly-radial ones with $r_{peri}/r_{apo} \sim$ 1:5, and 1:3.

The ICM distribution in our standard model from the previous chapters has a very narrow profile with $R_{c,ICM} = 13.4$ kpc. Since now we want to study the stripping effects occurring on orbits leading the galaxy to off-center cluster regions, a wider profile has to be used to achieve clear results. Therefore, in simulations we assume the ICM distribution with $R_{c,ICM}$ parameter

α	r_{per}/r_{apo}	v_{max} (km s^{-1})	$p_{ram,max}$ (cm^{-3}(km/s)^2)
0	–	1342	6888
0.1	1:17	1333	3690
0.3	1:5	1274	886
0.5	1:3	1170	318
0.7	1:2	1036	127
1	1:1	802	31

Table 8.1: Orbital characteristics for trajectories with various values of the parameter α: pericentric-to-apocentric ratio, maximum orbital velocity at the pericentric position, and the peak ram pressure.

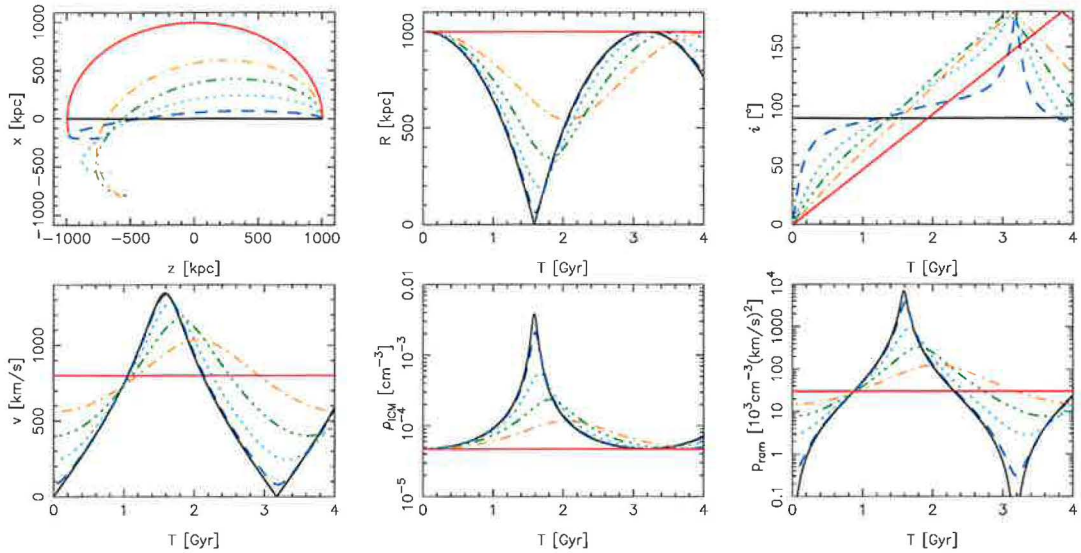

Figure 8.2: Orbital characteristics of orbits with values of the parameter $\alpha = 0$ (full), 0.1 (dashed), 0.3 (dotted), 0.5 (dot-dot-dashed), 0.7 (dot-dashed), and 1 (full red). First panel shows the galaxy's position in the orbital plane, next panels show the following quantities as functions of the orbital time: radial distance r from the cluster center, inclination i of the disk plane with respect to the instantaneous orbital direction, orbital velocity v, density of the ICM ρ_{ICM} encountered along the orbit, and profile of the ram pressure p_{ram} along the orbit.

equal to 53.6 kpc. Value of the central ICM density, and values of parameters describing the cluster dark matter distribution are unchanged and coincide with the standard model. So far, in all the simulations we have performed, the ICM particles were distributed within a sphere of 140 kpc radius about the cluster center. This configuration was chosen to achieve equally massive individual ICM and ISM particles in the standard simulation run, and was justified by the fact that mainly the central regions of the cluster are the most important for the ram pressure operation. Since now we are interested in orbits whose perictentric distances are larger than 140 kpc, we extend the computational area so that the substantial segments of the orbits traversed the ICM distribution. In the set of the three above simulations in mind, with $\alpha = 0.1$, 0.3, and 0.5, the ICM particles are thus spread up to 500 kpc radius and their number is increased by a factor of 4, i.e. $N_{ICM} = 480\,000$. The volume of the computational area is then about 45-times bigger, making the average number density of ICM particles decrease about 10-times. The dashed ring in Fig. 8.1 outlines the computational area. Then, the time intervals during which the galaxy occurs inside the ICM distribution are for the three orbits with $\alpha = 0.1$, 0.3, and 0.5 as follows: 1.2 – 2 Gyr, 1.25 – 2.1 Gyr, and 1.4 – 2.2 Gyr, respectively.

In the numerical runs, the galaxy sets out from the 1 Mpc starting position, hence entering the ICM distribution in an evolved state. Results of the simulations are shown in Fig. 8.3 depicting

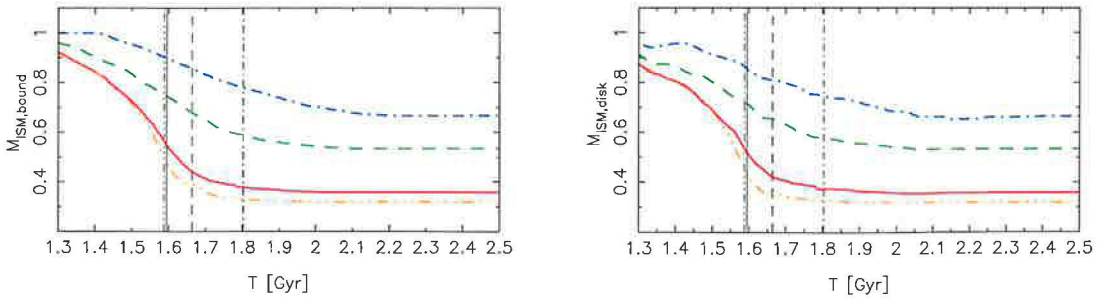

Figure 8.3: Total bound mass (left), and mass of the gas within 16 kpc radius of the disk and ±1 kpc about the disk plane, as functions of the orbital time, for the LM galaxy moving on three orbits with $\alpha =$ 0.1 (full), 0.3 (dashed), and 0.5 (dot-dashed). Vertical lines mark the corresponding time instant of the pericenter passage.

the time evolution of the total mass of the ISM bound to the galaxy, and the mass of the ISM occurring within 16 kpc radius and ±1 kpc layer about the disk plane. The full, dashed, and dot-dashed curves correspond to the orbits with $\alpha = 0.1$, 0.3, and 0.5, respectively. As expected, the stripping is more efficient for more radial orbits on which the galaxy gets to regions of higher ICM density. Further, the more is an orbit radial, the steeper is the decline of the number of ISM mass in the galaxy. Vertical lines mark the time instants of the pericenter passage for the corresponding orbit. Comparing the both panels, it is obvious that actually no reaccretion occurs in the simulations. Taking a glance on results of the face-on simulation with $R_{c,ICM} = 53.6$ kpc and $\rho_{0,ICM} = 4\ 10^{-3}$ cm^{-3} from Chapter 5, one sees that the reaccretion was absent there, as well.

Table 8.2 summarizes the simulation results. The final mass M_{final} corresponds to the amount of the bound ISM at the final time 2.5 Gyr. One notes that the retained mass of the ISM in the $\alpha = 0.1$ case is about 32% of the total ISM disk mass. But, the above mentioned simulation of the LM galaxy crossing the same cluster in the face-on configuration on strictly radial orbit in Chapter 5, shown to keep a higher fraction of the ISM, about 41%. This discrepancy is caused by that the ICM particles were in Chapter 5 spread only within 140 kpc sphere, but the effect of the ram pressure is in the wide cluster with $R_{c,ICM} = 53.6$ kpc important even outside this region. Then, it is clear that the previous result is underestimated due to the artificial cut in the ICM distribution. Therefore, we have redone this simulation in the actual setting with the computational area extended up to 500 kpc. The result is displayed with the dot-dot-dashed curve in Fig. 8.3. Now, the final mass decreased to 32%. Table 8.2 further indicates the stripping radii of the resulting ISM disks, $r_{strip,AV}$ and $r_{strip,95\%}$. The two values correspond to two various methods of the stripping radius determination described in the previous chapter. The former estimates the disk radius in twelve radial directions and makes the average, the latter searches in what radius 95% of the total bound ISM mass is enclosed.

α	M_{final} (%)	$M_{strip}/M_{strip}^{\alpha=0}$	$r_{strip,AV}$ (kpc)	$r_{strip,95\%}$ (kpc)
0	32	1	...	...
0.1	36	0.9	3.2	3.5
0.3	54	0.7	4.6	4.9
0.5	67	0.5	6.1	6.8

Table 8.2: Results of the simulation runs with LM galaxy moving on orbits with various values of the parameter α. Final retained fraction of the ISM mass, M_{final}, relative amount of the stripped mass M_{strip} with respect to its amount in the $\alpha = 0$ orbit, and the stripping radii r_{strip} are stated.

When the effect of the parameter α to the stripping results is explored, an interesting dependence reveals. The amount of the stripped ISM decreases on orbits with increasing values of α since the galaxy's pericenter grows. When the mass of the ISM stripped out of the galaxy, M_{strip},

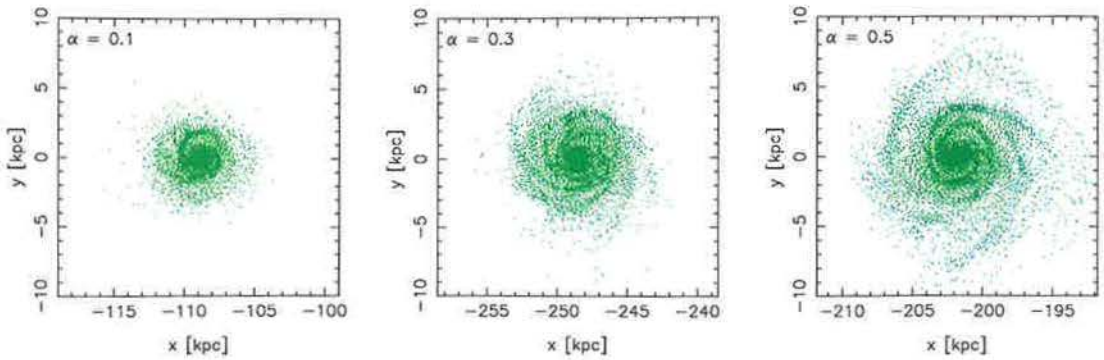

Figure 8.4: Snapshots of the ISM disk of galaxies moving on orbits with $\alpha = 0.1$, 0.3, and 0.5 (from left to right). The situation is depicted at a later orbital time after the passage through the densest cluster region. The disk is rather asymmetric in the $\alpha = 0.5$ case, which is a clear mark of an inclined stripping.

in individual cases is divided by its value in the strictly radial orbit $\alpha = 0$, one gets for $\alpha = 0.1$, 0.3, and 0.5 the following values: 0.9, 0.7, and 0.5, respectively (see Table 8.2. Clearly, it agrees with the $(1 - \alpha)$ values, indicating that the stripping efficiency of non-radial orbits could be estimated simply from the stripping result of the strictly radial orbit, and the value of α. For comparison, when dividing the maximum values of the ram pressure occurring in pericenters of the orbits by the value corresponding to the $\alpha = 0$ case, i.e. $p_{ram,max}/p^{\alpha=0}_{ram,max}$, a sequence of values 0.5, 0.1, and < 0.1 is obtained.

Fig. 8.4 displays the face-on snapshots of the ISM disks of galaxies on various orbits at the final simulation times. The increasing stripping radius is a clear consequence of the diminishing ram pressure on more circular orbits, and is connected to varying inclination angle of the disk with respect to the orbital direction, which is lower in the case of more circular orbits for a longer time.

In the following paragraph we present results of another numerical simulations focusing directly on the effect of inclination of the galaxy on an non-radial orbit. Since we have performed these simulation runs formerly, they do not follow the same setting of all the cluster and galaxy parameters as in our recent simulations described above. Nevertheless, the general trends remain valid and these results offer an insight into the role of the inclination angle to the stripping on non-radial orbits. Fig. 8.5 shows stripping results of four runs of a galaxy moving on a non-radial orbit with $\alpha = 0.7$ with varying initial orientation of the disk with respect to the orbital direction. Curves from top to bottom correspond to initial inclinations of 90°, 135°, 45°, and 0°. The axis of inclination is perpendicular to the orbital plane. Only the edge-on inclination ($i = 0°$) keeps its orientation constant during the orbit since the disk plane is laying in the orbital plane. Of course, even in the edge-on case, the direction of the oncoming ICM wind varies in time. The resulting amount of the stripped ISM after one flyby around the cluster center is in the above order 16%, 14%, 9%, and 6%. Thus, the initially face-on setting is the most susceptible to the ram pressure stripping, contrary to the edge-on case with about three-times less of the stripped ISM.

8.4 Analytic predictions

To easily estimate the amount of the ISM that is released from galaxies moving on various orbits to the inter-galactic space, enriching the intracluster environment, we can use one of the analytic formulae inferred in Chapter 6. Using the simplified approach of the formula (6.13), we can estimate the stripping results for the LM galaxy moving on orbits with various values of the parameter α. But, as discussed above, except the strictly radial one, all other orbits introduce a dependence of the disk plane inclination on the orbital time. Then, assuming that the galaxy is all the orbital time in the face-on orientation, the formula (6.13) should provide an upper limit of the stripping efficiency.

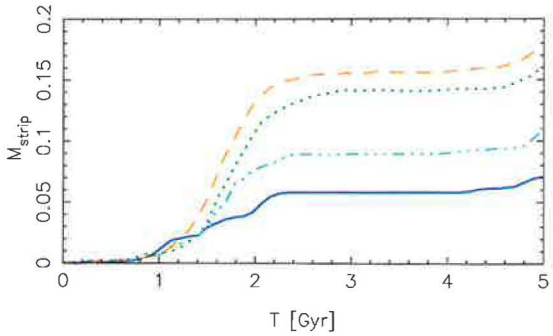

Figure 8.5: Stripping history of the galaxy moving on $\alpha = 0.7$ orbit for four different disk initial inclinations: 90° (face-on), 135°, 45°, and 0° (edge-on), from top to bottom.

Fig. 8.6 shows the stripping radius R_{strip} and final mass M_{final} of the LM galaxy as functions of the orbital parameter α. The value of the central ICM density is consistent with the above numerical simulations: $\rho_{0,ICM} = 4\ 10^{-3}$ cm^{-3}. Width of the ICM distribution $R_{c,ICM}$ varies over five values: 3.4 (orange), 6.7 (cyan), 13.4 (blue), 26.8 (green), and 53.6 (red) kpc. The last one then corresponds to the simulations. Dotted curve corresponds to the determination using the Gunn & Gott (1972) criterion for $R_{c,ICM} = 53.6$ kpc. Over the curves are marked the results of the numerical simulations from the previous section (black stars). These should be compared to the red curve.

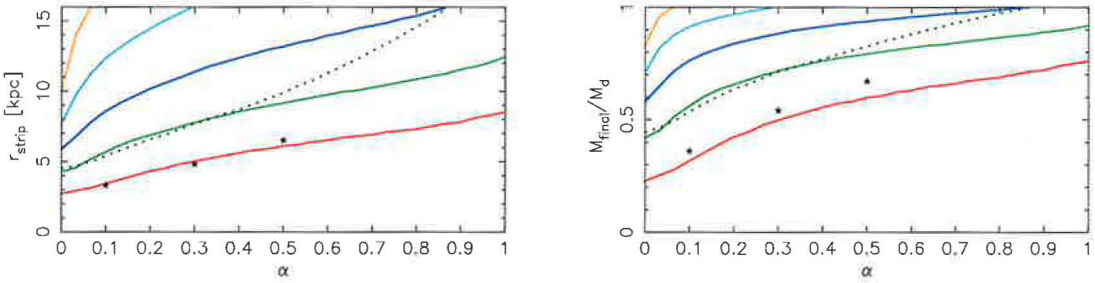

Figure 8.6: Stripping radius r_{strip} and final mass M_{final} determined using the formula (6.13) as functions of circularity of the galactic orbit. Colors correspond to different widths of the cluster: $R_{c,ICM} = 3.4$ (orange), 6.7 (cyan), 13.4 (blue), 26.8 (green), and 53.6 (red) kpc. Dotted curve corresponds to the Gunn & Gott (1972) prediction for $R_{c,ICM} = 53.6$ kpc. Black stars mark the simulation results.

Fig. 8.7 then depicts analogous curves of R_{strip} and M_{final} but providing clusters with the fixed width $R_{c,ICM} = 13.4$ kpc and varying the central ICM density: $\rho_{0,ICM} = 1$, 2, 4, 16, and 32 10^{-3} cm^{-3} (from top to bottom).

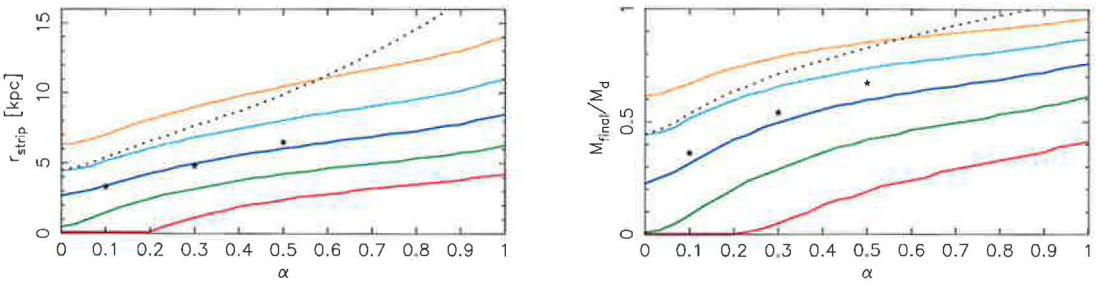

Figure 8.7: Same as Fig. 8.6 but for fixed $R_{c,ICM} = 13.4$ kpc and five values of the $\rho_{0,ICM}$: 1, 2, 4, 8, and 16 $\cdot 10^{-3}$ cm^{-3} (from top to bottom).

The comparison between the analytic estimates and the simulations shows that the former

indeed overestimate the effect of the ram pressure stripping due to neglecting the time dependence of the disk inclination and other simplifications discussed in Chapter 6. The numerical results correspond best to the formula for $R_{c,ICM} = 53.6$ kpc.

8.5 X-ray trails of galaxies

Fig. 8.8 show trails of the stripped ISM particles from the $\alpha = 0.1$, 0.3 and 0.5 orbital stripping events. Besides the trails, the mass and motion of the galaxy will tend to concentrate material behind it – to form gravitationally focused wakes (Stevens et al. 1999). Observations of such trails or wakes in the ICM, together with bow shocks in front of galaxies may provide information about the direction of motion of galaxies.

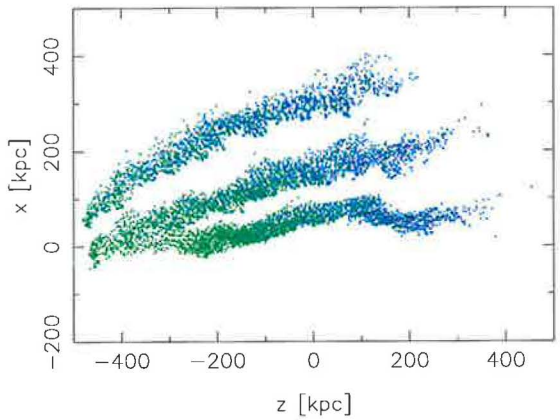

Figure 8.8: Trails of the stripped ISM particles from the LM–type galaxy crossing the standard cluster on three slightly elliptical orbits with $\alpha = 0.1$, 0.3 and 0.5.

Chapter 9

Conclusion and future prospects

9.1 Conclusion

The simulations performed in the present work allow us to better estimate the consequences of ram pressure stripping in clusters. If a galaxy like the Milky Way (our type LM) passes through the center of a cluster similar to Virgo (our standard cluster) in a purely radial trajectory and in face-on orientation, it loses about 29% of its interstellar gas. This constitutes a rather important amount of gas loss, but it is a maximum value, because the galaxy passes exactly through the central peak of the ICM.

According to additional simulations shown in Chapters 7 and 8, and to Roediger & Brüggen (2006) the efficiency of stripping does not depend strongly on the orientation of the galaxy, at least as far as the inclination is high: from 90° (face-on) to about 70°, the stripping is almost identical. However, for inclination of 45° the amount of the stripped material drops by a factor of almost 2, and for $i = 20°$ by a factor of 3, as compared to the face-on case. We find that the mass of the stripped material can be approximately estimated from the face-on case and from the inclination angle as $M_{strip}(i) = M^{90°}_{strip} \sin i$.

With this level of stripping, we may estimate the fraction of gas supplied to the ICM by stripping: The amount of gas lost by a LM–type galaxy is about 2 10^9 $M_\odot$. A much less massive Lm–type galaxy is more severely stripped, thus providing roughly the same amount of gas. EM and Em–types are subject to an even more effective stripping, but their gas disks are less massive. Our estimate is that the average contribution per spiral galaxy, late or early type, with different orientations in a radial orbit, is 1 - 2 10^9 $M_\odot$. This means that the total amount of hot gas in the central region of our standard cluster (6 10^{10} $M_\odot$) can be provided by 30 - 60 stripping acts. The amount of stripping from past to present is influenced with the decreasing gas content of galaxies, which is an obvious consequence of gas consumption by star formation: gas-rich galaxies in the past can provide more gas to intergalactic space. On the opposite, the growing ICM concentration in the center of the cluster leads to higher stripping efficiency now.

Note than only the contribution from galaxies on radial orbits is substantial. Galaxies on circular or elliptical orbits do not penetrate the dense parts of the ICM and thus are safe from being stripped. Depending on the fraction of galaxies in radial orbits in the cluster, which unfortunately is not well known, the stripping could supply a significant amount of gas to the ICM. This may explain the high metalicity of the ICM gas. Domainko et al. (2006) estimate that about 10% of the observed level of enrichment in the ICM within a radius of 1.3 Mpc is due to the ram pressure stripping.

Another consequence of our simulations is that we expect to find in any cluster a significant amount of relatively cold gas, as debris left over from recent stripping events. This gas is not yet mixed with the ICM, but forms large diffuse clouds as tails behind the galaxy keeping a fraction of its velocity. The mixing time should be comparable to the free-fall time, e.g. $\sim$ 1 Gyr. The density of gas in tails may be more than 10 times larger than the local hot ICM density, hence a tail could cause strong stripping for any galaxy which happens to cross it at a very different velocity. This can

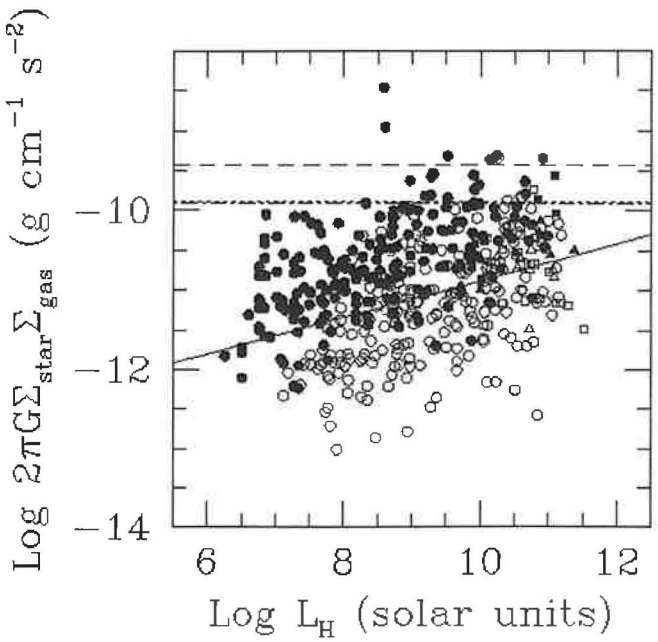

Figure 9.1: The relation between the gravitational forces per unit area and the H band luminosity. Filled symbols: galaxies with normal HI content, empty symbols: deficient galaxies (def¿0.3). Squares are for Coma galaxies, triangles for A1367 galaxies, and circles for Virgo galaxies. The dashed, dot-dashed and dotted lines show upper limit to the gravitational pressure for an efficient ram pressure stripping for Coma, A1367 and Virgo cluster, respectively, according to Gunn & Gott (1972) estimate. From Boselli & Gavazzi (2006)

then provide a nice explanation to the puzzling strong stripping recently observed in many regions where the hot ICM gas is not sufficient to strip. For instance NGC 4522 is apparently stripped at a large distance from the cluster center (Crowl & Kenney 2006), where the ICM density is not sufficient. A nice example of a cold HI tail almost 100 kpc long provides the galaxy CGCG 97-073 in the Coma cluster. This and similar tails may be the cause of ram pressure for other galaxies arriving at high speed.

Also ram-pressure stripping appears in small groups, where the X-ray gas is not detected (Rasmussen et al 2006). As we have shown in the work, the crucial effect of the ram pressure stripping is the pressure itself, the hydrodynamical effects play only a minor role. Therefore, not only the hot ICM is able to strip the galactic ISM, but debris from tidal interactions or previous stripping as well.

The main conclusion is that the stripping efficiency depends significantly on the duration of the ram pressure pulse, which in many cases means that Gunn & Gott (1972) prediction overestimates the amount of stripping. This is nicely shown by Boselli & Gavazzi (2006), see Fig. 9.1, where they compare the restoring force in spiral galaxies in Coma, A1367 and Virgo clusters to the maximum ram pressure. It turns that many galaxies with normal HI content should have been stripped if the ram pressure had acted for a sufficiently long time. Much more modest stripping is observed showing that Gunn & Gott (1972) prediction is an overestimation.

9.2 Future prospects

Star formation

Fujita et al. (1999) using a model of molecular cloud evolution show that because the ram pressure compresses the molecular gas of the galaxy, the star formation rate increases at most by a factor of 2. It further decreases rapidly on a timescales of 10^8 yrs when the stripping of the interstellar

material takes place. Koopmann et al. (2004) describe truncated star formation disks with the star formation suppressed significantly in the outer regions but normal or even enhanced in the center.

For studying the star formation history in a galaxy orbiting in the cluster, we plan to introduce another gaseous phase into our code. The cold gas ($\sim$ 10 K) component, whose large amount is observed in galactic disks, is fragmented in giant molecular clouds and thus it can not be described as a fluid by means of the SPH. Much convenient way is to use the sticky particles scheme in which the particles are subject to inelastic collisions and gravitational forces. Because of the number of particles that is allowed by current computational capabilities, each sticky particle represents one giant molecular cloud, similarly to the fact that each stellar particle in fact has a mass of a stellar cluster of the order of $\sim 10^6$ $M_\odot$.

These are the cold molecular clouds in which star formation is located. To add this process into our simulations we will implement the so-called "hybrid particles" method (Mihos & Hernquist 1994) in which every particle of the cold gas carries both gaseous and stellar portion. The gravitational forces on these particles are calculated based on their total mass, while the hydrodynamical forces and the properties are calculated using their gas mass. When conditions under which stars can be formed from the gas are fulfilled the star formation rate is calculated following the Schmidt law. Then as hybrid particle forms stars its gas mass is being reduced while its total mass stays fixed. And when the gas mass fraction drops below some fixed value, it is converted to a pure collisionless stellar particle.

A reverse process of distributing the energy produced by star formation activity, the supernovae feedback will be introduced as well. Since the energy release in supernovae explosions is huge it is important to try to model this phenomenon (Semelin & Combes 2002). Most of the feedback is in the form of thermal energy in the environment of newly formed stars, a small fraction is also in kinetic energy of expanding gas shells. The former can be simulated as conversion of small number of neighboring cold gas particles into the warm phase, the latter in the form of expanding motions added to the gaseous particles in the vicinity of young stars.
During the life of a galaxy, stars can return significant amount of their mass to the ISM through stellar winds and supernovae explosions (Jungwiert et al. 2001). This long lasting and continuous mass-loss from stars can be included as the time dependent mass exchange between stellar and gaseous particles.

To assure correctness of the thermal evolution of the gas, cooling and heating processes have to be taken into account (Sutherland & Dopita 1993, and others).

Galaxy harassment

Moore et al. (1996) have proposed a new mechanism for the Butcher-Oemler effect in clusters. At speeds of several thousand km s^{-1} at which galaxies orbit within the cluster, their close mutual encounters cause gravitational shocks that can damage galactic disks. The cumulative effect of such encounters changes a disk galaxy into a lenticular. We would like to include the effect of this phenomenon into our simulations by means of a simple approximation with point masses playing the role of encountered galaxies.

Virgo cluster

Schindler et al. (1999) state that the irregular structure of the Virgo cluster can be decomposed into three major subclusters centered on M87, M49, and M86 and they give values of parameters of β-profiles of these tree subclusters. In our recent simulations we use for modeling the galaxy cluster the parameters corresponding to the M87 subcluster of the Virgo cluster. In future, we want to simply extend our model to better fit the complex structure of the Virgo cluster by including its other important components. Similar approach have used Vollmer et al. (2001a).

Hickson groups

Hickson compact galaxy groups (Hickson 1997) consist of a small number of 4 to 10 member galaxies with low velocity dispersions of $\sigma \sim 200$ km s^{-1} within an area of only a few hundred kpc

in diameter. Their projected galaxy densities are similarly high as in the centers of some galaxy clusters but they are found in low galaxy density environments. The first example was found over one hundred years ago by Stephan (1877) – Stephan's Quintet is a small group of five galaxies, three of which show strong tidal distortions due to gravitational interaction, a second example was found 71 years later by Seyfert (1948) – Seyfert's Sextet is one of the densest groups known, having a median projected galaxy separation of only $6.8h^{-1}$ kpc.

9.2.1 Project prospects summary

In galaxy clusters, there are several competitive processes that can remove gas from member galaxies, with subsequent star formation quenching (Combes 2004). These are tidal stripping by the cluster potential, mutual tidal interactions between galaxies, and ram pressure stripping. What is relative importance of galaxy-galaxy interactions, when the tides open the gate for the gas to escape from galaxies, of the tidal effect of the cluster itself, and of the intracluster gas interaction with the galactic gas, leading to ram pressure stripping of galaxies? In this project we want disentangle the competing processes playing role in galaxy evolution, to determine the actual reason of the accelerated evolution in clusters, and accelerated star formation history. For these objectives we will deal with following items:

- Star formation & mass and energy release algorithm
- Simple model of galaxy harassment
- Model of the Virgo cluster
- Ram pressure stripping in the Hickson groups.

Bibliography

[1] Abadi, M. G., Moore, B., Bower, R. G., 1999, Ram pressure stripping of spiral galaxies in clusters, MNRAS, 308, 947

[2] Abell, G. O., 1958, The Distribution of Rich Clusters of Galaxies, 1958, ApJS, 3, 211

[3] Abell, G. O., Corwin, H. G. Jr., Olowin, R. P., 1989, A catalog of rich clusters of galaxies, ApJS, 70, 1

[4] Abraham, R. G., Smecker-Hane, T. A., Hutchings, J. B., Carlberg, R. G., Yee, H. K. C., Ellingson, E., Morris, S., Oke, J. B., Rigler, M., 1996, Galaxy Evolution in Abell 2390, ApJ, 471, 694

[5] Acreman, D. M., Stevens, I. R., Ponman, T. J., Sakelliou, I., 2004, Simulations of the effects of stripping and accretion on galaxy haloes in clusters, MNRAS, 341, 1333

[6] Agertz, O., Moore, B., Stadel, J., Potter, D., Miniati, F., Read, J., Mayer, L., Gawryszczak, A., Kravtsov, A., Monaghan, J., Nordlund, A., Pearce, F., Quilis, V., Rudd, D., Springel, V., Stone, J., Tasker, E., Teyssier, R., Wadsley, J., Walder, R., 2006, Fundamental differences between SPH and grid methods, astro-ph/10051A

[7] Arnaboldi, M., Freeman, K. C., Okamura, S., et al. 2003, Narrowband Imaging in [O III] and Hα to Search for Intracluster Planetary Nebulae in the Virgo Cluster, AJ, 125, 514

[8] Bahcall, N. A., 1996, Clusters and superclusters of galaxies, astro-ph/11148

[9] Balogh, M. L., Navarro, J. F., Morris, S. L., 2000, The Origin of Star Formation Gradients in Rich Galaxy Clusters, ApJ, 540, 113

[10] Balsara, D., Livio, M., O'Dea, C. P., 1994, Galaxies in clusters: Gas stripping and accretion, ApJ, 437, 83

[11] Barnes, J. E., 1998, Dynamics of Galaxy Interactions, giis-conf, 275

[12] Bautz, L. P., Morgan, W. W., 1970, On the Classification of the Forms of Clusters of Galaxies, ApJ, 162, 149

[13] Bekki, K., Couch, W. J., Shioya, Y., 2002, Passive Spiral Formation from Halo Gas Starvation: Gradual Transformation into S0s, ApJ, 577, 651

[14] Benatov, L., Rines, K., Natarajan, P., Kravtsov, A., Nagai, D., 2006, Galaxy orbits and the intracluster gas temperature in clusters, MNRAS, 370, 427

[15] Binggeli, B., Sandage, A., Tammann, G. A., 1985, Studies of the Virgo Cluster. II - A catalog of 2096 galaxies in the Virgo Cluster area, AJ, 90, 1681

[16] Biviano, A., 2002, Tracing the Cluster Internal Dynamics with Member Galaxies, ASPC, 268, 127

[17] Biviano, A., Katgert, P., 2003, The Orbits of Cluster Galaxy Populations as Evolutionary Constraints, Ap&SS, 285, 25

[18] Biviano, A., Katgert, P., 2004, The ESO Nearby Abell Cluster Survey. XIII. The orbits of the different types of galaxies in rich clusters, A&A, 424, 779

[19] Boselli, A., Gavazzi, G., 2006a, Environmental Effects on Late-Type Galaxies in Nearby Clusters, PASP, 118, 517

[20] A. Boselli, S. Boissier, L. Cortese, A. Gil de Paz, M. Seibert, B. F. Madore, V. Buat, D. C. Martin, 2006b, The fate of spiral galaxies in clusters: the star formation history of the anemic Virgo cluster galaxy NGC 4569, ApJ, astro-ph/0609020

[21] Bournaud, F., Combes, F., Jog, C. J., 2004, Unequal-mass galaxy merger remnants: Spiral-like morphology but elliptical-like kinematics, A&A, 418, 27

[22] Butcher, H., & Oemler, A., 1978, The evolution of galaxies in clusters. I - ISIT photometry of C1 0024+1654 and 3C 295, ApJ, 219, 18

[23] Butcher, H., & Oemler, A., 1984, The evolution of galaxies in clusters. V - A study of populations since Z approximately equal to 0.5, ApJ, 285, 426

[24] Byrd, G., Valtonen, M., 1990, Tidal generation of active spirals and S0 galaxies by rich clusters, ApJ, 350, 89

[25] Cayatte, V., van Gorkom, J. H., Balkowski, C., Kotanyi, C., 1990, VLA observations of neutral hydrogen in Virgo Cluster galaxies. I - The Atlas, AJ, 100, 604

[26] Cayatte, V., Kotanyi, C., Balkowski, C., van Gorkom, J. H., 1994, A very large array survey of neutral hydrogen in Virgo Cluster spirals. 3: Surface density profiles of the gas, AJ, 107, 1003

[27] Chemin, L., Cayatte, V., Balkowski, C., Amram, P., Carignan, C., Boselli, A., Adami, C., Marcelin, M., Garrido, O., Hernandez, O., Boulesteix, J., 2005, A Virgo high-resolution H? kinematical survey. I. NGC 4438, A&A, 436, 469

[28] Chemin, L., Balkowski, C., Cayatte, V., Carignan, C., Amram, P., Garrido, O., Hernandez, O., Marcelin, M., Adami, C., Boselli, A., Boulesteix, J., 2006, A Virgo high-resolution Hα kinematical survey - II. The Atlas, MNRAS, 366, 812

[29] Chyży, K. T., Soida, M., Bomans, D. J., Vollmer, B., Balkowski, Ch., Beck, R., Urbanik, M., 2006, Large-scale magnetized outflows from the Virgo Cluster spiral NGC 4569. A galactic wind in a ram pressure wind, A&A, 447, 465

[30] Clemens, M. S., Alexander, P., Green, D. A., 2000, Ram-pressure stripping of the interstellar medium in NGC 4485, MNRAS, 312, 236

[31] Colless, M., Peterson, B. A., Jackson, C., Peacock, J. A., Cole, S., et al., 2003, The 2dF Galaxy Redshift Survey: Final Data Release, astro-ph/0306581

[32] Combes, F., Dupraz, C., Casoli, F., Pagani, L., 1988, CO emission in NGC 4438 - A case for tidal stripping?, A&A, 203, 9

[33] Combes, F., 2004, IAU Symposium 217: Recycling intergalactic and interstellar matter, ASP Conference Series, Vol. XXX, P. - A. Duc et al.

[34] Cortés, J. R., Kenney, J. D. P., Hardy, E., 2006, The Nature of the Peculiar Virgo Cluster Galaxies NGC 4064 and NGC 4424, AJ, 131, 747

[35] Cowie, L. L., Songaila, A., 1977, Thermal evaporation of gas within galaxies by a hot intergalactic medium, Nature, 266, 501

[36] Crowl, H. H., Kenney, J. D. P., van Gorkom, J. H., Vollmer, B., 2005, Dense Cloud Ablation and Ram Pressure Stripping of the Virgo Spiral NGC 4402, AJ, 130, 65

[37] Crowl, H. H., Kenney, J. D. P., 2006, The Stellar Population of Stripped Cluster Spiral NGC 4522: A Local Analog to K+A Galaxies?, ApJ, 649, 75

[38] Dahlem, M., 1997, Gaseous Halos of Late-Type Spiral Galaxies, PASP, 109, 1298

[39] Domainko, W., Mair, M., Kapferer, W., van Kampen, E., Kronberger, T., Schindler, S., Kimeswenger, S., Ruffert, M., Mangete, O. E., 2006, Enrichment of the ICM of galaxy clusters due to ram-pressure stripping, A&A, 452, 795

[40] Dressler, A., 1980, Galaxy morphology in rich clusters - Implications for the formation and evolution of galaxies, ApJ, 236, 351

[41] Dressler, A., 1986, The morphological types and orbits of H I-deficient spirals in clusters of galaxies, ApJ, 301, 35

[42] Dressler, A., Oemler, A., Couch, W. J., Smail, I., Ellis, R. S., Barger, A., Butcher, H., Poggianti, B. M., Sharples, R. M., 1997, Evolution since $Z = 0.5$ of the Morphology-Density Relation for Clusters of Galaxies, ApJ, 490, 577

[43] Elmegreen, D. M., Chromey, F. R., Knowles, B. D., Wittenmyer, R. A., 1998, Observations of a Tidal Tail in the Interacting Galaxies NGC 4485/4490, AJ, 115, 1433

[44] Fabian, A. C., Allen, S. W., 2003, X-rays from clusters of galaxies, tsra-symp, 197

[45] Farouki, R., Shapiro, S. L., 1980, Computer simulations of environmental influences on galaxy evolution in dense clusters. I – Ram-pressure stripping, ApJ, 241, 928

[46] Farouki, R., Shapiro, S. L., 1981, Computer simulations of environmental influences on galaxy evolution in dense clusters. II - Rapid tidal encounters, ApJ, 243, 32

[47] Farouki, R., Shapiro, S. L., 1982, Simulations of merging disk galaxies, ApJ, 259, 103

[48] Finoguenov, A., David, L. P., Ponman, T. J., 2000, An ASCA Study of the Heavy-Element Distribution in Clusters of Galaxies, ApJ, 544, 188

[49] Forman, W., Jones, C., 1982, X-ray-imaging observations of clusters of galaxies, ARA&A, 20, 547

[50] Fujita, Y., 2001, Ram-Pressure Stripping of Galaxies in High-Redshift Clusters and the Influence of Intracluster Medium Heating, ApJ, 550, 612

[51] Fujita, Y., 2004, Pre-Processing of Galaxies before Entering a Cluster, PASJ, 56, 29

[52] Fujita, Y., Goto, T., 2004, The Evolution of Galaxies in and around Clusters at High-Redshift, PASJ, 56, 621

[53] Fujita, Y., Nagashima, M., 1999, Effects of Ram Pressure from the Intracluster Medium on the Star Formation Rate of Disk Galaxies in Clusters of Galaxies, ApJ, 516, 619

[54] Gaetz, T. J., Salpeter, E. E., Shaviv, G., 1987, Gasdynamical stripping of elliptical galaxies, Apj, 316, 530

[55] Gavazzi, G., Boselli, A., Scodeggio, M., Pierini, D., Belsole, E., 1999, The 3D structure of the Virgo cluster from H-band Fundamental Plane and Tully-Fisher distance determinations, MNRAS, 304, 595

[56] Gerhard, O., Arnaboldi, M., Freeman, K. C., Okamura, S., 2002, Isolated Star Formation: A Compact H II Region in the Virgo Cluster, ApJ, 580, 121

[57] Ghigna, S., Moore, B., Governato, F., Lake, G., Quinn, T., Stadel, J., 1998, Dark matter haloes within clusters, MNRAS, 300, 146

[58] Giovanelli, R., Haynes, M. P., 1982, Ram Pressure Stripping in the Virgo Cluster, BAAS, 14, 905

[59] Giovanelli, R., Haynes, M. P.,1985, Gas deficiency in cluster galaxies - A comparison of nine clusters, ApJ, 292, 404

[60] Goto, T., 2006, Environmental Effects on Galaxy Evolution Based on the SDSS, astro-ph/5203

[61] Gnedin, O. Y., 2003, Tidal Effects in Clusters of Galaxies, ApJ, 582, 141

[62] Gunn, J. E., Gott, J. R., 1972, On the Infall of Matter Into Clusters of Galaxies and Some Effects on Their Evolution, ApJ, 176, 1

[63] Haynes, M. P., 1988, Morphology and environment, SPC, 5, 71

[64] Hickson, P., 1997, Compact Groups of Galaxies, ARA&A, 35, 357

[65] Hidaka, M., Sofue, Y., 2002, Ram-Pressure Effects on Dense Molecular Arms in the Central Regions of Spiral Galaxies by Intracluster Medium, PASJ, 54, 33

[66] Homeier, N. L., Postman, M., Menanteau, F., Blakeslee, J. P., Mei, S., Demarco, R., Ford, H. C., Illingworth, G. D., Zirm, A., 2006, Imprints of Environment on Cluster and Field Late-Typr Galaxies at z$\sim$1, AJ, 131, 143

[67] Jungwiert, B., Combes, F., Palous, J., 2001, Continuous stellar mass-loss in N-body models of galaxies, A&A, 376, 85

[68] Kenney, J. D., Young, J. S., 1986, CO in H I-deficient Virgo cluster spiral galaxies, ApJ, 301, 13

[69] Kenney, Jeffrey D. P., Koopmann, Rebecca A., 1999, Ongoing Gas Stripping in the Virgo Cluster Spiral Galaxy NGC 4522, AJ, 117, 181

[70] Kenney, J. D. P., van Gorkom, J. H., Vollmer, B., 2004a, VLA HI Observations of Gas Stripping in the Virgo Cluster Spiral NGC 4522, AJ, 127, 3361

[71] Kenney, J. D. P., Crowl, H., van Gorkom, J., Vollmer, B., 2004b, Spiral Galaxy - ICM Interactions in the Virgo Cluster, IAUS, 217, 370

[72] King, I., 1962, The structure of star clusters. I. an empirical density law, AJ, 67, 471

[73] Knebe, A., Gill, S. P. D., Gibson, B. K., Lewis, G. F., Ibata, R. A., Dopita, M. A., 2004, Anisotropy in the Distribution of Satellite Galaxy Orbits, ApJ, 603, 7

[74] Kodama, T., Smail, I., 2001, Testing the hypothesis of the morphological transformation from field spiral to cluster S0, MNRAS, 326, 637

[75] Koopmann, R. A., Kenney, J. D. P., 2004, Hα Morphologies and Environmental Effects in Virgo Cluster Spiral Galaxies, ApJ, 613, 866

[76] Koopmann, R. A., Haynes, M. P., Catinella, B., 2006, A Comparison of Hα and Stellar Scale Lengths in Virgo and Field Spirals, AJ, 131, 716

[77] Kritsuk, A. G., 1984, Dynamics of the Sweeping of Interstellar Clouds from a Rotating Galaxy as it Moves in the Intergalactic Medium, Ap, 19, 263

[78] Kundić, T., Spergel, D. N., Hernquist, L., 1993, Dynamical Effects of Ram Pressure in Clusters of Galaxies, AAS, 183, 8708

[79] Larson, R. B., Tinsley, B. M., Caldwell, C. N., 1980, The evolution of disk galaxies and the origin of S0 galaxies, ApJ, 237, 692

[80] Lee, H., Richer, M. G., McCall, M. L., 2000, The Dwarf Irregular Galaxy UGC 7636 Exposed: Stripping at Work in the Virgo Cluster, ApJ, 530, 17

[81] Lucero, D. M., Young, L. M., van Gorkom, J. H., Ram Pressure Stripping in the Low-Luminosity Virgo Cluster Elliptical Galaxy NGC 4476, AJ, 129, 647

[82] Machacek, M., Jones, C., Forman, W. R., Nulsen, P., 2006, Chandra Observations of Gas Stripping in the Elliptical Galaxy NGC 4552 in the Virgo Cluster, ApJ, 644, 155

[83] Mamon, G. A., Sanchis, T., Salvador-Solé, E., Solanes, J. M., 2004, The origin of H I-deficiency in galaxies on the outskirts of the Virgo cluster. I. How far can galaxies bounce out of clusters?, A&A, 414, 445

[84] Marcolini, A., Brighenti, F., D'Ercole, A., 2003, Three-dimensional simulations of the interstellar medium in dwarf galaxies - I. Ram pressure stripping, MNRAS, 345, 1329

[85] Margoniner, V. E., de Carvalho, R. R., Gal, R. R., Djorgovski, S. G., 2001, The Butcher-Oemler Effect in 295 Clusters: Strong Redshift Evolution and Cluster Richness Dependence, ApJ, 548, 143

[86] Markevitch, M., Gonzalez, A. H., David, L., Vikhlinin, A., Murray, S., Forman, W., Jones, C., Tucker, W., 2002, A Textbook Example of a Bow Shock in the Merging Galaxy Cluster 1E 0657-56, ApJ, 567, 27

[87] Merritt, D., 1983, Relaxation and tidal stripping in rich clusters of galaxies. I - Evolution of the mass distribution, ApJ, 264, 24

[88] Mihos, J. C., Hernquist, L., 1994, Star-forming galaxy models: Blending star formation into TREESPH, ApJ, 437, 611

[89] Mihos, J. C., 2004, In Clusters of Galaxies: Probes of Cosmological Structure and Galaxy Evolution, ed. J. S. Mulchaey, A. Dressler & A. Oemler, Cambridge Univ. Press

[90] Moore, B., Katz, N., Lake, G., Dressler, A., Oemler, A., Jr., 1996, Galaxy harassment and the evolution of clusters of galaxies, Nature, 379, 613

[91] Moore, B., Lake, G., Katz, N., 1998, Morphological Transformation from Galaxy Harassment, ApJ, 495, 139

[92] Mori, M., Burkert, A., 2000, Gas Stripping of Dwarf Galaxies in Clusters of Galaxies, ApJ, 538, 559

[93] Mulchaey, J. S., 2000, X-ray Properties of Groups of Galaxies, ARA&A, 38, 289

[94] Murakami, I., Babul, A., 1999, Interaction between the intergalactic medium and galactic outflows from dwarf galaxies, MNRAS, 309, 161

[95] Murakami, I., Ikeuchi, S., 1994, Mass stripping of Lyman-Alpha clouds by Ram pressure under the minihalo model, ApJ, 420, 68

[96] Murante, G., Arnaboldi, M., Gerhard, O. et al. 2004, The Diffuse Light in Simulations of Galaxy Clusters, ApJ, 607, 83

[97] Mushotzky, R. F., 2004, Clusters of Galaxies: An X-ray Perspective, cgpc-symp, 123

[98] Navarro, J. F., Frenk, C. S., White, S. D. M., 1997, A Universal Density Profile from Hierarchical Clustering, ApJ, 490, 493

[99] Nulsen, P. E. J., 1982, Transport processes and the stripping of cluster galaxies, MNRAS, 198, 1007

[100] Okamoto, T., Nagashima, M., 2003, Environmental Effects on Evolution of Cluster Galaxies in a Λ-dominated Cold Dark Matter Universe, ApJ, 587, 500

[101] Phookun, B., Mundy, L. G, 1995, NGC 4654: A Virgo Cluster Spiral Interacting with the Intracluster Medium, ApJ, 453, 154

[102] Piontek, R. A., Stone, J. M., 2001, The Effect of ISM Mass on Ram Pressure Stripping, AAS, 199, 155.01

[103] Portnoy, D., Pistinner, S., Shaviv, G., 1993, Ram pressure stripping from elliptical galaxies. I - The mass contained in the Galaxy, ApJS, 86, 95

[104] Postman, M., Geller, M. J., 1986, The morphology-density relation - The group connection, ApJ, 281, 95

[105] Postman, M., Franx, M., Cross, N. J. G., Holden, B. et al., 2005, The Morphology-Density Relation in z $\sim$ 1 Clusters, ApJ, 623, 721

[106] Quilis, V., Moore, B., & Bower, R., 2000, Gone with the Wind: The Origin of S0 Galaxies in Clusters, Science, 288, 1617

[107] Rakos, K. D., Schombert, J. M., 1995, Color evolution from z = 0 to z = 1, ApJ, 439, 47

[108] Rasmussen, J., Ponman, T. J., Mulchaey, J. S., 2006, Gas stripping in galaxy groups - the case of the starburst spiral NGC 2276, MNRAS, 370, 453

[109] Roediger, E., Brüggen, M., 2006a, Ram pressure stripping of disc galaxies: the role of the inclination angle, MNRAS, 369, 567

[110] Roediger, E., Brüggen, M., and Hoeft, M., 2006b, Wakes of ram-pressure-stripped disc galaxies, MNRAS, 371, 609

[111] Roediger, E., Henlser, G., 2005, Ram pressure stripping of disk galaxies. From high to low density environments, A&A, 433, 875

[112] Rood, H. J., Sastry, G. N., 1971, "Tuning Fork" Classification of Rich Clusters of Galaxies, PASP, 83, 313

[113] Rosati, P., Borgani, S., Norman, C., 2002, The Evolution of X-ray Clusters of Galaxies, ARA&A, 40, 539

[114] Rudick, C. S., Mihos, J. C., McBride, C., 2006, The Formation and Evolution of Intracluster Light, ApJ, astro-ph/0605603

[115] Sakelliou, I., Acreman, D. M., Hardcastle, M. J., Merrifield, M. R., Ponman, T. J., Stevens, I. R., 2005, The cool wake around 4C 34.16 as seen by XMM-Newton, MNRAS, 360, 1069

[116] Sarazin, C. L., 1988, X-ray Emission from Clusters of Galaxies, Cambridge: Cambridge University Press

[117] Semelin, B., Combes, F., 2002, Formation and evolution of galactic disks with a multiphase numerical model, A&A, 388, 826

[118] Schindler, S., Binggeli, B., Böhringer, H., 1999, Morphology of the Virgo Cluster: Gas versus Galaxies, A&A, 343, 420

[119] Schindler, S., 2004, Gas in Groups and Clusters of Galaxies, Ap&SS, 289, 419

[120] Schindler, S., Kapferer, W., Domainko, W., Mair, M., van Kampen, E., Kronberger, T., Kimeswenger, S., Ruffert, M., Mangete, O., Breitschwerdt, D., 2005, Metal enrichment processes in the intra-cluster medium, A&A, 435, 25

[121] Schulz, S., & Struck, C., 2001, Multi stage three-dimensional sweeping and annealing of disc galaxies in clusters, MNRAS, 328, 185

[122] Smith, G. P., Treu, T., Ellis, R. S., Moran, S. M., Dressler, A., 2005, Evolution since $z = 1$ of the Morphology-Density Relation for Galaxies, ApJ, 620, 78

[123] Sofue, Y., 1994, Ram-pressure stripping of gas from companions and accretion onto a spiral galaxy: A gaseous merger, ApJ, 423, 207

[124] Solanes, J. M., Manrique, A., García-Gómez, C., González-Casado, G., Giovanelli, R., Haynes, M. P., 2001, The HI Content of Spirals. II. Gas Deficiency in Cluster Galaxies, ApJ, 548, 97

[125] Solanes, J. M., Sanchis, T., Salvador-Solé, E., Giovanelli, R., Haynes, M. P., 2004, The Three-dimensional Structure of the Virgo Cluster Region from Tully-Fisher and H I Data, AJ, 124, 2440

[126] Stevens, I. R., Acreman, D. M., Ponman, T. J., 1999, Galaxies in clusters: the observational characteristics of bow shocks, wakes and tails, MNRAS, 310, 663

[127] Sutherland, R. S., Dopita, M. A., 1993, Cooling functions for low-density astrophysical plasmas, ApJS, 88, 253

[128] Sun, M., Vikhlinin, A., 2005, Revealing the Interaction between the X-Ray Gas of Starburst Galaxy UGC 6697 and the Hot Intracluster Medium of A1367, ApJ, 621, 718

[129] Takeda, H., Nulsen, P. E. J., Fabian, A. C., 1984, Ram pressure stripping in a changing environment, MNRAS, 208, 261

[130] Toniazzo, T., Schindler, S., 2001, Gas dynamic stripping and X-ray emission of cluster elliptical galaxies, MNRAS, 325, 509

[131] Toomre, A., Toomre, J., 1972, Galactic Bridges and Tails, ApJ, 178, 623

[132] Tosa, M., 1994, Formation of a retrograde spiral arm induced by a Ram pressure, ApJ, 426, 81

[133] Valluri, M., 1993, Compressive tidal heating of a disk galaxy in a rich cluster, ApJ, 408, 57

[134] Valluri, M., Jog, C., 1991, H I deficiency in cluster spiral galaxies - Dependence on galaxy size, ApJ, 374, 103

[135] van Gorkom, J. H., 2003, Interaction of Galaxies with the ICM, in Carnegie Observatories Astrophysics Series, Vol. 3: Clusters of Galaxies: Probes of Cosmological Structure and Galaxy Evolution, ed. J. S. Mulchaey, A. Dressler, and A. Oemler, Cambridge Univ. Press

[136] Veilleux, S., Bland-Hawthorn, J., Cecil, G., Tully, R. B., Miller, S. T., 1999, Galactic-Scale Outflow and Supersonic Ram-Pressure Stripping in the Virgo Cluster Galaxy NGC 4388, ApJ, 520, 111

[137] Vollmer, B., Cayatte, V., Boselli, A., Balkowski, C., Duschl, W. J., 1999, Kinematics of the anemic cluster galaxy NGC 4548. Is stripping still active?, A&A, 349, 411

[138] Vollmer, B., Marcelin, M., Amram, P., Balkowski, C., Cayatte, V., Garrido, O., 2000, The consequences of ram pressure stripping on the Virgo cluster spiral galaxy NGC 4522, A&A, 364, 532

[139] Vollmer, B., Cayatte, V., Balkowski, C., Duschl, W. J., 2001, Ram Pressure Stripping and Galaxy Orbits: The Case of the Virgo Cluster, ApJ, 561, 708

[140] Vollmer, B., Braine, J., Balkowski, C., Cayatte, V., Duschl, W. J., 2001b, ^{12}CO(1-0) observations of NGC 4848: a Coma galaxy after stripping, A&A, 374, 824

[141] Vollmer, B., 2003a, NGC 4654: Gravitational interaction or ram pressure stripping?, A&A, 398, 525

[142] Vollmer, B., Huchtmeier, W., 2003b, Atomic gas far away from the Virgo cluster core galaxy NGC 4388. A possible link to isolated star formation in the Virgo cluster?, A&A, 406, 427

[143] Vollmer, B., Balkowski, C., Cayatte, V., van Driel, W., Huchtmeier, W., 2004a, NGC 4569: Recent evidence for a past ram pressure stripping event, A&A, 419, 35

[144] Vollmer, B., Beck, R., Kenney, J. D. P., van Gorkom, J. H., 2004b, Radio Continuum Observations of the Virgo Cluster Spiral NGC 4522: The Signature of Ram Pressure, AJ, 127, 3375

[145] Vollmer, B., Huchtmeier, W., van Driel, W., 2005a, NGC 4254: a spiral galaxy entering the Virgo cluster, A&A, 439, 921

[146] Vollmer, B., Braine, J., Combes, F., Sofue, Y., 2005b, New CO observations and simulations of the NGC 4438/NGC 4435 system. Interaction diagnostics of the Virgo cluster galaxy NGC 4438, A&A, 441, 473

[147] Vollmer, B., Soida, M., Otmianowska-Mazur, K., Kenney, J. D. P., van Gorkom, J. H., Beck, R., 2006, A dynamical model for the heavily ram pressure stripped Virgo spiral galaxy NGC 4522, A&A, 453, 883

[148] Voges, W., Boller, T., Dennerl, K., Englhauser, J., Gruber, R., Haberl, F., Paul, J., Pietsch, W., Trmper, J., Zimmermann, H. U., 1996, Identification of the ROSAT All-Sky Survey Sources, in: Proc. Röntgenstrahlung from the Universe, eds. Zimmermann, H.U., Trmper, J., and Yorke, H., MPE Report 263, p. 637-640

[149] Wang, Q. D., Owen, F., Ledlow, M., 2004, X-Raying A2125: A Large-Scale Hierarchical Complex of Galaxies and Hot Gas, ApJ, 611, 821

[150] Warmels, R. H., 1988a, The H I properties of spiral galaxies in the Virgo Cluster. I - Westerbork observations of 15 Virgo Cluster galaxies. II - One-dimensional Westerbork observations of 21 galaxies, A&AS, 72, 19

[151] Warmels, R. H., 1988b, The HI Properties of Spiral Galaxies in the Virgo Cluster - Part Two - One-Dimensional Westerbork Observations of 21 Galaxies, A&AS, 72, 57

[152] Warmels, R. H., 1988c, The HI properties of spiral galaxies in the Virgo Cluster. III - The HI surface density distribution in 36 galaxies, A&AS, 72, 427

[153] White, D. A., Fabian, A. C., Forman, W., Jones, C., Stern, C., 1991, Ram-pressure stripping of the multiphase interstellar medium of the Virgo cluster elliptical galaxy M86 (NGC 4406), ApJ, 375, 35